Proceedings of the 6th AAWE Workshop

Hosted online by the

Glenn Department of Civil Engineering
Clemson University

May 12-14, 2021

Table of Contents

Welcome and Introduction

Welcome to the 6th AAWE workshop hosted online by the Glenn Department of Civil Engineering at Clemson University. The workshop was held to fill a gap created by the COVID-19 induced postponement of the Americas Conference for Wind Engineering that is now scheduled for May 17-19, 2021 in Lubbock, Texas. The goal of the workshop is to give research students an opportunity to share their wind engineering research work with the wider wind engineering community.

Interest in the workshop has been very positive. We have received 82 abstracts from 28 different institutions across North America and beyond. The abstracts span a broad range of wind engineering research and are a very positive sign for the future of wind engineering research.

As well as the submitted papers, we also have three excellent keynote speakers. Dr. Anne Cope (IBHS) will launch the workshop with a talk about the impact of full-scale testing at the IBHS Research Center and critical needs in wind research for homes & businesses. The second day will begin with Dr. Tracy Kijewski-Correa (Notre Dame) with a talk on the role of wind engineers in advancing climate-responsive and risk-informed sustainable development. The final keynote will be by Dr. Pedro Fernandez-Caban (Clarkson) on enhancing the wind performance of civil infrastructure through “Online” Cyber-Physical Wind Tunnel Simulation.

We will also host Dr. Joy Pauschke (National Science Foundation program director) who will talk about funding options for wind engineering. The first days will end with social times and the opportunity to learn more about the Natural Hazards Engineering Research Infrastructure facilities. Wednesday will cover the experimental facilities at the University of Florida and Florida International University. On Thursday you can learn about the DesignSafe Cyber Infrastructure. The Workshop will close on with the quadrennial AAWE Awards ceremony.

I hope that you find the workshop invigorating and stimulating.

Nigel Berkeley Kaye, Workshop Chair
Clemson University

Scientific Committee

Members of the scientific committee assisted with recruiting keynote speakers, advice on workshop logistics, chairing sessions, and reviewing the large number of abstracts submitted. They are listed below in alphabetical order with their names hyperlinked to their webpages.

- Girma Bitsuamlak
- Luca Caracoglia
- Tommy Cousins
- Peter Datin
- Catherine Gorle
- Nigel Kaye (Chair)
- Greg Kopp
- Chris Letchford
- Frank Lombardo
- Murray Morrison
- M. Z. Naser
- Weichiang Pang
- David Prevatt
- Dorothy Reed
- David Roueche
- Brandon Ross
- Michael Stoner
- Ali Tohidi
- Ioannis Zisis

6th AAWE Workshop Program

Wednesday May 12

(Time key Eastern, Central, Mountain, Western)

11:00-11:10 **10:00-10:10** **9:00-9:10** **8:00-8:10**	**Welcome and workshop opening**	
11:10-12:10 **10:10-11:10** **9:10-10:10** **8:10-9:10**	**Keynote I Dr. Anne Cope** (Chair, Dr. Marc Levitan) "The impact of full-scale testing at the IBHS Research Center and critical needs in wind research for homes & businesses"	
12:10-1:50 **11:10-12:50** **10:10-11:50** **9:10-10:50**	**Parallel Session I**	
	Modelling and AI **(Chair Dr. M.Z. Naser)**	**Field Studies I** **(Chair Dr. Dorothy Reed)**
12:10-12:22 11:10-11:22 10:10-10:22 9:10-9:22	(041) "Statistical Investigation of Wind Duration Using A Refined Hurricane Track Model" Wang & Wu	(044) "Multi-event comparative analysis of common wind damage patterns from recent windstorms" Roueche & Nakayama
12:22-12:34 11:22-11:34 10:22-10:34 9:22-9:34	(077) "Data-driven simulation of asymmetric hurricane wind fields for community resilience planning" Guo & van de Lindt	(046) "Wind-induced failures and structural modeling of large-volume buildings impacted by Hurricane Michael (2018)" Marshall, Roueche, Berman, Roberts, & Blue
12:34-12:46 11:34-11:46 10:34-10:46 9:34-9:46	(015) "3D nonlinear tropical cyclone boundary layer model: From meteorological perspective to wind engineering applications" Hu & Kareem	(039) "Detection and classification of damages to civil infrastructure using a video-monitoring tool" Whiteman, Fernandez-Caban, Marin, Tezcan, Wu, & Cheng
12:46-12:58 11:46-11:58 10:46:10:58 9:46-9:58	(066) "Model for simulating extreme wind speed distribution parameters for hurricane winds" Dannemiller, Smith, & Morse	(058) "Wireless Sensor Network System Data Acquisition and Analysis using DesignSafe" Sridhar, Pinelli, Zhang, Subrumanian, Wang, Sun, Lazarus, & Besing
12:58-1:10 11:58-12:10 10:58-11:10 9:58-9:10	(024) "Deep Reinforcement Learning-based Decision Support System for Transportation Infrastructure Management under Hurricane Events" Li & Wu	(061) "Development of a Wireless Sensor Network" Wang, Sun, Subrmanian, Pinelli, Lazarus
1:10-1:22 12:10-12:22 11:10-11:22 10:10-10:22	(027) "Artificial Neural Network models to study wind-induced response of large-span roofs and suspension bridges" Rizzo & Caracoglia	(062) "Validation and Calibration of a Wireless Sensor Network" Zhang, Sridhar, Subramanian, Pinelli, Lazarus, Wang, Sun, & Besing
1:22-1:34 12:22-12:34 11:22-11:34 10:22-10:34	(080) "Applicability of DAD methodology for low-rise buildings to European and Italian wind load standards" Crisman, Caracoglia, & Noè	(047) "Field monitoring the wind-induced response of a large-area fabric membrane structure" Roueche, Marshall, Stiles, Jackson, Anderson, & Davidson
1:34-1:46 12:34-12:46 11:34-11:46 10:34-10:46	(007) "Active Machine Learning in Large Scale Wind Tunnel experiments" Chauhan, Ojeda-Tuz, Shields, Gurley, & Caterilli	(079) "The 3 March 2020 Cookeville, Tennessee Tornado Damage Report" Lopez & Lombardo

	24 minute break		
2:10-3:46 **1:10-2:46** **12:10-1:46** **11:10-12:46**	**Parallel sessions II**		
	Computational Wind Engineering I **(Chair Dr. Girma Bitsuamlak)**		**Structural response I** **(Dr. Weichiang Pang)**
2:10-2:22 1:10-1:22 12:10-12:22 11:10-11:22	(003) "Modeling Natural Ventilation in Refugee Healthcare Shelters" Hochschild & Gorle		(038) "A probabilistic composite resistance model for the vertical load path in typical residential construction" Rittelmeyer & Roueche
2:22-2:34 1:22-1:34 12:22-12:34 11:22-11:34	(073) "Using the Jupyter Notebooks as a tool for CFD simulations" Ding & Kareem		(042) "Probabilistic Wind Hazard Analysis for Performance-Based Wind Design of Buildings: Hazard Curve, Wind Demand and Loading Protocol" Wang & Wu
2:34-2:46 1:34-1:46 12:34-12:46 11:34-11:46	(075) "Generation of inflow velocity field for CFD analyses using GPUs" Ding & Kareem		(018) "A component-based interior and contents hurricane vulnerability model for low-rise residential buildings" Silva de Abreu, Pinelli, Gurley, & Yarasuri
2:46-2:58 1:46-1:58 12:46-12:58 11:46-11:58	(012) "Full-scale experimental investigations on a naturally ventilated building and validation of simulation models" Chen & Gorle		(033) "Performance and Fragility of Elevated Structures During Hurricane Events" Ibrahim, Elawady, & Prevatt
2:58-3:10 1:58-2:10 12:58-1:10 11:58-12:10	(036) "Large-eddy simulations of combined wind and buoyancy driven ventilation in a slum house in Dhaka, Bangladesh" Hwang & Gorle		(051) "Fragility analysis framework for transmission tower systems subjected to straight line winds" Dikshit & Alipour
3:10-3:22 2:10-2:22 1:10-1:22 12:10-12:22	(065) "Large-eddy Simulation of Wind Loads on a Roof-mounted Cube: A Means to Interpolate Experimental Data" Melaku, Doddipatla, & Bitsuamlak		(028) "Fatigue Life and Reliability Estimation of a Traffic Signal Structure using Long-Term Monitoring Data" Tsai & Alipour
3:22-3:34 2:22-2:34 1:22-1:34 12:22-12:34	(063) "Addressing Turbulence Model Form Uncertainty" Ciarlatani, Hao, & Gorle		(059) "Performance-Based Wind Design of Tall Buildings Considering the Nonlinearity in Building Response" Hareendram, Alipour, Shafei, & Sarkar
3:34-3:46 2:34-2:46 1:34-1:46 12:34-12:46	(022) "Evaluation of a multi-fidelity simulation framework for predicting wind pressure loads on buildings" Vargiemezis & Gorle		
	12 minute break		
4:00-5:00 **3:00-4:00** **2:00-3:00** **1:00-2:00**	**Panel discussion I - Dr. Dorothy Reed, Dr Greg Kopp, and Dr. Teng Wu.** "Future directions for wind engineering research"		
5:00-7:00 **4:00-6:00** **3:00-5:00** **2:00-4:00**	**Social hours and NHERI Experimental Facility workshop**		

Thursday May 13

11:00-12:00 **10:00-11:00** **9:00-10:00** **8:00-9:00**	**Keynote II Dr. Tracy Kijewski-Correa** (Chair, Dr. David Prevatt) "The Role of Wind Engineers in Advancing Climate-Responsive and Risk-Informed Sustainable Development: Opportunities and Responsibilities"
	10 minute break
12:10-1:46 **11:10-12:46** **10:10-11:46** **9:10-10:46**	**Parallel Session III**

	Windborne Debris (Chair Dr. Ali Tohidi)		**Field Studies II (Chair Dr. Frank Lombardo)**
12:10-12:22 11:10-11:22 10:10-10:22 9:10-9:22	(071) "Computational methods of windborne debris trajectories in a near-surface tornadic field" Chen & Lombardo		(045) "Automation of post-windstorm reconnaissance data enrichment using web scraping and machine learning" Rawajfih & Roueche
12:22-12:34 11:22-11:34 10:22-10:34 9:22-9:34	(026) "Modeling windborne debris trajectories in tornadoes" Abdelhady, Spence, & McCormick		(002) "An Absolute Pressure Sensing Mote for Measuring Full-Scale Wind Pressure Loads on Buildings" Hochschild & Gorle
12:34-12:46 11:34-11:46 10:34-10:46 9:34-9:46	(056) "Numerical modeling of debris flight in a one-cell tornado wind field" Tohidi		(057) "Characterization of surface roughness from LIDAR and anemometer measurements of near-surface storm winds." Besing, Lazarus, Sridhar, Wang, Subrmanian, Pinellie, Zhang, & Sun
12:46-12:58 11:46-11:58 10:46:10:58 9:46-9:58	(023) "Experimental and computational modeling of ember hot-spots on roofs during wildland fires" Nguyen & Kaye		(021) "Observations of the turbulent near wake of a bridge deck" Daniotti, Jackobsen, Snaebjornsson, & Cheynet
12:58-1:10 11:58-12:10 10:58-11:10 9:58-9:10	(008) "A stochastic model for the aerodynamics of irregularly shaped gravel" Ahsanullah & Kaye		(082) "Observations of incoming turbulent flow by dual wind lidar mounted on a bridge deck" Nafisifard, Jakobsen, Cheynet, Snaebjornsson, Sjoholm, & Mikkelsen
1:10-1:22 12:10-12:22 11:10-11:22 10:10-10:22	(016) Abstract Withdrawn		(006) "Retrieving wind speed and direction from WSR-88D single-Doppler measurements of thunderstorm winds" Ibrahim, Kopp, & Sills
1:22-1:34 12:22-12:34 11:22-11:34 10:22-10:34	(068) "Vulnerability Assessment of Structural Insulated Panels Subjected to Windborne Debris Impact" Saini & Shafei		(043) "Integrating survivor stories, tornado wind field models, and forensic investigations to reconstruct tornado events" Howie, Roueche, Lombardo, LaDue, & Mayeux
1:34-1:46 12:34-12:46 11:34-11:46 10:34-10:46	(078) "An analytical study into the performance of cross-laminated timber structures subject to tornado events" Stoner & Pang		(070) "Tornado Wind Speed Estimation Methods in Rural Forested Regions: The Alonsa, MB Tornado" Rhee, Stevenson, Lombardo, & Kopp

2:10-3:46 1:10-2:46 12:10-1:46 11:10-12:46	**Parallel sessions IV**		
	Computational Wind Engineering II **(Chair Dr. Catherine Gorle)**		**Wind Tunnels I** **(Chair Dr. David Roueche)**
2:10-2:22 1:10-1:22 12:10-12:22 11:10-11:22	(014) "New Model for Rain-Induced Interior and Contents Damage to Mid/High-Rise Buildings During Hurricane Events" Wei, Pinelli, Aghli, Jia, & Gurley		(034) "Wind Performance of Asphalt Shingles Using Full-Scale Experimentation" Tolera, Mostafa, Chowdhury, & Zisis
2:22-2:34 1:22-1:34 12:22-12:34 11:22-11:34	(025) "High Frequency Effect on Peak Pressure Computation on the TTU Building Using Synthetic Inflow Turbulence Generator" Mansouri & Selvam		(054) "Peak Wind Effects on Low-Rise Building Roofs and Rooftop PV Arrays" Braun, Chen, Chowdhury, Estephan, Gordon, Irwin, Johnson, Kennedy, Lyman, Raney, Reed, Sanford, & Wang
2:34-2:46 1:34-1:46 12:34-12:46 11:34-11:46	(029) "Numerical investigation of wind actions on elevated houses" Abdelfatah & Elawady		(049) "Wind speed maximum sustained, mean and gust factor comparison using publicly available H*WIND and Texas Tech University Hurricane Research Team data" Dannemiller, Smith, & Morse
2:46-2:58 1:46-1:58 12:46-12:58 11:46-11:58	(009) "Efficiency improvement and discussion of grid effects on the DSRFG method" Wang & Cai		(031) "Development of Standard Test Considering Pressure Equalization for Discontinuous Metal Roof (DMR) Systems." Lafontaine, Afanasyeva, & Prevatt
2:58-3:10 1:58-2:10 12:58-1:10 11:58-12:10	(064) "Hurricane Maria Hindcast Using WRF-LES: A Preliminary Comparison of Topographic Wind Speed-Up" Aponte-Bermudez, Masters, Santiago-Hernandez, & Cruz-Garcia		(019) "A partial-turbulence approach to estimate peak pressures on low-rise buildings with flat roofs" Guo, Wu, & Kopp
3:10-3:22 2:10-2:22 1:10-1:22 12:10-12:22	(067) "Time Variant Hurricane Modeling in Performance-based Wind Engineering" Ouyang & Spence		(013) "Examination of gust effect factor for side walls of rigid low-, mid-, and high-rise buildings" Wang & Kopp
3:22-3:34 2:22-2:34 1:22-1:34 12:22-12:34	(050) "On the computational efficiency of LES and hybrid RANS-LES models in building aerodynamics" Khaled & Aly		
3:34-3:46 2:34-2:46 1:34-1:46 12:34-12:46	(055) Abstract Withdrawn		
	14 minute break		
4:00-5:00 3:00-4:00 2:00-3:00 1:00-2:00	**Panel Discussion II** - Dr. Peter Datin (RMS), Dr. Maryam Asghari Mooneghi (AECOM), and Dr. Viet Le (ARUP). "Wind Engineering Practice"		
5:00-7:00 4:00-6:00 3:00-5:00 2:00-4:00	**Social hours and NHERI Design Safe workshop**		

Friday May 14

11:00-12:00 **10:00-11:00** **9:00-10:00** **8:00-9:00**	**Keynote III Dr. Dr. Pedro Fernandez-Caban** (Chair, Dr. Amal Elawady) "Enhancing the Wind Performance of Civil Infrastructure Through "Online" Cyber-Physical Wind Tunnel Simulation"		
	10 minute break		
12:10-1:22 **11:10-12:22** **10:10-11:22** **9:10-10:22**	**Parallel Session V**		
	Structural response II **(Chair Dr. Ioannis Zisis)**		**Wind Tunnels II** **(Chair Dr. Chris Letchford)**
12:10-12:22 11:10-11:22 10:10-10:22 9:10-9:22	(032) "A Scenario-based Hurricane Analysis Framework for Community-level Building Damage Estimation" Mazumder, Dumler, Enderami, & Sutley		(052) "Drag Coefficients and Wind Loads of Retrofitted Pipe Racks with High Blockage Ratios" Ou, Pang, & Stoner
12:22-12:34 11:22-11:34 10:22-10:34 9:22-9:34	(053) "High-Fidelity Probabilistic Collapse Assessment of Tall Steel Buildings under Extreme Winds" Arunachalam & Spence		(001) "Investigation of irregular-shaped buildings and their pressure distribution" Matus & Zisis
12:34-12:46 11:34-11:46 10:34-10:46 9:34-9:46	(072) "Probabilistic assessment of the nonlinear response of the 20-story SAC building under extreme wind loads through collapse" Ghaffay & Moustafa		(005) "Design and development of a new Boundary Layer Wind Tunnel at Florida International University" Matus, Mostafa, Sarma, Schwartz, & Zisis
12:46-12:58 11:46-11:58 10:46:10:58 9:46-9:58	(076) "Wind-induced response of buildings incorporating nonlinear fluid-structure interaction effects" Ghaffary & Moustafa		(040) "Aerodynamic testing and response evaluation of a large-scale high-rise building model at a high Reynolds number" Aly & Chapain
12:58-1:10 11:58-12:10 10:58-11:10 9:58-9:10	(010) "Structural Fragility Analysis of Tall Buildings and Towers via Artificial Neural Network Surrogate Modeling" Zhang & Caracoglia		(048) "Aerodynamics of low-rise buildings: large scale open-jet testing to address Reynolds number effects" Aly & Khaled
1:10-1:22 12:10-12:22 11:10-11:22 10:10-10:22	(004) "Stochastic flutter analysis of wind turbine blades via surrogate models: Artificial Neural Networks vs. Stochastic Collocation" Li and Caracoglia		(083) "Experimental Investigation of the Aerodynamics and Wind Loading of Buildings with Balconies" Ludena, Mooneghi, Chowdhury, & Irwin
	28 minute break		

1:50-2:50 **12:50-1:50** **11:50-12:50** **10:50-10:50**	**Parallel Session VI**		
	Structural response III **(Chair Dr. Michael Stoner)**		**Wind Tunnels III** **(Chair Dr. Murray Morrison)**
1:50-2:02 12:50-1:02 11:50-12:02 10:50-11:02	(011) "Estimation and Characterization of Nonstationary Inelastic Crosswind Responses of Base-Isolated Tall Buildings" Feng & Chen		(035) "Differences in flow structures of tornado vortex and efficiency of different tornado chambers" Verma & Selvam
2:02-2:14 1:02-1:14 12:02-12:14 11:02-11:14	(074) "Impact of Extreme Wind Loads on Sliding Glass Doors" Moravej, Arya, Simsir, & Jain		(017) "Uncertainty Quantification of Wind-tunnel Tests of a Low-Rise Building Model using the NIST Aerodynamic Database" Hubbard, Shelley, & Zhang
2:14-2:26 1:14-1:26 12:14-12:26 11:14-11:26	(020) "Assessment of load path through residential roofs using full-scale wind tunnel measurements" Stevenson, Morrison, & Kopp		(037) "Critical Evaluation of Roof Pressure Statistics over an Isolated Low-rise Building using NIST and TPU Aerodynamic Databases" Shelley, Hubbard, & Zhang
2:26-2:38 1:26-1:38 12:26-12:38 11:26-11:38	(081) "Fatigue performance of wood frame roof-to-wall connections with elastomeric adhesives under uplift cyclic loading" Alhawamdeh & Shao		(069) "A probabilistic loading model including the vertical angle of attack to estimate tornado loading" Zaldivar de Alba, Lombardo, Bodine, & Reinhart
2:38-2:50 1:38-1:50 12:38-12:50 11:38-11:50	(030) "Wind uplift resistance of Vinyl Siding- a standardized test protocol for multi-chamber pressure application" Lafontaine, Roueche, & Prevatt		(060) "Full-Scale Wind Testing to Determine the Role of Vertical Protrusions on Curtain wall Performance" Alawode, Vutukuru, Elawady, Chowdhury, & Lori
	10 minute break		
3:00-4:00 **2:00-3:00** **1:00-2:00** **12:00-1:00**	**Funding Options for Wind Engineering** **Dr. Joy Pauschke,** **National Science Foundation program director**		
	15 minute break		
4:15-5:00 **3:15-4:00** **2:15-3:00** **1:15-2:00**	**AAWE Quadrennial Awards Ceremony** **and** **Workshop Closing**		
5:00-7:00 **4:00-6:00** **3:00-5:00** **2:00-4:00**	**AAWE Members Meeting**		

The impact of full-scale testing at the IBHS Research Center and critical needs in wind research for homes & businesses

Dr. Anne Cope[a]

[a]*Institute for Business and Home Safety*

ABSTRACT:
Wind engineering spans a vast array of topics – bridges, high rise buildings, wind energy, and everyday homes and business. The Insurance Institute for Business & Home Safety (IBHS) focuses on the wind, wind-driven rain, and wind-borne embers that attack our homes and businesses. These hazards often lead to a cascade of damage that disrupt lives, displace families, and drive financial loss. Specifically, IBHS uniquely conducts full-scale testing on low-rise structures and building components and systems like asphalt shingles and garage doors. The IBHS Research Center features 105 fans generating winds up to 130 mph in the 21,000 square foot wind tunnel as well as smaller laboratory spaces enable this unique research. Full-scale investigation and demonstration of the vulnerability of these systems translates into real-world action through building codes, test standards, and voluntary participation in beyond-code programs like IBHS's FORTIFIED Home and FORTIFIED Commercial.

IBHS is a 501(c)3 fully sponsored by the property insurance and reinsurance industry and collaborates with universities and other research organizations on scientific initiatives that align with our mission to reduce the impact of severe weather on communities. IBHS also participates in code and test standard development committees to apply research findings and guide proposed changes with the physical science while advocating for the adoption and administration of modern building codes.

Post-disaster investigations and FEMA reports have highlighted the success of modern building codes in preventing avoidable losses, yet we continue to see damages to the building envelope. As a result, cladding loss and water ingress through fenestration remain critical areas for continued research to further strengthen codes. These research needs are echoed by our insurance company members, catastrophe modelers, FLASH, FEMA, and ICC partners as critical pieces of information that can continue to drive down losses from natural disasters.

The Role of Wind Engineers in Advancing Climate-Responsive and Risk-Informed Sustainable Development: Opportunities and Responsibilities

Tracy Kijewski-Correa[a]

[a]*co-Director, Integration Lab & Linbeck Associate Professor, Jointly Appointed in the Department of Civil and Environmental Engineering and Earth Sciences & Keough School of Global Affairs, University of Notre Dame*

ABSTRACT

To date the fields of disaster risk reduction, climate change adaptation and sustainable development have operated without great synergy, leading to not only inefficiencies but more often unintended consequences that undermine progress along any of these fronts. This realization has prompted increased calls to converge these efforts -- and the stakes could not be higher. Global populations continue to migrate to coastal areas exposed to cyclones whose frequency and intensity are increasing under the dynamics of a changing climate. As these migrations are also urbanizing, we are now concentrating more assets and lives in some of the most hazardous areas of the planet, particularly in developing economies. With exposure to climate-driven hazards rising globally (the US being no exception), new and persistent vulnerabilities are becoming increasingly difficult to ignore. In fact, global reinsurer Munich Re reported a record \$210B in damage caused by natural hazards in 2020 including \$95B in the US alone (Munich 2021). The record impacts of climate-driven hazards in 2020 (Erdman & Dolce 2021), all during a global pandemic, are only the latest in a decades-long trend. Wind damage is a considerable contributor to these losses, creating a great responsibility for wind engineers in leading the charge toward more resilient and sustainable communities worldwide.

This talk will introduce the unique opportunities for wind engineers to play a leadership role at the nexus between disaster risk reduction, climate change adaptation and sustainable development. Here we examine how contextually-appropriate solutions can meet the needs of vulnerable communities in the US as well as internationally. We further posit that an integrated, whole-of-society approach to assessing and mitigating disaster risk is essential to not only enhance community resilience but also to avoid "doing harm" through unintended consequences of short-sided development decisions. This presentation will further demonstrate the importance of a stakeholder-centered approach to ensure that research (1) not only responds to the expressed needs of wind-vulnerable communities, but (2) operates within the unique constraints and opportunities of that context, and (3) ultimately is viable for translation into policy and practice.

REFERENCES

Munich Re (2021) Record hurricane season and major wildfires – The natural disaster figures for 2020. January 07. https://www.munichre.com/en/company/media-relations/media-information-and-corporate-news/media-information/2021/2020-natural-disasters-balance.html#1351999949

Erdman, J. and Dolce, C. (2021) Record 22 Billion-Dollar Weather Disasters Struck the U.S. in 2020, NOAA Says, The Weather Channel, January 08. https://weather.com/storms/severe/news/2021-01-08-record-billion-dollar-us-weather-disasters-2020-noaa

Enhancing the Wind Performance of Civil Infrastructure Through "Online" Cyber-Physical Wind Tunnel Simulation

Pedro L. Fernández-Cabán, Ph.D.[a]

[a]*Assistant Professor, Clarkson University, Potsdam, NY*

ABSTRACT

Boundary layer wind tunnels (BLWT) remain the primary tool used in wind engineering for characterizing surface pressures on bluff bodies and fluid-structure interaction effects on wind sensitive civil infrastructure. Despite significant advancements in computational fluid dynamics (CFD) over the past few decades, the reliance on BLWT testing is partly attributed to the inability of numerical CFD models to accurately simulate the three-dimensional and highly turbulent features of atmospheric boundary layer flows near the earth's surface, and their interaction with the built environment. While the wind loading acting on a structure can be more accurately quantified in the BLWT, structural design and optimization procedures can only be performed numerically using high-level optimization algorithms. These algorithms can rapidly evaluate a wide range of competing designs to meet specified objectives. Therefore, the development of new cyber-physical approaches can couple the exploration of the design domain through numerical optimization algorithms with the accuracy of physical testing in the wind tunnel. Cyber-physical systems (CPSs) bridge the cyber world of computing and communications with the physical world to monitor, coordinate, and control physical processes. CPS components include sensing, actuation, communication interface systems, computational models or algorithms, and a physical system of interest.

This talk will present recently developed cyber-physical approaches that combine high-fidelity experimental BLWT testing, mechatronic building models, and numerically driven optimization strategies to autonomously improve the performance of civil infrastructure in the BLWT. The mechatronic models can bring about physical changes and adjust their aerodynamic or dynamic properties (through actuation) to enable exploration of a wide range of candidate designs in the BLWT. Two proof-of-concept studies of a low- and high-rise building are illustrated to demonstrate the potential of the CPS framework. Lastly, future opportunities in cyber-physical modeling and integration of novel optimization, machine learning, and decision-making strategies for evaluating and predicting wind-induced effects on structures will be discussed.

Investigation of irregular-shaped buildings and their pressure distribution

Manuel Matus [a*], Ioannis Zisis [b]

[a] *Florida International University, Miami, Florida, USA, mmatu016@fiu.edu*
[b] *Florida International University, Miami, Florida, USA, izisis@fiu.edu*

ABSTRACT:
Wind related damages on low-rise residential buildings have caused billions of dollars in losses. Building code provisions, that have been developed to mitigate such impact, were predominately based on testing models of regular plans. This study aims at evaluating the wind-induced loads on buildings with non-rectangular shapes. Six models with irregular shaped plans were tested at the Wall of Wind Experimental Facility at Florida International University. Preliminary results showed that separation zones are more complex than those observed in a regular shaped building and result in higher local and overall peak pressures. Preliminary area averaging curves have shown that current wind standards might underestimate the actual pressures building undergo. Additional testing is ongoing to better understand the effect of building shape in the local and overall pressure distribution.

Keywords: wind load, low-rise building, irregular-shaped

1. INTRODUCTION

Extreme wind events have caused billions of dollars in losses in the low-rise residential building sector and are expected to increase to 39 billion dollars by 2075 (USDOC 2010, CBO 2019). Current wind standards provide guidance for the safe design of residential structures to reduce potential damages due to wind induced loads (ASCE 7-16). These wind load provisions have been developed based on results obtained from wind tunnel testing on regular shaped structures in the late 1970’s (Akins et al., 1977, Davenport et al., 1977 and Stathopoulos 1979) and have been enhanced and improved over the next few decades through several wind tunnel studies. With advancements on technology and construction techniques, the shapes of structures have become considerably more complicated than just rectangular and squared shapes. As a result, several wind-tunnel and numerical investigations have been carried out to better understand the effects of extreme wind events on such structures; however, most have focused on mid- to high-rise structures (Shuai et al., 2019; Stathopoulos et al., 1993; Mashalkar et al., 2015; Gomez et al., 2005; Young et al., 2016; Souvik et al., 2014; Yi et al., 2016, 2017, 2020; Don-Xue et al., 2017).

Although current building codes provides guidance on how to account for building plan irregularities, there are no guidelines on how to account for the aerodynamic effects caused by complex shapes. Some investigations have concluded that there has been a lack of attention on the investigation on low-rise residential buildings and that the current building code wind provisions underestimates the actual wind loads on such structures (Stathopoulos 1984 and Jin et al., 2020).

2. METHODOLOGY AND TEST PLAN

* Manuel Matus

To obtain the most common irregular shapes of low-rise residential structures, several satellite images of South Florida residential areas were obtained and visually analysed. From these images, T, L and C were observed to be the most common shapes. Having identified the shapes, dimensions were obtained and a total of seven models were designed and constructed (two T-, L- and C- and one Rectangular-shaped model) out of 3/8” plexiglass, at a 1:50 scale and instrumented with approximately 350 pressure taps each. The models were tested at the Wall of Wind (WOW) Experimental Facility at Florida International University in Miami, Florida, with an open terrain exposure. The tests were carried out at 30 mph with a 15degree wind direction step.

3. RESULTS

From the experimental data obtained, pressure coefficients ($C_{p,mean}$ and $C_{p,3s}$) were acquired and some of the contour plots are presented here. The rectangular model served as the base model and was compared against NIST and TPU results with satisfactory agreement (Ho et al., 2005, Tamura 2012). Representative cases of the $C_{p,mean}$ for a T- and an L-shaped models at 0 degrees is presented in Figure 1 and Figure 2. The pressure distributions reveal that these structures develop more separation zones than a regular shaped structure due to the increased number of sharp edges/corners, thus experiencing more local and overall peaks. Area averaging calculations, for roof and walls, were also generated with peak pressure coefficients for all examined wind directions. These graphs provide information to estimate the critical pressures that components and cladding (C&C) elements can experience based on their different surface areas. They also provide the means to compare results to current building code wind load provisions envelope curves. This preliminary exercise showed that current recommendations may underestimate the wind-induced pressures on more complex building shapes.

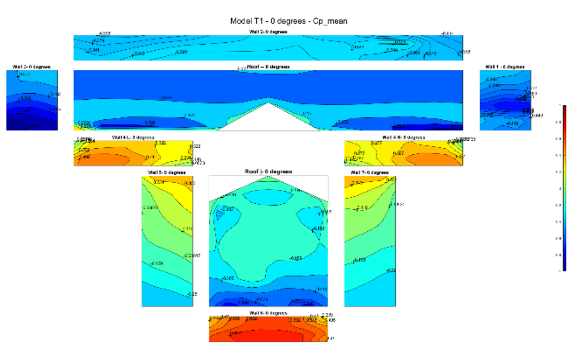

Figure 1. Mean Cps model T1

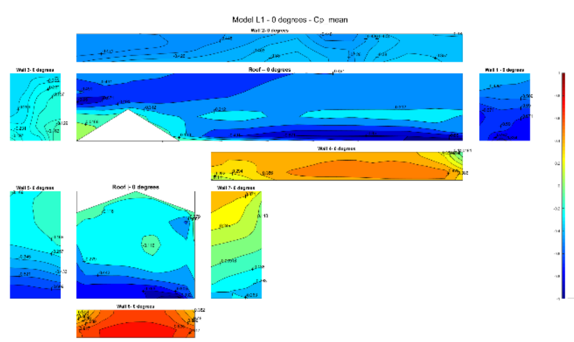

Figure 2. Mean Cps model L1

4. CONCLUSIONS

Low-rise residential structures are highly susceptible to wind-induced damage. Substantial economical loses indicate the urgent need to enhance the survivability and resilience of residential construction. Wind load provisions were developed based on regular-shaped isolated-models tested in wind tunnel over the past 40 years. Today’s built environment has evolved in structures having complex shapes making the design process of such structures somewhat intuitive. The work presented in this paper provides preliminary findings obtained from testing seven irregular shaped models at the WOW Experimental Facility. Results show that buildings having irregular plans have more edges where flow separation occurs, areas which are known to develop high suction zones thus resulting in high local and overall peak pressure coefficients. Area averaging curves developed from the tested cases, show that ASCE 7-16 might underestimate the loads that buildings with irregular shapes undergo. A comprehensive investigation is needed to fully understand the effect of irregular plans in the local and overall pressure distribution as well as the aerodynamics of such structures to mitigate wind induced damages.

5. REFERENCES

C. B. O. Congress of the United States, "Potential Increase in Hurricane Damage in the United States: Implications for the Federal Budget," June 2016.

Dong-Xue Zhao, Bao-Jie He. 2017. Effects of architectural shapes on surface wind pressure distribution: Case studies of oval-shaped tall buildings. Journal of Building Engineering. 2017. 12 (2017) 219-228. DOI:http://dx.doi.org/10.1016/j.jobe.2017.06.009

Gomes M. G., Rodrigues A. M., and Mendes P. 2005. Experimental and numerical study of wind pressures on irregular-plan shapes. Journal of Wind Engineering and Industrial Aerodynamics.

Ho, T. C. E., D. Surry, D. Morrish, and G. A. Kopp. 2005. The UWO contribution to the NIST aerodynamic database for wind loads on low buildings. Part 1: Archiving format and basic aerodynamic data. Journal of Wind Engineering and Industrial Aerodynamics. 93 (1): 1–30. https://doi.org/10.1016/j.jweia .2004.07.006.

Jin Wang, Gregory A. Kopp. 2021. Comparisons of aerodynamic data with the main wind force-resisting system provisions of ASCE 7-16. I. Low-rise buildings. Journal of Structural Engineering. DOI:10.1061/(ASCE)ST.1943-541X.0002925.

Mashalkar B. S., Patil G. R., and Jadhav A. S. 2015. Effect of plan shapes on the response of buildings subjected to wind vibrations. IOSR Journal of Mechanical and Civil Engineering (IOSR-JMCE).

Shuai Shao, Tuji Tian, Qingshan Yang, Ted Stathopoulos. 2019. Wind-induced cladding and structural loads on low-rise buildings with 4:12-sloped hip roofs. Journal of Wind Engineering and Industrial Aerodynamics, Beijing China.

Souvik C., Sujit K. D., and Ashok K. A. 2012. Wind load on irregular plan shaped tall building - a case study.

Stathopoulos T. 1984. Wind loads on low0rise buildings: a review of the state of the art. Engineering Structures. Vol. 6. Issue 2. 1 1984- 119-135.

Stathopoulos, Ted and Zhou, Y. 1993. Computation of wind pressures on L-shaped buildings. Journal of Engineering Mechanics.

Tamura, Y. (2012), Aerodynamic Database for Low-Rise Buildings, Global Center of Excellence Program, Tokyo Polytechnic University, Database.

United States Department of Commerce (USDOC). 2010. Coastline Population Trends in the United States: 1960-2008.

Yi Li, Q.S. Li, Fubin Chen. 2017. Wind tunnel study of wind-induced torques on L-shaped tall buildings. Journal of Wind Engineering and Industrial Aerodynamics. 167 (2017) 41-50. DOI:http://dx.doi.org/10.1016/j.jweia.2017.04.013.

Yi Li, Qiu-Sheng Li. 2016. Wind-induced response based optimal design of irregular shaped tall buildings. Journal of Wind Engineering and Industrial Aerodynamics. 155 (2016) 1978-207. DOI:http://dx.doi.org/10.1016/j.jweia.2016.06.001.

Yi Li, Ru-Biao Duan, QIU-Sheng Li, Yong-Gui Li, Chao Li. 2020. Research on the characteristics of wind pressures on L-shaped tall buildings. Advances in Structural Engineering. DOI:10.1177/1369433220906934.

Young Tae Lee, Soo Li Boo, Hee Chang Lim, kunio Misutani. 2016. Pressure distribution on rectangular buildings with changes in aspect ratio and wind direction. Wind and Structures. Vol. 23, No. 5 (2016) 465-483. DOI:http://dx.doi.org/10.12989/was.2016.23.5.465.

An Absolute Pressure Sensing Mote for Measuring Full-Scale Wind Pressure Loads on Buildings

John Hochschild [a,*], Catherine Gorlé [b]

[a] *Stanford University, Stanford, CA, jhochsch@stanford.edu*
[b] *Stanford University, Stanford, CA, gorle@stanford.edu*

ABSTRACT:
Several studies comparing wind loads measured at the full- and model-scale on low-rise buildings have found peak pressures to be underestimated at the wind tunnel scale. However, there is a lack of data comparing full- and model-scale wind loads over larger buildings. Our objective is to leverage a new generation of absolute pressure sensors, such as the BMP388, to measure wind loads on large buildings. First, we determined that the sensor has low enough noise (1.3 Pa RMS) to make meaningful C_p measurements, and we demonstrated that it is capable of measuring fluctuations on the time scales associated with turbulence in a wind tunnel experiment. Subsequently, we have designed a low-cost, compact, wireless mote that features the BMP388. Two motes have been deployed on a high-rise building as a pilot deployment, with more to follow soon.

Keywords: Pressure sensors, full-scale measurements, wind tunnel testing

1. INTRODUCTION
Over the past decade, damage to buildings and infrastructure from severe weather events has tripled globally, now totaling $150 billion each year (Bienert, 2014). Wind-resistant design of buildings and their components reduces losses, fatalities, and disruptions. Wind tunnel measurements offer a standard approach for assessing design loads, but comparison of wind loads measured at the full- and model-scale on low-rise structures have consistently found peak pressures to be underestimated at the wind tunnel scale. (Richardson et al., 1997; Morrison et al., 2011). For high-rise buildings, there is a lack of data comparing full- and model-scale loads, primarily because previous studies relied on obtrusive differential sensors, which are impractical for such buildings.

The objective of this research is to leverage recent advances in absolute pressure sensors and wireless technology to unobtrusively install sensors on large, operational buildings and obtain full-scale wind pressure measurements. The deployment of a network of these sensor "motes" will enable us to collect an unprecedented amount of full-scale data for comparison to wind tunnel measurements as well as Computational Fluid Dynamics (CFD).

2. MOTE DESIGN
2.1. Sensor selection
A literature review and initial testing identified two candidate absolute pressure sensors: the BMP388 and the LPS25HB. These sensors, along with a high-resolution differential sensor as a baseline, were embedded in the top surface of a 20 cm cube in a wind tunnel to measure pressure statistics in a turbulent separation region. During the test, velocity was incrementally increased and then decreased; Figure 1(a) shows the results for the mean, rms, and peak negative pressure

* Lead presenter

coefficients. For both sensors, repeatable C_p measurements are possible when U_∞ > 10 m/s, since the influence of measurement noise on C_p becomes negligible at these higher velocities. Because the BMP388 showed a slightly lower ambient noise of 1.3 Pa RMS, it was selected for use in our network of pressure sensors.

2.2. Mote design

A datalogging mote featuring the BMP388 sensor was designed. The resulting device, shown in Figure 2, was designed to be inexpensive, wireless, and weatherproof. Each mote has three ports that connect to three pressure sensors (for redundancy) via short pieces of tubing. The ports are covered with a water-resistant mesh, which was shown through wind tunnel testing not to affect the flow. Pressure data is collected at 12.5 Hz and streamed live to the cloud over the cellular network. This functionality is provided by an Arduino MKR 1400 GSM. Extensive testing several motes showed the design to be a robust data-acquisition system. Additionally, the components that comprise the mote cost ~$300, significantly less than comparable commercially-available systems.

3. FUTURE WORK

Two motes have been installed on the roof of Seattle's Space Needle building as a test deployment. Following findings from this deployment, we will distribute 20-30 motes on the Space Needle's exterior. We intend to compare the measured full-scale pressures with those predicted through wind tunnel testing and CFD analysis. The results of this comparison will be used to advance the predictive capabilities of CFD and wind tunnel testing.

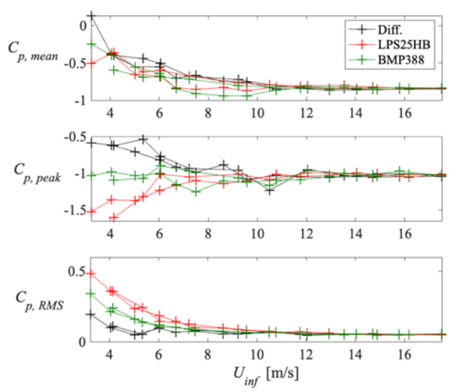

(a)

(b)

Figure 1. (a) Comparison of C_p statistics as a function of freestream velocity. Each sensor has two curves to assess repeatability. (b) Datalogging mote, top view. Each mote measures 24 x 21 x 4 cm.

ACKNOWLEDGEMENTS

This research is funded by NSF CAREER Award 1749610, and by Stanford's UPS endowment fund.

REFERENCES

Bienert, S., 2014. Extreme weather events and property values. Urban Land Institute.

Morrison, M., Brown, T., Liu, Z., 2011. Comparison of field and full-scale laboratory peak pressures at the IBHS research center, 13th International Conference on Wind Engineering, Amsterdam, Netherlands.

Richardson, G. M., Hoxey, R. P., Robertson, A. P., Short, J. L., 1997. The Silsoe structures building: comparisons of pressures measured at full scale and in two wind tunnels. Journal of Wind Engineering and Industrial Aerodynamics, 72: 187-197.

Modeling Natural Ventilation in Refugee Healthcare Shelters

John Hochschild [a,*], Catherine Gorlé [b]

[a] *Stanford University, Stanford, CA, jhochsch@stanford.edu*
[b] *Stanford University, Stanford, CA, gorle@stanford.edu*

ABSTRACT:
Natural ventilation can mitigate the airborne spread of the COVID-19 virus in refugee camp healthcare settings. We performed CFD simulations with the goal of finding configurations that achieve large ventilation rates while also mitigating reductions in indoor thermal comfort in hot climates. Based on the findings, we make three practical recommendations for refugee healthcare facilities in hot climates: first, infectious patients should be placed next to upper leeward windows if possible, so that exhaled viral particles are quickly drawn outside and diluted instead of spreading throughout the shelter. Second, during the day, lower windward windows and upper leeward windows should be opened, since the inflow of air over the cooler floor results in lower indoor air temperatures. Third, all windows should be opened overnight since this will both cool the shelter and minimize viral concentration.

Keywords: Natural ventilation, CFD, COVID-19

1. INTRODUCTION

The COVID-19 pandemic continues to affect displaced persons in refugee camps around the world. With populations of up to 800,000 people living in tightly-packed shelters, mitigating viral spread is imperative in these camps. In their official guidance on the design and construction of refugee camp COVID-19 healthcare facilities, the World Health Organization (WHO) recommends all facilities have 160 l/s of ventilation per person (WHO, 2020). Because it is now well-established that the SARS-CoV-2 virus spreads overwhelmingly through aerosols (Anderson et al., 2020), this high ventilation requirement will indeed limit the spread of the disease. However, many refugee camps see extreme temperatures in the summer months. Under these conditions, the prescribed ventilation rates can significantly worsen thermal comfort, potentially compromising adherence to the guidelines. This study's primary goal is to investigate the expected indoor temperatures in these settings, and to identify ventilation configurations that lower transmission risk while mitigating thermal comfort.

2. METHODS

2.1. Thermal model

A treatment shelter from the WHO guidelines document (WHO, 2020) was selected and a corresponding thermal model was constructed. The thermal model takes the indoor air volume, wall characteristics, and weather conditions as inputs and solves for wall and indoor air temperatures over time. The model assumes that each thermal body has a uniform temperature, and it uses an analytical envelope flow model relation to estimate the natural ventilation flow rates. The weather conditions input into the model were conditions representative of the Zaatari refugee camp, Jordan in July 2020. The wall temperatures predicted by the thermal model at the hottest

* Lead presenter

and coolest times of the day were used as boundary conditions in the CFD model to obtain a more accurate spatial representation of the ventilation flow patterns.

2.2. CFD model

Reynolds-Averaged Navier Stokes (RANS) simulations were performed with the k-ε turbulence model. Viral concentration was modeled by placing scalar sources at the locations of infectious patients. A high-resolution mesh of the shelter and surrounding environment was constructed, using 6.2 million cells. A log-law velocity profile was imposed at the inlet and the wall temperatures were specified following the thermal model results.

3. RESULTS

The simulation was performed for the five window configurations shown in Figure 1(a). Figure 1(b) shows how the mean viral concentration, averaged across a plane at height 1.5 m ("breathing plane"), is inversely related to air changes per hour (ACH). Figure 1(c) compares viral concentration with volume-averaged temperature for the different window configurations during the hottest time of day. We see how opening the lower windward windows and upper leeward windows (for a total of 16 windows) gives a 65-67% lower viral concentration but a similar indoor temperature compared with having just 4 windows open. If instead upper windward and lower leeward windows are open, the viral concentration is similar to the reversed case but the temperature is 0.4-0.5ºC higher. We therefore make the recommendation to open as many lower windward windows as possible during the day. Simulations for nighttime indicate that all windows should be opened since this will both cool the shelter to a more comfortable temperature and minimize viral concentration. Finally, for shelters in any climate we also recommend placing infectious patients next to upper leeward windows if possible, so that exhaled viral particles are drawn outside and diluted instead of spreading throughout the shelter.

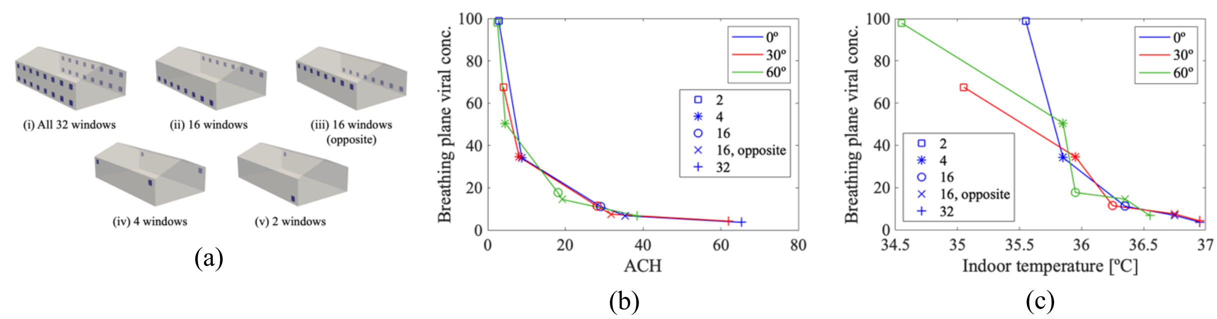

Figure 1. (a) Tested configurations, blue indicates an open window. (b)Viral concentration averaged across plane at z = 1.5 m versus air changes per hour. (c) Averaged viral concentration versus volume-averaged indoor temperature, for the daytime simulation.

ACKNOWLEDGEMENTS

This research is funded by a Stanford RISE COVID-19 Crisis Response grant.

REFERENCES

Anderson, E. L., Turnam, P., Griffin, J. R., Clarke, C. C., 2020. Consideration of the aerosol transmission for COVID-19 and public health. Risk Analysis, 902-907.

World Health Organization (WHO), 2020. Severe Acute Respiratory Infections Treatment Centre. WHO/2019-nCoV/SARI_treatment_center/2020.1.

6th American Association for Wind Engineering Workshop (online)
Clemson University, Clemson, SC, USA
May 12-14, 2021

Stochastic flutter analysis of wind turbine blades via surrogate models: Artificial Neural Networks *vs.* Stochastic Collocation

Shaoning Li[a,*], Luca Caracoglia[b]

[a]*Northeastern University, Boston, MA, USA, li.shao@northeastern.edu*
[b]*Northeastern University, Boston, MA, USA, lucac@coe.neu.edu*

ABSTRACT:
Recent studies have shown that flutter speed of rotating, wind turbine blades can be predicted accurately using a three-dimensional, analytically-based deterministic model. However, modelling uncertainties cannot be neglected since they influence the estimation of the flutter probability. Stochastic flutter analysis is therefore needed, accounting for relevant random input properties: (i) aerodynamic loads and (ii) blade structural properties. Physical Model Monte Carlo simulation is used for uncertainty quantification. This study proposes a novel approach, Surrogate Model-Monte Carlo methods to obtain the solution more efficiently in terms of computing time. Artificial Neural Networks (ANN) are proposed and investigated in this study as an alternative to other methods (e.g., Stochastic Collocation), generating a surrogate model. Numerical results indicate that ANN-based models are efficient for stochastic flutter analysis with acceptable prediction errors, and significant reduction of computing time.

Keywords: wind turbine blades, stochastic flutter analysis, surrogate models, artificial neural networks

1. INTRODUCTION

Coupled-mode flutter could happen in long and flexible wind turbine blades, which can lead to operational failure. Therefore, flutter is a non-negligible engineering problem during the design of large-scale wind turbine blades. Sensitivity analysis associated with a MW-sized wind turbine blade was investigated by Pourazarm et al. (2015); it was suggested that the uncertainty of blade parameters can influence the flutter speed and cause operational failure. In the case of stochastic flutter analysis of wind turbine blades, Physical Model Monte Carlo methods (PM-MC methods) are usually employed to investigate the influence of uncertainty and estimate flutter probability. Relying on a physical model within the MC environment is computationally inefficient, in the case of small probabilities requiring large sample populations. Therefore, Surrogate Model Monte Carlo methods (SM-MC methods) based on artificial neural networks (ANN) are proposed in this paper and compared to other methods to enable stochastic flutter analysis and reduce computing time.

2. MODEL AND METHODS

The differential equations of motion of the rotating, flexible blade are derived from the continuous deformable-body formulation by Houbolt & Brooks (1957). Theodorsen (1935) aerodynamic model is employed to represent the unsteady lift force and pitching moment. The Galerkin method is used to convert the differential problem into an equivalent eigenvalue problem at incipient instability. The vanishing of the damping (real part of any eigenvalue) at a specific value of angular velocity (i.e., blade angular speed) indicates the transition point between stable and unstable oscillation. In this study, the National Renewable Energy Laboratory (NREL) 5MW blade (Jonkman et al., 2009) is used; it is representative of modern, offshore wind turbine blades.

Prior to stochastic flutter analysis, a sensitivity analysis is considered to test the “robustness” of the blade model and to provide a functional relationship between the flutter speed and the random input parameters. ANN are examined in alternative to Stochastic Collocation, based on Lagrange

* Lead presenter

Polynomials (SC-LP), to build the SM-MC model and to predict stochastic flutter onset.

3. RESULTS AND DISCUSSION

Three input random variables are identified as the sources of uncertainty: (i) flow forces (lift), (ii) blade's torsional frequency, (iii) mass offset. Three scenarios are designed by selecting any two of three parameters to be independently and randomly generated; the third one is deterministic and equal to the baseline value. One of these scenarios, considering flow forces (represented by the slope of lift coefficient function at zero attack angle, $C_{L\alpha}$) and torsional blade frequencies (represented by torsional rigidity, *GJ*) as two independent random inputs, is presented in detail.

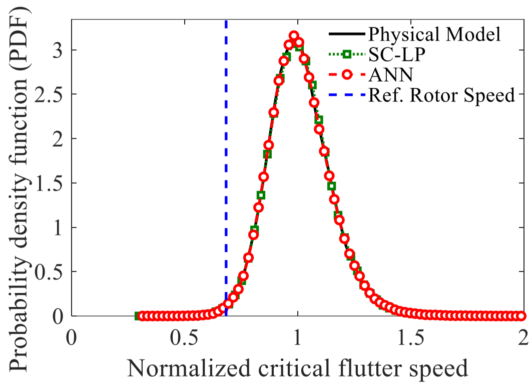

Figure 1. PDF of normalized critical flutter speed for independent, normally distributed input variables *GJ* and $C_{L\alpha}$.

Surrogate models are generated by both ANN (with calibrated layers and neurons) and SC-LP. The number of sampling points used is 10^5. Figure 1 illustrates, as an example scenario, the probability distribution of the normalized flutter speed for independent, normally distributed *GJ* and $C_{L\alpha}$. Inspection indicates that SM-MC methods, using ANN in particular, can provide robust approximation of the flutter solution. The computing time of PM-MC and SM-MC simulations is compared; SM-MC methods are generally 10 times faster than PM-MC methods. The details of other scenarios will be described in the final paper; SM-MC methods perform efficiently with acceptable errors in other cases as well.

4. CONCLUSIONS

SM-MC methods, in particular those exploiting the latest developments in the field of Artificial Intelligence, were successfully employed to replace PM-MC methods for stochastic flutter analysis. Three sources of uncertainty in the modelling of a reference blade were considered: (i) flow forces, (ii) torsional natural frequency, (iii) mass offset. Various scenarios were examined to predict the probability distribution of flutter speed, and the failure probability. Numerical results suggest that SM-MC methods can provide efficient and robust approximation of other PM-MC methods and can be employed to study uncertainty propagation and its effects on the performance of offshore wind turbine blades and their operational failure due to flutter.

ACKNOWLEDGMENTS: US National Science Foundation, Award CMMI-1462774.

REFERENCES

Houbolt, J. C. and Brooks, G. W., 1956. Differential equations of motion for combined flapwise bending, chordwise bending, and torsion of twisted nonuniform rotor blades. Report NACA TN 3905, NACA.

Jonkman, J., Butterfield, S., Musial, W., Scott, G., 2009. Definition of a 5-MW reference wind turbine. National Renewable Energy Laboratory. Report NREL/TP-500-38060.

Pourazarm, P., Caracoglia, L., Lackner, M. and Modarres-Sadeghi, Y., 2015. Stochastic analysis of flow-induced dynamic instabilities of wind turbine blades. Journal of Wind Engineering and Industrial Aerodynamics 137, 37–45.

Design and development of a new Boundary Layer Wind Tunnel at Florida International University

Manuel Matus *[a], Karim Mostafa *[b], Hrishikesh Dev Sarma *[c], Brian Schwartz [d], Ioannis Zisis [e]

[a] *Florida International University, Miami, FL, USA, mmatu016@fiu.edu*

[b] *Florida International University, Miami, FL, USA, kmost002@fiu.edu*

[c] *Florida International University, Miami, FL, USA, hsarm004@fiu.edu*

[d] *Florida International University, Miami, FL, USA, bschw026@fiu.edu*

[e] *Florida International University, Miami, FL, USA, izisis@fiu.edu*

ABSTRACT:
Wind tunnels are powerful tools when studying wind-structure interaction problems. The design and construction of a new atmospheric boundary layer wind tunnel involves various assumptions and intricacies depending on the wind-field requirements, and spatial, budgetary, and technological constraints. This paper describes the process involved in the design and development of a new small-scale atmospheric boundary layer wind tunnel in the Laboratory for Wind Engineering Research (LWER) at Florida International University (FIU). A model of the wind tunnel was initially built to verify scaled-down wind field characteristics. The design was proven to be adequate based on the model and consequently the construction of the proposed small-scale wind tunnel was completed. The wind field characteristics of the wind tunnel based on smooth flow condition are presented.

Keywords: Atmospheric boundary layer, Wind tunnel design, Wind field measurements, Large-scale testing, open circuit.

1. INTRODUCTION

Wind tunnels are essential tools when studying the effect of wind on buildings and other structures. Despite the developments in the field of Computational Fluid Dynamics (CFD), wind tunnels are still one of the most reliable tools for wind simulations. This paper discusses the process adopted in building a new atmospheric boundary layer (ABL) wind tunnel from conceptualization to design and construction. A typical ABL wind tunnel simulates the flow in the atmosphere between the earth surface and the gradient height. This is achieved through a combination of a fan system for initiating the air flow, a specially designed duct for treating the flow, and components such as spires and roughness elements for achieving the required velocity profile and turbulence characteristics. The design of these components is governed mainly by the test section velocity,

* Manuel Matus, Karim Mostafa, Hrishikesh Dev Sarma

test section dimensions and fan power. The design of several components involved in the flow treatment is based on empirical data and literature from earlier designs of similar wind tunnels. The target velocity for the wind tunnel under consideration was 33 ft/s (10 m/s) and the test section dimensions were 8 ft wide by 6 ft high. The construction of the new wind tunnel was completed, and preliminary measurements of the wind field were carried out. The results of the tests for smooth flow condition, i.e., without any spires or roughness elements are discussed in this paper.

2. METHODOLOGY

The construction process of a wind tunnel may vary depending on factors such as space restrictions, wind speed, test section dimensions, type of wind tunnel, etc. The two major factors that dictated the overall design of the proposed wind tunnel were the availability of space to construct the wind tunnel (i.e. approximately 60 ft) and the use of two fans that were available at the Laboratory for Wind Engineering Research at FIU. The type that was selected was a blowdown open circuit wind tunnel, which is comprised of several components/sections, such as fans, a diffuser, a settling chamber, a contraction and a fetch. The process to design the wind tunnel started by designing each individual component based on the fan capacity to generate a target wind speed. The fans were 75 hp each and had an inlet diameter of 55 inches resulting in a capacity of approximately 130,000 cfm. Taking into consideration the available capacity of the fans it was estimated that the wind tunnel could be designed to achieve a constant wind speed of 33 ft/s at the turntable located at the end of the fetch section. The section attached right next to the fans, the wide-angle diffuser, was designed to expand the area where the airflow enters to slow it down to reduce, as much as possible, any turbulence induced by the blades of the fans. The design of this section is critical as if it is not carefully determined, separation may occur, and considerable turbulence could be introduced into the airflow. To ensure a reduction of airflow speed and thus diminishing possible separation zones, several screens of different sizes were installed inside it (Mehta, 1979). The wide-angle diffuser expands the inlet area by a ratio of 1 to 2 where it then gets attached to the next section providing a cross-sectional area of 12 ft by 8 ft width and height. The settling chamber is the section taking the flow coming from the diffuser section and further treats the flow for reducing the flow’s turbulence and any separation that might have been developed in the diffuser by means of fine screens and a honeycomb wall (Dommelen et al., 2013). This section’s main purpose is to achieve a homogenous flow across the entirety of the 12 ft by 8 ft cross-sectional area that will be fed to the contraction section. The contraction section is responsible for accelerating the smooth flow fed from the settling chamber and diffuser (Mauro et al., 2017). This section reduced the cross-sectional area by a ratio of 2:1 providing an outlet area of 8 ft wide by 6 ft high. This section, like the diffuser, is critical as due to the curvature, it can induce separation zones that could introduce significant turbulence into the flow (Marshall, 1985). The last section attached to the contraction is the fetch, which is responsible for housing the floor roughness, castellated-walls, and spires to achieve the required boundary layer characteristics. At the end of this section, a turntable of 7.5 ft diameter was installed for the models to be rotated during testing.

3. PRELIMINARY RESULTS

The first wind field measurements were carried out without any roughness elements, spires or castellated walls upstream of the test section. For this, 13 pitot tubes and 4 Cobra Probes were installed at the centre of the fetch section in front of the turntable. The heights were 1, 2, 3, 5, 7, 9, 21, 26, 31, 36, 41, 46 and 71 in for the pitot tubes and 4, 18.5, 38.5 and 64.5 in for the cobra probes. Preliminary results (Figure 1 and Figure 2) show a smooth flow with no induced turbulence due to separation at any critical section. The 33 ft/s (10 m/s) target wind speed was also achieved as originally planned in the design. These preliminary results provide assurance to continue with the ongoing calibration process without any unwanted interference in the flow.

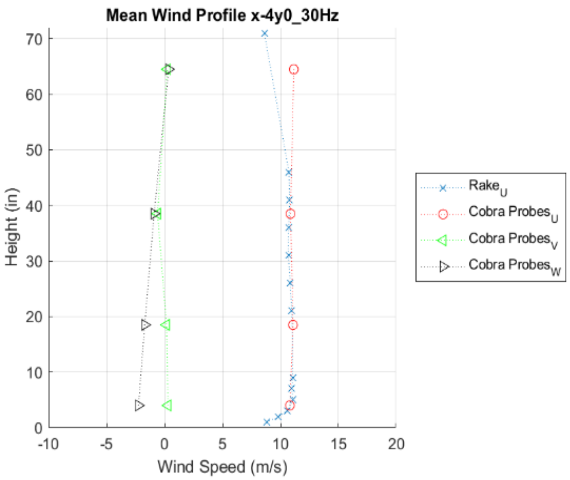

Figure 1. Wind speed profile

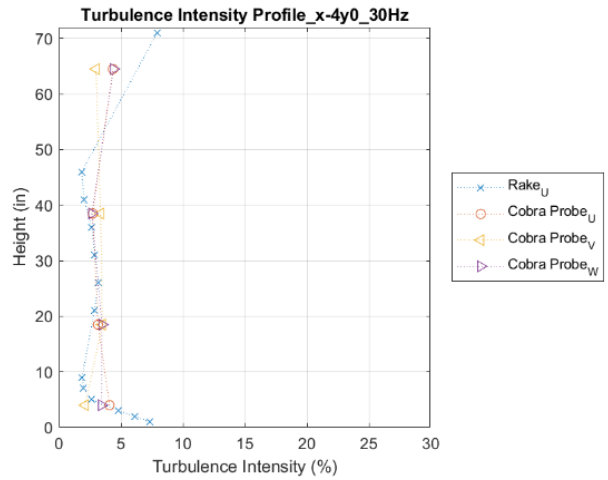

Figure 2. Turbulence intensity profile

4. CONCLUSION

A blow-down open-jet wind tunnel was conceptualized, designed and constructed at the Laboratory for Wind Engineering Research at FIU. The fans, diffuser, settling chamber, contraction and fetch were designed according to site and cost limitations. The final design produced a 48 ft long wind tunnel with a test section of 8 ft wide by 6 ft high. Preliminary results indicate a smooth (low turbulence) flow that will be further studied by adding the necessary for the ABL wind field spires and roughness elements.

REFERENCES

Mehta, R.D. 1979. “The Aerodynamic Design of Blower Tunnels with Wide-Angle Diffusers.” Progress in Aerospace Sciences, 18: 59–120.

Dommelen, V.R. 2013. “Design of an Atmospheric Boundary Layer Wind Tunnel.” Master’s Thesis, Technische Universiteit Eindhoven, Eindhoven, Netherlands.

Marshall, R.D. 1985. “Performance Requirements and Preliminary Design of a Boundary Layer Wind Tunnel Facility.” U.S. Department of Commerce, National Bureau of Standards, Center for Building Technology.

Mauro, S., Brusca S., Lanzafame, R., Famoso, F., Galvagno, A., Messina, M. 2017. “Small-scale open-circuit wind tunnel: Design Criteria, Construction and Calibration.” International Journal of Applied Engineering Research 12, no. 23, 2017.: 13649-13662.

Retrieving wind speed and direction from WSR-88D single-Doppler measurements of thunderstorm winds

Ibrahim Ibrahim[a,*], Gregory A. Kopp [b], David M. L. Sills [c]

[a] *Northern Tornadoes Project (Western University), London, ON, Canada, iibrah6@uwo.ca*
[b] *Northern Tornadoes Project (Western University), London, ON, Canada, gakopp@uwo.ca*
[c] *Northern Tornadoes Project (Western University), London, ON, Canada, david.sills@uwo.ca*

ABSTRACT:
The evaluation of wind load values is dependent on the historical wind speeds recorded by field measurements, mainly anemometers. Such one-point measurement procedure is sufficient for dealing with structures of smaller scales. Nevertheless, special structures like long-span bridges and electricity transmission lines need a more comprehensive procedure, especially for regions prone to extreme wind events of limited size like thunderstorms. These events are less probable to be picked up by one-point measurements. Accordingly, the current study explores the use of Doppler weather radar measurements to estimate wind speeds associated with thunderstorm weather systems. The study estimates localized wind speeds down to the scale of hundreds of meters by implementing an algorithm to separate different weather systems within each radar scan and resolving them separately. The estimated peak event wind speeds are compared with ASOS anemometer measurements for comparison.

Keywords: Doppler Radar, Wind Retrieval, NEXRAD, Non-synoptic Wind

1. BACKGROUND

Providing loading guidelines for the design of safe structures is one of the main concerns of Wind Engineering. Extreme value analysis is performed on a set of historical wind speed anemometer recordings. This results in estimates of the adequate design wind speeds corresponding to given return period for the analysed location. An example of this procedure is shown in the work done by (Lombardo et al, 2009). This procedure, when used with single anemometers or widely spaced anemometers, inherently assumes point-based loading which is adequate for structures with limited spatial extent. In the case of special structures like long-span bridges or electricity transmission line structures, evaluating wind loads based on anemometers will miss the effect of wind events with limited size, specifically, thunderstorms. To overcome this limitation, the current study explores the use of Doppler radar meaurements to estimate wind speeds and how they relate to anemometer measurements.

Weather radars were used by meteorologists after World War II. They can be operated under different scanning modes. The most common is Plan Position Indicatior (PPI). In this mode, the radar revolves around a vertical axis and scans a “cone’s surface” plane as the beam is tilted at an elevation angle upwards from the horizontal.The lowest elevation angle closest to the horizontal plane is typically around 0.5 degrees.During each rotation of a modern weather radar, the main parameters measured are reflectivity and Doppler velocity. The first parameter measures the strength of the signal reflected from air-borne reflectors (snow, rain droplets, dust, insects, etc.) back to the radar. The returning signal strength can indicate the type of reflector and thus helps meteorlogists with understanding the type of weather event scanned by the radar. Alternatively, the Doppler velocity measures the velocity component of reflectors towards or away from the

* Lead presenter

radar, which is directly associated with wind speeds. As early as 1968, (Browning and Dexlar, 1968) proposed an algorithm that estimates the mean wind speed using the Doppler velocity readings. As shown in Fig. 1, the measurements taken at a constant distance away from the radar (along a circumference) exhibit a harmonic trend. With the assumption that the measured points have the same wind magnitude and direction, the readings can be fitted to a harmonic wave where the amplitude and phase of the wave would be correspondent to the horizontal wind magnitude and direction respectively. This is applicable for the case where the elevation angle is very small (0.5^o) so the vertical component of wind velocity can be ignored.

The idea of fitting a complete horizontal scan to a harmonic wave is applicable only if the scanned surface represents the synoptic-scale wind. In the case where the scanned surface is comprised of more than one type of weather phenomenon (e.g., synoptic-scale winds plus winds generated by a thunderstorm), it is important to deal with each separately.Fig. 1 shows how a scan with two types of weather phenomena present can be processed to fit each in isolation.

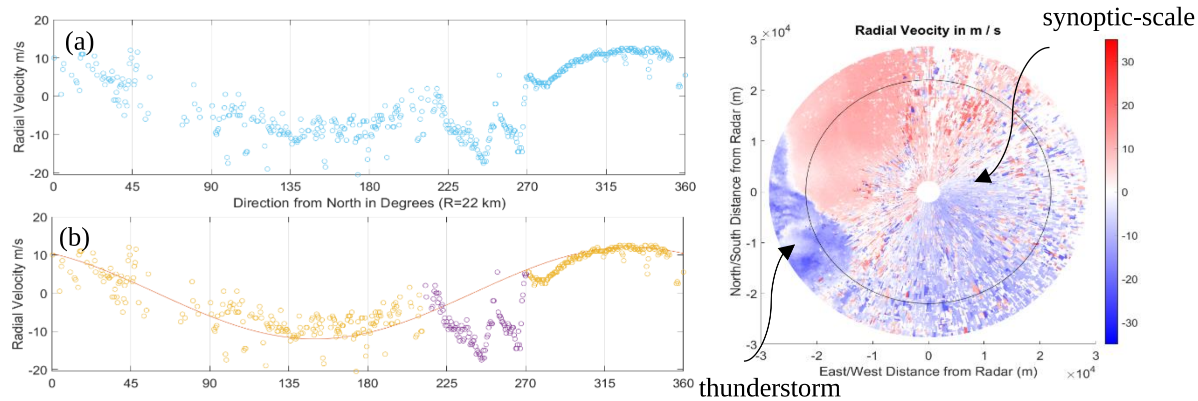

Figure 1. Measured points along circumference (a) with no separation, (b) with separation

2. METHODOLOGY AND RESULTS

The data processed is NEXRAD Level II data, which is provided by NOAA's NCEI[1]. The archived data (1991-present) from 160 radars are available for public use. The data are available in a format that can be processed using (Helmus and Collis, 2016) Py-ART python based library. Radar data were initially processed using the python toolkit before exporting them to a format that is readable by MATLAB.

After importing the pre-processed scans to MATLAB, a multi-step algorithm is then applied starting with functions from the Image Processing Toolbox. The aim is to produce a segmented version of the horizontal scan such that each segment would correspond to a distinct weather system. The sequence shown in Fig. 2 illustrates how the algorithm proceeds until it reaches the segmented scan.

The last step is to analyse each segment separately and estimate the wind speed and direction by fitting every cluster of subsequent points to a harmonic wave. The fitting procedure is repeated at every mesh-grid point using 10-degree segments around the analyzed point. The diagrams shown

[1] https://www.ncei.noaa.gov/access/metadata/landing-page/bin/iso?id=gov.noaa.ncdc:C00345

in Fig. 3 present the estimated magnitude and direction for a 1-km resolution grid of points from the scan in Fig. 1.

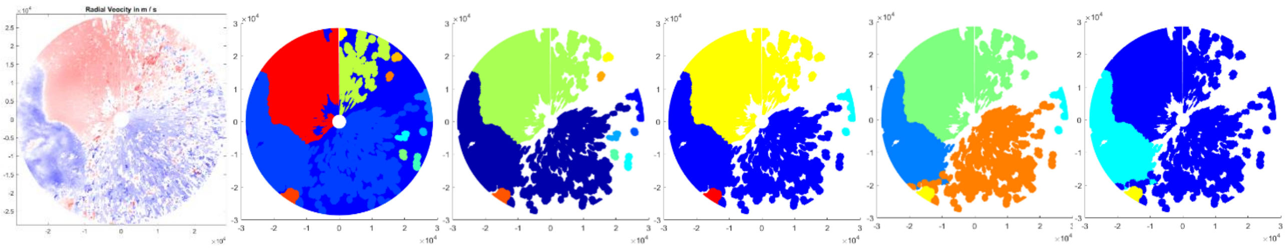

Figure 2. Different steps of the algorithms ending up with the final segmentation on the right

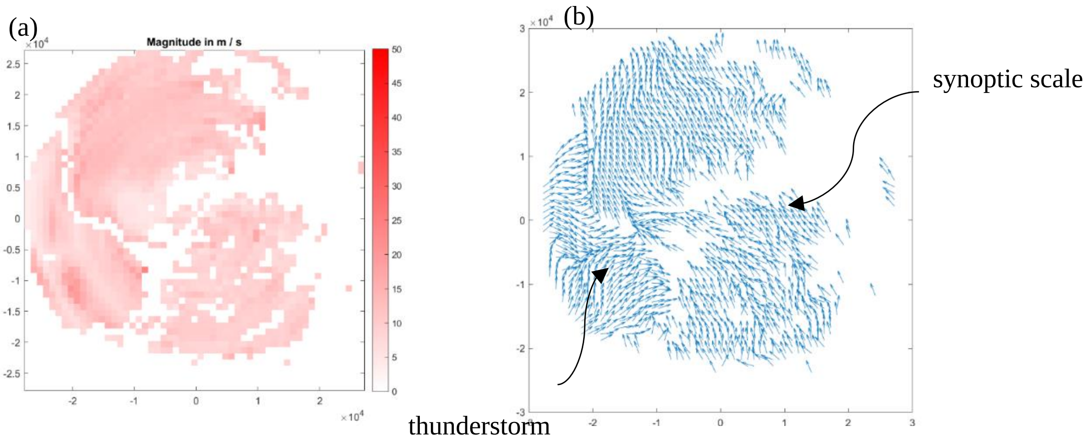

Figure 3. (a) Magnitude and (b) direction of retrieved wind and whitespace for missing data

3. CONCLUSION

The results produced by the algorithm show its ability to retrieve wind from more than one phenomenon with distinct features for each. The retrieved wind magnitudes and directions can be compared to wind anemometer measurements. Investigation of the relation between radar retrieved wind (typically at heights > 50 m from the ground) and anemometer results (typically at 10 m heights) can test the validity of using radar results in estimating close-to-ground wind speeds. If proven valid, the radar estimates have the advantage of spatial coverage, which can be considered as a network of anemometers. Such an approach would be a great advantage for estimating wind loads for special structures like long-span bridges and electricity transmission line structures.

REFERENCES

Browning, K.A., Wexler, R., 1968. The Determination of Kinematic Properties of a Wind Field Using Doppler Radar. Journal of Applied Meteorology.

Helmus, J.J., Collis, S.M., 2016. The Python ARM Radar Toolkit (Py-ART), a Library for Working with Weather Radar Data in the Python Programming Language. Journal of Open Research Software. 4-1.

Lombardo, F.T., Main, J.A., Simiu, E., 2009. Automated extraction and classification of thunderstorm and non-thunderstorm wind data for extreme-value analysis. Journal of Wind Engineering and Industrial Aerodynamics. 97, 120–131.

Active Machine Learning in Large Scale Wind Tunnel Experiments

Mohit Chauhan [a,*], Mariel Ojeda-Tuz [b,*], Michael Shields [c], Kurtis Gurley [d], Ryan Catarelli [e]

[a] *Johns Hopkins University, Baltimore, Maryland, USA, mchauha1@jhu.edu*
[b] *University of Florida, Gainesville, Florida, USA, ojedatuzm@ufl.edu*
[c] *Johns Hopkins University, Baltimore, Maryland, USA, michael.shields@jhu.edu*
[d] *University of Florida, Gainesville, Florida, USA, kgurl@ce.ufl.edu*
[e] *University of Florida, Gainesville, Florida, USA, rcatarelli@ufl.edu*

ABSTRACT:
Boundary Layer Wind Tunnel (BLWT) facilities are commonly used for assessing wind loads on structures. Although BLWT facilities routinely match 1st and 2nd-order wind field models, evidence suggests that turbulence in the roughness sublayer and the inertial sublayer exhibit non-Gaussian higher-order properties. These non-Gaussian properties can influence peak wind pressures, which govern certain structural limit states and play an important role in design. In this project, Machine learning methods are employed to identify relationships between roughness element configurations and higher-order statistical properties of the wind field. A semi-automated framework with an active learning portion and a wind tunnel experimental procedure is developed. The learning framework adaptively selects roughness profiles and launches new experiments in order to identify differing profiles with equivalent second-order equivalent flow. The premise is that second-order equivalent wind fields can differ in higher-order properties and therefore extreme value derived peak loads.

Keywords: Boundary Layer Wind Tunnel, Adaptive Learning, Machine Learning, peak wind loads

1. BACKGROUND AND MOTIVATION

This ongoing NSF sponsored research project (CMMI 1930389 & 1930625) investigates whether commonly achieved matching of first and second order wind field properties in BLWT flow is sufficient for producing consistent expected value peak wind pressures. We hypothesize that multiple roughness element configurations can produce equivalent second-order wind fields, but impart different higher-order properties and therefore different peak load metrics derived from extreme value analysis. Despite this widely recognized open question, such investigations have been limited in the past due to a lack of both suitable facilities to accommodate a large number of terrains and a means of rapidly informing and changing the test matrix between experiments.

This study harnesses the recent availability of two tools that, when used in tandem, improve the efficient high volume throughput of experimental wind tunnel investigations. The control system for an automated, high degree of freedom, rapidly reconfigurable roughness element grid and instrument gantry are integrated with a machine learning algorithm that chooses the next roughness configuration to investigate based upon the accumulated outcomes of every previous experiment. A Gaussian process regression based adaptive learning framework searches a bounded but flexible parameter space describing the possible roughness configurations to identify the parameter subspace that corresponds to second order equivalent boundary layer profiles. The next phase will then investigate the higher-order characteristics of this second-order equivalent subspace.

* Lead presenter

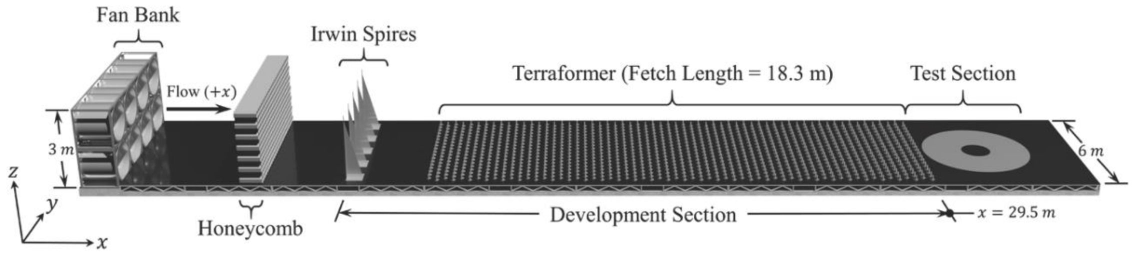

Figure 1. UFBLWT configuration

The University of Florida Boundary Layer Wind Tunnel (Fig. 1) offers a unique automated terrain roughness element system (Terraformer) which can independently reconfigure each of 1116 individual elements in less than 90 seconds (Catarelli et al. 2020). Three vertically aligned turbulence measuring Cobra probes are mounted on an automated articulating gantry (Fig. 2) programmed to move in three dimensions. In this manner, vertical turbulence profiles are measured during each experiment. This shared use facility is accessible through the NSF sponsored Natural Hazards Engineering Research Infrastructure (NHERI) program (CMMI 1520842 & 2037725).

2. METHODOLOGY

Two different wind profiles, produced by any pair of roughness element configurations ‘a’ and ‘b’, are considered second order equivalent if the turbulence intensity profiles in u (longitudinal) wind direction are equal in a statistical sense within the inertial sublayer and satisfy:

$$d(\boldsymbol{x}, \boldsymbol{x}^*) = \|I_u(\boldsymbol{x}) - I_u(\boldsymbol{x}^*)\|_2 \quad (1)$$

In Eq. (1), the distance metric ($d(\boldsymbol{x}, \boldsymbol{x}^*)$) of two different profiles is defined. $I_u(.)$ is the turbulence intensity profile in u direction, $\boldsymbol{x}$ and $\boldsymbol{x}^*$ are different Terraformer configurations. This equivalence metric is used to inform the learning algorithm that adaptively explores the bounded two-parameter Terraformer domain to identify second-order equivalent configurations. The approach in this study exploits the Adaptive Kriging-Monte Carlo Simulation (AK-MCS) (Echard et al. 2011) algorithm with a modified U learning function applied to the profile distance measure. Gaussian Process (GP) Regression is a non-parametric Bayesian approach to construct a surrogate model that, in our case, predicts the distance between two profiles and the associated prediction uncertainty at new (untested) terraformer configurations. The learning function then selects new Terraformer parameters based on the existing test data with the goal of identifying Terraformer configurations that produce second-order equivalent profiles.

Fig. 2 illustrates the main framework of this study. A semi-automated approach is adopted, where the adaptive learning portion is automated, and the user has full control over the wind tunnel experimental procedure. The framework begins by conducting a benchmark experiment against which second-order equivalence will be measure. A small number of initial experiments are conducted by sampling from the Terraformer parameters, the distance from the benchmark is computed, and these distances serve as training data to fit the GP regressor. The defined learning function selects a new sample and defines the next Terraformer configuration for the user to initialize the experiment and data collection. Following the experiment, the resulting profile is automatically collected, the distance from the benchmark computed, the GP surrogate model is updated, learning function evaluated and a new test initiated.

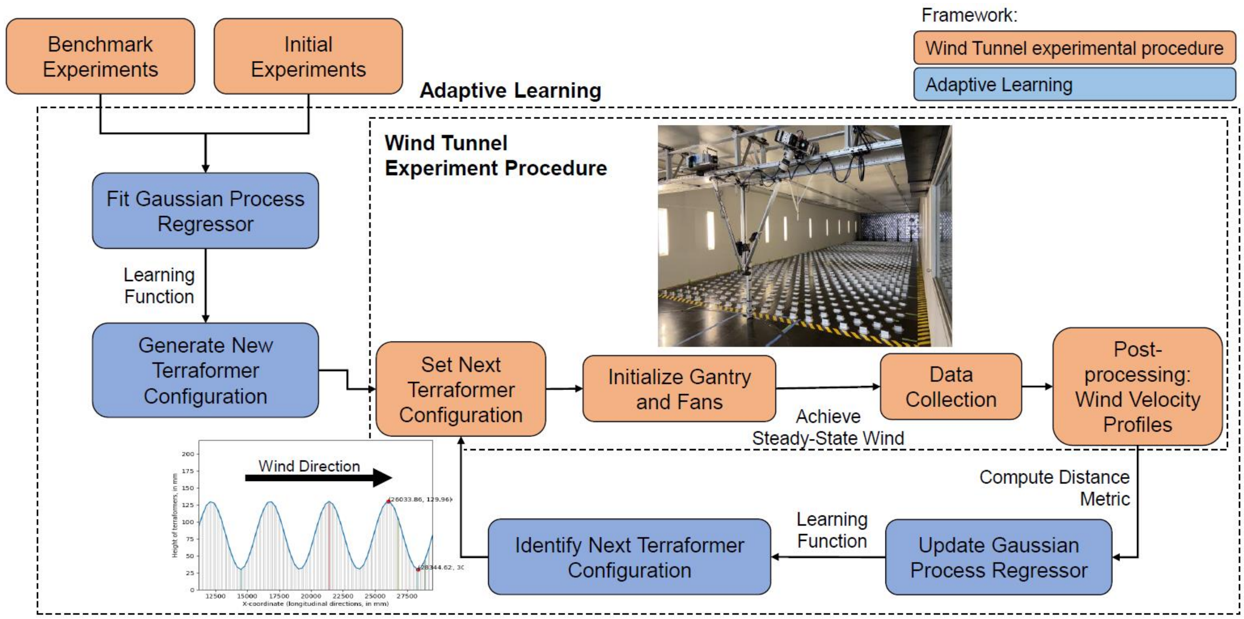

Figure 2. Flowchart of the adaptive learning based experimental procedure

3. CURRENT STATUS

The integrated Terraformer, gantry and adaptive learning experimental procedure has been successfully conducted for 287 element roughness configurations over a period of four weeks. The latest results and implications will be presented during the workshop. Currently, the data collected from the experimental procedure is being curated for publication in the NHERI DesignSafe Data Repository within the next 12 months.

ACKNOWLEDGEMENTS

This material is based upon work supported by the National Science Foundation under Grants CMMI-1930389, 1930625, 1520842, 2037725.

REFERENCES

Catarelli, R. A., Fernández-Cabán, P. L., Phillips, B. M., Bridge, J. A., Masters, F. J., Gurley, K. R., and Prevatt, D. O. (2020). “Automation and new capabilities in the University of Florida NHERI boundary layer wind tunnel.” Frontiers in Built Environment, 6

Echard, B., Gayton, N., and Lemaire, M., “AK-MCS: An active learning reliability method combining Kriging and Monte Carlo Simulation,” Struct. Saf., vol. 33, no. 2, pp. 145–154, 2011.

A stochastic model for the aerodynamics of irregularly shaped gravel

Md Safwan Ahsanullah [a,*], Nigel B Kaye [b]

[a]*Glenn Department of Civil Engineering, Clemson University, Clemson, SC, USA, mahsanu@clemson.edu*
[b]*Glenn Department of Civil Engineering, Clemson University, Clemson, SC, USA, nbkaye@clemson.edu*

ABSTRACT:
Damage from hurricanes hitting the U.S. between 1980 and 2018 totaled $862 billion (NHC). Post-storm investigations show wind-borne debris is a major contributor to total economic loss. This paper investigates the flight of compact wind-borne debris which has previously only been treated as spherical, ignoring lift forces and shape irregularity, resulting in a two-dimensional flight. However, the trajectory of a piece of gravel is not two-dimensional as its orientation changes during flight, altering the drag force and generating lift forces. This study proposes a stochastic model to resolve some key aspects of the trajectory due to the change in orientation of the debris particle during its flight. The model shows good agreement with experiments. Improved modeling of compact debris will improve our understanding of the risk of damage from windborne debris and enable improved mitigation measures resulting in more resilient communities.

Keywords: compact debris, debris flight, numerical, stochastic model, gravel, windborne debris

1. INTRODUCTION

Wind-borne debris and missiles in events of severe windstorms, hurricanes and other strong wind events have been observed to cause significant damage to the built environment. Reports after notable wind events show that the wind-borne debris had been a major contributor to the total economic loss (Minor, 2005). To address the issue of damage from wind-borne debris, building design codes have gone through several modifications over time. However, there still exists a significant knowledge gap around the motion initiation and resulting flight of a gravel. These problems can be solved only with a deeper understanding of the forces acting on particles of random shapes.

The standard flight equations treat debris particles as spheres (Baker, 2007; Holmes, 2004) and fail to model the stochastic nature of actual debris flight. This study proposes a stochastic model in an attempt to resolve some key aspects of the stochastic nature of the flight that originates due to the change in orientation of the debris particle during its flight, and, as a result, the alteration of the projected cross-sectional area, the lift and the drag coefficients.

2. EXPERIMENTS AND OBSERVATIONS

To gain insight on the motion of irregularly shaped gravel pieces moving through a fluid, a simple experimental setup is designed for this study. The setup consists of a clear-sided tank filled with water and gravel pieces of different sizes as representative of a typical compact debris. The main objective of the experiment is to observe the spread and the radial distances of the landing locations

* Lead presenter

of dropped gravel pieces. Five gravel sizes are used in the drop experiments while a total of 200 gravel pieces were dropped per gravel size.

The gravel pieces are observed to change their orientation during their flight, leading to alteration of drag forces and generation of lift forces, and their trajectories are neither linear, vertical nor self-repeating. All these findings contradict the underlying assumptions of standard debris flight equations. Due to these factors, the landing locations of the gravel pieces spread around the center, with a finite mean and standard deviation of radial distances of landing locations from the center of the base. This is qualitatively similar to the drop experiments for rod-like debris (Tohidi and Kaye, 2017).

3. MODEL DEVELOPMENT

The proposed stochastic model numerically solves the following coupled three-dimensional rectilinear differential equations that govern the motion of debris particles:

$$\frac{d^2\mathbf{x}}{dt^2} = \frac{\sum \mathbf{F}}{m} \tag{1}$$

$$\frac{d\mathbf{x}}{dt} = \mathbf{u} \tag{2}$$

where, $\mathbf{x}$ is the position vector, $\mathbf{u}$ is the velocity vector, $\Sigma\mathbf{F}$ is the net force acting on a debris particle and m is the mass of a debris particle. The bolded symbols here represent Cartesian vectors. The net force in Eq. 1 is the resultant of constant weight and buoyancy forces and varying drag and lift forces. The model randomly varies the drag and lift forces at each time-step during the debris flight by perturbing the non-dimensional projected area of the gravel piece (α), the aerodynamic force coefficients (C_D and C_L) and the lift force direction, $\mathbf{n}_L$. The overall range of C_D, C_L and α are determined based on wind tunnel measurements of the force coefficients (Chai et al, 2019) and laboratory measurements of gravel geometry. The lift force direction is altered by randomly perturbing the direction of the reference lift angle (θ) within the range $0° \leq \theta \leq 60°$.

4. MODEL RESULTS AND COMPARISON

The model varies the magnitudes of perturbations (δC_D, δC_L, $\delta\theta$ and $\delta\alpha$) of each of the varying parameters within their global ranges and simulates gravel drops for different combinations of perturbation magnitudes. The perturbation ranges $\delta C_D, \delta C_L$ and $\delta\alpha$ were varied from 0 to 50% of the overall range of the respective parameter in increments of 2.5% of the overall range while $\delta\theta$ was varied from 0° to 60° in 1.5° increments. This leads to a total of 41×21^3 possible combinations, and for each combination, simulation of 200 drops per gravel size leads to approximately 380 million drop simulations. Finally, an optimized combination of perturbation parameters, $(\delta C_D, \delta C_L, \delta\theta, \delta\alpha)_{opt}$, is obtained that results in good agreement between the numerical and experimental range of radial distances of landing locations. Fig. 1 shows how the numerical spread of landing locations for gradation A (largest gradation) and ranked radial distances compare to those obtained from the experiments. The solid line in the right-hand side figure shows perfect agreement line of unit slope.

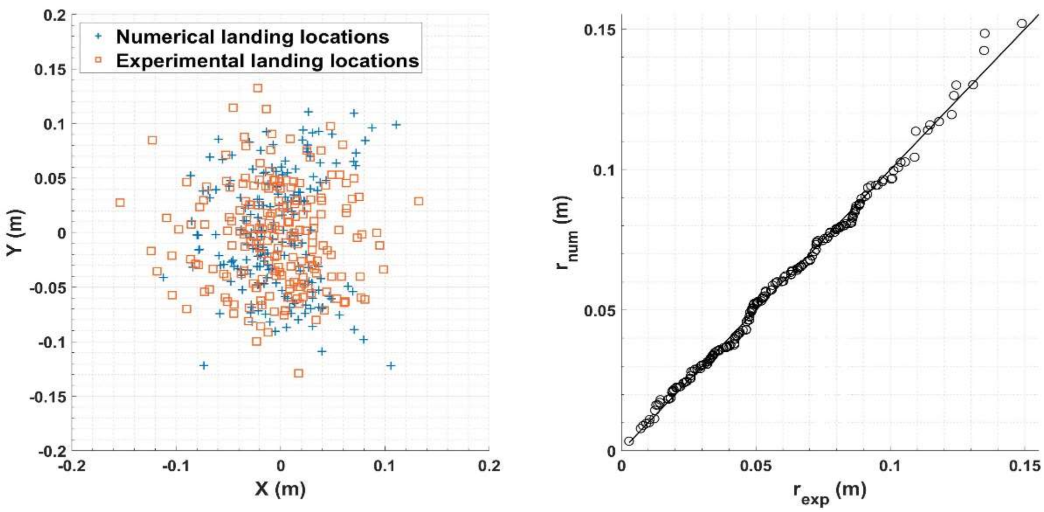

Figure 1. Comparison between numerical and experimental spreads of landing locations and ranked radial distances from the model against those from experiments. (Gradation A)

Gaining a thorough understanding of the motion of windborne debris can bring great benefit for us to reduce the impact of such debris during extreme wind events. From accurate predictions of landing locations of flying debris and missiles, we can take preemptive measures to reduce the overall loss of property and lives in case of such extreme events.

ACKNOWLEDGEMENTS

The authors gratefully acknowledge the insights provided by Dr. Abdul A. Khan and Dr. William C. Bridges Jr on different aspects of this study during a discussion session. They also thank Megan Holmes for her work on the experiments. This material is based upon work supported by the National Science Foundation under Grant No. 1760999. Any opinions, findings, and conclusions or recommendations expressed in the material are those of the author and do not necessarily reflect the views of the NSF.

REFERENCES

Baker, C. J., 2007. The debris flight equations. Journal of Wind Engineering and Industrial Aerodynamics, 329-353.

Chai, V., Parkhi, D., Boopathy, S., Xiang, J. and Schlüter, J., 2019. A model for the aerodynamic coefficients of rock-like debris. Comptes Rendus Mecanique, 19-32.

Holmes, J., 2004. Trajectories of spheres in strong winds with application to wind-borne debris. Journal of Wind Engineering and Industrial Aerodynamics, 9-22.

Minor, J. E., 2005. Lessons learned from failures of the building envelope. Journal of Architectural Engineering, 10-13.

Tohidi, A. and Kaye, N. B., 2017. Aerodynamic characterization of rod-like debris with application to firebrand transport. Journal of Wind Engineering and Industrial Aerodynamics, 297-311.

Efficiency improvement and discussion of grid effects on DSRFG method

Xiangjie Wang [a,*], Steve C.S. Cai [b]

[a]*Louisiana State University, Baton Rouge, Louisiana, USA, xwan133@lsu.edu*
[b]*Louisiana State University, Baton Rouge, Louisiana, USA, cscai@lsu.edu*

ABSTRACT:
In this paper, the inflow generator Discretizing and Synthesizing Random Flow Generation (DSRFG) method is reviewed at first. The efficiency of the DSRFG method is improved by modifying the way of discretising the energy spectra. The numerical grid effects on the DSRFG method is examined numerically and the results show that the DSRFG method is not sensitive to the grid effects when being applied in a Large Eddy Simulation(LES).

Keywords: LES, DSRFG, Efficiency, Divergence-free, Grid Effects

1. A BRIEF INTRODUCTION TO THE DSRFG METHOD

In Large Eddy Simulation (LES), generating an appropriate inflow condition is crucial for the accurate prediction of the wind effects on the target buildings or structures. As one of the synthetic random Fourier methods, DSRFG (discretizing and synthesizing random flow generation) can generate the anisotropic fluctuating inflow that fits to any prescribed arbitrary power spectral models (Huang et al, 2010).

$$\boldsymbol{u}(\boldsymbol{x},t)=\sum_{m=0}^{M}\boldsymbol{u}_m(\boldsymbol{x},t)=\sum_{m=0}^{M}\sum_{n=1}^{N}\left[\boldsymbol{p}^{m,n}\cos\left(\tilde{\boldsymbol{k}}^{m,n}\cdot\tilde{\boldsymbol{x}}+\omega_{m,n}t\right)+\boldsymbol{q}^{m,n}\sin\left(\tilde{\boldsymbol{k}}^{m,n}\cdot\tilde{\boldsymbol{x}}+\omega_{m,n}t\right)\right] \tag{1}$$

where, M is the amount of the wave-number points $(k_0,k_1,\cdots,k_M)$ to discretize the energy spectra $E(k)$; N is the sampling times in each wave-number segment, i.e., N random wave-number vectors $\boldsymbol{k}^{m,n}$ with a length equal to k_m in a certain random manner; $\tilde{\boldsymbol{k}}^{m,n}=\boldsymbol{k}^{m,n}/k_0$. $\boldsymbol{x}$ is the coordinates of the inlet points, and $\tilde{\boldsymbol{x}}=\boldsymbol{x}/L_s$ is the scaled coordinate with $L_s=\theta\sqrt{L_u^2+L_v^2+L_w^2}$ (L_u, L_v and L_w are the integral turbulence length scales in streamwise, spanwise and vertical direction and θ is a constant and varies from 1 to 2). More details of Eq.(1) is referred to Huang et al. (2010).
To ensure the divergence-free condition, the amplitude vector should satisfy $\boldsymbol{p}^{m,n}\cdot\boldsymbol{k}^{m,n}=0$ and $\boldsymbol{q}^{m,n}\cdot\boldsymbol{k}^{m,n}=0$. For anisotropic turbulent inlet flow, Castro and Paz(2013) proposed: $p_i^{m,n}=sign(r_i^{m,n})\sqrt{\frac{4c_i}{N}E_i(k_m)\Delta k_m\frac{(r_i^{m,n})^2}{1+(r_i^{m,n})^2}}$ and $q_i^{m,n}=sign(r_i^{m,n})\sqrt{\frac{4c_i}{N}E_i(k_m)\Delta k_m\frac{1}{1+(r_i^{m,n})^2}}$. $r_i^{m,n}$ is a random coefficient uniformly distributed in the range of $[-1,1]$ and $sign(r_i^{m,n})$ returns the signal of $r_i^{m,n}$; $c_i=U_{avg}$; $\boldsymbol{k}^{m,n}$ could be derived from $\boldsymbol{p}^{m,n}$ and $\boldsymbol{q}^{m,n}$.

2. EFFICIENCY IMPROVEMENT OF THE DSRFG METHOD

The computational cost of the DSRFG method is proportional to $M\times N$. To ensure the generated

* Lead presenter

inlet flow fit well to the target power spectral model, the wave numbers are recommended to set as an equivalency sequence $[k_0, k_0\alpha, k_0\alpha^2, \cdots, k_0\alpha^{M-1}]$. This would ensure there are enough wave-number points in the low frequency region, where most of the kinetic energy concentrates as well. The generated inlet flow could fit to the target power spectral model well even with a small value of M ($M = 100$), compared to the arithmetic sequence $[k_0, k_0 + \Delta k, k_0 + 2\Delta k, \cdots, k_M]$ ($M = 2000$).

3. DRID EFFECTS ON THE DSRFG METHOD

Saad and Sutherland (2016) pointed out that Kraichnan's method (Kraichnan, 1970) is no longer divergence-free when being applied in numerical simulation. Unphysical pressure fluctuations (which should be solenoidal as **Figure 1.b**) would arise at the inlet boundary as shown in **Figure 1.a**. Since DSRFG is a subsequent method of Kraichnan's method, it's necessary to examine the grid effects on it.

a) non-strictly divergence-free inlet boundary ($\boldsymbol{p}^{m,n} \cdot \boldsymbol{k}^{m,n} = 0$, $\boldsymbol{q}^{m,n} \cdot \boldsymbol{k}^{m,n} = 0$)

b) strictly divergence-free inlet boundary (considering the grid effects)

Figure 1 Pressure fluctuations at inlet boundary

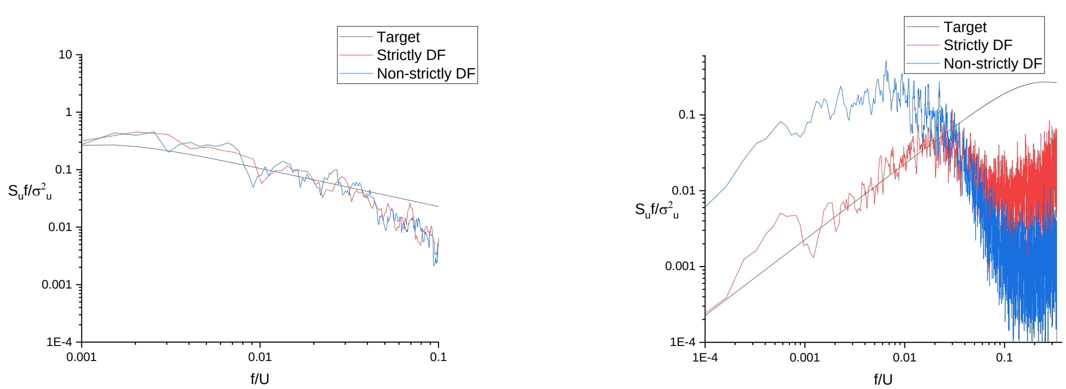

a) $\Delta x / L_s = 0.001$

b) $\Delta x / L_s = 1.4$

Figure 2 Streamwise power spectral density with different inlet generation method

A strictly divergence-free DSRFG method is proposed and compared with the original DSRFG method (non-strictly divergence-free) in two sets of numerical simulations by the open-source toolbox OpenFOAM. The streamwise power spectral density at the reference point inside the computational domain are plotted in **Figure 2** with different grid sizes Δx. The results show that the original DSRFG method is not sensitive to the grid effects unless it is adopted in an extremely coarse meshed computational domain, as shown in **Figure 2.b**, which would never happen in a correct LES.

4. CONCLUSION

In this paper, the proposed way of discretizing the energy spectra would improve the efficiency of the DSRFG method. The grid effects on the DSRFG method are examined and the results show that the DSRFG method is not sensitive to the grid effects and could be adopted in LES without further modification.

ACKNOWLEDGEMENTS

This research is funded by the Economic Development Assistantship from Louisiana State University, and is also supported by HPC@LSU high performance computing resources.

REFERENCES

Castro, H. G., & Paz, R. R. (2013). A time and space correlated turbulence synthesis method for Large Eddy Simulations. Journal of Computational Physics, 235, 742-763.

Huang, S. H., Li, Q. S., & Wu, J. R. (2010). A general inflow turbulence generator for large eddy simulation. Journal of Wind Engineering and Industrial Aerodynamics, 98(10-11), 600-617.

Kraichnan, R. H. (1970). Diffusion by a random velocity field. The physics of fluids, 13(1), 22-31.

Saad, T., & Sutherland, J. C. (2016). Comment on "Diffusion by a random velocity field"[Phys. Fluids 13, 22 (1970)]. Physics of Fluids, 28(11), 22

Structural Fragility Analysis of Tall Buildings and Towers via Artificial Neural Network Surrogate Modeling

Lei Zhang[a,*], Luca Caracoglia[b]

[a]*Northeastern University, Boston, MA, USA, zhang.lei1@northeastern.edu*
[b]*Northeastern University, Boston, MA, USA, lucac@coe.neu.edu*

ABSTRACT:
Although the standard Monte-Carlo simulation has been widely used in today's PBWE framework due to its robustness and convenience, it is rather time-consuming and computationally expensive. Drawing motivation from a challenge encountered by the wind engineering community, this study proposes a novel simulation approach, based on surrogate modeling, to computationally analyze structures under wind loads more efficiently compared to both Model-Monte Carlo and other simulation methods(e.g., Stochastic Approximation), examined by the Authors. Artificial Neural Networks (ANN) are proposed and investigated in this study to generate a "surrogate model". Numerical results indicate that ANN-based models are efficient for stochastic structural analysis of tall buildings and towers with acceptable prediction errors. Particular consideration will be devoted to the study of wind loads and response in mixed wind climates, characterized by the presence of both tropical hurricanes and extra-tropical depressions.

Keywords: high-rise buildings, hurricane simulation, fluid-structure interaction, surrogate models, artificial neural networks

1. INTRODUCTION

Performance-based wind engineering (PBWE) has emerged as an active research field due to potential applications into design standards e.g., by the American Society of Civil Engineers in the United States of America (ASCE, 2019). Novel and accurate methodologies are needed to implement practice-oriented guidelines. This study will examine the use of surrogate models, utilizing the paradigm of artificial neural networks (ANN) in Machine Learning to conduct wind-induced structural dynamic analysis. Fluid-structure interaction and dynamic effects will be examined. Both serviceability and ultimate limit states will be considered in the context of PBWE. Application to vertical tower and building structures is envisioned. Multi-layer ANNs will be employed as surrogate models to reproduce fragility curves and surfaces, as a function of both mean wind speed and direction, examining various relevant limit states (e.g. non-structural damages on the façade, acceleration discomfort levels for occupants, demand-to-capacity indices of selected structural elements).

The study utilizes a recently developed surrogate model and method, designated as Layered Stochastic-Approximation Monte-Carlo (LSAMC; Giaccu and Caracoglia, 2018) to compare the results, found by ANN-based models, assessing the performance of a standard tall building and a monopole tower structure against turbulent wind loads. Furthermore, standard Monte-Carlo sampling simulations will be considered as well to assess adequacy of ANN-based surrogate models.

2. MODEL AND METHODS

The ANN-based, surrogate model is based on a typical ANN topology, formed by combining ANN neurons and organizing them in an input layer (input random variables), hidden layer(s), and an output layer. The variables of the input layer are generally user-defined, e.g. aerodynamic force coefficients, vortex shedding and wake excitation properties, structural properties and other

* Lead presenter

physical quantities. The hidden layers are the result of calculations from the input layer. Finally, the output layer is the result of the calculations. In an ANN, each node in each layer is connected to each node in the adjacent layer. An ANN will be employed to predict selected probabilities of failure associated with specified limit states of two structural examples, i.e. "fragility" conditional on mean wind speed and direction. Predictions follow a training process, which is carried out using an existing set of input–output data ("supervised learning"). The training of an ANN is commonly performed through a back-propagation algorithm and a minimization process that has three steps.

Similar to the idea of the Latin Hypercube sampling, the LSAMC method uses a layered sampling of the random variables within a Monte-Carlo simulation environment. The key steps of the LSAMC method include: (i) dividing the range of each random variable into a finite number of adjacent, non-overlapping equally-probable intervals; (ii) constructing a subspace of the random variables for each iteration, consisting of one of the equally-probable intervals for every random variable; (iii) feeding the subspace to the standard Stochastic Approximation (SA) algorithm (Spall, 2005), to find one root of the examined problem subjected to random wind load perturbation. Thus, iterating through all the possible subspaces of the original random variable set yields a sequence of roots to the perturbed problem, which are employed to evaluate the effects of the perturbation noises in a structural system through statistical moments, derived from the root sequence.

3. PRELIMINARY RESULTS

In this preliminary study, the only source of uncertainty considered is the static flow forces (drag coefficient of the load, C_D). A number of scenarios are designed to examine wind-induced damage through violation of a serviceability limit state (e.g., the rooftop lateral drift and acceleration) and an ultimate limit state (e.g., the yielding of a steel corner-column). One of these scenarios, considering drag flow forces as an independent random input, is presented in detail.

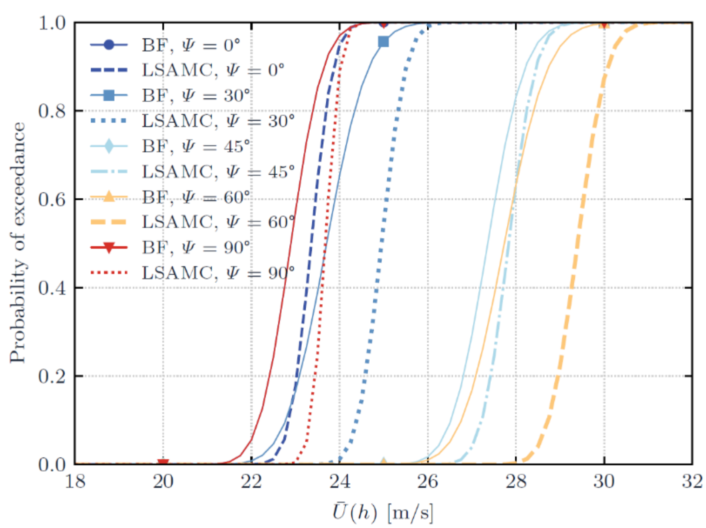

Figure 1. Fragility against the peak lateral rooftop drift of the CAARC standard building with random parameter C_D comparisons between the brute-force Monte-Carlo simulations (BF) and LSAMC method results.

Figure 1 illustrates an example of fragility analysis and examines the peak lateral drift of the CAARC standard building as a function of mean wind speed $\overline{U}(h)$, referenced at rooftop $h =$

183 m, and mean-wind direction Ψ. The details of other scenarios and results exploiting ANN-based surrogate models will be described in the final presentation.

4. DISCUSSION AND CONCLUSIONS

Surrogate models, in particular those exploiting the latest developments in the field of Artificial Intelligence, have been explored to replace the standard Monte-Carlo method, and later developments, such as the LSAMC method. Various scenarios have been studied to predict selected structural "failure" probabilities. Numerical results suggest that ANN-based methods can provide efficient and robust approximation of fragility, and can be employed for life-cycle cost analysis of wind-induced damage on tall buildings and towers in turbulent, synoptic wind environments.

ACKNOWLEDGMENTS: US National Science Foundation, Award CMMI-1852678.

REFERENCES

ASCE, 2019. Prestandard for Performance-Based Wind Design. American Society of Civil Engineers, Reston, VA, USA.

Giaccu, G. F., Caracoglia, L., 2018. Wind-load fragility analysis of monopole towers by Layered Stochastic-Approximation-Monte-Carlo method. Eng. Struct., 174, 462-477.

Spall, J. C., 2005. Introduction to stochastic search and optimization: estimation, simulation, and control, vol. 65. John Wiley & Sons.

Zhang, L., Caracoglia, L., 2021. Layered Stochastic Approximation Monte-Carlo method for tall building and tower fragility in mixed wind load climates. Eng. Struct., in press.

Estimation and Characterization of Nonstationary Inelastic Crosswind Responses of Base-Isolated Tall Buildings

Changda Feng [a,*], Xinzhong Chen [b]

[a]*AIR Worldwide, Boston, MA, USA, cfeng@air-worldwide.com*
[b]*Texas Tech University, Lubbock, TX, USA, xinzhong.chen@ttu.edu*

ABSTRACT:
This study investigates crosswind responses of base-isolated tall buildings under nonstationary wind excitations. The base isolation system has hysteretic restoring force characteristics. Response time history analysis (RHA) is performed. The numerical examples show that the transient effect of non-stationary excitations reduces when yielding becomes significant which leads to increase in system damping. This study also presents analytical solution of nonstationary time-varying response statistics. The time-varying standard deviations (STDs) of crosswind responses are estimated from the statistical linearization with Gaussian assumption combined with evolutionary spectra analysis.

Keywords: Base-isolation; Tall buildings; Inelastic responses; Nonstationary wind; Statistical linearization

1. INSTRUCTION

The potential benefit of high-rise buildings from base isolation has attracted great attention in recent years for considerations of comfort of occupants, functionality of buildings, non-damage to acceleration-sensitive contents and non-structural elements. There are a number of studies on wind-induced responses of base-isolated tall buildings under stationary wind excitations (e.g., Kareem 1997, Katagiri et al. 2012, Feng and Chen 2019a and b). In addition, the nonstationary winds can have very distinct load effects on buildings as compared to stationary winds (e.g., Chen 2008; Solari et al. 2015; Feng and Chen 2018; Kareem et al. 2019). This study characterizes and provides an effective analytical approach to estimate the inelastic crosswind responses of base-isolated tall buildings under nonstationary wind excitations.

2. ANALYSIS FRAMEWORK

The bilinear hysteretic model is used for the restoring shear force of base isolation system, and is modeled in Bouc-Wen hysteretic force model. The upper building is linear elastic and modeled as multiple degrees of freedom shear building. The building damping matrix is assumed to be proportional to stiffness matrix. The building displacements are further expressed in modal displacements. The nonstationary crosswind story wind forces are represented in their evolutionary power spectral density (EPSD) functions. Response history analysis is carried out using Runge-Kutta method, where the time histories of story forces are generated from their spectra. The time-varying STDs of inelastic responses are also qualified analytically using statistical linearization approach combined with evolutionary spectra analysis.

A 50-story tall building of 200 m in height with a square cross section in urban area is considered. The first modal frequency and damping ratio of fixed-base building are 0.21Hz and 1% with a linear mode shape. The base isolation system is consisted of damper system and linear rubber

* Lead presenter

bearings. The yield restoring shear force of the damper system is 2% of total building weight with a yielding displacement of 0.025 m. The second stiffness ratio is 0.12. With the initial stiffness, the first modal frequency of base-isolated building is 0.196 Hz. The time-varying mean wind speed of nonstationary field is modelled as $U_H(t) = U_{H,max}\exp\left[-(t-\delta_0)^2/2D_t^2\right]$, where $U_{H,max}$ is maximum mean wind speed at building top over the time duration and D_t is wind storm duration parameter. The EPSD of crosswind base bending moment coefficient is defined based on the PSD under stationary wind suggested by Architectural Institute of Japan (AIJ 2004).

3. RESULTS AND DISCUSSIONS

Figures 1 and 2 show the time history sample of base displacement and the restoring force-deformation relation of the base-isolation system with $U_{H,max} = 50$ m/s and $D_t = 180$ s. Figure 1 shows that the yielding causes low-frequency drift, which is similar to response under stationary wind (Feng and Chen 2019a). The hysteretic loop is symmetric around the centre.

Figure 3 shows the time-varying STDs of base displacement for $U_{H,max} = 30$ and 50 m/s and $D_t = 60$ s and 180 s, which are estimated from ensample average of 1000 response time history samples. To highlight the transient dynamic effect, the quasi-stationary response STDs are determined under stationary wind with corresponding wind speed over the duration of 600 s, referred to as 'RHA, QS'. It is observed that there exists clear transient structural dynamic effect at $U_{H,max} = 30$ m/s, especially when D_t is shorter, i.e., the variation of wind speed is significant. The transient effect leads the time-varying STD under nonstationary excitation lower than that of quasi-stationary response. The maximum of time-varying response STD is observed after the mean wind speed reaches its peak. The transient effect is considerably reduced at $U_{H,max} = 50$ m/s, which is attributed to the increase in system damping resulted from more significant yielding of base isolation system. The similar observations can be found for base shear force, building top displacements and acceleration.

The estimations of statistical linearization approach with Gaussian assumption combined with evolutionary spectra analysis are also shown in Figure 3. The linearization approach provides good estimation at lower wind speeds where the yielding is insignificant. At higher wind speeds, the linearization approach underestimates the base displacement due to its strong non-Gaussian distribution at large yielding level (Feng and Chen 2019b). For other responses, the linearization approach provides good estimations of building top displacement and base shear, while underestimates the building acceleration at higher wind speed. The linearization approach well captures the transient structural dynamic effects.

4. CONCLUSIONS

The transient effect reduces in response and causes a delay in variation of the response STD compared with that of quasi-stationary response. When wind speed increases, the transient effect reduces with increase in system damping due to yielding. The statistical linearization with Gaussian assumption combined with EPSD approach well capture the transient effect. The linearization approach with Gaussian assumption provides good estimations of building top displacement and base shear, while underestimates the base displacement and building acceleration at higher wind speed due to their non-Gaussian character at high yielding level.

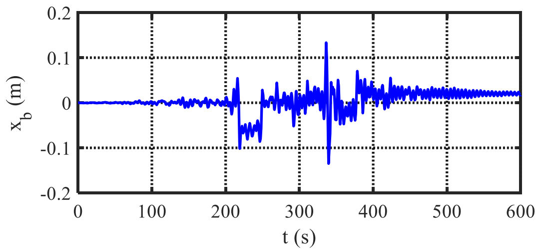

Figure 1. Time history sample of base displacement ($U_{H,max}$ = 50 m/s, D_t = 180 s)

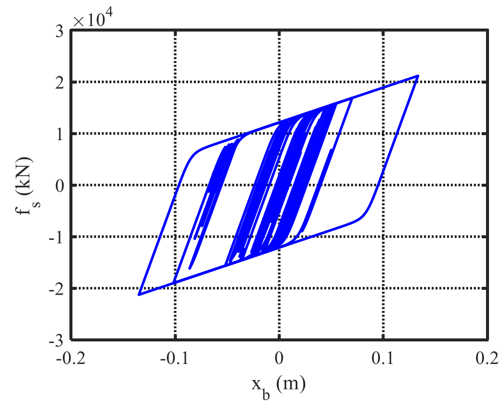

Figure 2. Restoring force and base displacement relation ($U_{H,max}$ = 50 m/s, D_t = 180 s)

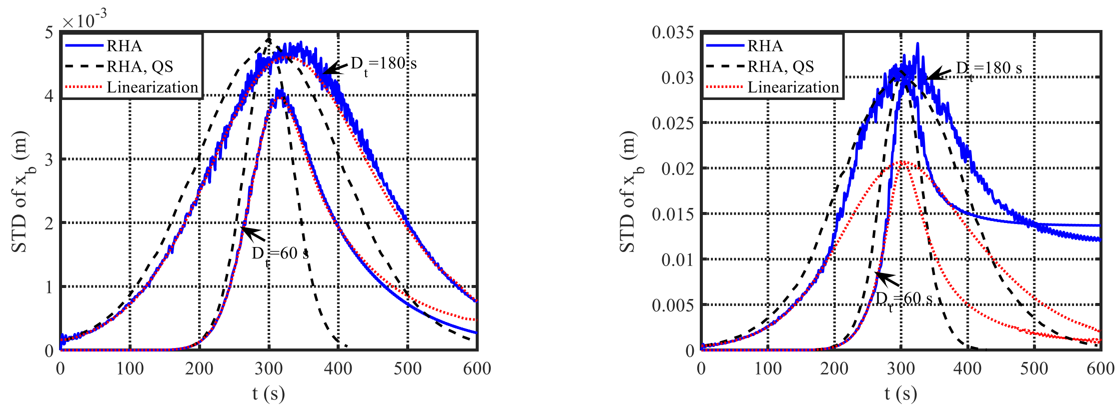

a) $U_{H,max}$ = 30 m/s

b) $U_{H,max}$ = 50 m/s

Figure 3. Time-varying STD of crosswind base displacement

ACKNOWLEDGEMENTS

The support for this work provided in part by NSF grant No. CMMI-1536108 is greatly acknowledged.

REFERENCES

Architectural Institute of Japan (AIJ). (2004). AIJ Recommendations for Load on Buildings, AIJ, Tokyo, Japan.

Chen, X. (2008). “Analysis of alongwind tall building response to transient nonstationary winds.” J. Struct. Eng., 134(5), 782-791.

Feng, C., and Chen, X. (2018). “Estimation of Nonstationary Crosswind Response of Tall Buildings with Nonlinear Aeroelastic Effect.” J. Eng. Mech, 144(7), 04018053.

Feng, C., and Chen, X. (2019a). “Evaluation and characterization of probabilistic alongwind and crosswind responses of base-isolated tall buildings.” J. Eng. Mech, 145(12), 04019097.

Feng, C., and Chen, X. (2019b). “Estimation of Inelastic Crosswind Response of Base-Isolated Tall Buildings: Performance of Statistical Linearization Approaches.” J. Struct. Eng. 145(12), 04019161.

Kareem, A. (1997). “Modelling of base-isolated buildings with passive dampers under winds.” J. Wind Eng. Ind. Aerodyn., 72, 323-333.

Kareem, A., Hu, L., Guo, Y., and Kwon, D. K. (2019). Generalized Wind Loading Chain: Time-Frequency Modeling Framework for Nonstationary Wind Effects on Structures. J. Struct. Eng, 145(10), 04019092.

Katagiri, J., Ohkuma, T., Marukawa, H., and Yasui, H. (2012). “Unstable aerodynamic responses of base-isolated high-rise buildings.” J. Struct. and Constr. Eng., AIJ, 77 (681), 1637-1644 (In Japanese).

Solari, G., De Gaetano, P., and Repetto, M. P. (2015). “Thunderstorm response spectrum: fundamentals and case study.” J. Wind Eng. Ind. Aerodyn., 143, 62-77.

Full-scale experimental investigations on a naturally ventilated building and validation of simulation models

Chen Chen [a,*], Catherine Gorlé [b]

[a,*] *Stanford University, Stanford, California, U.S., chenc2@stanford.edu*
[b] *Stanford University, Stanford, California, U.S., gorle@stanford.edu*

ABSTRACT: (10 pt)
The use of natural ventilation (NV) offers significant potential for energy and cost savings, but the performance of a NV system highly depends on climate and weather conditions and building operating conditions. Air flow and temperature predictions obtained using computational models can provide insight into this variability, provided that the accuracy of the models can be guaranteed. This study uses a full-scale experiment conducted in an operational educational building with night-time ventilation to validate two different computational models. The experiment was carefully designed and executed to validate (1) a building thermal model that predicts the volume-averaged building temperature, and (2) a computational fluid dynamics (CFD) model that predicts the time-varying temperature field in the building. The CFD model is found to predict the measured point-wise temperatures with an RMSE of less than 0.8°C. In regions not directly adjacent to windows, the RMSE can be smaller than 0.3 °C.

Keywords: natural ventilation, full-scale experiment, CFD, building thermal model, validation

1. INTRODUCTION

Natural ventilation is a key solution for significantly reducing building energy consumption, but the performance is highly affected by local climate and weather conditions and building operating conditions. A well-functioning NV system design requires profound knowledge of the complex governing flow and heat transfer; thus, NV models are essential to provide adequate information during the design process. In a previous study, a multi-fidelity computational framework with uncertainty quantification (UQ) was proposed to predict the volume-averaged indoor air temperature during night-time ventilation in one of the atria of Stanford's Yang and Yamazaki Environment and Energy (Y2E2) building (Lamberti & Gorlé, 2018). Comparison of the results with building sensor measurements indicated that the building sensors are located in regions with higher-than-average temperatures, such that the measurements are not representative of the volume-averaged temperature. A more carefully designed full-scale experiment is needed to support validation of (1) a building thermal model that predicts the volume-averaged building temperature, and (2) a CFD model. In this abstract, we summarize: (1) the use of CFD and UQ to identify optimal locations for temperature sensors under uncertain boundary and initial conditions; (2) the experimental campaign performed during several nights under a variety of outdoor temperature and wind conditions; (3) a comparison between experimental measurements and a CFD model prediction for one single night, where the specific experimental conditions were reproduced in the CFD model to validate the model set-up.

2. BUILDING DESCRIPTION AND EXPERIMENT SETUP

2.1. Building description

* Lead presenter

The Y2E2 building has 14,000 m^2 of floor space on three above ground levels and one basement level, connected through hallways and four atria (Fig. 1(a)). The building uses a night-time NV system, which operates from 8:00 p.m. to 6:00 a.m., to cool the common spaces (hallways, open areas, and lounges connected to the central atria). Motorized windows in the common spaces on each floor are controlled separately and open on the condition that the outdoor temperature is lower than the indoor air temperature and the indoor temperature is greater than 22.35°C. If the temperature drops to 20.35°C, the motorized windows on that floor close again. Meanwhile, based on the measured wind direction, the two leeward sides of the louver banks at the top of the atria are opened, generating a buoyancy-driven flow that brings in cool air through the windows and flushes out warmer air through the louvers.

(a) (b)

Figure 1: (a) Atrium D of the Y2E2 building (left), atrium louvers (top right), and indoor view of Atrium D (bottom right); (b) Computational grid

2.2. Experiment setup

The sensor locations were selected based on a CFD-based design of experiments that has been described in detail in Chen and Gorlé (2019). CFD and UQ were employed to make sure that the temperature sensors are located where (1) the temperature difference between the volume-averaged temperature and the point-wise temperature is small, and (2) the temperature is higher or lower than average over the duration of the night-time ventilation. In combination, these measurements will support validation of the building thermal model that predicts the volume-average temperature in building, as well as validation of the CFD model. The full-scale experiments were conducted from 8:00 p.m. to 6:00 a.m. 20 temperature sensors were placed in the optimal locations distributed throughout atrium D. Each location had one data logger connected to up to 4 thermistors with a sampling rate of 1 second; one thermistor was used to measure the indoor air temperature, while the others were used to measure nearby floor, sidewall, and ceiling temperatures. The temperature sensors were calibrated using a temperature calibrator with an accuracy of ± 0.3°C, which included measurement errors caused by the sensor response time.

3. CFD MODEL

The computational domain is comprised of the common areas and hallways of atrium D and the surrounding outdoor area (Fig. 1(b)). The far field boundary is at least 25 m (around one building height) away from the building, which is sufficiently large to ensure there are no unwanted effects of the boundary conditions on the prediction of the buoyancy-driven ventilation flow. A grid-dependence study resulted in the selection of a mesh of 2.6 million cells with a minimum resolution of 0.09 m around the window regions. The CFD simulation was performed using ANSYS Fluent, solving the Reynolds-averaged conservation of mass, momentum, and energy equations. The Reynolds stresses are modelled using the Reynolds Stress Model (RSM). The temperature profiles recorded during the experiments were imposed on the floors, walls and ceilings. A constant uniform pressure condition is imposed on the far field boundary, together with the outdoor temperature as a function of time recorded by the outdoor temperature sensor of the Y2E2 building. The initial condition for the indoor air temperature on each floor is specified as the volume-averaged temperature recorded by the temperature sensors at the start of the experiment.

4. RESULTS AND DISCUSSION

In the following, we present results for one measurement night with a light SW wind (0.51 m/s recorded at the Stanford Weather Station) and a 3.8 ℃ initial temperature difference at the start of the night-time ventilation. The time-varying indoor air temperatures were recorded for a three-hour period during night-time ventilation. Comparison of the CFD results to the full-scale measurements indicates that the point-wise temperature predictions from the CFD simulation agree well with the experimental data recorded by the temperature sensors. The root mean square error (RMSE) for sensors located in regions that are not directly exposed to the windows is lower than 0.3℃ (Fig. 2 (a)). In the zones adjacent to the windows, the RMSE goes up to 0.8℃ (Fig. 2 (b)). Thus, the results indicate that CFD models can provide an accurate prediction of buoyancy-driven natural ventilation, provided that accurate initial and boundary conditions are specified. Ongoing work is focusing on validating an integral model with the full-scale experiment.

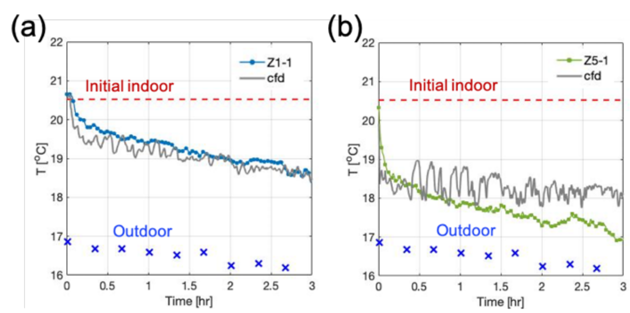

Figure 2: Comparison of CFD results and experimental data in the Atrium D during night-time ventilation

ACKNOWLEDGEMENTS

We want to thank Lup Wai Chew and Jack William Hochschild for their invaluable support in executing the field measurement, as well as the Stanford University Science & Engineering Quad Building Management Team, Land, Stanford's Land, Buildings & Real Estate Facilities Maintenance Technician and Stanford's Fire Marshal's Office for their assistance during the full-scale experiment. This research was supported by a Seed Research Grant from the Center for Integrated Facility Engineering at Stanford University.

REFERENCES

Lamberti, G. and Gorlé, C., 2018. Uncertainty quantification for modeling night-time ventilation in Stanford's Y2E2 building. Energy and Buildings, 168:319–330.

Chen, C. and Gorlé, C., 2019. Temperature measurements in Stanford's Y2E2 building for validation of natural ventilation models. The 15th International Conference on Wind Engineering, Beijing, China

Examination of gust effect factor for side walls of rigid low-, mid-, and high-rise buildings

Jin Wang [a*], Gregory A. Kopp [b]

[a] *University of Western Ontario, London, Ontario, Canada, jwan2225@uwo.ca*
[b] *University of Western Ontario, London, Ontario, Canada, gakopp@uwo.ca*

ABSTRACT:
The gust effect factors for side walls of rigid low-, mid- and high-rise buildings are examined in this paper. Statistical characteristics of side wall pressures, such as skewness, kurtosis, and peak factors, are examined along with parameters related to the wind spectra and the aerodynamic admittance. The results show that low-rise buildings tend to follow a Gaussian distribution, which allows the measured peak factors for low-rise buildings match with the model in ASCE 7. However, this does not happen for mid- and high-rise buildings due to the vortex shedding over side walls. Solari's model adopted in ASCE 7-16 is unable to assess the measured gust effect factor for side walls of mid- and high-rise buildings because unsteady, highly correlated body-generated flow features like vortex shedding are not involved in the model. Evidently, other body-generated fluctuations can be accounted for with the ASCE 7 model as long as the area-averaged fluctuations remain approximately Gaussian.

Keywords: Building Aerodynamics, gust effect factor, aerodynamic admittance, vortex shedding, horseshoe vortex

1. INTRODUCTION

The gust effect factor model developed by Solari (1993a, b) and adopted in ASCE 7 is for base shear based on the Quasi-steady theory, and the body-generated turbulence, such as vortex shedding, are not included in the gust effect factor model. This model assumes a stationary Gaussian distribution based on the work of Davenport (1977) and adopts the aerodynamic admittance for overall windward wall loads to account for the lack correlation of pressures over building surfaces. Therefore, the building surfaces influenced by the flow separation or vortex shedding, i.e., roofs, side walls and leeward walls, would not be highly accurately assessed because it is well known that within regions of separated flow that the aerodynamic forces are non-Gaussian (Solari 1993a, b; Ginger and Letchford, 1993; Liu et al., 2020). Wang and Kopp (2021) systematically studied the gust effect factors for windward walls of low-rise, mid-rise and high-rise buildings, and observed the horseshoe vortices make the windward wall pressures follow non-Gaussian distribution for low-rise buildings, which results in the mismatch between the measured data with Solari's model. Liu et al. (2020) experimentally measured the wind pressures for high-rise buildings with height ratio of 8.3, which is the ratio of building height to the least horizontal dimension, and studied the gust effect factors for the area-averaged wall pressures. The mismatch between the aerodynamic admittance of the measured data and Solari's model is observed for side walls and leeward walls, due to the vortex shedding over side walls, in Liu et al. (2020). However, it is uncertain for the performance of the gust effect factor model in ASCE 7 for the low-rise and mid-rise buildings, which deserves further studies.

The objective of this paper is to examine the gust effect factor model in ASCE 7 and investigate the mechanisms behind the gust effect factor for side walls of low-, mid- and high-rise buildings.

* Lead presenter

2. METHODOLOGY

2.1. Wind tunnel experiment

The two datasets used in the present study are primarily from the NIST database for low-rise buildings (Ho et al., 2005) and a database for mid-, and high-rise buildings (Wang and Kopp, 2021b). For the NIST database, the data derived for the open terrain with roughness length of z_o = 0.03m were used in the present analysis. Wang and Kopp (2021b) completed the wind tunnel experiment for mid- and high-rise buildings for the open terrain with z_o = 0.034 m in equivalent full scale. A total of 58 buildings with roof slope less than 10° from Ho et al. (2005) and 30 building from Wang and Kopp (2021b) were analyzed in the present study. More details can be found in Ho et al. (2005) and Wang and Kopp (2021b).

2.2. Gust effect factor model for rigid buildings

In the present study, we consistently adopt the gust effect factor model in Wang and Kopp (2021) for the measured data. More details can be found in Wang and Kopp (2021), which will not be repeated herein. We just present the expressions used in this study, as follows:

$$G = \frac{1+2g_pI_uQ}{G_u^2} = \frac{1+2g_pI_uQ}{(1+g_uI_u)^2} \approx \frac{1+2g_pI_uQ}{1+2g_uI_u} \quad (1)$$

where, g_p and g_u are the peak factors of wind pressures and wind speed, respectively; I_u is the free stream turbulence intensity; and Q is the background response factor, which relates the dynamics of wind pressures to the oncoming turbulence. Note that the peak factor, g_u, for the present measured data is taken 3.0.

For Solari's model, which is developed from the perspective of frequency domain, it can be expressed as,

$$G = \frac{1+2g_pI_u\sqrt{Q_0}}{1+2g_uI_u\sqrt{P_0}} \quad (2)$$

where P_0 is a factor considering the averaging time effects by introducing a filter, and Q_0 is background response factor, which is similar to Q in Eq. (1). However, Q_0 in Eq. (2) also takes the averaging time effects into account. Note that the peak values and gust effect factors for the measured data in the present study are derived from the instantaneous time history. Therefore, in order to make the comparisons accurately, we will present the results using the Solari's model both with and without filter.

3. RESULTS

Gust effect factors obtained using Eq. (1) and Eq. (2) are presented in Figure 1. The black dot denotes the gust effect factor model as shown in Eq. (2) with the filter function ($\tau = 3$ sec), whereas the red dot indicates the model without filter. The red solid line with a fixed number of 0.85 is the simplification from ASCE 7-16, whereas the red dashed line with a fixed value of 0.92 (≈0.85/0.925) denotes the gust effect factor without a reduction factor of 0.925. Wang and Kopp (2021a) discussed the aerodynamic data for side walls and roofs depend on the non-dimensional geometric parameter *H/L* for low-rise buildings, where *H* is roof height and *L* is the plan dimension parallel to wind direction. However, three parameters, *H*, *L*, and *B* (*B* is the plan dimension normal to wind direction), are of importance for mid- and high-rise buildings. Figure 1 presents the measured gust effect factors along with the model (Solari 1993a, b) in ASCE 7 varied with the non-dimensional parameter *L/B*. The results for other non-dimensional parameters, such as *H/L* and *H/B*, were also calculated and analyzed, while they are not illustrated herein due to the lengthy limitation. Overall, G for side walls is scattered around 1.2 for low-rise buildings under normal winds and this number reduces to 1.0 under critical winds. H, together with B and L play the roles on the distribution of gust effect factors for mid- and high-rise buildings. Figure 1 indicates that Solari's model cannot match well with the measured data. Eqs. (1) and (2) indicates that the peak factor of wind loads, g_p, background response factor, Q, turbulence intensity, I_u, and peak factor of wind speed, g_u, determine the gust effect factors of rigid buildings. As the free-stream winds follow Gaussian distribution, indicating the peak factor of wind speed, g_u, is consistent in Eqs. (1) and (2). Therefore, the main differences between the measured data and Solari's model are caused by the peak factor of wind loads, g_p, and the background response factor, Q, which will be discussed in great details in the full paper.

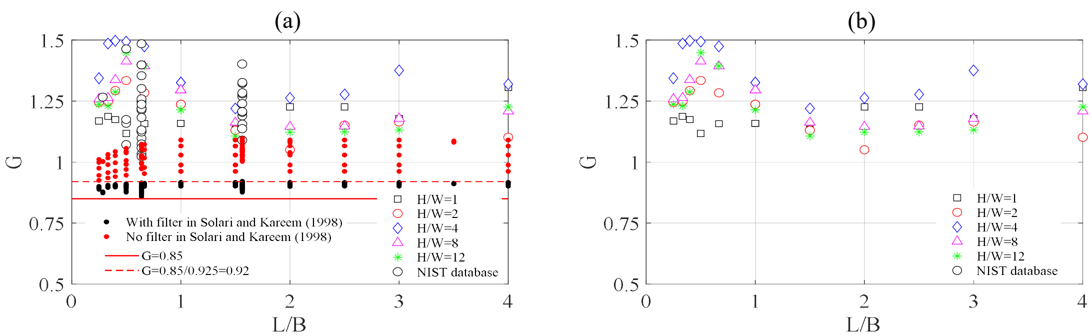

Figure 1. Gust effect factors of area-averaged side wall pressures under the winds normal to building walls: (a) gust effect factors for all buildings; (b) gust effect factors for mid- and high-rise buildings.

ACKNOWLEDGEMENTS

The authors gratefully acknowledge the partial financial support of the Natural Sciences and Engineering Research Council (NSERC) of Canada through the Discovery Grants program. The authors are grateful to an advisory group made up of members of the ASCE 7-22 Wind Loads Sub-Committee, chaired by Don Scott. GAK gratefully acknowledges the support of ImpactWX and the University of Western Ontario.

REFERENCES

Davenport, A.G., 1977. Wind Loads on Low Rise Buildings: Final Report of Phases I and II. Part I: Text and Figures.

Ginger, J.D. and Letchford, C.W., 1993. Characteristics of large pressures in regions of flow separation. Journal of Wind Engineering and Industrial Aerodynamics, 49(1-3), pp.301-310.

Liu, Y., Kopp, G.A. and Chen, S.F., 2020. An examination of the gust effect factor for rigid high-rise buildings. Frontiers in Built Environment, 6, p.221.

Solari, G., 1993a. Gust buffeting. I: Peak wind velocity and equivalent pressure. Journal of Structural Engineering, 119(2), pp.365-382.

Solari, G., 1993b. Gust buffeting. II: Dynamic along-wind response. Journal of Structural Engineering, 119(2), pp.383-398.

Wang, J. and Kopp, G.A., 2021a. Comparisons of Aerodynamic Data with the Main Wind Force–Resisting System Provisions of ASCE 7-16. I: Low-Rise Buildings. Journal of Structural Engineering, 147(3), p.04020347.

Wang, J. and Kopp, G.A., 2021b. Comparisons of Aerodynamic Data with the Main Wind Force–Resisting System Provisions of ASCE 7-16. II: Mid-and High-Rise Buildings. Journal of Structural Engineering, 147(3), p.04020348.

Wang, J., Gregory A. Kopp, 2021. Gust effect factors for windward walls for rigid buildings with various aspect ratios. Journal of Wind Engineering and Industrial Aerodynamics, (Accepted)

New Model for Rain-Induced Interior and Contents Damage to Mid/High-Rise Buildings During Hurricane Events

Zhuoxuan Wei [a, *], Jean-Paul Pinelli [b], Nima Aghli [c], Jingyun Jia [d], Kurtis Gurley [e]

[a]*Graduate student, Dept. of Civil Engineering, Florida Institute of Technology, Melbourne, FL 32901. E-mail: weiz2018@my.fit.edu*
[b]*Professor, Dept. of Civil Engineering, Florida Institute of Technology, Melbourne, FL 32901. E-mail: pinelli@fit.edu*
[c]*Doctoral candidate, Dept. of Computer Engineering and Sciences, Florida Institute of Technology, Melbourne, FL 32901. E-mail: naghli2014@my.fit.edu*
[d]*Doctoral candidate, Dept. of Computer Engineering and Sciences, Florida Institute of Technology, Melbourne, FL 32901. E-mail: jiaj2018@my.fit.edu*
[e]*Professor, Dept. of Civil and Coastal Engineering, University of Florida, Gainesville, FL 32611. E-mail: kgurl@ce.ufl.edu*

ABSTRACT:
Past hurricane events have revealed the vulnerability of commercial residential mid/high-rise buildings (CR-MHR) to hurricane-induced water ingress. A new methodology is proposed to produce realistic estimates of the interior and contents damage in CR-MHR. This research extends to a new CR-MHR interior and contents damage model, the results of previous efforts on rain admittance factor, surface runoff coefficients, and water propagation in apartment units, derived from Wall of Wind tests (Baheru et al., 2014; Raji et al., 2020; Silva de Abreu et al., 2020), for commercial residential low-rise buildings, within the framework of the Florida Public Hurricane Loss Model (FPHLM). The new physics-based methodology combines estimates of envelope defects and breaches, with estimates of direct impinging and surface runoff from wind driven rain (WDR), rainwater ingress, propagation, and percolation, and components cost analyses to produce estimates of the interior and contents damage in CR-MHR. The basis for the methodology are the mechanisms of rainwater ingress, distribution and propagation. The methodology was implemented into a deterministic combined vulnerability and actuarial model (DCM) and into a probability vulnerability model (PVM).

At the heart of the DCM is a scenario analysis engine, which loads the exposure data from the insurance portfolio and the 3-second gust actual terrain wind speeds at 10 meters for all policies. The DCM takes the mean value of the key parameters and produces the expected insured losses for the building, interior, exterior and contents for each policy in the portfolio. At the heart of the PVM is a Monte Carlo simulation engine which runs thousands of simulations looping over combinations of wind speeds and wind directions, for defined building classes. The key parameters are randomly selected for each simulation. The outputs of the PVM are vulnerability matrices and vulnerability curves for building, interior and contents. The PVM outputs two kinds of vulnerability matrices and curves: damage ratio as a function of wind speed (WS) and damage ratio as a function of the WDR. In addition, the model outputs vulnerability surfaces with damage ratio as a combined function of both WS and WDR.

The coding is in the Python3 language which is a favourable language for statistical models and data analysis due to the ease of use and a wide range of analytical libraries available. The coding incorporates a matrix implementation, which combines iteration and Hadmard product to improve the computing speed and reduce the RAM memory usage. Both DCM and PVM have 2 modules (pre-processing module and approach module) accompanied by a configuration file (detailed in Figure 1).

* Lead presenter

The authors verified that neither the DCM nor the PVM models ran afoul of established logical relationships to risk. In addition, the research team compared the output of the DCM model against the output of several commercial models, available in Form V-1 of the vulnerability standard from the Florida Commission on Hurricane Loss Projection Methodology (FCHLPM). The results show that the output of the DCM compares favourably to other models.

The presentation will describe the development of the model, the challenges that the authors had to overcome, and present results from both the deterministic and the probabilistic model.

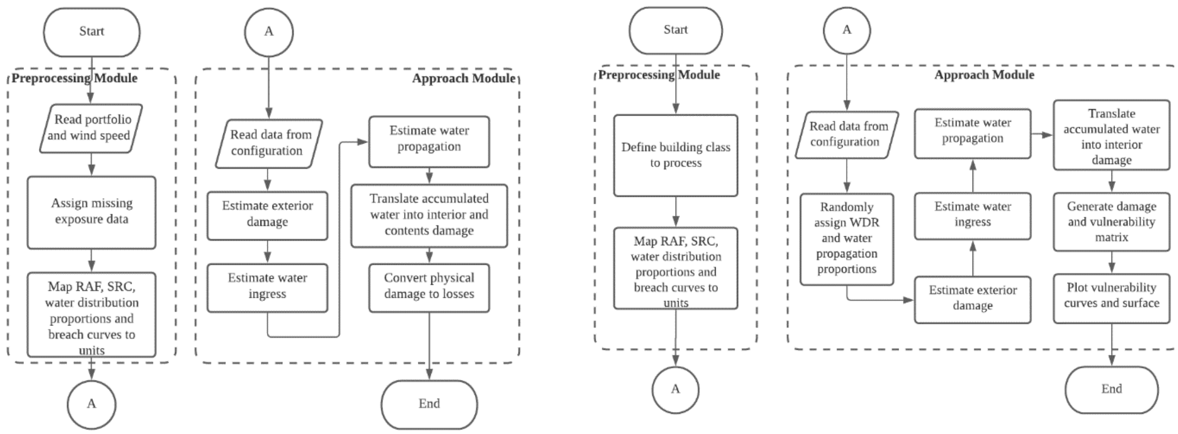

Figure 1. Generic flowcharts of DCM (left) and PVM (right)

Keywords: mid/high-rise building, rainwater ingress, interior damage, contents damage, vulnerability model

ACKNOWLEDGEMENTS
The National Science Foundation supports the Center for Wind Hazard and Infrastructure Performance (WHIP-C) through grant # 1841523, and the Industrial Advisory Board of the WHIP-C supported this work through grant number WHIP2020_06. The opinions, findings, and conclusions presented in this paper are those of the author alone, and do not necessarily represent the views of the NSF or the WHIP-C.

REFERENCES

Baheru, T., Chowdhury, A. G., Pinelli, J. P., & Bitsuamlak, G. (2014). Distribution of wind-driven rain deposition on low-rise buildings: Direct impinging raindrops versus surface runoff. *Journal of Wind Engineering and Industrial Aerodynamics*, 133, 27-38.

Raji, F., Zisis, I., & Pinelli, J. P. (2020). Forthcoming “A wind tunnel study to quantify the wind-driven rain propagation in the interior of residential structures,”. *ASCE Journal of Structural Engineering*, 146(7).

Silva de Abreu, R. V., Pinelli, J. P., Raji, F., & Zisis, I. (2020). Testing and modeling of hurricane wind-driven rain water ingress, propagation, and subsequent interior damage in residential buildings. *Journal of Wind Engineering and Industrial Aerodynamics*, 207, 104427.

3D nonlinear tropical cyclone boundary layer model: From meteorological perspective to wind engineering applications

Liang Hu [a,*], Ahsan Kareem [b]

[a] *NatHaz Modeling Lab, University of Notre Dame, Notre Dame, IN, peettr@gmail.com*
[b] *NatHaz Modeling Lab, University of Notre Dame, Notre Dame, IN, kareem@nd.edu*

ABSTRACT:
This study focuses on updating the tropical cyclone boundary layer (TCBL) model in the context of TC winds simulation in performance-based wind engineering (PBWE). To this end, it first introduces the 3D nonlinear TCBL model, which is so far the most rigorous TC diagnostic model in marine conditions, into the PBWE. The effect of land-sea roughness contrast on the boundary layer of landfalling TCs, which is critical for applying the model to the coastal structures, is then investigated. The ensemble of results obtained from the updated TCBL model is being validated using measurements, reanalysis data, and universal full-physics mesoscale simulations. As the PBWE is sensitive to the probabilistic characteristics of TC winds, it is expected that the work in this thesis may enhance the accuracy and reduce uncertainty in a PBWE analysis.

Keywords: tropical cyclone boundary layer nonlinear model performance-based wind engineering

1. BACKGROUND

Extreme winds in tropical cyclones (TC, hurricanes/typhoons) are responsible for the considerable loss of civil infrastructures in TC-prone areas. To assess the risk/loss of these structures to TC winds, the performance-based wind engineering (PBWE) paradigm is being utilized as a simulation-based framework (Spence and Kareem, 2014). As part of the hazard analysis module, estimation of TC-induced extreme winds by the Monte Carlo simulation is one of the fundamental steps in PBWE. On the other hand, modeling tropical cyclones in meteorology has progressed substantially in the past decades due to increased computational capacity, accumulated measurement data, and the emergence of machine learning techniques. Meteorological TC models not only can resolve intricate structures embedded in TCs (e.g., low-level jet, rainband, eyewall replacement, intensification) but also are able to include the impact of climate variability. At this juncture, to further refine PBWE for TC applications, it needs a new perspective rooted in TC meteorology, i.e., tailoring the cutting-edge TC models to leverage the PBWE practice.

2. IMPLEMENTING THE TROPICAL CYCLONE BOUNDARY LAYER MODEL

As one of the essential parts in TC wind simulation, the three-dimensional (3D) fully nonlinear tropical cyclone boundary layer (TCBL) wind field model (Kepert and Wang, 2001) is investigated. Forced by gradient winds characterized by a series of parameters (central pressure deficiency, radius to maximum wind, and Holland-B, etc.), this model solves a shallow (~2000m) version of the primitive equations by using the time-splitting finite difference method to resolve both the wind and thermal structure in the TCBL. The solution procedure of this model is outlined. Through numerical experiments, the sensitivity of some of the computational algorithms in the model on the wind speed prediction are discussed, e.g., horizontal diffusion, the order of difference algorithm, and thermal effects. These features lead to a reasonable vetting of the TCBL model

* Lead presenter

presented, which is stable and has gone through validation against existing results. Finally, the model is utilized to simulate the extreme winds at a specified site leading to the assessment of roof damage of an example low-rise building at the site. Comparison with results obtained by other conventional TCBL models (3D linear and 2D slab) reveals an apparent difference in both the extreme mean wind speed field and expected annual loss ratio, as shown in Figure 1.

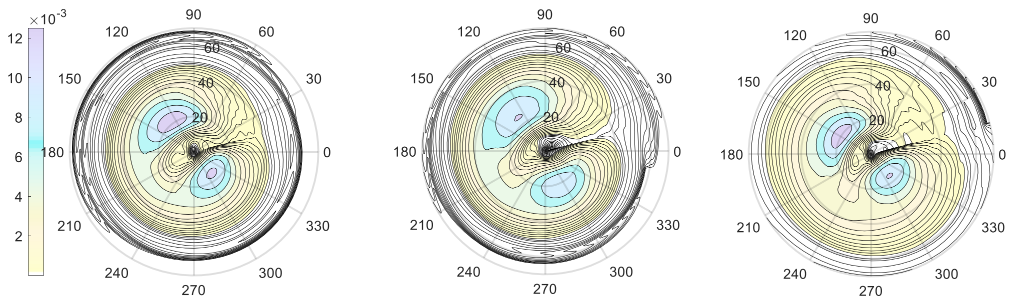

Figure 1. Joint probability density function of wind speed-direction at 10m generated by: (a) 3D nonlinear model; (b) 3D linear model; and (c) 2D slab model.

3. EFFECTS OF LAND-SEA ROUGHNESS CONTRAST

The boundary layer structure of landfalling tropical cyclones (TC) involves additional asymmetry resulting from the land-sea roughness contrast, which consequently influences the performance of buildings in TC-prone areas (Wong and Chan, 2007). This contrast-induced asymmetry in TCBL and its influence is investigated by utilizing a series of idealized numerical simulations by the 3D TCBL model. In this model, the contrast-induced asymmetry in TCBL results from the discontinuity of drag coefficients at the coastline. A series of numerical experiments are carried out with various settings to explore the contrast-induced asymmetry in both stationary and translating TCs. The asymmetry is demonstrated in the radial, azimuthal, and total surface wind speed, inflow angle, and their variation with height, and the surface wind reduction factor, and in terms of the joint difference (difference against the all-land and all-sea situations overland and oversea) as the primary measure. In this context, both the in-plane distribution pattern and intensity based on the statistics (RMS, maximum) of the asymmetry are of concern, as well as the underlying mechanism. Numerical results show that the contrast-induced asymmetry may result in maximum surface wind speed higher than both the all-land and all-sea situations overland and oversea concurrently. A conceptual model, which characterizes the contrast-induced asymmetry as the combination of the transitional effect around the coastline and the global distortion effect maximized near the TC eyewall, is proposed and successfully. It is observed that the translation-induced asymmetry may intensify the contrast-induced asymmetry and slightly change its distribution pattern, while their interaction may intensify the total asymmetry and shift the location of the maximum surface wind speed, depending on the parameters. Results also reveal the analogous patterns between a portion of the global distortion in the contrast-induced asymmetry and the translation-induced asymmetry. Finally, the TCBL with the land-sea roughness contrast is applied to assess wind-induced damage to a low-rise building near a coastline. The relative difference in extreme wind speed and annual damage ratio (as shown in Figure 2) can be as large as 40% and 50% for a single TC event or 8% and 23% in the ensemble, necessitating that this asymmetry-induced effect is captured in PBWE.

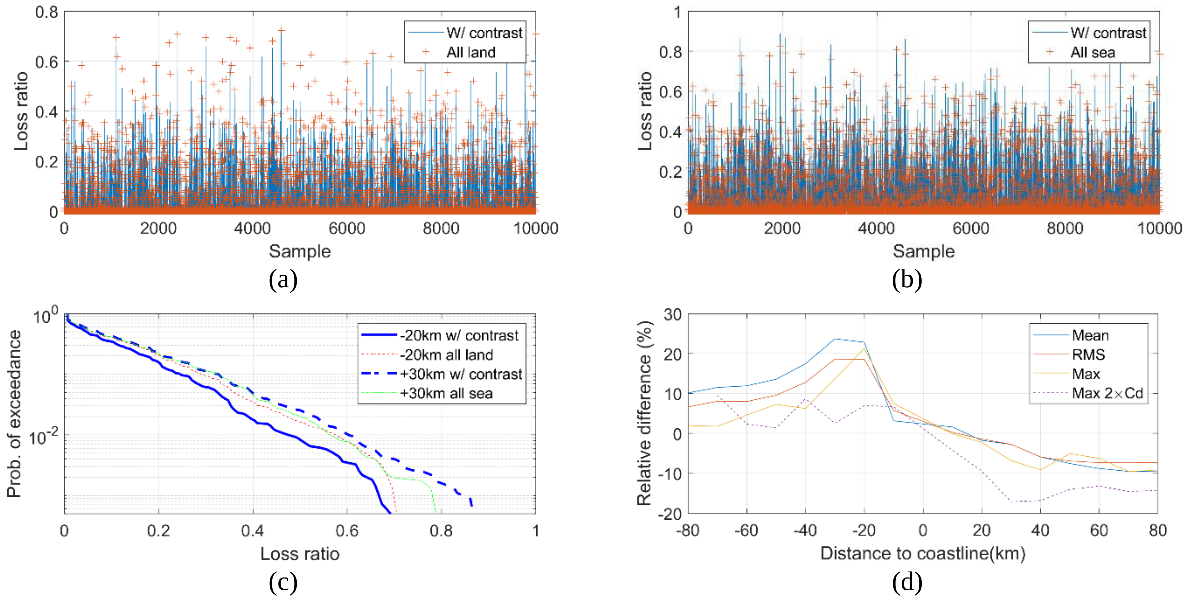

Figure. 2 Difference in the annual loss ratios of the example low-rise building in performance-based wind engineering. (a), (b) and (c) denote the sample and probability of exceedance of difference in annual loss ratio. (d) denotes the relative difference of the statistics of the annual loss ratio.

4. ONGOING VERIFICATION OF THE MODEL

Validation of the TCBL kinematics against measurement results is necessary for not only assessing the simulation accuracy but also ensuring its feasibility for engineering practice. The validation in this study starts from hurricane Isabel 2003 and covers about 30 selected hurricanes in the North Atlantic and the Gulf of Mexico basins during 1995-2015, both for a single TC event and as an ensemble average. The TCBL simulation results by the diagnostic models, such as 3D fully nonlinear, 3D linear, and 2D slab TCBL models, and by the full-physics WRF simulation are compared to the ECMWF reanalysis data, H*Wind surface wind fields, surface station and dropsonde measurements. The input of diagnostic models will be calibrated using the objectively-fitted TC tracks accounting for the gradient balance. Moreover, the WRF simulation is being carried out in different modes, i.e., without assimilation but with/without bogus inserted. Unlike customary focus in meteorology, surface wind speed, direction, and wind profiles below 500m are of interest for PBWE. With respect to these characteristics, the model comparison will be evaluated in terms of indicators carefully selected.

ACKNOWLEDGEMENTS

The authors wish to acknowledge the financial supports from the U.S. National Science Foundation (CMMI 1562244).

REFERENCES

Kepert, J., and Wang, Y. (2001). "The Dynamics of Boundary Layer Jets within the Tropical Cyclone Core. Part II: Nonlinear Enhancement." *Journal of the Atmospheric Sciences*, 58(17), 2485-2501.

Spence, S. M. J., and Kareem, A. (2014). "Performance-based design and optimization of uncertain wind-excited dynamic building systems." *Engineering Structures*, 78, 133-144.

Wong, M. L. M., and Chan, J. C. L. (2007). "Modeling the Effects of Land–Sea Roughness Contrast on Tropical Cyclone Winds." *Journal of the Atmospheric Sciences*, 64(9), 3249-3264.

Abstract Withdrawn

* Lead presenter

Uncertainty Quantification of Wind-tunnel Tests of a Low-Rise Building Model using the NIST Aerodynamic Database

Erin Hubbard [a] *, Erick Shelley [b], Wei Zhang [c]

Department of Mechanical Engineering, Cleveland State University, Cleveland Ohio, U.S.
[a]*Graduate Student, Erin.P.Hubbard@nasa.gov*
[b]*Graduate Student, Erick.Shelley@gmail.com*
[c]*Associate Professor, W.Zhang13@csuohio.edu*

ABSTRACT:
Wind-induced roof pressures of low-rise buildings are often measured in boundary-layer wind tunnels. It has been documented that pressure statistics on reduced-scale building models differ considerably among different boundary-layer wind tunnels. Flow facility capability, model design and manufacturing, instrumentation, test setup and procedures, and specific data reduction methodology as well as researchers' experience are among the many factors that affect measured data and results in wind-tunnel experiments. Considering the aforementioned list of variables, it is no wonder that results often differ since each variable brings in potential error sources. To identify driving uncertainty sources in the pressure statistics obtained from wind-tunnel tests, a detailed uncertainty quantification analysis is performed via Monte Carlo simulation using the NIST aerodynamic database. The work demonstrates specifically how measurement uncertainty propagates to quantities of interest in a wind-tunnel test. It will also provide an improved understanding of critical measurements, uncertainty sources, and may reveal hints as to why differences exist between pressure statistics results.

Keywords: Boundary-layer wind tunnel, roof pressure, uncertainty quantification, Monte Carlo method

1. INTRODUCTION

Boundary-layer (BL) wind tunnel tests of wind loading on building models have served as primary means to determine the minimum design wind loads by the American Society of Civil Engineers (ASCE) provisions. It is well known that wind-tunnel results often show considerable discrepancies even when significant efforts are put into model preparation, experimental setup, equipment/instrumentation calibration and common data reduction methodology. The variability of wind pressure data from six wind tunnel laboratories is reported with a coefficient of variation in the results ranging from 10% to 40% (Fritz et al, 2008). Even with this level of variability, results are often reported without uncertainty quantification (UQ).

Uncertainty quantifies a probabilistic interval within which a "true value" is likely to fall from some reported result. If an experiment were to be performed repeatedly under the same conditions, the observed variation in the result would represent a random component of uncertainty, or that resulting from the inherent randomness present in any real environment. Systematic uncertainty components are those that produce a bias effect on data. Systematic uncertainty is easy to overlook and hard to quantify since it tends to bias an entire set of repeats by an undetectable amount unless further effort is expended. Even when random and systematic sources of uncertainty are acknowledged, experimentalists and researchers often publish results without uncertainty specified because of the additional effort required to perform repeats and statistical analyses to capture random uncertainty, and an uncertainty propagation analysis to capture systematic uncertainty.

* Lead presenter

This not only hinders a fair comparison among different research results, but also hinders an increased understanding of the driving uncertainty sources introduced at different stages of wind-tunnel tests. "The uncertainty is as important a part of the result as the estimate itself…An estimate without a standard error is practically meaningless" (Jefferys 1967 in Higdon et al. 2006). Without uncertainty defined as part of the results, meaningful comparisons cannot be made between two tests, or between a test and computational result for validation purposes. Additionally, when uncertainty sources and their impacts on a result are less understood, ways to effectively improve tests and increase the fidelity of the results remain elusive. In view that BL wind tunnel test cases and results are increasingly used to validate computational fluid dynamics (CFD) simulation, it is imperative to provide uncertainty quantification of the wind-tunnel test data and results.

2. UNCERTAINTY QUANTIFICATION METHOD

This study will estimate uncertainty, particularly systematic uncertainty, in pressure statistics using the Monte Carlo method of uncertainty propagation from wind-tunnel experiments archived in the NIST aerodynamic database. The test cases were performed at University of Western Ontario's (UWO) Boundary-Layer Wind Tunnel Laboratory, using a 1:100 scaled model of a low-rise building in suburban terrain.

The Monte Carlo Method (MCM) of uncertainty propagation is a fully probabilistic approach to UQ in which random draws are made from assumed error distributions for all pertinent uncertainty sources, errors are added to appropriate seed data values, and data is reduced to results of interest (Coleman and Steele, 2018). This procedure is repeated through n iterations until the probability distribution of the outcomes is stable and well-defined. For example, for outcome distributions of a Gaussian nature, convergence criteria can be selected for the sample standard deviation s such that $\frac{|s_n - s_{n-1}|}{s_n} < 0.001$, indicating that the n^{th} Monte Carlo sample caused less than 0.1% change to the sample standard deviation from the previous iteration. A probabilistic interval can then be defined as the uncertainty in the result (typically a 95% level of coverage). The process is depicted in Fig. 1. To determine uncertainty source sensitivities, the Monte Carlo simulation can be run the same way with each uncertainty source being applied one at a time to discover the relative impact of each on the calculated result.

3. RESULTS AND DISCUSSION

The uncertainty in several variables of interest will be quantified, such as the inflow wind speed profile, inflow turbulence intensity profile, and building pressure statistics. A sensitivity analysis of input uncertainties will provide insight into the dominant uncertainty sources. If time allows, a second uncertainty propagation simulation will be performed for a similar wind-tunnel test by the Tokyo Polytechnic University (TPU). With uncertainty estimates for both wind-tunnel tests, meaningful conclusions may be drawn about the agreement or disagreement of the building pressure statistics. If uncertainty levels are unacceptably high, the sensitivity test results will help guide decisions being made in the planning phase of an upcoming wind tunnel test that involves a similar setup to the UWO test. These UQ results ensure the adequate capture of critical parameters in future tests. Additionally, an uncertainty propagation code will be created that, with a few tweaks to the simulation, produce uncertainty estimations applicable to other similar wind-tunnel tests.

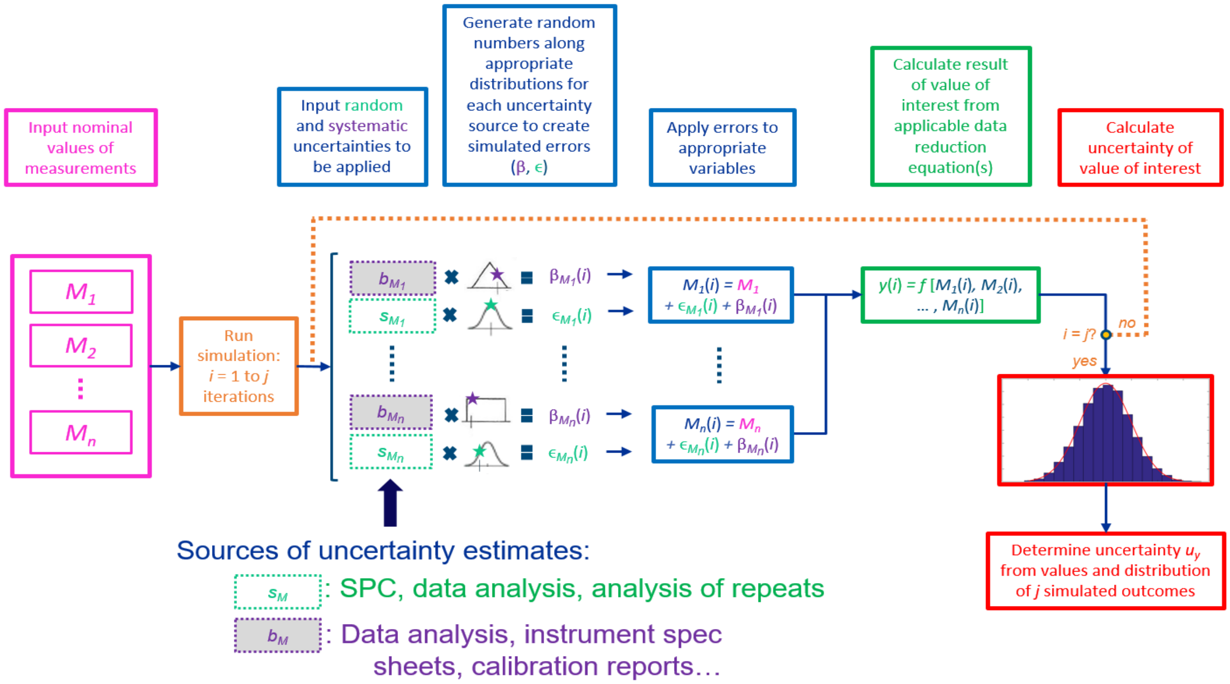

Figure 1. Monte Carlo method of uncertainty propagation (based on Stephens et.al, 2016)

4. CONCLUSIONS

Wind tunnel tests of building models remain an important research approach to improve design of minimal wind loading. Using the NIST aerodynamic database, this work will demonstrate how the uncertainty propagates with given error sources of wind-tunnel measurements. These results may improve understanding of critical measurements, uncertainty sources, and reveal hints as to why differences exist between reported pressure statistics.

ACKNOWLEDGEMENTS

E. Hubbard acknowledges the generous support of the Ohio Space Grant Consortium (OSGC) Master's Fellowship. E. Shelley acknowledges the OSGC university internship. W. Zhang acknowledges the National Science Foundation (NSF) CAREER grant (Award# 1944776) and the OSGC Faculty Research Initiation Grant Project (FRIGP).

REFERENCES

Coleman, H. and Steele, W., 2018. *Experimentation, Validation, and Uncertainty Analysis for Engineers*. John Wiley & Sons, Inc., Fourth edition, Hoboken, New Jersey, USA.

Fritz, W.P., Bienkiewicz, B., Cui, B., Flamand, O., Ho, T.C.E., Kikitsu, H. Letchford, C.W., and Simiu, E., 2008. International Comparison of Wind Tunnel Estimates of Wind Effects on Low-Rise Buildings: Test-Related Uncertainties. Journal of Structural Engineering, ASCE 134(12): 1887-1890.

Higdon, D., Klein, R., Anderson, M., Berliner, M., Covey, C. Ghattas, O., Graziani, C. Habib, S., Sefcik, J., Stark, P., and Steward, J., 2006. Uncertainty Quantification and Error Analysis. Workshop on Scientific Challenges in National Security: the Role of Computing at the Extreme Scale, Los Alamos National Laboratory, 10-00262.

Ho, T.C.E., Surry, D., Morrish, D., and Kopp, G.A. 2005. The UWO Contribution to the NIST Aerodynamic Database for Wind Loads on Low Buildings: Part 1. Archiving Format and Basic Aerodynamic Data. Journal of Wind Engineering and Industrial Aerodynamics, 93(1):1-30.

Stephens, J., Hubbard, E., Walter, J., and McElroy, T., 2016. Uncertainty Analysis of the NASA Glenn 8x6 Supersonic Wind Tunnel. Contractor Report, National Aeronautics and Space Administration, NASA/CR-2016-219411: 91.

A component-based interior and contents hurricane vulnerability model for low-rise residential buildings

Roberto Vicente Silva de Abreu[a,*], Jean-Paul Pinelli[b], Kurtis Gurley[c], Karthik Yarasuri[d]

[a]*Ph.D. candidate, Dept. of Civil Engineering, Florida Institute of Technology, Melbourne, FL 32901. E-mail: rsilvadeabre2014@my.fit.edu*
[b]*Professor, Dept. of Civil Engineering, Florida Institute of Technology, Melbourne, FL 32901. E-mail: pinelli@fit.edu*
[c]*Professor, Dept. of Civil Engineering, University of Florida, Gainesville, FL 32611. E-mail: kgurl@ce.ufl.edu*
[d]*Ph.D. candidate, Dept. of Civil Engineering, University of Florida, Gainesville, FL 32611. E-mail: karthiky@ufl.edu*

ABSTRACT:
Hurricanes cause damage from both wind and rain intrusion. Wind pressure affects mostly the exterior part of the building, such as walls, roof cover, and openings, while water ingress is the main cause for interior and contents damage. Although the interior of a residence can represent up to 80% of the total cost and 50% or more of the total building damage, interior and contents vulnerability models are still very primitive. The Florida Public Hurricane Loss Model (FPHLM) is a probabilistic risk model capable of estimating insured losses on residential infrastructure due to hurricanes (FPHLM, 2020). The FPHLM engineering team have been working on a component-based interior and contents vulnerability model. The foundations of this new model are test results on rain admittance and surface run-off, and water propagation inside a residence from the Florida International University Wall of Wind (WoW). The model is part of the FPHLM version 8.1 and provides improvements in comparison to the previous version. The new model combines an updated cost analysis, with the new water ingress, propagation, and percolation model, and new components-based interior and contents damage models.

First, the method divides the building floor area into six compartments. Within these compartments, interior components, such as ceiling, partitions, and flooring, are assumed uniformly distributed. Using engineering judgment and reports (USACE, 2006), the team assumed a collection of commonly found contents in a residence. These contents split into 5 categories, water absorbing (WA), non-water absorbing (NA), appliances (AP), water absorbing condo association (WA-CA), and non-water absorbing condo association (NA-CA). Second, the model defines the water absorption capacity of each interior and contents components. To account for the uncertainty, these capacities are treated as random variables where their probability density functions (pdfs) are based on manufacturer catalogs and standards. Third, the model computes the water ingress through defects and breaches on the building envelope as determined by a separate Monte Carlo simulation of physical exterior damage. Fourth, the model uses tests results from the Wall of Wind (Raji, Zisis and Pinelli, 2020) to propagate this water ingress among interior and contents components. If the volume of water at any component is higher than its absorption capacity, the excess water is estimated and percolated to other components. Figure 1 shows the propagation and percolation of water ingress inside the building. Fifth, the model transforms

* Lead presenter

absorbed volume of water into moisture contents (MC) for interior components and height of water (h) at each floor for contents components and estimate the damage of these components based on MC and h. Finally, the model generates vulnerability matrices for building, interior, apartment building contents and condo association contents. The results of this new model show great reduction in the vulnerability with respect to the previous version of the model at mid and high range wind speed for building vulnerabilities (Silva de Abreu et al., 2020). The presentation will focus on the incorporation of the WoW water propagation tests results into the model and the modeling of interior and contents components.

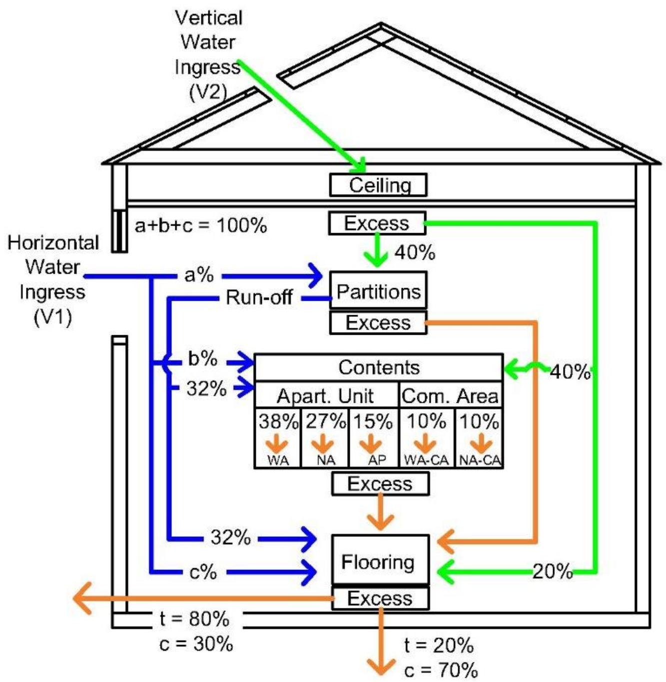

Figure 1 – Water propagation and percolation scheme

Keywords: Hurricane, Interior, Contents, Vulnerability, Component-based, FPHLM

ACKNOWLEDGEMENTS

The Florida Sea Grant College Program (FSGCP) supported this work [grant number: R/C-S- 63-B]. The opinions, findings, and conclusions presented in this article are those of the authors alone, and do not necessarily represent the views of the FSGCP. This work was also support Florida Office of Insurance Regulation (FOIR). The opinions, results, discussion, and conclusions are not necessarily those of the FSGCP or the FOIR.

REFERENCES

FPHLM - Florida Public Hurricane Loss Model 8.0. (2020). Florida public hurricane loss projection model (FPHLPM), Laboratory for insurance, financial, and economic research. International Hurricane Research Center (IHRC), Miami, FL.

Raji, F., Zisis, I., Pinelli, J.-P. (2020). Experimental Investigation of Wind-Driven Rain Propagation in a Building Interior. ASCE Journal of Structural Engineering.

Silva de Abreu, R.V., Pinelli, J.-P., Raji, F., Zisis, I. (2020), Testing and Modeling of Hurricane Wind-Driven Rainwater Ingress, Propagation, and Subsequent Interior Damage in Residential Buildings. Journal of Wind Engineering & Industrial Aerodynamics.

USACE. United States Army Corps of Engineers. (2006). Depth-damage relationships for structures, contents, and vehicles and content-to-structure value ratios (CSVR) in support of the Donaldsonville to the gulf, Louisiana, feasibility study.

A partial-turbulence approach to estimate peak pressures on low-rise buildings with flat roofs

Yitian Guo [a], Chieh-Hsun Wu [b], Gregory A. Kopp[c]

[a,c]*Boundary Layer Wind Tunnel Laboratory, Faculty of Engineering, University of Western Ontario, London, ON N6A 5B9, Canada,* [a] *yguo287@uwo.ca*, [c] *gakopp@uwo.ca*

[b]*Department of Civil Engineering, Tamkang University, Taipei, 25137, Taiwan, 157094@mail.tku.edu.tw*

ABSTRACT:
A new method is developed for estimating peak pressure coefficients on low-rise buildings with flat roofs based on a partial-turbulence approach. Wind tunnel tests have been conducted for a 1:50-scale low-rise building model for 6 different upstream turbulence conditions. The time histories of pressure coefficients on the roof were measured synchronously with the upstream velocity vector. Quasi-Steady (QS) vector models are conducted by a conditional-averaging technique. Pressure decomposition is achieved by subtracting the quasi-steady pressure component from the original pressure signal, and a statistical model is developed to account for the pressure component induced by small-scale and body-generated turbulence. Peak pressure coefficients are obtained by combining it with the QS model using a Monte-Carlo approach in the time domain. The new model provides reasonably good predictions of peak pressure coefficients for area-averaged panels subject to suction loads of flow separation.

Keywords: building aerodynamics; peak pressure coefficients; partial turbulence simulation; quasi-steady theory; low-rise buildings.

1. INTRODUCTION

The QS vector model is an engineering model which assumes the instantaneous pressure on the building surface is a function of the instantaneous upstream velocity vector. Mathematically it takes the form:

$$\Delta p(t) = \frac{1}{2}\rho V(t)^2 Cp(\theta, \beta) \tag{1}$$

where $\Delta p(t)$ denotes the pressure time series on building surfaces, ρ is the density of air, $V(t)$, θ and β denotes the magnitude, azimuth, and elevation angles of the velocity vector respectively. Most research agrees that the QS vector model can effectively capture the pressure fluctuation due to large-scale turbulence, but turn to miss the effects of small-scale and body-generated turbulence. As a result, it turns to underestimate peaks significantly (e.g., Richards and Hoxey, 2004; Wu and Kopp, 2016, 2018). Therefore, to obtain accurate peak pressures from the QS approach, the effects of the small-scale and body-generated turbulence must be somehow accounted for.

The idea of partial turbulence approach arises from the so-called partial turbulence analysis (PTS), which refers to only simulating the small-scale portion of the turbulence spectrum in the wind tunnel, while using the QS vector model to do correction for the large-scale portion (e.g., Irwin, 2008). In this study, the pressure component induced by small-scale and body-generated turbulence is studied, a statistical model have been proposed to account for the effect, and a method to estimate peak pressure coefficients is developed.

2. METHODOLOGY

Wind tunnel tests were conducted in Boundary Layer Wind Tunnel Laboratory of the University of Western Ontario (UWO) using a 1/50 scale model of Texas Tech University (TTU) WERFL building (Levitan and Mehta, 1992). The model has plan dimension of 27.5 cm×18.3 cm and a height of 8 cm. A total of 204 pressure taps were uniformly distributed across the building surfaces. Pressure signals were sampled at 625 Hz for 200 seconds, for 19 nominal wind directions (0^o to 90^o in 5^o increments). The velocity measurements are made using Cobra probes, synchronized with the pressure measurements. The location of the velocity measurements is at one building height (8 cm) above the middle point of the front edge of the building roof. Six upstream terrain roughness conditions were created in Boundary Layer Wind Tunnel II at UWO, which can be characterized by the turbulence intensity and integral scale. More details of the experimental set up can be found in Wu and Kopp (2016) and Wu and Kopp (2018).

The QS vector models are conducted using a conditional-averaging technique, which is modified from the method shown in Wu and Kopp (2018). Both the azimuth and the elevation effects of the velocity vector are included. Pressure decomposition are processed by the following equation in the time domain:

$$p_{local} = \Delta p(t) - \frac{1}{2}\rho \mathrm{V}_s^2(t)Cp(\theta,\beta) \tag{2}$$

where p_{local} denotes to the pressure component induced by small-scale and body-generated turbulence. V_s^2 is the velocity vector that applied with a moving average filter, with the window size corresponding to the turbulence length scale of 30 times of the mean roof height, so that the uncorrelated small-scale fluctuations is removed from the QS component.

In order to develop a general method for estimating p_{local}, it is necessary to normalize it so that the difference in distributions due to terrain and nominal wind direction can be reduced, which leads to the definition of the non-dimensional coefficients R:

$$R = \frac{p_{local}}{\rho \times k \times |Cp(\theta,\beta)|} \tag{3}$$

where $|Cp(\theta,\beta)|$ denotes the magnitude of the QS function, and k denotes to the turbulence kinetic energy, which is defined as:

$$k = \frac{1}{2}\left[\overline{(u')^2} + \overline{(v')^2} + \overline{(w')^2}\right] \tag{4}$$

where u', v' and w' are the three fluctuating velocity components.

A three-parameter T-scale distribution is selected to fit the distribution of R data, thus, a statistical model to account for the pressure component induced by small-scale and body-generated turbulence is developed. The pressure time series can be then obtained by reversing equation (2) using a Monte-Carlo approach, which takes the form:

$$\Delta p(t) = \frac{1}{2}\rho \mathrm{V}_s^2(t) \times Cp(\theta,\beta) + R_r \times k \times |Cp(\theta,\beta)| \tag{5}$$

where R_r is a random variable sampled from the fit statistical model. The peak pressure coefficients are then obtained through extreme value analysis of the pressure time series.

3. RESULTS AND CONCLUSIONS

The CDF functions of *R* from different terrains and nominal wind directions roughly yields to a single curve after normalization, and therefore, can be represented by a fit statistical model. For different panel cases, this model distribution is not significantly affected by panel size, but is dependent on panel locations. Particularly, for panels that subject to suction loads due to flow separations, the distributions of *R* are similar enough to be represented by a single model.

Figure 1 shows the peak pressure coefficients estimated from the combined model, compared with the measured data and a pure QS model. The case is for a relatively large area-averaged panel at an Open terrain, with the probability of non-exceedance of 0.99 in 1-minute model-scale time. The panel is located at the roof corner, which is subject to suctions loads due to flow separation at most of the wind directions. It can be seen that the results provided by the combined model matches the measured data reasonably while, which is much better compared to a pure QS model, as the latter one underestimates the peak significantly.

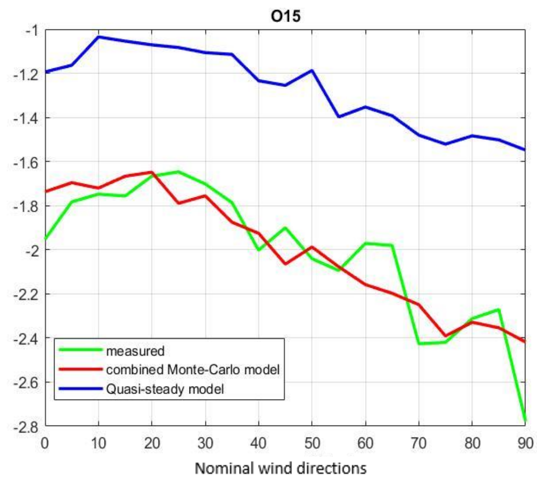

Figure 1. 99% probability of non-exceedance pressure coefficients in 1-minute time period for a roof-corner area-average panel in an Open terrain, obtained from the combined Monte-Carlo model using the partial-turbulence approach, compared with the pure QS model and the measured data

ACKNOWLEDGEMENTS

This work was funded by the Natural Sciences and Engineering Research Council (NSERC) of Canada and the Institute for Catastrophic Loss Reduction (ICLR) under the Collaborative Research and Development Grants Program. GAK also gratefully acknowledges the support provided by ImpactWX and Western University.

REFERENCES

Irwin, P. A. (2008). Bluff body aerodynamics in wind engineering. Journal of Wind Engineering and Industrial Aerodynamics, 96(6-7), 701-712. doi:10.1016/j.jweia.2007.06.008

Richards, P. J., & Hoxey, R. P. (2004). Quasi-steady theory and point pressures on a cubic building. Journal of Wind Engineering and Industrial Aerodynamics, 92(14-15), 1173-1190. doi:10.1016/j.jweia.2004.07.003

Wu, C-H., & Kopp, G. A. (2016). Estimation of Wind-Induced Pressures on a Low-Rise Building Using Quasi-Steady Theory. Frontiers in Built Environment, 2. doi:10.3389/fbuil.2016.00005

Wu, C-H., & Kopp, G. A. (2018). A quasi-steady model to account for the effects of upstream turbulence characteristics on pressure fluctuations on a low-rise building. Journal of Wind Engineering and Industrial Aerodynamics, 179, 338-357. doi:10.1016/j.jweia.2018.06.014

Assessment of load path through residential roofs using full-scale wind tunnel measurements

Sarah A. Stevenson[a*], Murray J. Morrison[b], Gregory A. Kopp[c]

[a]Boundary Layer Wind Tunnel Laboratory, Faculty of Engineering, University of Western Ontario, London, ON, Canada, ssteve72@uwo.ca
[b]Insurance Institute for Business and Home Safety, Richburg, SC, USA, mmorrison@ibhs.org
[c]Boundary Layer Wind Tunnel Laboratory, Faculty of Engineering, University of Western Ontario, London, ON, Canada, gakopp@uwo.ca

ABSTRACT
The Continuous Load Path (CLP) experiments carried out at the Insurance Institute for Business & Home Safety (IBHS) Research Center provide detailed measurements of the wind load transfer through critical links in the load path of an archetype residential structure. The extensive database provides load path measurements from non-destructive testing of the archetype house, as well as select measurements from destructive testing of a demonstration house with the same specifications. Of current interest, the non-destructive tests provide time histories of wall, roof, and internal pressures and loads at the roof-to-wall connection and building anchorage under constant and fluctuating wind load cases. Several phases of testing were carried out to observe the load path behaviour before and after installation of interior sheathing, as well as the difference in loads measured by load cells supporting the roof trusses versus instrumented hurricane straps at the roof-to-wall connection. Different anchor bolt spaces, representing the International Residential Code and FORTIFIED Homes recommendations, were also tested.

The current research validates the aerodynamic measurements of the CLP project by comparing it to wind tunnel data for model houses of similar roof shape and checking the equilibrium of the roof pressures with the load cell measurements, and investigates the distribution of roof pressures into the roof-to-wall connections. The current test case is taken from the phase after the interior drywall was installed - sealing the attic space from the living space - and before the load cells were removed from the roof-to-wall connections. This is selected as the base case because it allows for the roof load path to be studied including the influence of internal pressure, but without the influence of hurricane strap stiffness. Figure 1 shows the exterior of the house and the interior wall-to-ceiling seal in this phase. The gaps between the roof structure and walls are sealed using plastic sheeting taped to the interior and exterior roof and wall surfaces to prevent leakage of internal pressures.

* Lead presenter

Figure 1. Test house in IBHS wind tunnel and interior view of wall-to-ceiling seal and internal pressure sensors.

Preliminary assessment of the roof uplift load balance between the net pressures and the load cells at the roof supports indicates that the loads nearly balance, with higher uplift measured by the load cells than is captured by the net pressures using the external and internal pressure taps. These differences may be attributed to experimental uncertainty. Figure 2 shows a comparison of the mean, absolute maximum and minimum, and standard deviation of total roof uplift measured using the load cells and the internal and external roof pressure taps.

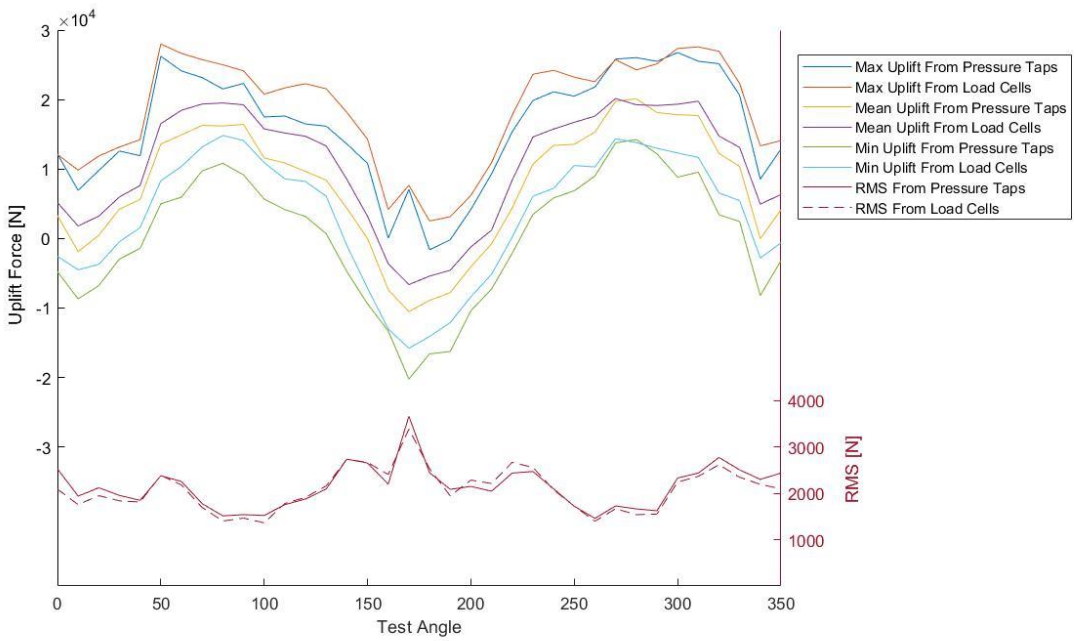

Figure 2. Comparisons of total roof uplift calculated using time-histories of load at the roof-to-wall connection load cells and internal and external roof pressure taps.

Uplift on individual trusses is also computed to observe the distribution of roof pressure between trusses. When the archetype house was subjected to loading normal to the gable end walls, it is observed that a vast majority of the uplift pressures near the windward end of the roof (6 – 8 trusses) are distributed to the gable end truss. As shown in Figure 3, the load cells supporting the trusses immediately inside of the gable end truss experience lower uplift than the aerodynamic loads that are applied to their tributary areas. This deficit appears to be carried by the gable end truss, as indicated by the end truss load cell measurements being 3-4 times larger than in neighbouring trusses. This implies that load sharing among roof trusses may be significant, especially in houses with relatively stiff gable end trusses.

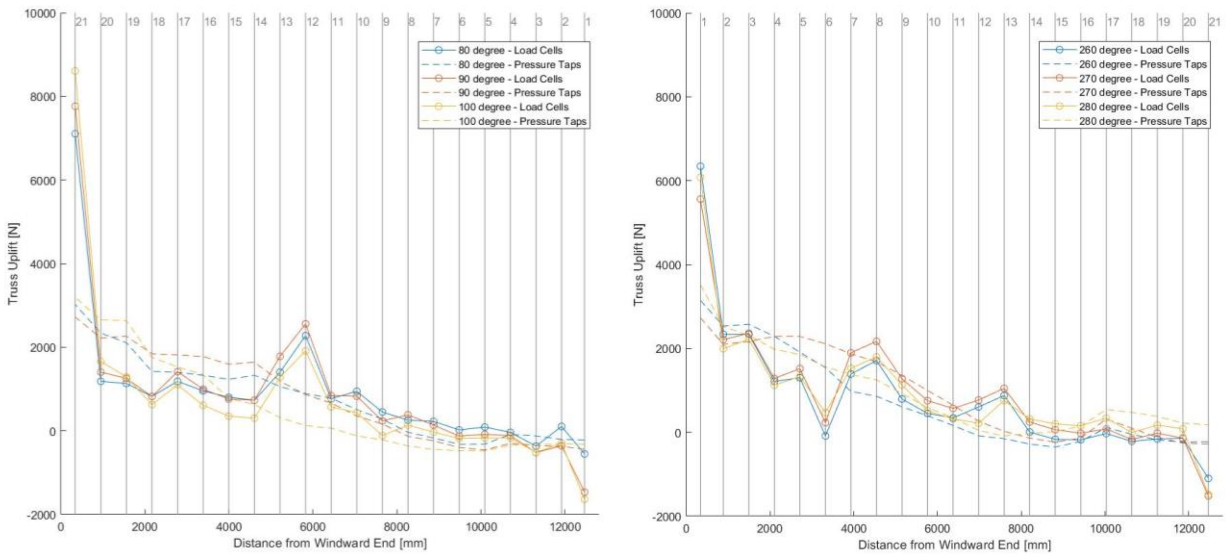

Figure 3. Net uplift on roof trusses measured by roof-to-wall connection load cells, compared to aerodynamic uplift loads calculated based on tributary area loading. 90° and 270° angles of attack shown, indicating loads concentrated at windward gable end.

Other data gathered during the CLP testing that will be utilized in upcoming work include time histories of force in anchor bolts at the foundation, horizontal displacement in walls acting as shear walls, and axial loads in select truss members. These data from the non-destructive tests will be applied to validate linear 3-dimensional finite element models of the same structures. This work contributes to understanding the load path through residential structures under wind loads. When paired with capacity estimations, these data and the subsequent finite element modelling can help predict the weak links in the load path and the wind speeds at which failures are expected to initiate.

Keywords: continuous load path, full-scale wind tunnel testing, residential structures, IBHS, FORTIFIED Homes

Observations of the turbulent near wake of a bridge deck

Nicolò Daniotti[a], Jasna Bogunović Jakobsen[b], Jónas Snæbjörnsson[c] and Etienne Cheynet[d]

[a]*Department of Mechanical and Structural Engineering and Materials Science, University of Stavanger, Stavanger, Norway, nicolo.daniotti@uis.no*
[b]*Department of Mechanical and Structural Engineering and Materials Science, University of Stavanger, Stavanger, Norway, jasna.b.jakobsen@uis.no*
[c]*School of Science and Engineering, Reykjavik University, Reykjavík, Iceland, jonasthor@ru.is*
[d]*Geophysical Institute and Bergen Offshore Wind Center, University of Bergen, Bergen, Norway, etienne.cheynet@uib.no*

ABSTRACT
The turbulent near wake of a bridge deck is studied based on velocity records acquired by two sonic anemometers located $0.74D$ (where D is the depth of the deck) away from the trailing edge. Both the mean flow characteristics and one-point velocity spectra are explored to gain insight into the aerodynamics of a bridge deck at full-scale Re numbers in an atmospheric turbulence. In particular, the emphasis is on the vortex shedding process.

Keywords: Bridges, Aerodynamics, Near wake, Vortex shedding, Wind turbulence, Full-scale.

1 INTRODUCTION

In full-scale, the aerodynamic characteristics of a bridge deck can be investigated by measuring the wind-induced surface pressures around the girder (Frandsen, 2001, Li et al., 2011). A system of synchronized continuous-wave Doppler wind lidar instruments can also be employed to characterise the flow past a bridge deck (Cheynet et al., 2017). An accurate direct estimate of the Strouhal number, which defines the vortex shedding frequency, is of particular interest. Hence, it is appealing to utilize 3D sonic anemometers to study the vortex formation in the near-wake region of the bridge deck. In fact, sonic anemometers generally withstand a wide range of weather conditions and do not require regular maintenance, thereby making them ideal for continuous monitoring.

The velocity records utilized in the present study are acquired on the Lysefjord Bridge, a suspension bridge located at the inlet of a narrow fjord in the south-western part of Norway. The bridge has a main span of $446\,\mathrm{m}$ and an hexagonal closed box-girder with an aspect ratio of $B/D = 4.6$, with its midspan located $55\,\mathrm{m}$ above sea level (Figure 1). The bridge is instrumented with a variety of different sensors (Cheynet et al., 2019), but the present study focuses on the data acquired by two 3-D sonic anemometers (3D WindMaster HS from Gill Instruments) designated as D08W and D08E, which are mounted at the deck level, $2\,\mathrm{m}$ away from the leading/trailing edge (Figure 1). These sensors have been operating since August 2020. The measurement location was chosen to investigate the turbulence structure and vortex formation in the near wake region. The instruments are designed with a horizontal head to minimize the sensor body-induced distortion of the vertical turbulence component. The undisturbed turbulence is studied using simultaneous measurements at $6\,\mathrm{m}$ height above the deck on the upwind and downwind sides (Cheynet et al., 2019). The primary goal of this study is to explore the capabilities of such an instrumentation setup to capture the wind flow characteristics in the near wake region.

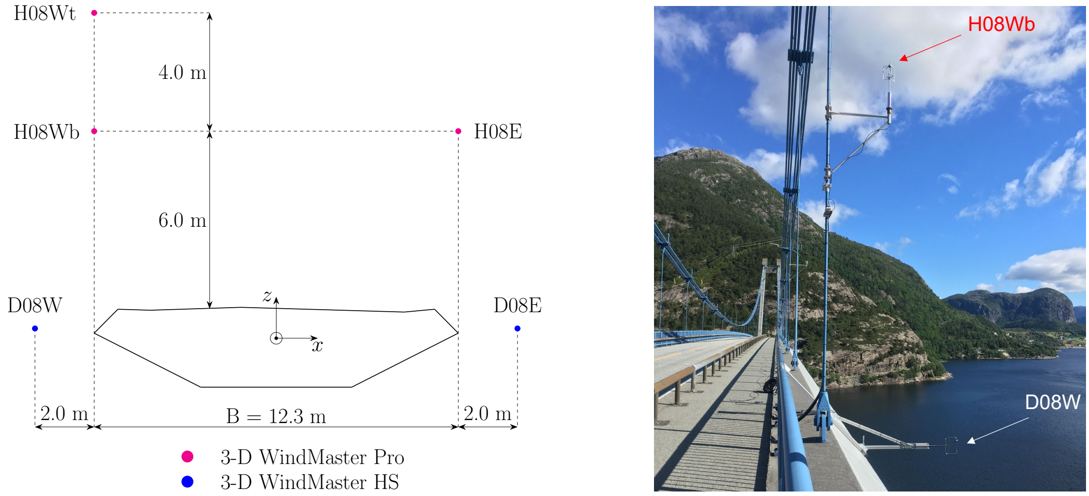

Figure 1. Location of the sonic anemometers at hanger 08 (120 m from midspan) of Lysefjord Bridge (left panel) and view of the sensors on the west side of the deck (right panel).

2 RESULTS

The statistics of turbulence are computed based on 10 min-long stationary time series associated with $\bar{u} > 5\,\mathrm{m\,s^{-1}}$, wind directions from NNE with yaw angles $-45° < \beta < 45°$, and neutral thermal stratification of the atmosphere. As an example, Figure 2 compares the vertical turbulence component w measured in the near wake (D08W) to the one estimated 6 m above the deck (H08E). The normalized variance $(\sigma_w/\bar{u}_0)^2$, where $\bar{u}_0$ is the undisturbed mean wind speed, is larger in the near wake, with an average ratio $(\sigma_w)_{downstream}/(\sigma_w)_{undisturbed} = 1.25$. The right panel of Figure 2 shows the ensemble average of the normalized velocity spectra S_w as a function of the reduced frequency $fD/\bar{u}_0$. The normalization is based on the variance recorded by the corresponding anemometers. In the near wake, an evident distortion of the spectral shape as well as a shift of the spectral content toward higher reduced frequencies can be observed. The maximum value of the normalized spectrum S_w estimated in the wake occurs at $fD/\bar{u}_0 = 0.18$, which identifies the vortex shedding frequency based on the Strouhal relationship. Hence, the measurement setup is found promising to provide insight into the flow characteristics in the near wake region of a bridge deck.

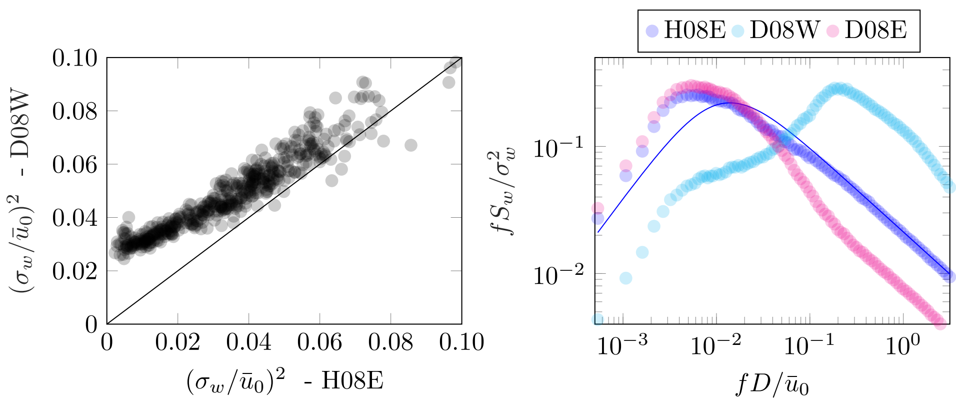

Figure 2. Correlation between $(\sigma_w/\bar{u}_0)^2$ recorded 6 m above the deck (H08E) and in the near wake (D08W) (left panel) and vertical velocity spectrum S_w at three locations (right panel). The solid blue line represents the Busch-Panofsky spectrum (Busch and Panofsky, 1968).

References

N. E. Busch and H. A. Panofsky. Recent spectra of atmospheric turbulence. *Quarterly Journal of the Royal Meteorological Society*, 94(400):132–148, 1968.

E. Cheynet, J. B. Jakobsen, J. Snæbjörnsson, N. Angelou, T. Mikkelsen, M. Sjöholm, and B. Svardal. Full-scale observation of the flow downstream of a suspension bridge deck. *Journal of Wind Engineering and Industrial Aerodynamics*, 171:261–272, 2017.

E. Cheynet, J. B. Jakobsen, and J. Snæbjörnsson. Flow distortion recorded by sonic anemometers on a long-span bridge: Towards a better modelling of the dynamic wind load in full-scale. *Journal of Sound and Vibration*, 450:214–230, 2019.

J. Frandsen. Simultaneous pressures and accelerations measured full-scale on the Great Belt East suspension bridge. *Journal of Wind Engineering and Industrial Aerodynamics*, 89(1):95–129, 2001.

H. Li, S. Laima, J. Ou, X. Zhao, W. Zhou, Y. Yu, N. Li, and Z. Liu. Investigation of vortex-induced vibration of a suspension bridge with two separated steel box girders based on field measurements. *Engineering Structures*, 33(6):1894–1907, 2011.

6th American Association for Wind Engineering Workshop (online)
Clemson University, Clemson, SC, USA
May 12-14, 2021

Evaluation of a multi-fidelity simulation framework for predicting wind pressure loads on buildings

Themistoklis Vargiemezis [a,*], Catherine Gorlé [b]

[a]*Stanford University, Stanford, CA, USA, tvarg@stanford.edu*
[b]*Stanford University, Stanford, CA, USA, gorle@stanford.edu*

ABSTRACT
Wind-resistant design of buildings and their components plays an important role to reduces losses from extreme wind events. LES provide a powerful tool to calculate wind loads on buildings, but the computational cost remains high. The objective is to investigate if multi-fidelity simulation techniques can reduce the overall computational cost, while maintaining the high accuracy required for design. We consider two methods for creating high-fidelity surrogate models by combining RANS simulations for 15 wind directions with LES for only 3 wind directions: 1) a polynomial chaos expansion and 2) Kriging interpolation. A surrogate is built for the mean and rms C_p discrepancies between RANS and LES and added to the RANS results. The multi-fidelity methods significantly improve the accuracy of the rms C_p predictions; for predictions at a 20° wind direction they result in a root-mean-square error that ranges from 6.1% – 7.1% compared to 22% for a standard RANS solution.

Keywords: Computational Fluid Dynamics (CFD), multi-fidelity, polynomial-chaos expansion (PCE), Kriging

1. INTRODUCTION

Computational Fluid Dynamics (CFD) can offer a powerful tool for calculating wind loads on buildings, but the simulations often require a trade-off between accuracy and computational cost. Reynolds-averaged Navier-Stokes (RANS) simulations solve the time-averaged Navier-Stokes equations, resulting in a low computational cost, but also a reduced accuracy. Predictions of turbulence statistics, such as the fluctuating pressure coefficient, can be particularly compromised, since these requires the use of empirical models. On the other hand, large-eddy simulations (LES) apply a spatial filter to the unsteady Navier-Stokes equations to provide a higher-fidelity solution, although at a significantly higher computational cost than RANS. LES is the method of choice for wind loading applications, which require accurate estimates of the turbulent fluctuations in the wind pressures, but the high computational cost is a limiting factor for adoption in the design process.

In this presentation, we investigate a multi-fidelity approach to obtain accurate predictions of the mean and root-mean-square (rms) pressure coefficients on a high-rise building, without relying exclusively on computationally expensive LES evaluations. The main idea is that a cost-effective approximation of the high-fidelity LES prediction as a function of the wind direction can be found with a surrogate model based on many low-fidelity model evaluations in combination with a few evaluations of the discrepancy between the low- and high-fidelity models. We explore two approaches to build the surrogates: 1) a non-intrusive polynomial chaos expansion (PCE) and 2) kriging interpolation. In this abstract, we focus on the results for the rms C_p, since this is a more challenging problem than the prediction of the mean C_p.

* Lead presenter

2. METHODOLOGY

The model is based on wind tunnel experiments conducted in the atmospheric boundary layer (ABL) wind tunnel at the Politecnico di Milano (Lamberti et al. 2020). It is a 1:50 scale high-rise building model, with model scale dimensions 2 x 1 x 0.3 m. We focus on wind directions from 0° - 90° due to the symmetry of the geometry.

Fig. 2 depicts the multi-fidelity framework. First, we evaluate the mean and fluctuating pressure coefficients with the RANS and LES models. For the RANS model, the fluctuating pressure coefficient, C_p', is evaluated using the Paterson-Holmes empirical model (Paterson and Holmes, 1989). Then, we calculate the discrepancy between the two model predictions at a small number of wind directions, and we build a surrogate model for this discrepancy with either PCE or Kriging interpolation (Ng et al., 2012; Van Beers et al., 2004). Finally, the surrogate model for the discrepancy is added to a surrogate model obtained from RANS results for a large number of wind directions. The resulting multi-fidelity surrogate model can then be used to evaluate the statistics for any wind direction. As indicated in Fig. 2, we used 15 RANS and 3 LES (at 0°, 45°, and 90° for the Kriging model, and at 13°, 45°, and 77° for the PCE) to construct the surrogate model.

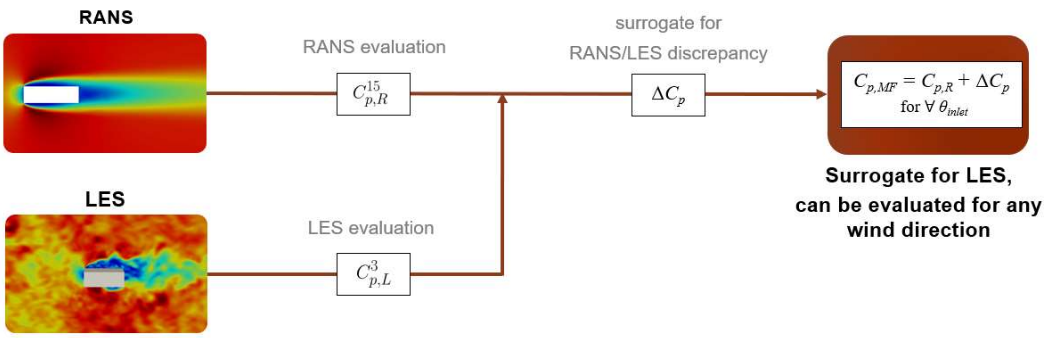

Figure 2. Multi-fidelity workflow

3. RESULTS

Fig. 3 shows the contours of C_p' on the building surface for the 20° wind direction, comparing the results of the Paterson-Holmes model (Fig. 3a), the LES (Fig. 3b), and the MF results of the Kriging interpolation (Fig. 3c) and PCE (Fig. 3d). Note that the LES result for the 20° wind direction were not used as input to the multi-fidelity model; it only serves as a validation data set.

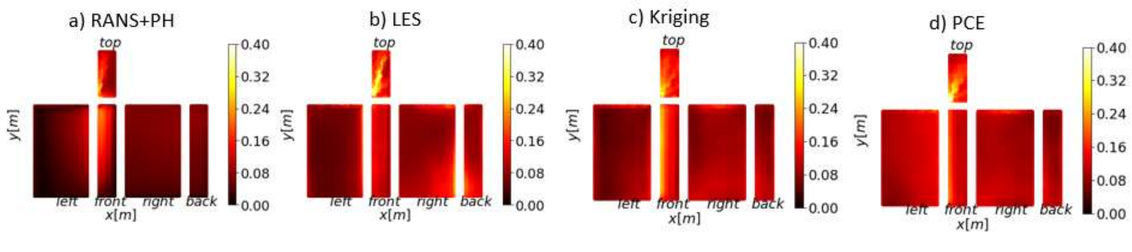

Figure 3. Contours of rms pressure coefficient at 20°.

Both multi-fidelity approaches provide a significant improvement over the Paterson-Holmes model, with a root mean square error (RMSE) of 22% for Paterson Holmes, 6.1% for the Kriging approach and 7.1% for the PCE. Fig. 4 plots the profiles of C_p' along different perimeters of the building; this more detailed analysis confirm that the MF models provide a significant improvement over the empirical model, but it also indicates a few locations near the building corners and on the roof with discrepancies between the multi-fidelity and LES results.

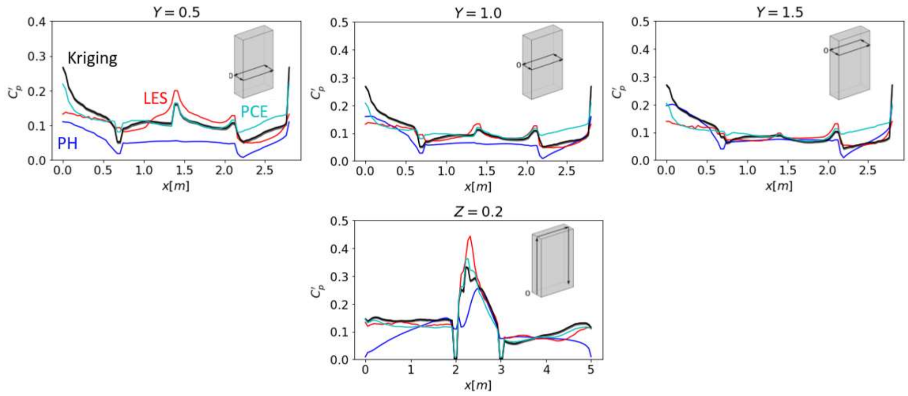

Figure 4. Profiles of rms pressure coefficient at 20º.

4. CONCLUSIONS AND FUTURE WORK

This study aims to investigate the use of a MF framework that combines information from RANS simulations at a large number of wind directions with LES at a small subset of wind directions, to improve the prediction of mean and rms pressure coefficients on buildings. We explored both a non-intrusive PCE and a Kriging interpolation approach to approximate the discrepancy function between low- and high-fidelity models, and subsequently build a multi-fidelity surrogate model that can be used to evaluate the quantities of interest for every desired wind direction.

The results indicate that the prediction of mean and fluctuating pressure coefficients from RANS can be significantly improved by leveraging additional information from the results of 3 LES. Future work will focus on investigating strategies that could reduce some of the local discrepancies observed between the multi-fidelity and LES solutions and on modelling more complex geometries. This will likely require the incorporation of data from additional LES; in this respect, Kriging interpolation, which can incorporate information from any wind direction, is expected to offer a more flexible approach.

6. REFERENCES

Lamberti, G. and Gorlé, C., 2020. Sensitivity of LES predictions of wind loading on a high-rise building to the inflow boundary condition. Journal of Wind Engineering and Industrial Aerodynamics, 206, p.104370.

Ng, L.W.T. and Eldred, M., 2012. Multifidelity uncertainty quantification using non-intrusive polynomial chaos and stochastic collocation. In 53rd AIAA/ASME/ASCE/AHS/ASC Structures, Structural Dynamics and Materials Conference 20th AIAA/ASME/AHS Adaptive Structures Conference 14th AIAA (p. 1852).

Paterson, D.A. and Holmes, J., 1989. Computation of wind flow around the Texas Tech Building.

Van Beers, W.C. and Kleijnen, J.P., 2004, December. Kriging interpolation in simulation: a survey. In Proceedings of the 2004 Winter Simulation Conference, 2004. (Vol. 1). IEEE.

Experimental and computational modeling of ember hot-spots on roofs during wildland fires

Dac Nguyen [1], Nigel B. Kaye[1]

[1]*Clemson University, Clemson, USA, dacn@clemson.edu*

Summary
Ember accumulation on and around buildings is known as the main cause of ignitions of structures during wildfires (Mell et al.2010). There are numerous studies on ember formation, flight, and spot fire ignition, though not on ember accumulation on buildings (Tohidi & Kay 2017, Suzuki et al. 2016). A series of experiments was carried out in the Clemson University atmospheric boundary wind tunnel, in which the roofs of model homes were covered in embers and then removed by the wind to investigate the roof regions which are vulnerable to the accumulation of embers under the various conditions including roof slope, wind speed and wind direction. Results shown that the susceptible area on roofs where embers tend to stay in place under a wind load is a function of ember Tachikawa number, roof slope, and wind direction.

Keywords: *ember accumulation, spot fire, wildfire.*

INTRODUCTION

Spot fires due to ember accumulation is the main culprit of structure destruction during wildfires. However, there is lack of study on the conditions under which the embers will be accumulated on houses. In this study, a series of ember removal experiments was carried out to investigate this phenomenon.

EXPERIMENTAL PROCEDURE

At the first stage of experiments, model buildings and embers were prepared in the lab scale with the satisfaction of geometrical similarity. The building roof fabric also was tested and selected to make sure it has the same friction coefficient as those of a full scale roof shingle. During each experiment, model roof houses were covered by model embers and then exposed to the wind with various wind direction and wind speeds. The process of ember removal on the roof was recorded by a high resolution video camera. The recorded video then was analyzed using the MATLAB image processing tools to identify the regions from which embers had been removed for a given wind direction and wind speed. Based on the analyzed images, the percentage of roof area on which embers were retained was obtained for different roof slope with various wind conditions. The images of retained embers on roofs also enabled the development of roof top contour maps of the critical Tachikawa number (non-dimensional wind speed) at which embers would be removed from the roof. Herein the Tachikawa number is defined as

$$K = \frac{\rho_a U^2}{2\rho_p g L} \tag{1}$$

where ρ_a is the air density, ρ_p the particle density, g is gravitational acceleration, U is the reference wind speed, and L is a characteristic length scale for the ember. The Tachikawa number, in this context, is an instability parameter that is the ratio of the aerodynamic loading to the gravitational fixing force of the ember to the rooftop.

EXPERIMENTAL RESULTS

Ember removal from rooftops was highly sensitive to the variation of not only wind speed but also wind direction and building slope. For gable roofs with different slopes, the fraction retained embers are quite different when comparing the flat roof and steep roof (10/12 pitch). However, increasing the roof angle does not always result in decreasing the fraction of the roof on which embers remain. See the data shown in figure 1.

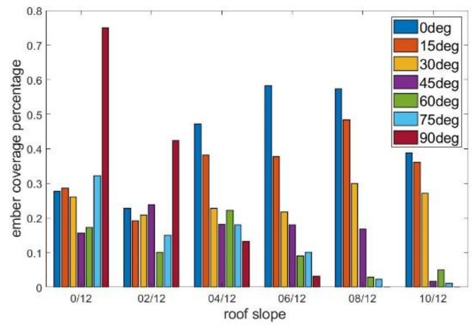

Figure 1. Ember retained coverage percentage for the maximum tested win speed, Tachikawa number K=5.9

The removal of embers from the roof is due to the imbalance between the wind load on the embers, the embers weight and the friction force between the ember and the roof surface. Hence, there is a relationship between regions of high wind shear and regions of ember removal. A preliminary investigation showed that regions in which the inverse critical Tachikawa number is low (low ember stability) correspond to regions of higher surface shear stress (calculated using NIST's Fire Dynamics Simulator).

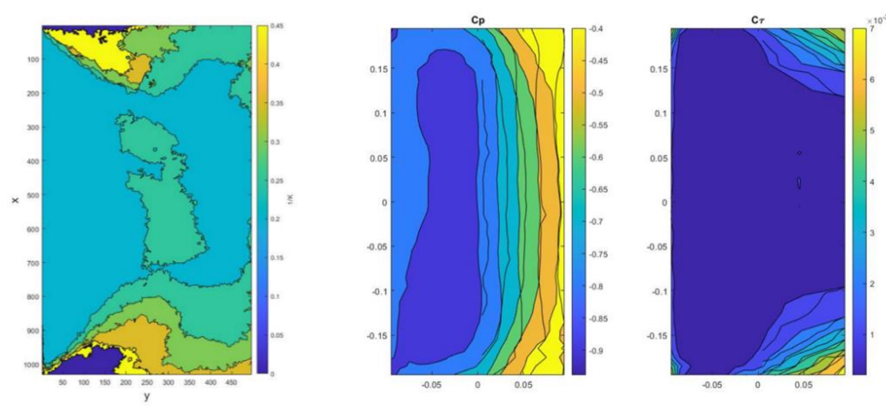

(a) (b) (c)

Figure 2. Contour plots of the (a) experimental measurements of inverse critical Tachikawa (a), (b) pressure coefficient ($C_p = 2\Delta P/\rho_a U^2$), and (c) shear stress coefficient ($C_\tau = 2\tau/\rho_a U^2$) for a flat roofed building with wind from left to right.

CONCLUSIONS

The area of a rooftop on which embers will not be removed by wind is a complex function of the rooftop geometry, wind speed, wind angle, and the properties of the embers. The experiments presented highlight this complexity. However, the results also suggest that the regions of ember stability can be correlated with the aerodynamic loading on the rooftop. Future work will investigate the probability of windborne embers landing and remaining on a building rooftop.

ACKNOWLEDGEMENTS

This work was performed under financial assistance award 70NANB17H213 from U.S. Department of Commerce, National Institute of Standards and Technology. The authors thank Yifu An, Zach Davis, Andrew Hopkins, Matthew Lehr, Tajon Jordan and Hunter Reux for their help in running experiments and image analysis.

REFERENCES

Mell, William E., Manzello, Samuel L., Maranghides, Alexander, Butry, David, and Rehm Ronald G. (2010) The wildland urban interface fire problem current approaches and research needs. *International Journal of Wildland Fire*, 19:238–251,

Tohidi, Ali, and Kaye, Nigel Berkeley. (2017) Comprehensive wind tunnel experiments of lofting and downwind transport of non-combusting rod-like model firebrands during firebrand shower scenarios. *Fire Safety Journal*, 90:95 – 111,

Suzuki, Sayaka, Nii, Daisaku, and Manzello, Samuel L. (2016) The performance of wood and tile roofing assemblies exposed to continuous firebrand assault. *Fire and Materials*, 41(1):84–96,

Deep Reinforcement Learning-based Decision Support System for Transportation Infrastructure Management under Hurricane Events

Shaopeng Li [a, *], Teng Wu [b]

[a]*University at Buffalo, Buffalo, NY, USA, sli85@buffalo.edu*
[b]*University at Buffalo, Buffalo, NY, USA, tengwu@buffalo.edu*

ABSTRACT:
During hurricane weather and traffic conditions, stakeholders may need to make a series of decisions to close or restrict the traffic of vulnerable components in the transportation network (e.g., aerodynamics-sensitive long-span bridges, hydrodynamics-sensitive coastal bridges and inundation-sensitive road segments) for the balance of traffic safety and mobility. It is essentially a stochastic sequential decision problem and can be formulated as a Markov decision process. Hence, this study proposes a deep reinforcement learning (RL)-based decision support system for stakeholders to manage these critical components for the purpose of minimizing the network-level losses induced by hurricanes. The decision policy, i.e., the mapping from high-dimensional continuous traffic/weather information to traffic control decision, is represented by a deep neural network (DNN) while the optimal policy (represented by DNN weights) is obtained using the RL methodology. A numerical example of a hypothetical transportation network under hurricane conditions is utilized to demonstrate the good performance of this novel scheme.

Keywords: decision support system; transportation infrastructures; hurricanes; traffic; reinforcement learning; deep neural network.

1. INTRODUCTION

Hurricanes are among the most devastating natural hazards that result in enormous life losses and economic damages. It is imperative for stakeholders from government to private sectors to make a series of decisions for the purpose of reducing the hurricane-induced losses. A frequently encountered decision-making scenario during hurricanes involves travel risk mitigation and essential functionality maintenance of transportation network considering that both may be greatly impacted by hurricanes. For example, flexible long-span bridges may suffer from the high hurricane wind speed; low-lying coastal bridges with weak connection between substructure and superstructure are vulnerable to storm surges and waves; flooding-sensitive road segments are prone to inundations caused by heavy rainfall. Based on the hurricane weather and traffic condition, the stakeholders may need to make sequential decisions to close or restrict the traffic of these vulnerable components in the transportation network for the balance of traffic safety and mobility. Current decision-making practices for traffic under adverse weather conditions are mainly based on empirical judgements (e.g., road/bridge closure when wind/wave/surge/inundation exceeds certain threshold) and usually performed independently for each critical component (FHWA, 2012). These component-level decision policies may be unable to minimize the overall network-level impact considering the high interdependencies among these infrastructure components, which calls for improved decision support system to minimize the hurricane-induced losses on the transportation network.

This study proposes a novel decision support system based on deep reinforcement learning (RL).

* Lead presenter

Specifically, the sequential decision-making problem in the complex stochastic weather-traffic environment is formulated as a Markov decision process (MDP), where the goal is to find the optimal decision to minimize the accumulated losses on the traffic network over the whole hurricane-impacted period. The optimal solution to a typical MDP problem could be obtained by techniques of dynamic programming (DP) or reinforcement learning (RL) (Sutton and Barto, 2018). It is noted that the existing weather-traffic system models are usually considered as "black-box" simulators involving several coupled modules from different disciplines (e.g., hurricane module, traffic network module and their interactions) with no close-form expressions. However, implementation of DP requires analytical system dynamics explicitly expressed in the form of state-transition probability. RL, on the other hand, can obtain the optimal solution to MDP in a trial-and-error fashion through interacting with the "black-box" simulators, which eliminates the needs for explicit system dynamics. Hence, it will be utilized in this study to obtain the optimal policy for hurricane-impacted traffic network. Furthermore, a deep neural network (DNN) is utilized to represent the decision policy, i.e., mapping from high-dimensional continuous weather/traffic information to the traffic control decisions while the optimal policy (represented by DNN weights) is obtained using the algorithm of deep Q learning (Mnih et al., 2015). For the proof of concept, a numerical example of a hypothetical transportation network under hurricane condition is utilized to demonstrate the good performance of the proposed scheme.

2. DEEP RL-BASED DECISION SUPPORT SYSTEM FOR A HURRICANE-IMPACTED TRANSPORTATION NETWORK

The management of transportation infrastructures under a hurricane event is a typical stochastic sequential decision problem, which could be formulated as a MPD. At time step *t*, the MDP state s_t includes both the traffic $\boldsymbol{u}_t$ and weather information $\boldsymbol{w}_t$ for components in the traffic network, i.e., $s_t = [\boldsymbol{u}_t, \boldsymbol{w}_t]$, which may involve both current observation (denoted by superscript *o*) and future prediction (denoted by superscript *p*), i.e., $\boldsymbol{u}_t = [\boldsymbol{u}_t^o, \boldsymbol{u}_{t+1}^p, \dots, \boldsymbol{u}_{t+h}^p]$ and $\boldsymbol{w}_t = [\boldsymbol{w}_t^o, \boldsymbol{w}_{t+1}^p, \dots, \boldsymbol{w}_{t+h}^p]$ (where *h* denotes the prediction horizon). The weather information could be obtained from the wind/wave/surge/inundation condition at critical locations using sensor measurements and/or prediction models. The traffic information, e.g., traffic flow on each road link, could come from the traffic surveillance and/or prediction systems. Based on current state $s_t = [\boldsymbol{u}_t^o, \boldsymbol{u}_{t+1}^p, \dots, \boldsymbol{u}_{t+h}^p, \boldsymbol{w}_t^o, \boldsymbol{w}_{t+1}^p, \dots, \boldsymbol{w}_{t+h}^p]$, stakeholders are required to take actions a_t, to decide to open or close each critical infrastructure component. At next time step *t*+1, the system states evolve to $s_{t+1} = [\boldsymbol{u}_{t+1}^o, \boldsymbol{u}_{t+2}^p, \dots, \boldsymbol{u}_{t+h+1}^p, \boldsymbol{w}_{t+1}^o, \boldsymbol{w}_{t+2}^p, \dots, \boldsymbol{w}_{t+h+1}^p]$ due to the change of hurricane weather, travel demand and the traffic reassignment caused by road opening/closure. It is noted that the analytical solutions of such complicated state-transition dynamics involving coupled hurricane-traffic interactions are currently not available. A reward r_t (negative value of cost), i.e., $r_t = -f_m(\boldsymbol{u}_{t+1}^o) - f_s(\boldsymbol{u}_{t+1}^o, \boldsymbol{w}_{t+1}^o)$, is received at each time step, which could be designed by stakeholders to consider both the cost from traffic mobility $f_m(\boldsymbol{u}_{t+1}^o)$ and safety $f_s(\boldsymbol{u}_{t+1}^o, \boldsymbol{w}_{t+1}^o)$. The cost from traffic mobility $f_m(\boldsymbol{u}_{t+1}^o)$ is related to the sum of travel time of all vehicles in the traffic network, while the safety-related cost $f_s(\boldsymbol{u}_{t+1}^o, \boldsymbol{w}_{t+1}^o)$ results from the traffic accidents in the adverse weather conditions, and hence depends on both traffic $\boldsymbol{u}_{t+1}^o$ and weather condition $\boldsymbol{w}_{t+1}^o$. The goal of decision-making for stakeholders is to maximize the expected cumulative reward $\mathrm{E}(\sum_{k=0}^{\infty} \gamma^k r_{t+k})$, where E is the expected value used to consider the uncertainties from hurricane weather, traffic condition and model predictions. The high interdependencies among different components makes the optimization problem very complicated.

In this study, the stochastic sequential decision problem formulated by MDP is approached by RL methodology empowered by DNN-based function approximations. As shown in Fig. 1, the RL environment is the transportation network under hurricane impact, which is simulated by coupled modules from different disciplines. Specifically, the hurricane wind is simulated using a height-resolving model, and the travel risk on the long-span bridge is represented by a vehicle accident fragility curve. Hurricane surge and wave are considered to related to the wind intensity, and the surge/wave-induced coastal bridge damage is represented by a deck unseating fragility curve. Hurricane rainfall and hence the inundation is considered to be related to wind intensity, and the travel risk on the flooding-sensitive road segment is represented by a vehicle damage fragility curve. Considering the high-dimensional continuous state from weather/traffic information and the complex state-action relations, a DNN with powerful function approximation abilities is utilized to output the optimal traffic control actions (bridge/road closure or traffic flow restriction) for the critical infrastructures. During the training process, the DNN weights (the policy) are updated towards optimal values by the maximizing the user-defined reward using RL algorithm of deep Q learning (Mnih et al., 2015).

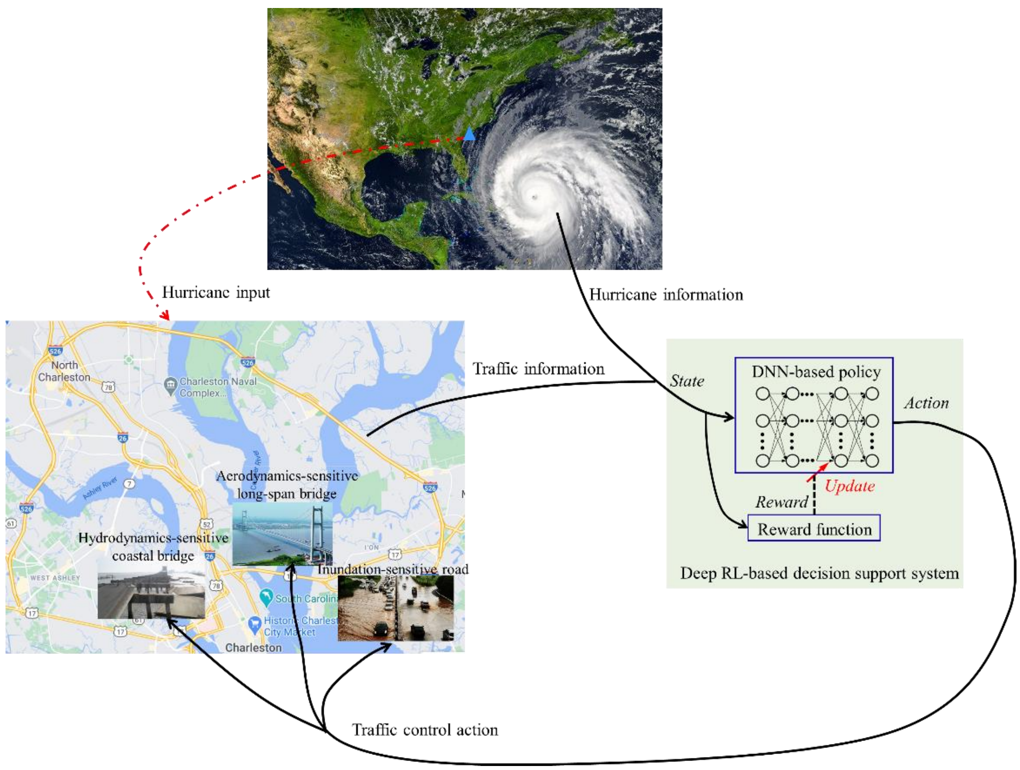

Figure 1. A deep RL-based decision support system for a hurricane-impacted transportation network

REFERENCES

FHWA, 2012, Best Practices for Road Weather Management. Report number: FHWA-HOP-12-046. https://ops.fhwa.dot.gov/publications/fhwahop12046/fhwahop12046.pdf

Mnih, V., Kavukcuoglu, K., Silver, D., Rusu, A.A., Veness, J., Bellemare, M.G., Graves, A., Riedmiller, M., Fidjeland, A.K., Ostrovski, G. and Petersen, S., 2015. Human-level control through deep reinforcement learning. *Nature*, 518(7540), 529-533.

Sutton, R.S. and Barto, A.G., 2018. *Reinforcement learning: an introduction*. MIT press.

High Frequency Effect on Peak Pressure Computation on the TTU Building Using Synthetic Inflow Turbulence Generator

Zahra Mansouri[1], Rathinam Panneer Selvam[2] Ph.D., P. Eng, Arindam Gan Chowdhury[3] Ph.D., A.M.ASCE

[1]BELL 4190, University of Arkansas, Fayetteville, AR 72701, USA, zmansour@uark.edu
[2]BELL 4190, University of Arkansas, Fayetteville, AR 72701, USA, rps@uark.edu
[3]Florida International University, Miami, FL, email: chowdhur@fiu.edu

ABSTRACT:
The peak pressures are computed using computational fluid dynamics (CFD) with the inflow turbulence and compared with 1:6 scale TTU wind tunnel measurements. The inflow turbulence is calculated using Consistent Discrete Random Flow Generation (CDRFG) method. The maximum and minimum frequencies of the wind spectrum from the field or wind tunnel measurements are given as input to the inflow turbulence generator. This produces high pressure error. For one case, more than 600% peak pressure error on the sidewalls and 100% peak pressure error on the roof are observed. This error may be due to not considering the grid spacing frequency in the input. By varying maximum frequencies systematically for a specific computational mesh and comparing the velocities at the inflow and the building location without building, the possible cause of the error is explained. Some improvements are suggested in using synthetic inflow turbulence generation.

Keywords: Computational fluid dynamics, Synthetic inflow turbulence, Peak pressure, Large eddy simulation.

1. INSTRUCTION

Several infrastructure damages, economic losses, and even deaths are caused by strong windstorms such as hurricanes, and tornadoes. Most of these devastating events occur due to wind peak pressure loads. The higher wind intensity and stronger storm frequency comparing to those in the past demands a better understanding of wind load and subsequently wind peak pressure on buildings. To optimize cost and time and obtain more details of the flow field, the experimentally verified numerical modeling of wind-structure interaction is advantageous.

A critical aspect of the numerical investigation is defining the right inflow turbulence boundary condition satisfying specific spectra and correlations. Based on these criteria, enormous methods are developed which are categorized as (a) precursor database, (b) recycling method, and (c) synthetic turbulence (Keating et al., 2004). The weakness of the first method is the need of the precursor database that makes this method computationally expensive. The second method is not practical because it is computationally costly and is sensitive to roughness (Aboshosha et al., 2015). Hence, using the synthetic turbulence methods as inflow boundary condition is preferred (Aboshosha et al., 2015; Ding et al., 2019). Furthermore, if the inflow turbulence field is not

* Lead presenter

divergence-free, it leads to imbalance in mass inflow. This imbalance produces unrealistic pressure fluctuations in the pressure-velocity coupling step and subsequently, it leads to inaccurate pressure prediction.

Furthermore, choosing maximum and minimum frequencies based on the field or wind tunnel (WT) spectrum as an input for inflow methods regardless of their maximum grid size leads to production of high error in peak pressure results. For a given grid spacing h, the wavelength L of a wave in the form of sine or cosine function transported by a finite difference grid will be $4h$ as mentioned by (Kravchenko and Moin, 1997).The relation between frequency and wavelength is $L = U_H/n$. Subsequently, the non-dimensional wavelength λ and frequency f are calculated using by $\lambda = L/H = U_H/Hn = 1/f$. Hence the corresponding frequency f_{grid} can be calculated as $f_{grid} = H/L = H/4h$. In the Large Eddy Simulation Method (LES) also, only a certain range of frequency can be transported by a specific maximum grid spacing (Chow & Moin, 2003; Ferziger & Perić, 2002). For a grid spacing of h, f_{LES} is the largest frequency could be resolved by the grid and in the LES studies f_{LES} = f_{grid} =$H/4h$.

Hence, in the current study, the peak and mean pressures are computed using computational fluid dynamics (CFD) and compared with 1:6 scale TTU wind tunnel measurements. The inflow turbulence field used as the inflow boundary condition is calculated with various maximum frequency via the Consistent Discrete Random Flow Generation (CDRFG) method. To validate the numerical model, normalized mean wind speed and turbulence intensity profiles are compared with TTU wind tunnel measurements. Moreover, the velocity spectrum is compared with the targeted spectrum (i.e, von Karman Spectrum). Finally, effects of high frequency beyond f_{LES} on peak and mean pressure results are reported.

It should be noticed that this study is done for various grid spacing sizes such as H/8, H/16, and H/24. The inlet velocities are calculated using the CDRFG method for f_{max} =10 and f_{LES} for all grids. As the case with grid size of H/16 was in good agreement with WT results, it was chosen for further investigation. In the current study only, some results related to H/16 are presented due to the space limitation.

2. RESULTS

For the various f_{max} (i.e.,2,4,8, and 10), the inlet velocities are calculated using the CDRFG method for H/16 grid. For all the cases, the f_{min} is kept as 0.1 to match with the 1:6 scale TTU building study WT wind spectrum as reported by Mooneghi et al. (2016). The peak pressure coefficients C_p on the TTU building and inlet velocity spectrums are computed. The computed mean and peak C_p are compared with WT pressure coefficients provided by Moravej (2018). In all the plots, the WT peak pressures are called WT6. From the comparisons, as f_{max} decreases from 10 to 4, the peak pressures on the roof approach the WT measurements.

2.1.Velocity Spectrum at the Inlet

The inlet velocity spectrums as well as the corresponding velocity spectrums at the windward edge of the building without building are shown in Figure 1 at the building height of f_{max}=2, 4 and 10 as a sample. The targeted f_{max} is realized at the inflow as shown in Figures 1 (a) to 1(c). A dashed vertical line is placed in each figure to show the f_{max} point. Using these inlet velocities, the building peak pressures are calculated to compare with WT measurements. One can also see that at the building location, the high-frequency amplitude or energy is cut off beyond f_{max}=4 as shown in the Figure 1 (a) due to the grid resolution effect. This error is less for f_{max} equal to 4 or less. There is a reasonable correlation between the inlet and building location spectrum in the Figure 1 (b) and (c) when the f_{LES} is less than or equal to 4 or f_{grid}.

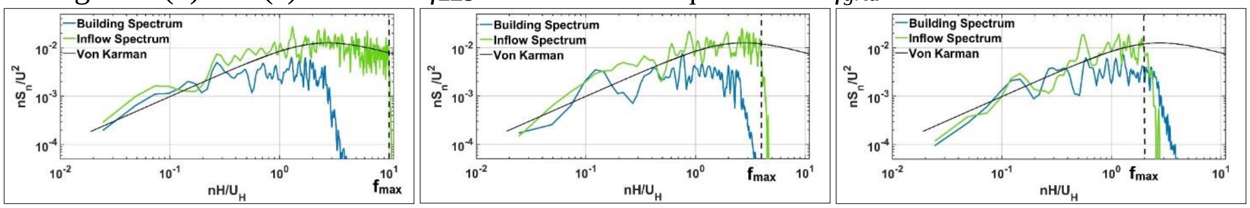

Figure 1. Velocity spectrum at the inlet and building location without building for various f_{max} using *H*/16 grid (a) $f_{max}=10$ (b) $f_{max}=4$ and (c) $f_{max}=2$.

2.2.Comparison of mean pressure coefficients for various f_{max} with WT

The mean pressure coefficients C_p are calculated from 10 time units to 100 time units at each point along the centerline of the TTU building. The mean C_p values are comparable with WT6 as shown in Figure 2 (a) to (d) for the four f_{max} considered. Only minimum difference from one plot to another is noticed. The maximum error of 20% between WT and CFD is noticed at the windward roof edge, and other places the errors are less than this value. This discrepancy could be due to the particular inflow turbulence method used. This is under further investigation.

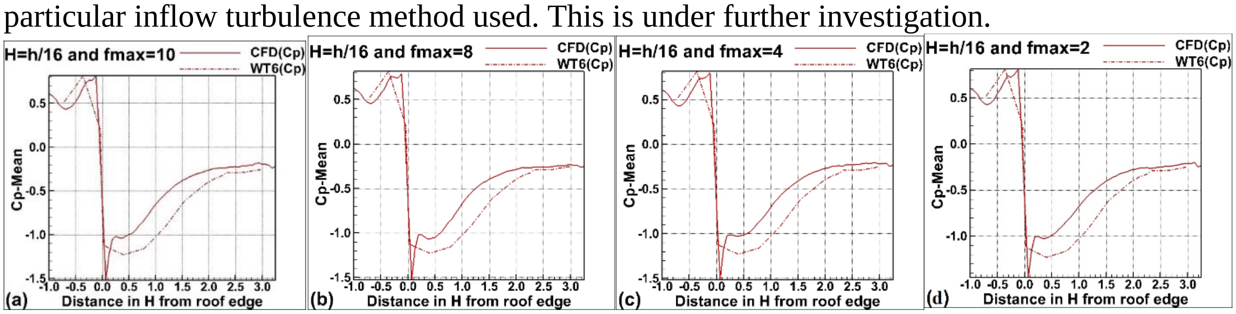

Figure 2. Mean pressure coefficients for various f_{max} using H/16 grid spacing (a) $f_{max}=10$, (b) $f_{max}=8$, (c) $f_{max}=4$, (d) $f_{max}=2$.

2.2. Comparison of minimum peak pressures for various f_{max} with WT

The minimum peak pressure coefficients C_{pmin} for the four f_{max} cases are plotted in Figure 3 for *H*/16 grid. The minimum values are calculated using the same 10 time units to 100 time units data. The CFD peak pressures are compared with WT6 data. The error on the roof is very high for f_{max}=10 (Figure 3 (a)), and as f_{max} decreases, the error decreases systematically (Figure 3 (b) to (d)). The maximum errors on the roof are around 100%, 92%, 33%, and 33% for f_{max} values of 10, 8, 4, and 2, respectively. Although the errors are far higher in all the four cases on the windward and leeward side, the errors are reduced somewhat for lower f_{max}.

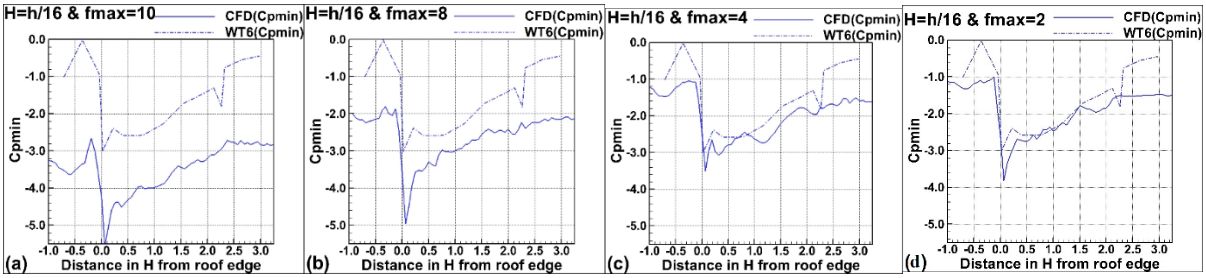

Figure 3. Minimum pressure coefficients for various f_{max} using H/16 grid spacing (a) $f_{max}=10$, (b) $f_{max}=8$, (c) $f_{max}=4$, (d) $f_{max}=2$.

3. CONCLUSION

In the current study, the peak and mean pressures are computed using computational fluid dynamics (CFD) and compared with 1:6 scale TTU wind tunnel measurements for various maximum frequency as input for inflow generator. This study indicated that the largest grid spacing h in the computational domain determines the highest frequency of the velocity fluctuations transported by the grid from the inflow turbulence. In the LES computation, the suggested highest frequency transported in the flow using finite difference method (FDM) is $f_{LES} = H/4h$ where H is reference height and h is grid spacing size. If $f_{max}>f_{LES}$ velocity spectrum is considered at the inlet, these velocities give unrealistic pressures at the velocity-pressure coupling step (more than 600% error on sidewall and 100% on the roof for *H/16* grid). This is illustrated by comparing the CFD peak pressure with WT measurement for the TTU building. Furthermore, mean pressure results do not show any difference in all cases, whereas differences from one case to another are considerable in peak pressure results.

ACKNOWLEDGMENTS

Ms. Zahra Mansouri acknowledges the financial support from the James T. Womble Professorship from the University of Arkansas. The authors acknowledge the help provided by Dr. M. Moravej from Walker Consultants in delivering the wind tunnel data in a way we could use it in this work. The authors also acknowledge Dr. G. Bitsuamlak and his research group for providing the CDRFG MATLAB code to generate the inflow turbulence.

REFERENCES

Aboshosha, H., Elshaer, A., Bitsuamlak, G. T., and El Damatty, A., 2015. Consistent inflow turbulence generator for LES evaluation of wind-induced responses for tall buildings. Journal of Wind Engineering and Industrial Aerodynamics, 142, 198–216.

Chow, F. K., and Moin, P., 2003. A further study of numerical errors in large-eddy simulations. Journal of Computational Physics, 184, 366–380.

Ding, F., Kareem, A., & Wan, J., 2019. Aerodynamic Tailoring of Structures Using Computational Fluid Dynamics. Structural Engineering International, 29, 26–39.

Ferziger, J. H., and Perić, M., 2002. Computational methods for fluid dynamics. Berlin: springer.

Keating, A., Piomelli, U., Balaras, E., and Kaltenbach, H. J., 2004. A priori and a posteriori tests of inflow conditions for large-eddy simulation. Physics of Fluids, 16, 4696–4712.

Kravchenko, A. G., and P. Moin. 1997. "On the effect of numerical errors in large eddy simulations of turbulent flows." *J. Comput. Phys*., *131*, 310-322.

Mooneghi, M. A., Irwin P., and Chowdhury A. G., 2016. "Partial turbulence simulation method for predicting peak wind loads on small structures and building appurtenances." J. Wind. Eng. Ind. Aerodyn., 157, 47-62.

Moravej, M., 2018. "Investigating scale effects on analytical methods of predicting peak wind loads on buildings." Ph.D. thesis, FIU. Miami, Florida.

Modeling windborne debris trajectories in tornadoes

Ahmed U. Abdelhady [a,*], Seymour M.J. Spence [b], Jason McCormick [c]

[a]*University of Michigan, Ann Arbor, Michigan, USA, auhady@umich.edu*
[b]*University of Michigan, Ann Arbor, Michigan, USA, smjs@umich.edu*
[c]*University of Michigan, Ann Arbor, Michigan, USA, jpmccorm@umich.edu*

ABSTRACT
To ensure the safety of residential communities in the event of a tornado strike it is required to consider the impact of windborne debris. Therefore, it is important to estimate both the landing location of windborne debris as well as their energy/momentum upon landing. These estimates can be carried out using a three-dimensional (3D) six-degree-of-freedom (6DOF) debris trajectory model. However, existing 3D 6DOF models focus on estimating the debris trajectory in straight-line winds. This research presents a 3D 6DOF debris trajectory model for describing the flight of windborne debris in tornadoes. The proposed solution strategy is based on a predictor-corrector time-marching scheme which solves the equations of motion for each time step while updating the wind field from an appropriate tornado wind model. The proposed strategy is then used to show the significant difference in modeling the debris trajectories in tornado wind fields as compared to straight-line winds.

Keywords: Windborne debris; Tornadoes; Debris Trajectory Modeling; Debris Impact

1. INTRODUCTION

Existing six-degree-of-freedom debris trajectory models are developed for straight-line wind which is a wind field that has predominant wind speed and direction over the debris flight time (e.g., Richards et al., 2009). This assumption is reasonable for modeling the flight of debris in hurricanes since they are generally characterized by a relatively slow rate of change in wind speed and direction. This behavior cannot be assumed for tornadoes that are transitory in nature and will generally produce rapid changes in wind direction. Therefore, this research presents a 6DOF debris trajectory model for tornado wind fields.

2. EQUATIONS OF MOTION

A flying debris object can be assumed as a rigid body in space, therefore six degrees of freedom are required to describe its motion. Based on the debris geometric classification provided by (Minor, 1994), the rectangular hexahedron in Fig. 1 is used to model the geometry of the debris objects of interest. The object is subjected to gravity and aerodynamic forces. Under these forces, the equations of motion can be written as follows,

$$m\dot{\mathbf{V}}_D = \mathbf{F}_{aero} - mg\mathbf{i}_2 \quad (1)$$
$$\dot{\mathbf{L}}_p = \mathbf{M}_{aero} + \mathbf{M}_D - \boldsymbol{\omega} \times \mathbf{L}_p \quad (2)$$

where m is the mass of the debris object; $\mathbf{V}_D$ and $\boldsymbol{\omega}$ are the debris translational and rotational velocities; g is the magnitude of the gravitational acceleration; $\mathbf{i}_2$ is the unit vector of the axes; $\mathbf{L}_p$ is the angular momentum vector of the debris object; $\mathbf{M}_{aero}$ is the aerodynamic moment; $\mathbf{M}_D$ is the damping moment introduced by (Richards et al., 2009) to prevent unbounded debris rotation.

* Lead presenter

Equations 1 and 2 are solved using a predictor-corrector time marching scheme (Abdelhady et al., 2021). To estimate the aerodynamic forces and moments, tornado wind velocity is required. The tornado wind velocity is estimated using the tornado wind field model introduced by Baker et al., (2020).

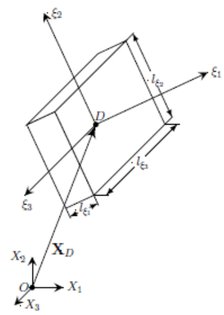

Figure 1. Reference systems used for describing the debris trajectory.

3. APPLICATION

The 6DOF trajectory model is used to estimate the trajectory of a typical roof sheathing subject to a tornado as shown in Fig. 2 (a). The tornado properties are: maximum circumferential velocity = 80 m/s, maximum radial velocity = 20 m/s, translational velocity = 4 m/s, and radius to maximum circumferential velocity (R) = 200 m. The tornado track is positioned such that $|X_{T3}|/R = 1$. Figure 2 (b) shows the significant difference between the trajectories generated using the tornado wind field as opposed to a straight wind field. This significant difference emphasizes the need for developing trajectory models for tornado wind fields.

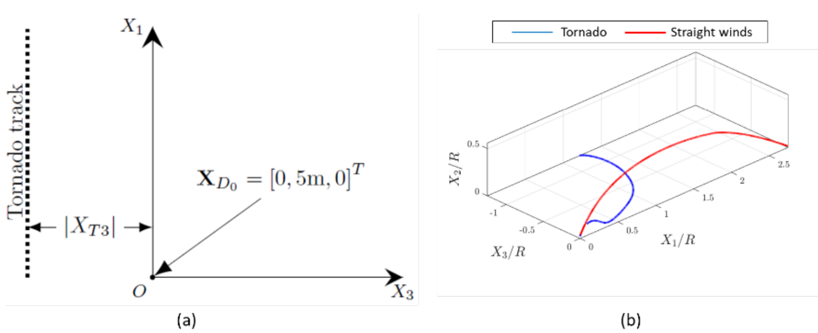

Figure 2. (a) Layout of the application problem; (b) debris trajectories for a straight and tornado wind**.**

REFERENCES

Abdelhady, A. U., Spence, S. M. J., & McCormick, J. (2021). A three-dimensional six-degree-of-freedom windborne debris trajectory model for tornadoes. *Journal of Wind Engineering and Industrial Aerodynamics*, Under Review.

Baker, C., Sterling, M., & Jesson, M. (2020). The lodging of crops by tornadoes. *Journal of Theoretical Biology*, *500*, 110309.

Minor, J. E. (1994). Windborne debris and the building envelope. *Journal of Wind Engineering and Industrial Aerodynamics*, *53*(1–2), 207–227.

Richards, P. J., Williams, N., Laing, B., McCarty, M., & Pond, M. (2008). Numerical calculation of the three-dimensional motion of wind-borne debris. *Journal of Wind Engineering and Industrial Aerodynamics*, *96*(10–11), 2188–2202.

6th American Association for Wind Engineering Workshop (online)
Clemson University, Clemson, SC, USA
May 12-14, 2021

Artificial Neural Network models to study wind-induced response of large-span roofs and suspension bridges

Fabio Rizzo [a,*], Luca Caracoglia [b]

[a]*Dept. of Engr. & Geology, G. D'Annunzio University, Pescara, Italy, fabio.rizzo@unich.it*
[b]*Dept. of Civil & Env. Engr., Northeastern University, Boston, MA, USA lucac@coe.neu.edu*

ABSTRACT:
Artificial Neural Networks (ANNs) are a valid approach to analyze structural response. For example, they can be used to avoid experimental evaluation of wind loads during preliminary design of a structure. This document discusses recent applications of ANN-based surrogate models to predict wind-induced vertical displacements of cable net supporting hyperbolic paraboloid roofs and the flutter velocity of (pedestrian) suspension bridges. The ANN-based model, trained using wind tunnel data and numerical structural analyses, can predict the structural response with an error no larger than 10%.

Keywords: surrogate models, Artificial Neural Networks, wind tunnel tests, cable-net roofs, suspension bridges.

1. INTRODUCTION

Since the late 1990s, Artificial Neural Networks (ANNs) have been used as an effective approach to solve many problems in the field of civil engineering because of their ability to approximately model the structural response and simultaneously taking into account the uncertainty from several sources (Chen et al., 2008). Predictions via ANN have been used for: structural safety and decision-making, estimation of cable tension from vibrations, dynamic response of buildings under seismic excitation and estimation of seismic-induced structural damage through fragility curves. In the field of wind engineering ANN approaches have been explored to: control vortex shedding of circular cylinders (Fujisawa, 2002), investigate aeroelastic instability of long-span bridges (Rizzo and Caracoglia, 2020) and investigate aerodynamic wind loads due to interference of adjacent buildings. In addition, the ANN approach has been employed to interpolate experimental, wind-induced pressure time series of a low-rise building (Chen et al., 2002) and predict mean and fluctuating pressure coefficients (Dongmei et al., 2017). This study describes two recent application examples of ANNs in the field of wind engineering, i.e. the study of a cable net supporting a large roof and a suspension bridge. In the case of the cable net, the ANN estimates wind-induced vertical displacements and, for the bridge the ANN evaluates the critical flutter velocity.

2. METODOLOGY

The ANN neurons are organized in one input layer, one hidden layer and one output layer. The variables of the input layer are user-defined, e.g. geometric properties, structural properties and other physical quantities. The neurons in the hidden layer are selected by trial and error; they contain the result of intermediate calculations from the input layer. Finally, the output layer is the result of the final calculations. In an ANN, each node in each layer is connected to each node in the adjacent layer. An ANN-based surrogate model can be used for predictions only after a training

* Lead Presenter

process, which is carried out using an existing set of input–output data. The training of an ANN is commonly performed through a back-propagation, learning algorithm. This algorithm involves a minimization process that feed-forwards the input data to generate the output data.

3. ANN TRAINING USING WIND TUNNEL DATA

Wind tunnel results are used to train the ANN-based models. Pressure coefficients for several geometries of large-span hyperbolic paraboloid roofs (Rizzo et al, 2021) and a set of flutter derivatives measured for a closed-box section model of a pedestrian suspension bridge (Rizzo and Caracoglia, 2020) are employed and initially expanded through suitable polynomial representation of relevant parameters. In the case of the large-span roof, a new set of geometries is defined through polynomial representation by varying cable sags and roof spans. For the bridge section model, flutter derivatives extracted through repetition of wind tunnel tests are randomized through Monte-Carlo simulation. Figure 1 illustrates the workflow of the entire process from the wind tunnel tests to the randomization of wind tunnel data, their polynomial representation, and structural analysis results.

The ANN is trained using structural responses. For the case of cable net roofs, wind-induced vertical displacements are estimated by static, nonlinear FEM analysis. For the bridge case, the critical flutter velocity is found by generalized, two-mode (degree of freedom) model (Scanlan and Tomko, 1971). The logistic sigmoid function is employed as the transfer function between adjacent neurons. The ANN overfitting is examined by varying the number neurons from 5 to 50 and examining the errors between physical model predictions and ANN-based approximations.

4. DISCUSSION AND CONCLUSIONS

Satisfactory approximation of physical model results has been achieved, using 70% of experimental data for training, 15% for validation and 15% for testing. The coefficient of determination R is consistently larger than 0.9. In the case of the large-span roof, relative errors between FEM predictions and ANN approximations are less than 10% for 80% of the 15840 combinations of numerical calculations. For the bridge case, the relative error is less than 5% for 90% of the results.

REFERENCES

Chen C H, Wu J C, Chen J H., 2008. Prediction of flutter derivatives by artificial neural networks. Journal of Wind Engineering and Industrial Aerodynamics, 96(10-11), 1925–1937.

Chen Y, Kopp G A, Surry D, 2003. Prediction of pressure coefficients on roofs of low buildings using Artificial Neural Networks. Journal of Wind Engineering and Industrial Aerodynamics, 91(3), 423-441.

Dongmei H, Shiqing H, Xuhui H, Xue Z, 2017. Prediction of wind loads on high-rise building using a BP neural network combined with POD. Journal of Wind Engineering and Industrial Aerodynamics, 170(0),1-17.

Fujisawa N., 2002. Neural network control of vortex shedding from a circular cylinder using rotational feedback oscillations. Fluid and Structures, 16(1), 113-119.

Rizzo F, Caracoglia L., 2020. Artificial Neural Network model to predict the flutter velocity of suspension bridges. Computers and Structures, 233, 106236.

Rizzo F, Kopp A G, Giaccu G., 2021. Investigation of wind-induced dynamics of a cable net roof with aeroelastic wind tunnel tests. Engineering Structures, 229, 111569.

Scanlan R.H. and Tomko, J.J., 1971. Airfoil and bridge deck flutter derivatives. Journal of Engineering Mechanics, ASCE, 97(EM6), 1717-1737.

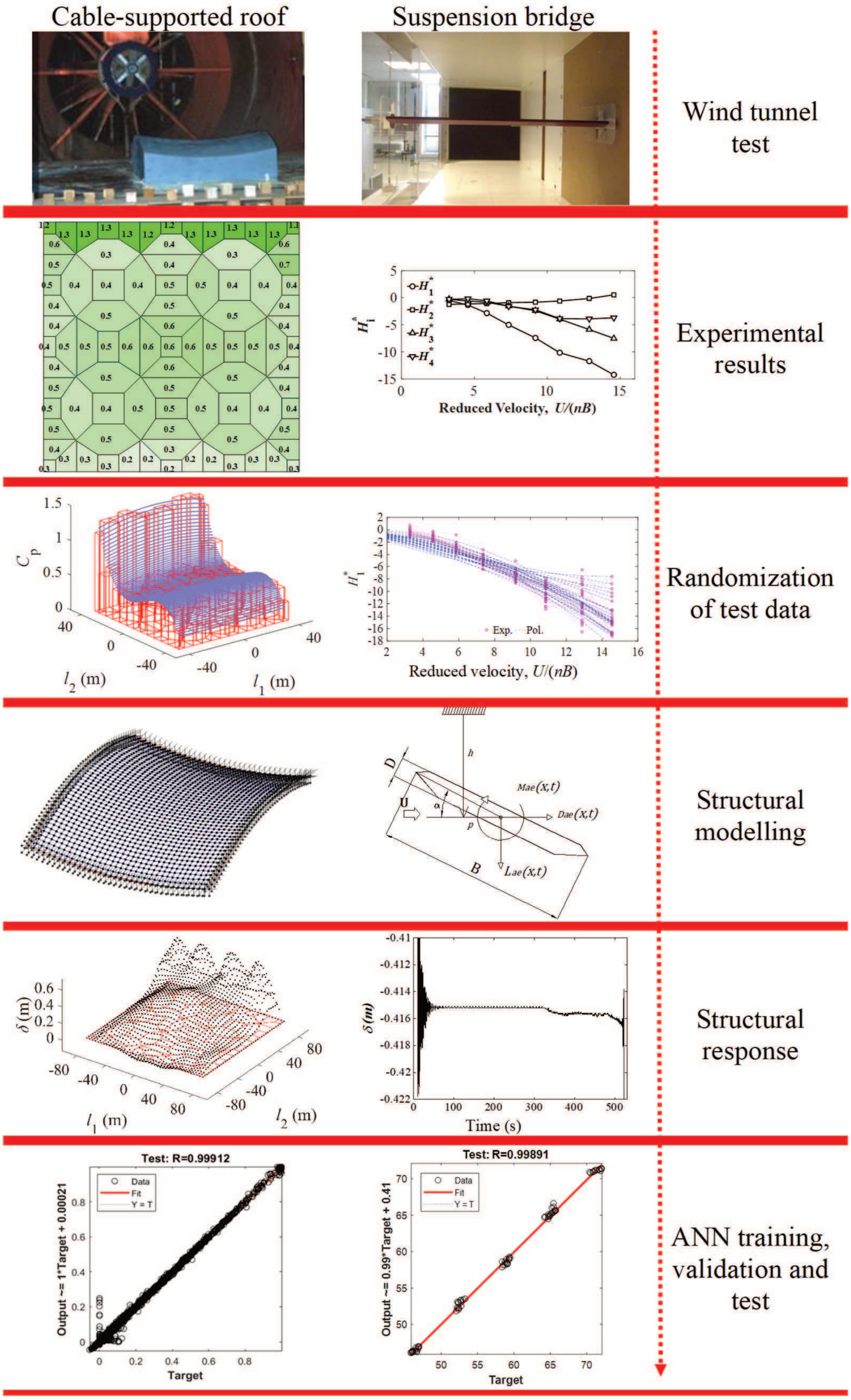

Figure 1. Workflow of the ANN-based surrogate modeling

Fatigue Life and Reliability Estimation of a Traffic Signal Structure using Long-Term Monitoring Data

Li-Wei Tsai [a], Alice Alipour [b,*]

[a] *Department of Civil, Construction and Environmental Engineering, Iowa State University, Ames, IA, USA, liwei@iastate.edu*
[b] *Department of Civil, Construction and Environmental Engineering, Iowa State University, Ames, IA, USA, alipour@iastate.edu*

ABSTRACT:
Recent failures of cantilevered-arm traffic signal structures have revealed the vulnerability of such structures to wind force. The heavy mast arm causes high stress at the pole-to-arm connection during the wind-induced vibration, and because of low mechanical damping, stress cycles accumulate and eventually cause fatigue damage at the pole-to-arm connection. Many failures have been reported in the United States, creating a need to study the fatigue performance of cantilevered-arm traffic signal structures. In this study, a holistic framework was proposed for estimating fatigue life and reliability of a traffic signal structure, based on the long-term monitoring data. Interestingly, the monitoring data associated with the August 2020 Iowa Derecho was also included, representing the case for the more extreme wind conditions. The monitoring stress data at the mast-arm base was used to build a fatigue-damage fraction function showing the relation between fatigue damage and mean wind speed. Fatigue life at a specific location was then estimated by combining the damage fraction function and the local wind probability. This method bypasses the complexity and uncertainties of simulating the wind-induced stress response of a traffic signal structure. In reliability analysis, uncertainties considered were the wind probability, the fatigue resistance of the pole-to-arm connection, and the value of Miner's sum. Monte Carlo simulations were conducted to generate a probability-of-failure curve. The proposed framework could be widely used on other structures suspected of fatigue damage due to wind-induced vibration, and the results from reliability analysis can serve as a reference in determining the period of regular maintenance for such structures.

Keywords: traffic signal structures, wind engineering, long-term monitoring, fatigue life, reliability analysis

* Lead presenter

Numerical investigation of wind actions on elevated houses

Nourhan Abdelfatah [a*], Amal Elawady [b,c]

[a]*The Department of Civil and Environmental Engineering, Florida International University, Miami, Florida, USA, nabde006@fiu.edu*
[b] *The Department of Civil and Environmental Engineering, Florida International University, Miami, Florida, USA, aelawady@fiu.edu*
[c] *International Hurricane Research Center, Florida International University, Miami, Florida, USA*

ABSTRACT:
During recent hurricane seasons, different levels of damage have been observed for elevated coastal houses due to wave and wind actions. Along the coastline, elevated residential houses are venerable to flooding and strong wind hazards. The structure unique aerodynamics are not well addressed in the current design guidelines. Although the structural design considers the velocity increase due to the increase in building height when elevated, recent post-hurricane surveys reveal severe damages on elevated building's walls and roof surfaces. The air flow through the building is affected by the presence of the air gap, the model dimensions, and height. This study uses the Computational Fluid Dynamics (CFD) numerical tool to perform a parametric study on elevated houses with different stilt heights and different aspect ratios. This study identifies the most critical configurations and geometrical ranges found to cause the maximum global forces on the structure.

Keywords: Elevated house, CFD, streamlines, wind tunnel, wind force, and stilt height.

1. INTRODUCTION

Coastal regions are considered the most attractive and strategical areas for population, business, and tourism. However, several tropical houses have experienced considerable wind-induced damages during recent hurricanes, including roof and wall cover loss (Amini and Memari, 2020). A recent example is Hurricane Sally, in 2020, which hit the southern coast of the United States with a wind speed of 165 km/h (105mph) (NOAA, 2020), caused total insured losses between one billion and three billion dollars (Behnken and (NASA), 2020). Hurricane Laura and Delta hit southwest Louisiana and caused a $5 billion total insurance loss. To reduce the risk of combined wind and wave actions on vulnerable coastal communities, FEMA and the construction industry have recommended elevating coastal houses to avoid flooding hazards. However, as the house is elevated on stilts, the wind speed increases (i.e. higher height), and the presence of the air gap beneath the building affects the overall wind actions on the building surfaces. Recent post-hurricanes surveys for elevated houses with different configurations have sustained severe damages (StEER, 2019). These houses were elevated using different stilt heights and a wide range of aspect ratios. Therefore, more investigation is needed to provide a comprehensive methodology to predict wind loads acting on elevated houses. The study presented here reports an extensive numerical analysis performed using Computational Fluid Dynamics (CFD) to investigate the aerodynamics of a single-story house. This study focused on identifying the geometrical controlling parameters which can assist in designing future experimental studies on elevated structures for codifying purposes.

* Nourhan Abdelfatah

2. NUMERICAL MODEL DESCRIPTION

The numerical simulation was performed on a gable-roof typical residential building in full-scale. A typical low-rise gable roof model was adopted for this study. The model horizontal dimensions were 8.76 m long, 6.4 m wide, which is the same as the elevated house prototype tested in the Wall of Wind (WOW) Experimental Facility (EF) (Abdelfatah et al., 2020). The developed CFD model was first calibrated against the experimental results obtained from the WOW testing (Abdelfatah et al., 2020). After that, a parametric study was conducted using the Reynolds-Averaged Navier–Stokes (RANS) model to visualize the wind flow around the building and assess wind actions on elevated structures and their variations with the building stilt height and aspect ratio. The CFD study covers a wide range of building plan aspect ratios, by changing the model length, varying from 1 to 2.5 with a 0.25 increment. A wide range of stilt heights has been considered varying between 0 (i.e. on ground) to 4.8m with a 0.6m increment. For each case, the model was tested under three wind directions: 0^{o} (i.e. acting along the ridge line), 45^{o}, and 90^{o}.

The turbulent model named RNG k-ε was used to perform the simulation as recommended by (Jeong et al., 2002; Tominaga et al., 2015). Where, k is the turbulent kinetic energy, and ε is the turbulent dissipation rate. This model can moderately predict and enhance the turbulent kinetic energy. As recommended by (Franke and Baklanov, 2007), the domain dimensions were chosen to avoid any external effect by means of the domain walls. The domain region was divided into three million cells to precisely monitor the flow streamlines, as shown in Fig. 1. All the necessary boundary conditions were calculated precisely to define the exact wind profile to match this simulated at the WOW (Abdelfatah et al., 2020).

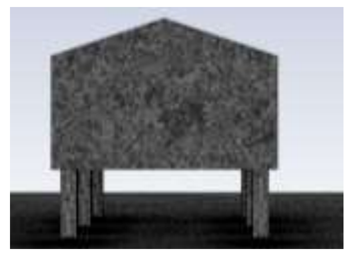

Figure 1. Numerical model of the 1.8m elevated house

3. RESULTS

The developed CFD model was first validated using the experimental results obtained from the WOW testing (Abdelfatah et al., 2020). Fig. 2 shows the plots of the mean pressure coefficient variation with model length (L) and model height (H) in both methods. The slices have been taken at the mid span of the 1.8m stilt case in case of zero wind direction. The figures reveal a good agreement between the experimental and numerical results. The differences between the results do not exceed 10%.

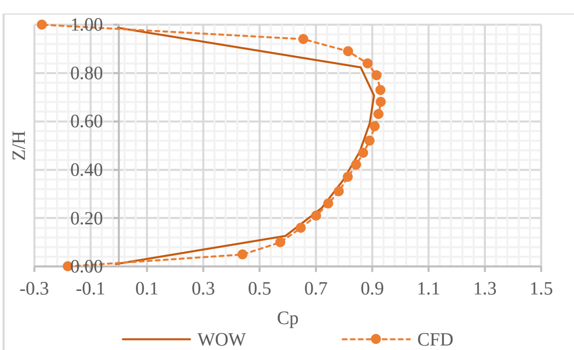

(a) 1.8m stilt case

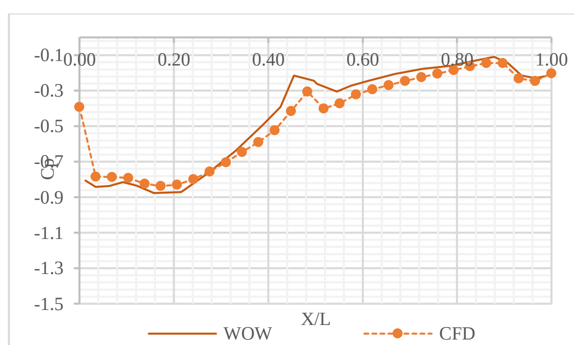

(b) 4.8m stilt case

As mentioned in the introduction, the parametric study covers two variables: the stilt height and the building plan aspect ratio. For all the studied cases, the mean pressure coefficient was calculated using the 3-sec velocity at the mean roof height as a reference velocity. By increasing the stilt height, the difference in the mean pressure coefficient was not significant for the 0º and 90º wind directions. However, for the 45º wind direction, there was a high suction around the stilt which increases as the stilt height increases. The resulting local mean pressure coefficients were similar for the elevated house's different aspect ratios in case of wind acting parallel to the roof ridge. However, for 45º and 90º wind directions, the suction occurring on the roof surface and the floor surface was significantly higher for larger aspect ratio.

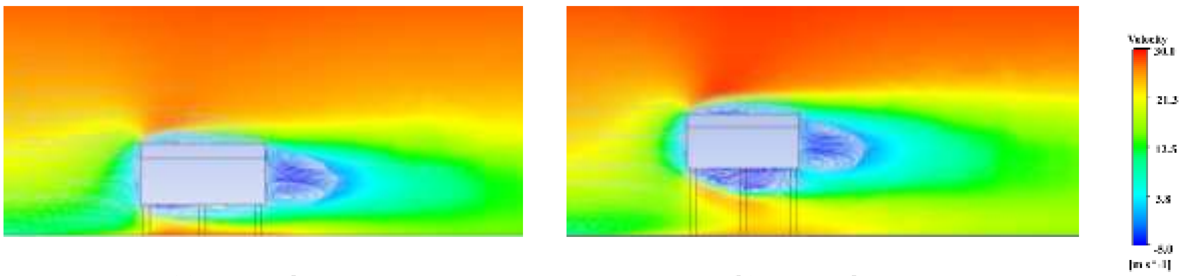

(a) 1.8m stilt case (b) 4.8m stilt case

Figure 3. Flow streamlines for wind acting @ 0º direction

The flow streamlines showed differences in the vortices size and location, which clarify the variation in the resulting wind pressures for each case, as shown in Fig. 3. The size of the flow separation region increased as the stilt height increased. However, the flow separation region decreased by increasing the model aspect ratio. The air movement speeds up as it passed through the air-gap, and the velocity is higher in the small stilt cases, as shown in Fig. 3.

This paper also investigates the effect of changing the stilt height and aspect ratio on the total uplift, shear force, and overturning moments. By changing the model stilt height or the aspect ratio, the normalized forces were calculated by dividing the total force of the stilt case by the on-ground case's total force. The total shear force acting on the foundation showed a considerable increase as the stilt height increases, as shown in Fig. 4. On the contrary, the total uplift force was reduced by elevating the house due to the new suction force acting on the floor surface. A significant increase of the overturning moment was observed and varied between 450% and 800% increase compared to its on-ground counterpart.

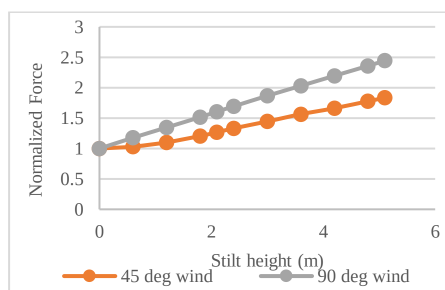

Figure 4. Normalized shear force relation with the stilt height

4. CONCLUSION

The current numerical study showed that the aspect ratio and elevation from the ground level of an elevated structure affect the air flow characteristics, including the size of vortices, the wind speed, and the wind shear stresses acting on the model surfaces. Consequently, the resulting wind pressure, uplift force, shear force, and overturning moment are affected as well. More details about the flow characteristics, mean pressures, and wind forces will be provided in future work.

ACKNOWLEDGEMENTS

The authors would like to express their gratitude to the National Science Foundation (NSF) for funding this research. The authors acknowledge the contribution of The State of Florida Division of Emergency Management (FLDEM).

REFERENCES

Abdelfatah, N., Elawady, A., Irwin, P., Chowdhury, A.G., 2020. Wind Pressure Distribution on Single-Story and Two-Story Elevated Structures, in: 5th Residential Building Design & Construction Conference. pp. 1–8.

Amini, M., Memari, A.M., 2020. Performance of Residential Buildings in Hurricane Prone Coastal Regions and Lessons Learned for Damage Mitigation, in: 5th Residential Building Design & Construction Conference. https://doi.org/https://www.researchgate.net/publication/340062711 Performance

Barry, M., Shepherd, D., Beaman, J., Maniscalco, J., 2020. Hurricane Sally – 2020 Hurricane Season (NOAA). https://doi.org/https://www.weather.gov/mob/sally

Behnken, B., (NASA), 2020. 2020 Atlantic Hurricane Season. Cent. Disaster Philanthr. https://doi.org/https://disasterphilanthropy.org/disaster/2020-atlantic-hurricane-season/accessed in March 2021

Franke, J., Baklanov, A., 2007. Best practice guideline for the CFD simulation of flows in the urban environment: COST action 732 quality assurance and improvement of microscale meteorological models.

Jeong, U.Y., Koh, H.-M., Lee, H.S., 2002. Finite element formulation for the analysis of turbulent wind flow passing bluff structures using the RNG k−ε model. J. Wind Eng. Ind. Aerodyn. 90, 151–169. https://doi.org/https://doi.org/10.1016/S0167-6105(01)00190-8

NSF, 2019. The National Science Foundation (NSF), Network, and Structural Extreme Events Reconnaissance (StEER), Fulcrum App. https://web.fulcrumapp.com.

Tominaga, Y., Akabayashi, S., Kitahara, T., Arinami, Y., 2015. Air flow around isolated gable-roof buildings with different roof pitches: Wind tunnel experiments and CFD simulations. Build. Environ. 84, 204–213. https://doi.org/https://doi.org/10.1016/j.buildenv.2014.11.012

Wind uplift resistance of Vinyl Siding- a standardized test protocol for multi-chamber pressure application

Oscar Lafontaine [a,*], David B. Roueche [b], David O. Prevatt [c]

[a]*University of Florida, Gainesville, FL, USA, oscar.lafontaine@ufl.edu*
[b]*Auburn University, Auburn, AL, USA, dbr0011@auburn.edu*
[c]*University of Florida, Gainesville, FL, USA, dprev@ce.ufl.edu*

ABSTRACT:
Recent post hurricane studies showed that vinyl siding is likely to fail prematurely in hurricanes, but no reasons are clearly established. Studies at IBHS and Western University confirm that external pressure gradients are a key driver of pressure equalization factors (PEFs) on vinyl siding yet are not considered in design standards. This study uses a multi-chamber pressure testing apparatus with four feedback-controlled pressure loading actuators to investigate the effects of uniform and spatially varying pressure time histories (stochastic, sinusoidal, static) on the PEFs for vinyl siding. Results showed that when stochastic spatially varied wind pressures are used, the PEFs at peak pressures are between 0.6 and 0.8. On the other hand, if the same systems are subjected to uniform pressures with or without temporal variations the PEF falls to 0-0.34. The results strongly suggest that an appropriate test method should include spatial variations of wind pressures to reliably predict PEFs.

Keywords: vinyl siding, pressure equalization, air-permeable cladding, multi-chamber, pressure loading actuators

1. INTRODUCTION

Vinyl siding is among a class of discontinuous cladding systems, which have joints and gaps that allow air flow between the external surface of the panels and cavity area formed by the underside of the vinyl siding and the solid wall substrate. The air flow exchange enables pressure equalization to occur and is quantified by a pressure equalization factor (PEF).

The PEF used in current vinyl siding design standards (ASTM D3679 2017; ASTM D5206 2013) is based on uniform pressure chamber testing by the Architectural Testing, Inc. (ATI) (2002). Cope et al. (2012) and Miller et al. (2017) showed that external pressure gradients are a key driver of the PEFs and must be considered to obtain accurate net pressures on vinyl siding.

This research seeks to develop a simplified laboratory-based test procedure for replicating the net pressures on vinyl siding systems considering realistic spatio-temporal wind variations. A multi-chamber pressure test bed with four feedback-controlled pressure loading actuators (PLA), and a pressure trace protocol (stochastic wind traces, sinusoidal, static) were developed. The relationship between PEFs and applied loading is used to evaluate the feasibility obtaining similar PEFs between a fully stochastic wind series and simpler trace protocols.

2. MATERIALS AND METHODS

A multi-chamber test bed (four chambers) was constructed which had the following constrains: 1) accommodate a full-scale vinyl siding specimen; 2) nominally airtight to prevent airflow between the chambers; 3) flexible to allow free deflection of the vinyl siding. Two chambers had dimensions of 2 ft. by 8 ft. and the remaining two were 4 ft by 8 ft. A latex barrier similar to Miller et al. (2017) was used to seal each pressure chamber and comply with the flexibility requirement.

* Lead presenter

Each chamber was connected to a PLA with Proportional Integral Derivative (PID) control.

Five vinyl siding 10 ft. by 12 ft. wood frame wall specimens were constructed. Three different types of vinyl siding panels were tested. Each pressure chamber was instrumented with one pressure tap at its center location, and a cavity pressure tap under the vinyl siding panels.

A pressure trace protocol for the testing of each wall was developed with stochastic wind traces, dynamic (sinusoidal), and static traces for three levels of peak pressure. The protocol had segments of both uniform and spatially varying pressure loading. The relationship between PEFs and applied loading is used to evaluate the feasibility obtaining similar PEFs between a fully stochastic wind series and simpler trace protocols (i.e., static, dynamic (slow sinusoid)).

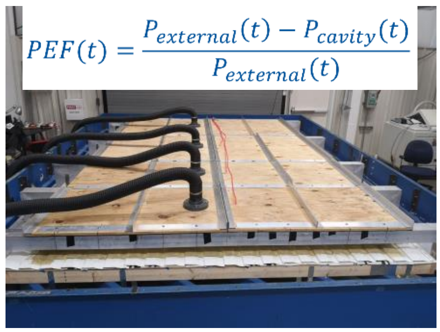

Figure 1. Overview of multi-chamber test assembly.

3. RESULTS AND DISCUSSION

The main takeaway is that establishing an appropriate spatial variation is the most important feature to evaluate PEFs. Figure 2 shows PEFs up to five times larger during spatially varied stochastic wind series than spatially uniform static loading (used in current design standards).

During uniform loading conditions, the cavity pressures respond directly to the external pressures, remaining uniform across all chambers and resulting in low values of PEFs (max. 0.34). For stochastic wind traces which contain spatial variation based on area averaging of pressure taps, cavity pressures retain elements of the frequencies of all pressure traces, akin to summing the various traces present, ultimately leading to higher PEFs ranging (0.6-0.8) at peak pressures.

Table 1 shows results for all test types on one specimen. The spatially varying dynamic tests resulted in the highest PEFs suggesting there may be dependence of the PEFs on the correlation of the pressure traces; all specimens followed the same general trends.

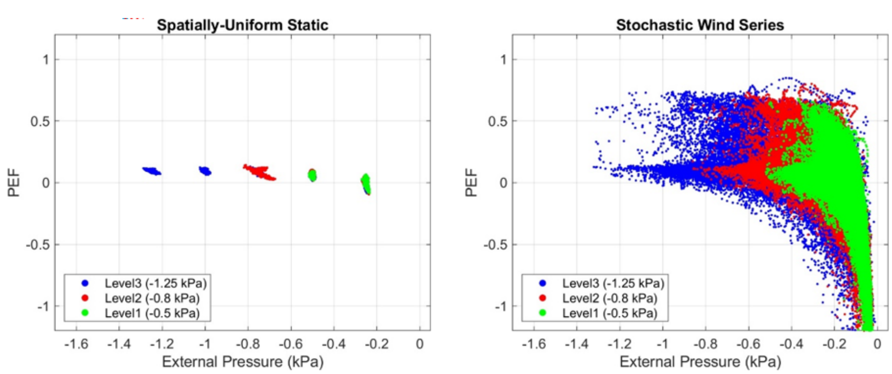

Figure 2. Comparison between PEFs for spatially uniform static (left) and stochastic wind series (right).

Table 1. PEF range and magnitude at or near maximum suction applied for each test type.

PEF Statistic	Uniform Static	Varying Static	Uniform Dynamic	Varying Dynamic	Stochastic
Level 1					
Range	[-0.16,0.15]	[-0.15,0.45]	[-0.64,0.33]	[-4.05,1.02]	[-2.09,0.66]
PEF -0.5 kPa	**0.09**	**0.5**	**0.18**	**0.83**	**0.65**
Level 2					
Range	[-0.15,0.19]	[-0.12,0.45]	[-0.50,0.54]	[-3.03,2.59]	[-1.43,0.71]
PEF -0.8 kPa	**0.10**	**0.55**	**0.2**	**0.89**	**0.7**
Level 3					
Range	[-0.03, 0.13]	[-0.10,0.30]	[-1.05,1.12]	[-3.96,0.90]	Not tested
PEF -1.25 kPa	**0.10**	**0.55**	**0.2**	**0.84**	**Not tested**

4. CONCLUSIONS

This study seeks to develop a simplified laboratory-based test procedure for replicating the net pressures on vinyl siding systems considering realistic spatio-temporal wind variations.

- The spatial pressure gradient is the driving factor behind the obtained PEFs for all tests; PEFs ranging from 0.6- 0.9 (maximum ~0.9 with the least correlated sine waves).
- Temporal wind variations by themselves were not a driver of the PEFs resulting in low values of PEFs ranging from 0 to a maximum of 0.30.
- Increases in the magnitude of the applied external pressures showed little variation in terms of the maximum observed PEFs beyond 0.5 kPa (agreement within 18%).
- The spatially varying static tests are suggested for future simplified standardized testing procedures since these were able to produce meaningful PEFs over a wide range (0 – 0.75).
- There may be dependence of the PEFs on the correlation of the pressure traces which is affected by turbulence levels in the case of stochastic wind traces.

ACKNOWLEDGEMENTS

This research was sponsored Florida Building Commission (FBC) Project #P0150335. The authors are grateful to all members of the project Advisory Committee.

REFERENCES

Architectural Testing, I. A. (2002). "Wind Pressure Equalization Research Project Report. ."the Vinyl Siding Institute, Washington, DC. .

ASTM D3679 (2017). "Standard Specification for Rigid Poly(Vinyl Chloride) (PVC) Siding."West Conshohocken, PA; ASTM International.

ASTM D5206 (2013). "Standard Test Method for Windload Resistance of Rigid Plastic Siding."West Conshohocken, PA; ASTM International.

Cope, A. D., Crandell, J. H., Johnston, D., Kochkin, V., Liu, Z., Stevig, L., and Reinhold, T. "Wind loads on components of multi-layer wall systems with air-permeable exterior cladding."

FEMA (2020). "FEMA P-2077 Hurricane Michael in Florida."

Miller, C. S., Kopp, G. A., Morrison, M. J., Kemp, G., and Drought, N. (2017). "A Multichamber, Pressure-Based Test Method to Determine Wind Loads on Air-Permeable, Multilayer Cladding Systems." *Frontiers in Built Environment*, 3, 7.

Prevatt, D. O., and Roueche, D. B. (2020). "Hurricane Michael Data Enhancement (Phase II), Performance of Modular Houses and FEMA Recovery Advisory Reviews."

Development of Standard Test Considering Pressure Equalization for Discontinuous Metal Roof (DMR) Systems.

Oscar Lafontaine [a,*], Irina Afanasyeva [b], David O. Prevatt [c]

[a]*University of Florida, Gainesville, FL, USA, oscar.lafontaine@ufl.edu*
[b]*University of Florida, Gainesville, FL, USA, irina.afanasyeva @ufl.edu*
[c]*University of Florida, Gainesville, FL, USA, dprev@ce.ufl.edu*

ABSTRACT:
The most critical line of defense against property damage from high winds and rain is roof coverings, yet roofing damage is the major driver of recent economic losses in residential structures. Discontinuous metal roofing (DMR) systems have gained market share in residential structures. DMR systems allow airflow through joints in the panels enabling pressure equalization as shown in IBHS studies. As part of a new standard test, a methodology was developed to determine if DMR systems are sufficiently air-permeable to experience reduced wind loading. Researchers constructed a pressure chamber to which DMRs are mounted and air is drawn through the head lap and side laps for pressures ranging from 25 Pa to 3 kPa. Results are plotted on a log-log paper, and the resulting relationship is used to deem if the DMR is sufficiently air-permeable to experience pressure equalization compared to DMRs tested at IBHS.

Keywords: discontinuous metal roof (DMR), pressure equalization, air permeable cladding, laminar flow element

1. INTRODUCTION

In a permeable roofing system where the panels interlock, gaps allow sufficient airflow from the air space below the roofing system (cavity) to the exterior of the building relieving the upward loads on the surfaces and fastening system. Morrison and Miller (2017) conducted full-scale experiments on discontinuous metal roof systems (DMRs) which proved they are air-permeable cladding materials and their ultimate wind resistance design should be based upon calculating a pressure equalization factor (PEF). However, the uplift capacity of these systems is evaluated using component testing such as UL-1897 (1988) which treat these panels as impermeable roof systems.

The University of Florida tried to quantify the real wind pressures DMRs via: 1) wind tunnel testing; 2) uniform pressure chamber testing (Rahate 2017). However, results showed that an appropriate PEF cannot be determined without considering spatial variations of wind.

This research proposes a methodology that correlates the airflow-rate through the seams of DMR systems with the obtained values of PEFs during full-scale testing. The test setup consists of a DMR panel installed on an air-pressure box attached to a centrifugal blower fan that generates air through-flow. Air through-flow rates are measured by a Laminar Flow Element (LFE), over a range of net pressures. By plotting results on ln-ln paper, the resulting straight-line graph can be extrapolated to the net pressure range at failure of the DMR system, and so an appropriate air through-flow rate for suction pressure at failure is determined. The gradient of the ln-ln relationship (air permeance coefficient) is used to determine whether DMR systems are sufficiently air permeable to be assigned a PEF of 0.7 based on IBHS testing (Morrison and Miller 2017).

* Lead presenter

2. MATERIALS AND METHODS

The laboratory test setup was developed to measure air flow rates over a range of net pressures on a roofing system ranging from 25 Pa to 3000 Pa (based on (ASTM International E2178-13 2013)). The setup consists of a sealed five-sided box made of OSB wood sheathing, with dimensions measuring 68 in x 48 in x 12 in deep, connected to a centrifugal fan through a 6 in. diameter tube. A linear flow element (LFE) device is installed in series between the chamber and the centrifugal fan, approximately 10 diameters away from the chamber to monitor airflow-rates. A pressure transducer was installed in the pressure chamber to monitor the pressure differentials.

Specimens for DMR 1 low profile shingle panel 12 in. wide, DMR 2 medium profile shingles 12 in wide, DMR 3 high profile panel installed on wood batten and DMR4: 12 in. wide architectural aluminum with 2 in. standing seam were constructed. The specimens simulated roof field conditions and were connected through head laps (4 specimens) and both head and side laps (5 specimens). The last DMR4 specimen had a rake support through its perimeter simulating roof panels in roof eave or ridge areas. The specimens are installed on the top surface of the chamber that has large openings to allow free air flow to be drawn through the DMR specimen.

Each specimen was first tested in a tare condition where a polyethylene plastic bag was used to cover the entire pressure chamber, including the DMR specimen seams. The test was repeated without the tare, and airflow-rate results were subtracted to eliminate extraneous leakage. Airflow-rate results were plotted in a log-log graph for each benchmark pressure differential.

Figure 1. DMR pressure chamber and LFE test setup.

3. RESULTS AND DISCUSSION

Results are summarized in figure 2 which shows the airflow-rate to pressure differential relationship for the first three DMR systems on a ln-ln plane. Table 1 shows trendline relationships for the low-pressure range and high-pressure range for all DMR systems.

DMR1 specimens show an overall good linear trend considering the entire pressure range. Independent trendline equations considering only the high-pressure range have R^2 values of 0.96 and 0.96. At the high-pressure range, vertical deflections started to be noticeable for DMR1 specimens which can cause changes in the DMR seam sizes slightly reducing the amount of airflow-rate. DMR1 was the specimen with overall less airflow-rate.

DMR2 specimens show a consistent linear relationship considering pressures differentials from 25 Pa to 1500 Pa. Independent trendline equations also show R^2 =0.99 for both the low-pressure range and high pressure. No noticeable differences were observed between the specimen with side lap and without the side lap (agreement within 1%).

DMR3 specimens were tested for the low-pressure range, and one high pressure range point (500 Pa) for the specimen with the side lap. The low pressure trendline equation shows an R^2=0.99 for both specimens, which extends to the high pressure point during the test with side lap. DMR3 has slightly higher airflow-rate magnitudes possibly caused by the batten space in its connection to the wood sheathing. No noticeable differences were observed between the specimen with side lap and without the side lap (agreement within 1%).

All DMR4 specimens have a linear relationship R^2 =0.99 at the low-pressure range. DMR4 specimens which simulates roof field locations (DMR4-SL1, DMR4-SL0) showed agreement (within 8%) between their air permeance coefficients. Both specimens exhibited a polynomial airflow-rate to pressure differential relationship at the high-pressure range as the panels began to deflect. The last DMR4 specimen (DMR4-SL1-Res) had a linear relationship (R^2 =0.99) for the high-pressure range, albeit its air permeance coefficient increased by nearly 50%. Results for DMR4 will be shown during the presentation similar to figure 2.

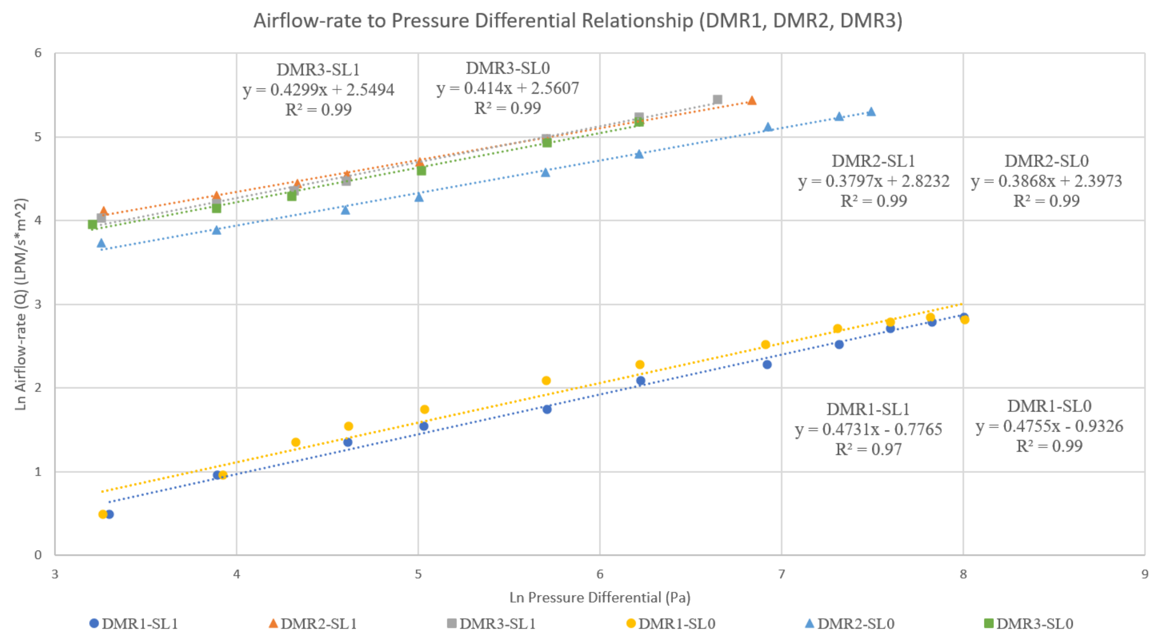

Figure 2. Results of airflow-rate to pressure differential relationship of DMR1, DMR2 and DMR3.

Table 1. Airflow-rate to pressure differential relationship for DMRs with side lap (SLI) and no side lap (SL0); pressure differential units (ln (Pa)) and airflow-rate units (ln (LPM/s*m^2)).

DMR Specimen	**Low Pressure Range**	**High Pressure Range**
DMR1-SL1	y = 0.28x + 1.30, R^2 =0.99	y = 0.20x + 1.78, R^2 =0.96
DMR1-SL0	y = 0.66x – 1.64, R^2 =0.99	y = 0.32x + 0.25, R^2 =0.96
DMR2-SL1	y = 0.36x + 2.92, R^2 =0.99	y = 0.38x + 2.82, R^2 =0.99
DMR2-SL0	y = 0.37x + 2.49, R^2 =0.99	y = 0.321x + 2.894, R^2 =0.99
DMR3-SL1	y = 0.42x + 2.61, R^2 =0.99	Only 500 Pa tested
DMR3-SL0	y = 0.41x + 2.56, R^2 =0.99	Not tested
DMR4-SL1	y = 0.52x - 0.85, R^2 =0.99	y = 0.58x^2 - 7.11x + 24.142, R^2 =0.99
DMR4-SL0	y = 0.48x - 0.59, R^2 =0.99	y = 0.52x^2 - 6.50x + 22.64, R^2 =0.99
DMR4-SL1-Eave/Ridge	y = 0.63x - 1.97, R^2 =0.99	y = 0.98x - 4.03, R^2 =0.99

4. CONCLUSIONS

Experimental tests were conducted on DMR systems to assess their air permeability. DMR systems with an air permeance coefficient equal or higher in magnitude than those tested in IBHS are assigned a PEF of 0.7. Otherwise, a PEF of 1 will be assigned treating this system as impermeable.

- DMR1, DMR2, and DMR3 showed linear relationships; future test standards can test the low-pressure range and extrapolate high pressure range air-permeance coefficients
- DMR4 panels consistently showed non linearities at the high-pressure range suggesting the use of an air-permeance coefficient is not suitable to evaluate its pressure equalization potential.
- Overall results show consistent linearity of the air-flow rate to pressure differential relationship independent of test facility. However, the magnitude of the obtained gradients is dependent on the test setup and sealing mechanisms.

ACKNOWLEDGEMENTS

This research was sponsored by the Metal Contractors Association (MCA) #00108448. The authors are grateful to all members of the project's Advisory Committee.

REFERENCES

ASTM International E2178-13 (2013). "Standard Test Method for Air Permeance of Building Materials.", ASTM International, West Conshohocken.

Morrison, M. J., and Miller, C. (2017). "Wind Loads on Discontinuous Metal Roofing."

Rahate, S. (2017). "Determination of Design Wind Loads and Uplift Capacities of Discontinuous Metal Roofing Systems." Master of Science, University of Florida.

Underwriters Laboratory (UL) (1988). "Subject 1897: Outline of investigation for uplift resistance for roofing systems."Underwriters Laboratory, Inc., Northbrook, Ill.

A Scenario-based Hurricane Analysis Framework for Community-level Building Damage Estimation

Ram K. Mazumder[a*], Meredith Dumler[b], S. Amin Enderami[c], Elaina J. Sutley[d]

[a]*Postdoctoral Researcher, Civil, Environmental and Architectural Engineering, University of Kansas, Lawrence, KS, USA, Email: rkmazumder@ku.edu*
[b]*Undergraduate Research Assistant, Civil, Environmental and Architectural Engineering, University of Kansas, Lawrence, KS, USA, Email: meredithdumler@ku.edu*
[c]*Graduate Research Assistant, Civil, Environmental and Architectural Engineering, University of Kansas, Lawrence, KS, USA, Email: a.enderami@ku.edu*
[d]*Chair's Council Assistant Professor, Civil, Environmental and Architectural Engineering, University of Kansas, Lawrence, KS, USA, Email: enjsutley@ku.edu*

ABSTRACT
This study presents a scenario-based hurricane analysis framework for predicting community-level damage to buildings subjected to hurricane winds. The hurricane scenario is modelled using historical hurricane data. The approach presented estimates peak gust wind speeds at building sites considering the spatial variation of wind intensities. The building damage states are assigned stochastically using existing HAZUS fragility functions, peak gust wind intensity, and randomly generated number for each scenario realization. The framework is demonstrated with a virtual testbed of the hurricane-prone community of Onslow County, North Carolina.

Keywords: Hurricanes; building damage; scenario-based analysis; losses; community

1. INTRODUCTION

Hurricanes pose the greatest threat to coastal property and life, and often result in severe disruption to coastal communities. In the past five years 13 hurricanes have caused $381 billion (USD) in losses and killed 2,402 people in the U.S (NOAA 2021). There is great need for more research on hurricanes, including hazard analysis that includes the hurricane's impact on the built environment. A scenario-based hurricane analysis framework is proposed here considering spatially distributed hurricane winds to develop a community-level building damage portfolio. The primary contributions of the work are simulating a real hurricane trajectory, and estimating building-specific wind speed and damage assignments within a regional analysis.

2. PROPOSED HURRICANE ANALYSIS FRAMEWORK

The proposed hurricane analysis framework consists of two modules: hazard analysis, and vulnerability analysis. In the hazard analysis module, building-specific peak gust wind intensities are determined for a hurricane scenario where characteristics of the hurricane are obtained from the HURDAT2 database (NOAA 2021). In the vulnerability analysis module, the probability of exceeding four damage states, namely minor, moderate, severe, and complete, of a building is determined using existing HAZUS fragility functions and peak gust wind speed. A damage state is then assigned to a building stochastically by comparing the maximum peak gust wind speed, damage state probabilities, and a randomly generated number. This information is then aggregated to represent the community's building portfolio damage.

* Lead presenter

3. HURRICANE HAZARD MODELING

The strongest hurricane wind occurs at the eye wall, and wind intensity decays as the location moves away from the hurricane center (Xu and Brown 2008). Gradient wind speed at building location is estimated using the radial wind profile model provided by Holland (1980), as follows:

$$V_G = \left[\left(\frac{R_{max}}{r}\right)^B \cdot \left(\frac{B\Delta p \cdot \exp\left[-\left(\frac{R_{max}}{r}\right)^B\right]}{\rho}\right) + \frac{r^2 f^2}{4}\right]^{\frac{1}{2}} - \frac{rf}{2} \tag{1}$$

where R_{max} is the radius of the maximum wind speed, r is the distance from hurricane eye to the building site, B is the Holland pressure profile parameter, Δp is the central pressure difference estimated subtracting central pressure from atmospheric pressure of 1013 millibars, ρ is the air density, and f is the Coriolis parameter (=$2\Omega \cdot \sin\varphi$, where φ is the latitude, Ω is the earth's angular velocity) (Xu and Brown 2008). The radius of the maximum wind is estimated using the model provided by FEMA (2012), as below:

$$\ln R_{max} = 2.556 - 0.000050255\Delta p^2 + 0.042243032\psi \tag{2}$$

where ψ is the storm latitude and Δp is the central pressure difference. Holland pressure profile parameter is estimated using the model developed by Powell et al. (2005), as follows:

$$B = 1.881 - 0.00557R_{max} - 0.01097\psi \tag{3}$$

4. HURRICANE ANALYSIS

To exemplify the framework, a virtual testbed of the hurricane-prone community of Onslow County, NC is developed using the data and maps obtained from the county government website and OpenStreetMap (Onslow County 2021; OSM 2020). The testbed has an area of 767 square miles and is home to 197,000 people. The Onslow testbed contains 63,923 buildings assigned 22 structural archetypes, including residential buildings, manufactured homes, commercial and industrial buildings, as shown in Figure 2(a).

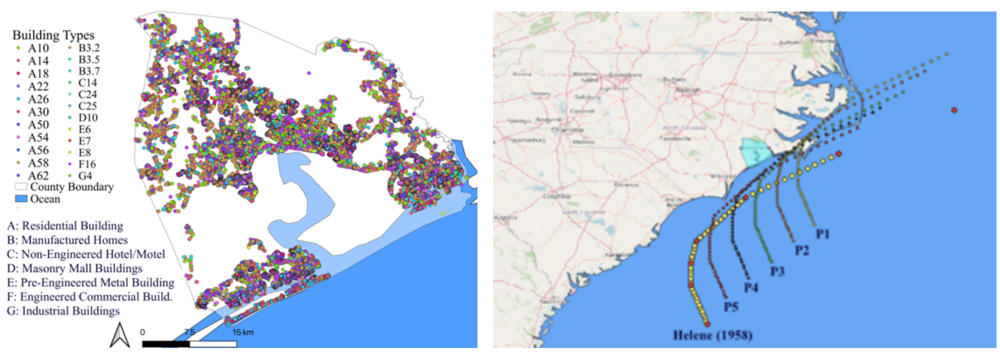

Figure 2. (a) Onslow building inventory; (b) six scenario hurricanes tracks

Hurricane Helene (1958), the strongest hurricane that hit Onslow County in the past 160 years, is adopted here for analysis. To examine the scenarios closely related to Helene, five hypothetical tracks are projected by offsetting the original track while maintaining the original central pressures and intensities of Hurricane Helene. These six hurricane tracks are mapped in Figure 2(b), where P1-P5 denote the five hypothetical tracks. Ranges of the maximum wind speed radius, central pressure difference, and Holland parameters are 36.2-42 km, 70-83 millibars, and 1.27-1.32, respectively. Each hurricane scenario analysis is performed for 24 hours at 30 minute intervals. Figure 3 shows estimated maximum peak wind speeds for the six scenarios; the color gradients are such that dark red is faster wind speeds (160 - 165 mph), and the blue is lower wind speeds (100 - 115 mph). Damage state probabilities are determined based on the wind intensities and fragility functions. This information is used to assign a damage state to each building stochastically using the maximum peak gust wind speed, damage state probabilities, and a random number.

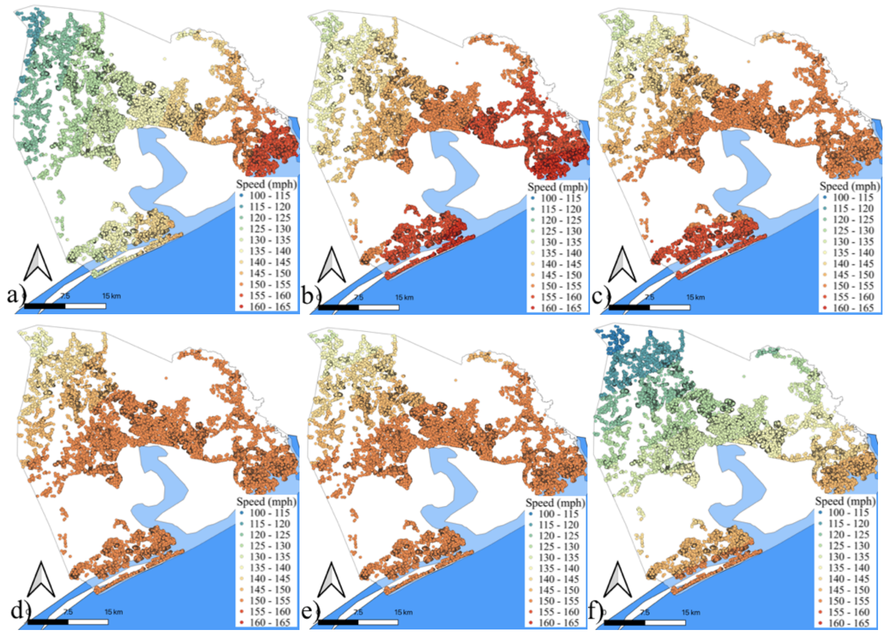

Figure 3. Maximum peak gust wind speed maps for hurricanes: a) P1, b) P2, c) P3, d) P4, e) P5, and f) Helene.

Figure 4 shows building damage maps, and Table 5 summarizes the outcomes of the damage simulation. Hurricane P4 is the most severe; Helene's actual track caused the least damage considering all six scenarios. Hurricanes Helene and P1 resulted in 31% and 36% of buildings experiencing either severe or complete damage, respectively. Hurricanes P2-P4 resulted in about 60% of buildings experiencing either severe or complete damage.

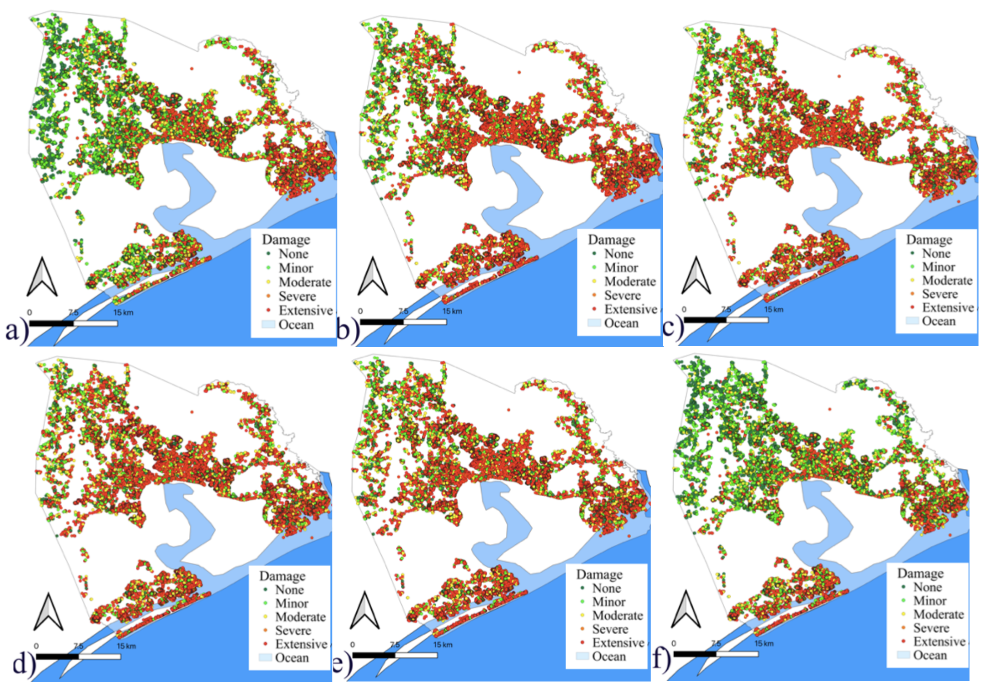

Figure 4. Building damage maps for hurricanes: a) P1, b) P2, c) P3, d) P4, e) P5, and f) Helene.

Table 1. Building damage summary.

	Projected-1	Projected-2	Projected-3	Projected-4	Projected-5	Helene
None	9264	3182	3270	2866	3053	11134
Minor	16941	8802	9226	8573	8942	18227
Moderate	14956	12902	13490	13205	13390	14841
Severe	6093	8385	8340	8507	8432	5635
Complete	16669	30652	29597	30772	30106	14086

5. CLOSING REMARKS

This research is on-going. The proposed framework is expected to feed into a loss estimation model to then assist decision-makers in prioritizing buildings for risk mitigation efforts. Future work also intends to extend the hazard analysis to include other hurricane hazards in addition to wind.

ACKNOWLEDGEMENTS

This work was partially supported by the National Science Foundation under Grant No. CMMI 1847373.The views expressed are those of the author(s), and do not necessarily reflect the views of the funding agency.

REFERENCES

FEMA. (2012). Multi-hazard loss estimation methodology hurricane model technical manual. Hazus-MH 2.1-Technical manual.

Holland, G. J. (1980). An analytic model of the wind and pressure profiles in hurricanes. Monthly weather review, 108(8), 1212-1218.

NOAA (2021). Revised Atlantic hurricane database (HURDAT2), National Oceanic and Atmospheric Administration, https://www.aoml.noaa.gov/hrd/hurdat/Data_Storm.html, retrieved on Jan 08, 2021

Onslow County (2021). Onslow County government website, https://www.onslowcountync.gov/, accessed on 03/2021

OSM (2020) OpenStreetMap, https://www.openstreetmap.org/, accessed on 09/2020.

Xu, L., & Brown, R. E. (2008). A hurricane simulation method for Florida utility damage and risk assessment. IEEE Power & Energy Society General Meeting-Conversion & Delivery of Electrical Energy in the 21st Century, 1-7.

Performance and Fragility of Elevated Structures During Hurricane Events

Haitham A. Ibrahim[a,*], Amal Elawady [a,b], David O. Prevatt [c]

[a]*Department of Civil and Environmental Engineering, Florida International University, Miami, Florida, USA, hmoha026@fiu.edu*
[b]*International Hurricane Research Center, Florida International University, Miami, Florida, USA, aelawady@fiu.edu*
[c]*University of Florida, Gainesville, Florida, USA, dprev@ufl.edu*

ABSTRACT:
Elevating coastal houses that are close to the shoreline has been found to be an effective technique to mitigate flooding and storm surge hazards. However, elevated structures are exposed to stronger winds and unique aerodynamics characteristics due to the presence of air gap beneath the floor. This leads to wind loads on roof, floor, walls, and piles that are different from those on a slab on grade counterpart and not yet defined in building codes. Thus, it is of critical importance to assess the vulnerability of elevated structures to wind hazards. Utilizing available data from post-hurricane damage reconnaissance, this paper analyses the wind resistance performance observed for 900 elevated structures, located in Florida and Texas, United States, which were impacted by Hurricanes Irma, Michael, and Harvey. We report on observed damage to structural and non-structural components and relate these to the estimated failure wind speeds. Furthermore, the data is used to empirically develop fragility curves for elevated structures subjected to strong winds. Results showed that besides wind speed, building age, location, and elevation height may affect the damage level of elevated structures.

Keywords: Elevated structures, Fragility, Empirical, Wind effects

1. INTRODUCTION

The United States suffers from landfalling hurricanes that impose multi-hazards on coastal communities on an annual basis. Coastal structures experience severe damage due to flooding, storm surge, and strong winds(Amini & Memari, 2020). To mitigate flooding and storm surge hazards, the Federal Emergency Management Agency recommends elevating coastal structures to a safe level known as Base Flood Elevation level (FEMA P-550). Of the several benefits of such a mitigation technique on the resiliency of such structures, elevating buildings may increase their vulnerability to wind hazards since they would be exposed to higher wind speeds (Kim et al., 2020). Yet, there are unknown changes in the wind loading acting on an elevated structure due to the changes in the aerodynamics created by air gap under the floor. To fill this gap, Abdelfatah et al. (2020) carried out large-scale aerodynamic tests on four models which represent low rise gable roof single story elevated structure with four different elevation heights. Results showed that, for elevated structure, the floor surface experiences suction pressure. Moreover, increasing the elevation height leads to increasing the critical suction zones' area.

Although hurricanes are multi-hazard events, the current research considers only the effect of strong winds and their induced damage. Precisely, this paper analyses the performance and fragility of coastal elevated structures. First, Data sources and damage classification method for the damaged elevated structures, located in Texas and Florida, are briefly introduced. Second,

* Lead presenter

effect of elevation height on the observed damage level is examined. Finally, fragility functions are developed for elevated structures using empirical approach.

2. METHODOLOGY

Following the landfall of Hurricanes Irma, Harvey, and Michael, several reconnaissance efforts have been organized to collect data about damaged structures. For example, the Structural Extreme Events Reconnaissance (StEER) Network initiated and executed virtual and field assessment study following Hurricane Michael which impacted the state of Florida (Kijewski-Correa et al., 2020). Also, RAPID-reconnaissance studies were executed following the landfall of Hurricanes Irma and Harvey which impacted Florida and Texas, respectively (Kijewski-Correa et al., 2018; Roueche et al., 2018). It should be noted that the collected metadata for the damaged elevated structures is published on the Natural Hazard Engineering Research Infrastructure (NHERI) DesignSafe-CI platform. Assessment teams have categorized the level of damage of each structure into five distinctive states, namely: DS0 (no damage), DS1 (minor damage), DS2 (moderate damage), DS3 (severe damage), and DS4 (destroyed damage state). Readers are referred to (Roueche et al., 2018) for more information about the quantitative guidelines used for assigning an overall damage rating for each structure.

2. DAMAGE OBSERVATIONS

Following these criteria and to investigate the effect of elevation height on the damage level that a house may experience during a hurricane event, the damage data used in the current study is divided into 5 groups of elevation heights as shown in Figure 1(a). Obviously, percentage of houses that experiences DS0 and DS1 is inversely proportional to the increase in elevation height. For example, almost 60% of structures with elevation height of 2.0 – 4.0 ft showed no or minor damage. However, this percentage decreases to 26% for structures with 4.0 to 8.0 ft elevation height and decreases to 40% (on average) in case of elevation height ≥ 8.0 ft. With respect to DS4 (i.e., destroyed damage), groups with elevation height >4.0 ft have higher percentage than that of the group with elevation height of 2.0 – 4.0 ft. Remarkably, 45% of houses with elevation height between 4.0 and 8.0 ft experienced DS4. This percentage is 3-4 times that of the other groups. It should be noted that 75% of the damaged houses in this group (i.e., with elevation height between 4.0 and 8.0 ft) were constructed in State of Texas.

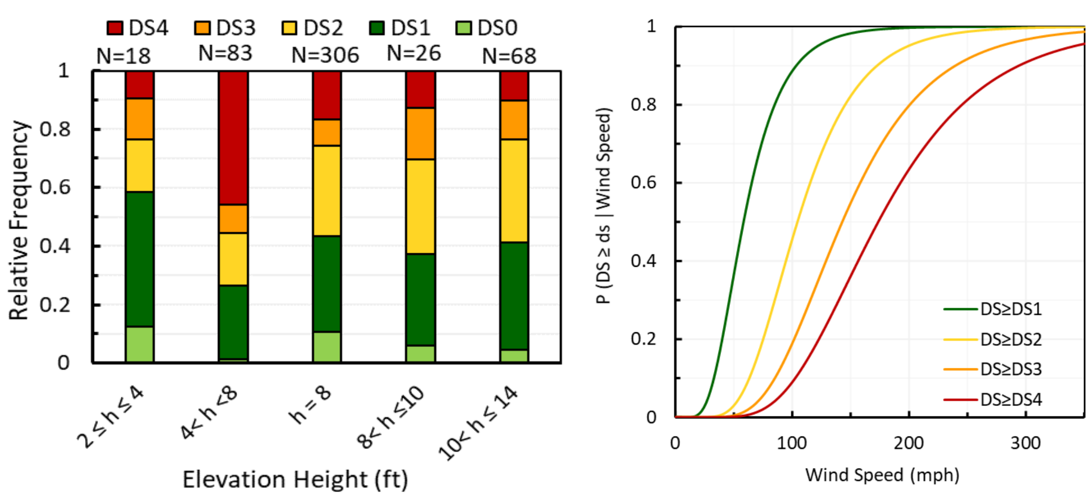

Figure 1. (a) Elevation height effect on the damage distribution and (b) fragility curves for elevated structures.

3. FRAGILITY FUNCTIONS OF ELEVATED STRUCTURES

Following the procedures proposed by (Roueche et al., 2017), empirical fragility curves for elevated structures are developed as shown in Figure 1 (b). As can be seen, the median wind speed increases while moving from DS1 (lowest) towards DS4 (i.e., highest median wind speed). Precisely, the median wind speeds to be in or exceeding DS1, DS2, DS3, or DS4 are 58.3, 104.4, 142.72, and 173.5 mph, respectively. Interestingly, difference between each two damage measures is not constant and decreases as damage level increases. For example, the difference in median failure wind speed between DS1 to DS2 (46.1 mph) is 50% higher than that between DS3 to DS4 (30.8 mph). That can be attributed to the progressive nature of the wind induced damage at higher damage states (Amini & Memari, 2020). For example, at DS3, if an elevated structure experiences damage to roof/wall sheathing panels, windows, doors, and slight roof structure failure, this can quickly lead to DS4 damage level if pressurization, loss of loading path, or loss of lateral supports to walls occur.

4. CONCLUSIONS

Based on this preliminary investigation, it can be concluded that elevation height is a key parameter in determining the damage level that an elevated structure may experience. Furthermore, work is ongoing to develop fragility functions at building and component level for both elevated and slab-on-grade structures.

ACKNOWLEDGEMENTS

The authors acknowledge the financial support provided by the Florida Sea Grant (FSG) Program. Also, the authors acknowledge Risk Management Solutions (RMS), Inc. for providing the wind field footprints. The content expressed in this paper are the views of the authors and do not necessarily represent the opinions or views of FSG and RMS.

REFERENCES

Abdelfatah, N., Elawady, A., Irwin, P., & Chowdhury, A. (2020). A study of aerodynamic pressures on elevated houses. *Wind and Structures*, *31*(4), 335-350.

Amini, M., & Memari, A. M. (2020). Review of Literature on Performance of Coastal Residential Buildings under Hurricane Conditions and Lessons Learned. *Journal of Performance of Constructed Facilities*, *34*(6), 04020102. doi: 10.1061/(asce)cf.1943-5509.0001509

FEMA P-550. (2009). Recommended Residential Construction for Coastal Areas: Building on Strong and Safe Foundations. *Washington, DC*(Second Edition).

Kijewski-Correa, T., Prevatt, D., Roueche, D., Robertson, I., Berman, J., Mosalam, K., & Grilliot, M. (2020). PRJ-2113 | StEER - Hurricane Michael. *DesignSafe-CI [publisher]*, Dataset, doi: 10.17603/ds17602-17605aej-e17227

Kijewski-Correa, T., Roueche, D., Pinelli, J.-P., Zisis, I., Gurley, K., Haan Jr, F., . . . Rhode-Barbarigos, L. (2018). RAPID: A Coordinated Structural Engineering Response to Hurricane Irma (in Florida). *DesignSafe-CI [publisher]*, Dataset. doi: 10.17603/DS2TX0C

Kim, J. H., Moravej, M., Sutley, E. J., Chowdhury, A., & Dao, T. N. (2020). Observations and analysis of wind pressures on the floor underside of elevated buildings. *Engineering Structures*, *221*, 111101.

Roueche, D. B., Krupar III, R. J., Lombardo, F. T., & Smith, D. J. (2018). Collection of Perishable Data on Wind-and Surge-Induced Residential Building Damage During Hurricane Harvey (TX). *DesignSafe-CI [publisher]*, Dataset, doi:10.17603/DS17602DX17622

Roueche, D. B., Lombardo, F. T., & Prevatt, D. O. (2017). Empirical Approach to Evaluating the Tornado Fragility of Residential Structures. *Journal of Structural Engineering*, *143*(9), 04017123. doi: 10.1061/(asce)st.1943-541x.0001854

Wind Performance of Asphalt Shingles Using Full-Scale Experimentation

Ameyu B. Tolera [a*], Karim Mostafa [b], Arindam Gan Chowdhury [c], Ioannis Zisis [d]

a Florida International University, Miami, FL, USA, atole066@fiu.edu
b Florida International University, Miami, FL, USA, kmost002@fiu.edu
c Florida International University, Miami, FL, USA, chowdhur@fiu.edu
d Florida International University, Miami, FL, USA, izisis@fiu.edu

ABSTRACT:
Asphalt shingles constitute more than 80% of the roofing materials in current residential housing in the United States. Many post-disaster surveys have reported the failing of these roofing elements below the design level wind event. Research to realistically model aerodynamics of asphalt shingles at full scale is limited. As a result, knowledge gaps exist pertaining to peak wind loads and effects of permeability for asphalt shingles. In this study, a full-scale experimental campaign was performed at Florida International University's Wall of Wind (WOW) Experimental Facility (EF) to study the aerodynamics and wind resistance of asphalt shingles by using a monoslope deck subjected to different wind speeds and directions. The experimental protocols included both aerodynamic and failure assessments, whereby the former dealt with studying the pressure and near-surface velocity distribution over the shingled roof while the latter dealt with studying the failure mechanisms of asphalt shingles under high wind speeds.

Keywords: Asphalt shingles, Peak wind loads, Permeability, Speedup factor, Full-scale testing.

1. INTRODUCTION

Hurricane wind events have been responsible for the major disasters in the United States. National Oceanic and Atmospheric Administration's (NOAA) Office for Coastal Management reports the insured losses due to hurricane wind events in the United States between 1986 to 2015 were more than USD 515 billion. Just in 2017, the insured losses for hurricanes Harvey, Irma and Maria were more than USD 92 billion. Many post disaster surveys confirmed that major insured losses in residential buildings due to wind events were as a result of the failure of roofing elements and subsequent water intrusion (Gurley et al. 2011; Taylor et al. 2011). No matter how insignificant a local failure of roofing elements may seem, a roof breach would lead to water intrusion, as extreme wind events are usually accompanied by heavy rain. Thus, it is important to study the wind resistance of roof coverings and design them against any slight liftoff that can cause water intrusion. This study focuses on the wind resistance of asphalt shingles. Among roofing elements in the United States, asphalt shingles constitute more than half of the roofing system, as they provide the cheapest roofing solution. Therefore, investigation of their wind performance is important in terms of assessing their vulnerability to wind loads.

Previous tests on asphalt shingles provided the essential start of studying them and so far, have laid of the fundamental procedural lay out for assessing their wind resistance. On this regard, (Peterka et al. 1997) and preceding reports from the same authors provided the first testing method for shingles, identified the failure mechanism associated with them and developed an analytical model used to predict net peak loads on these members. These works have been used as the basis for the current testing standards for wind resistance of asphalt shingles. Later studies by (Dixon et al. 2014) further extended these works to consider aging effects using full-scale experimentation.

* Lead presenter

While these literatures have provided essential knowledge on the wind resistance of asphalt shingles, the distribution of external and net peak wind loads on the shingled roof surfaces have not been fully studied. Moreover, knowledge gaps exist pertaining to peak wind loads, and extent of pressure equalization or escalation due to permeability of asphalt shingles. Therefore, this study focuses on addressing these gaps using a state-of-the-art full-scale testing facility.

2. METHODOLOGY

Full-scale experimental tests were conducted at the 12 fan Wall of Wind (WOW) Facility at Florida International University (FIU). A 3:12 mono-slope roof shingled with class H asphalt shingles with dimensions 161.25” x 155.25” was used. Two different sets of full-scale tests were conducted: aerodynamic and failure assessment tests. For the aerodynamic tests, the roof was divided into two symmetrical halves. One half was instrumented with pressure tabs and the other half was instrumented with Irwin sensors to record the wind pressures and near-surface wind speeds over the roof, respectively. The Irwin sensor calculates the wind speed at a particular height above the surface, h_s through a calibrated equation for a specific height h_s / h, where h is the probe height (Irwin 1981). In total 306 pressure taps (18 taps on a typical shingle, 9 external and 9 underneath) and 35 Irwin sensors were placed in critical areas. Once these data were recorded, distortions in amplitude and phase of the measured pressures were corrected using appropriate tubing transfer functions and the data were corrected accordingly (Irwin et al. 1979). A post-test partial turbulence simulation (PTS) was later performed to account for the missing low frequency turbulence (Mooneghi et al. 2016; Moravej 2018). These tests were conducted at a mean wind speed of 60mph at mean roof height and an open terrain exposure for wind directions ranging from 0° to 360° with an increment of 10° and the four corners (45°,135°,225° and 315°), with a sampling time of 60 second for each direction. The high-speed failure assessment test was performed at wind speeds ranging from 90 mph to 140 mph with an increment of 10 mph for the 5 principal wind directions: 0°,45°,90°,135°, and 180°, for the same terrain roughness.

3. RESULTS AND DISCUSSION

During the aerodynamic tests, cornering winds from the high-end corners of the monoslope were found to be critical for both surface pressures and velocities. This is consistent with previous studies on monoslope bare decks (Stathopoulos and Mohammadian 1986). For this wind direction, the worst peak external and net pressure coefficients (Cp) recorded were -9.62 and -8.4, respectively. Moreover, high mean pressure values consistent with these peak values were also indicative of the effect of conical vortices in these areas. Expressing the near surface wind speed recorded in terms of a speed up factor, which is the ratio of the near surface wind speed recorded to the mean wind speed of the approaching flow at mean roof height, the highest peak speed-up factor for this critical direction was found to be 4.0. These wind speeds were measured at the roof surface and were still found to be higher than the upper bound suggested by previous research which measured them at 25mm from the roof surface.

Area averaged pressure coefficients were also computed for areas ranging up to a full shingle size, as load will not be shared between adjacent shingles this size was deemed sufficient. Area averaged peak external and net pressure coefficients were then compared with provisions from ASCE7-16 for the same slope (American Society of Civil Engineers 2017). The results showed that the provisions in the ASCE 7-16, which do not consider the effects of permeable roofing elements (such as shingles), underestimated the wind loads, especially for edge zones, see Figure 1. Increased net suction compared to external peak loads were also observed for zones 1 and 2. This is expressed through a permeability factor, β, which is the ratio of peak net to external Cps, see Figure 2.

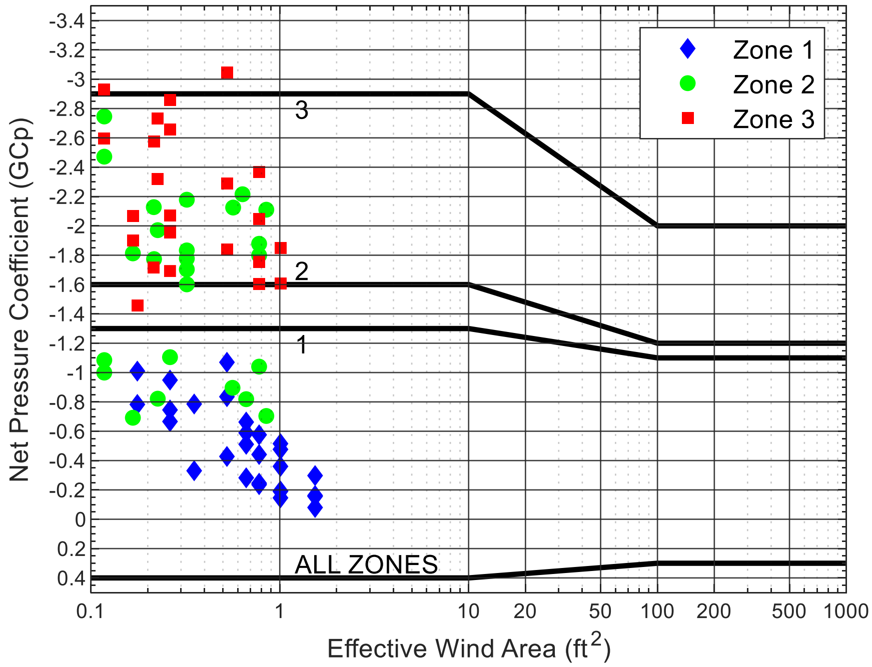

Figure 1 Area averaged net pressure coefficients compared to ASCE 7-16 GCp plot

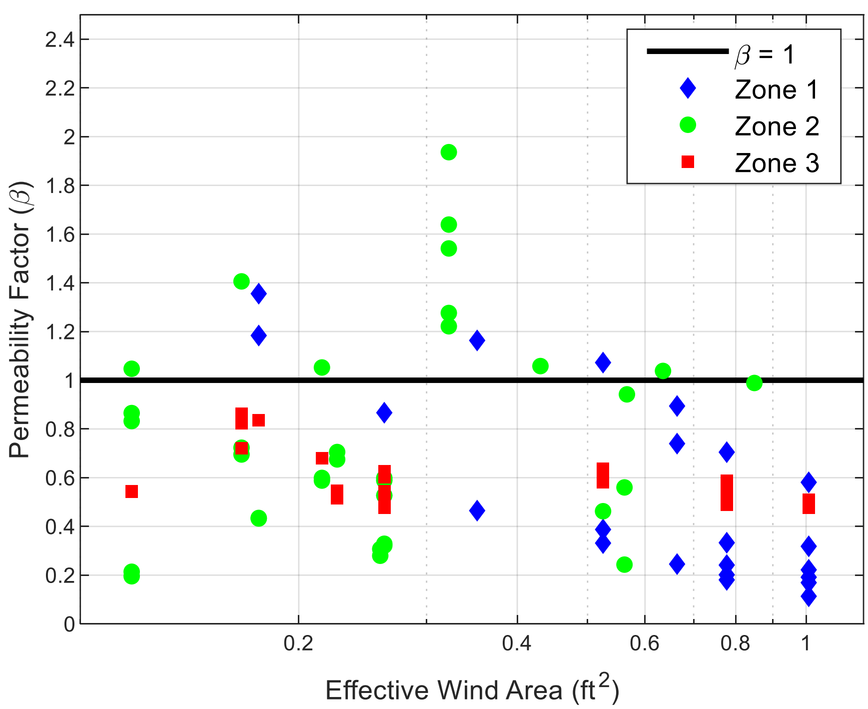

Figure 2 Permeability factor for area averaged Cps for ASCE 7-16 monoslope zones

Finally, the high-speed failure assessment tests helped in identifying two different failure mechanisms. The first failure occurred in the region of high external suction due to cornering winds at the high corners of the monoslope, consistent with the result from the aerodynamic test discussed earlier. Even though there was a significant pressure equalization that reduced the net suction on the roof, it was still high enough to cause liftoff. These types of failure modes were not addressed previously for asphalt shingles. (Peterka et al. 1997) stated that shingle liftoff would rather occur in the zone of reattachment due to a wind flow directed perpendicular to the leading edge of the roof eave. And this lift off would be caused by suction on the leading edge of the shingle due to surface flow and a positive pressure in the cavity acting together. This was the second failure case identified in this study. It occurred in the region of low peak external suction and was accompanied by pressure escalation.

4. CONCLUSION

Using full-scale low-speed aerodynamic and the high-speed failure assessment tests, the wind resistance of asphalt shingles was studied. This research showed that asphalt shingles could fail, not just due to local wind speed-up over the top surface of the leading edge as suggested by previous works, but both due to high global and local wind-induced pressures. Therefore, wind effects from both components should be considered in the design and testing of asphalt shingles.

ACKNOWLEDGEMENTS

This work is sponsored by the US National Science Foundation under the awards IIP 1841503 and I/UCRC WHIP2019-06. The authors would also like to thank GAF for providing materials for the asphalt shingled full-scale model and technical assistance. The opinions, findings, conclusions, or recommendations expressed in this article are solely those of the authors and do not represent the opinions of the funding agencies.

REFERENCES

American Society of Civil Engineers. (2017). *ASCE 7-16. Minimum design loads for buildings and other structures*. American Society of Civil Engineers.

Dixon, C. R., Masters, F. J., Prevatt, D. O., Gurley, K. R., Brown, T. M., Peterka, J. A., and Kubena, M. E. (2014). “The influence of unsealing on the wind resistance of asphalt shingles.” *Journal of Wind Engineering and Industrial Aerodynamics*, Elsevier, 130, 30–40.

Gurley, K. R., Asce, M., Masters, F. J., and Asce, M. (2011). “Post-2004 Hurricane Field Survey of Residential Building Performance.” *Natural Hazards Review*, 12(4), 177–183.

Irwin, H., Cooper, K. R., and Girard, R. (1979). “Correction of distortion effects caused by tubing systems in measurements of fluctuating pressures.” *Journal of Wind Engineering and Industrial Aerodynamics*, Elsevier, 5(1–2), 93–107.

Irwin, H. P. A. H. (1981). “A simple omnidirectional sensor for wind-tunnel studies of pedestrian-level winds.” *Journal of Wind Engineering and Industrial Aerodynamics*, Elsevier, 7(3), 219–239.

Mooneghi, M. A., Irwin, P., and Chowdhury, A. G. (2016). “Partial turbulence simulation method for predicting peak wind loads on small structures and building appurtenances.” *Journal of Wind Engineering and Industrial Aerodynamics*, Elsevier, 157, 47–62.

Moravej, M. (2018). “Investigating scale effects on analytical methods of predicting peak wind loads on buildings.” Florida International University.

Peterka, J. A., Cermak, J. E., Cochran, L. S., Cochran, B. C., Hosoya, N., Derickson, R. G., Harper, C., Jones, J., and Metz, B. (1997). “Wind uplift model for asphalt shingles.” *Journal of Architectural Engineering*, American Society of Civil Engineers, 3(4), 147–155.

Stathopoulos, T., and Mohammadian, A. R. (1986). “Wind loads on buildings with mono-slope roofs.” *Journal of Wind and Engineering*, 23, 81–97.

Taylor, P., Cochran, L., Levitan, M., Cochran, L., and Levitan, M. (2011). “Lessons from Hurricane Andrew Lessons from Hurricane Andrew.” (February 2015), 37–41.

Differences in flow structures of tornado vortex and efficiency of different tornado chambers

Sumit Verma [a*], R. Panneer Selvam [b]

[a]*University of Arkansas, Fayetteville, AR 72701, USA, sv015@uark.edu*
[b]*University of Arkansas, Fayetteville, AR 72701, USA, rps@uark.edu*

ABSTRACT:
Identifying similarities in flow pattern such as the way in which flow enters, progresses and exits tornado chamber (TC), different TCs are classified into five major categories. Experimental and CFD TCs falling in each of five categories are listed and the differences in flow structure of tornado vortex in those TCs are analysed by comparing touchdown swirl ratio (S_T). However, while comparing S_T of different TCs, it was found that different definitions of swirl ratio (S) are used in different works of literature. So, in this work, different definitions of S are converted into a consistent form for comparison. Besides, efficiency of different TCs is also analysed by comparing S_T. The higher the S_T, the higher the energy a TC needs as well as higher is the CFD computations. From analysis, the TCs with side openings and fully open outlet at top are found to be more efficient than others.

Keywords: swirl ratio, touchdown, efficiency

1. INTRODUCTION

With increasing swirl ratio (S), a single-celled vortex first touches down and then transforms into a double-celled vortex. The swirl ratio at which vortex touches the base of tornado chamber (TC) is termed as touchdown swirl ratio (S_T). The effect of geometrical differences and/or the flow generation mechanism of different tornado chambers may have their own contribution to disparity of S_T values observed in different chambers but different ways of defining swirl ratios by choosing different radial locations of flow domain is also a major factor for the disparity and a wide range of S_T values in different TCs. In Fig. 1, a sketch of a typical tornado chamber is shown and some associated notations used to describe chamber geometry and tornado flow is labeled.

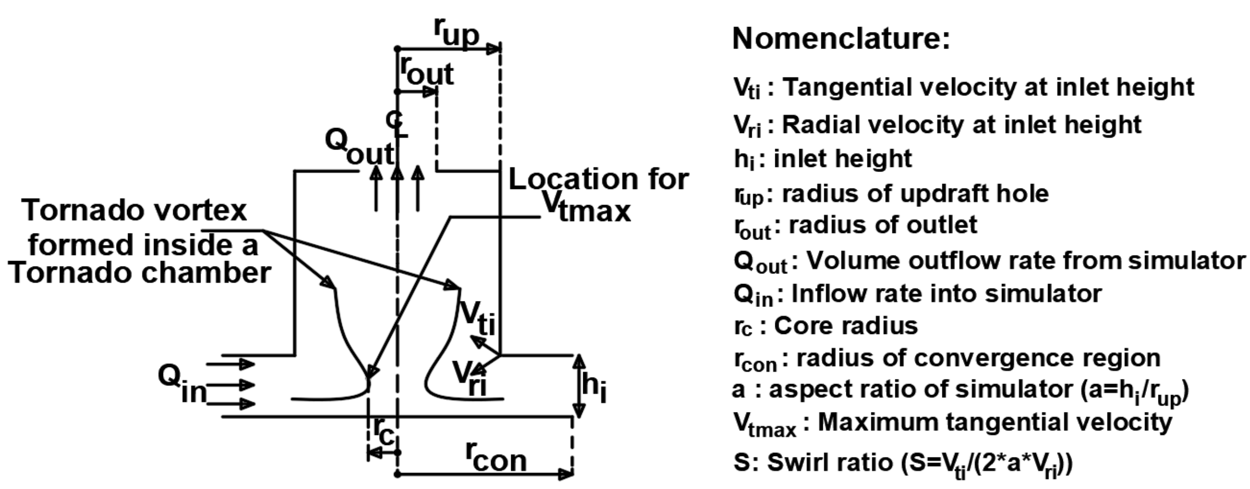

Figure 1. Graphical representation of notations used to describe geometry and tornado flow in a tornado chamber

* Lead presenter

2. RESULTS

Tornado chambers around the world have differences in geometry and tornado flow generation mechanism. However, identifying the macroscale flow similarities such as the manner in which flow enters, progresses and exits via outlet, tornado chambers can be broadly categorized into 5 major types, viz. (a) Side Opening System (SOS) (b) Top Full Opening System (TFOS) (c) Top Partial Opening System (TPOS) (d) ISU and (e) WindEEE. In Table 1, the value of S_T of different TCs is documented along with ratio of outlet to updraft section whereas in Table 2, the total computation time required for tornado chambers with different S_T is documented.

Table 1. Documentation of touchdown swirl ratio in different tornado chambers using consistent definition of 'S'

S.N.	Tornado Chamber	References	r_{out}/r_{up}	Outlet Condition	S_T
1	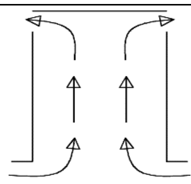	a) Tang et al. (2018) - EXP b) Verma and Selvam (2020) - CFD c) Harlow and Stein (1974) – CFD	a) 0.18 b) 0.18 c) 0.22	SOS	a) 0.22-0.36 b) 0.22-0.36 c) 0.29
2	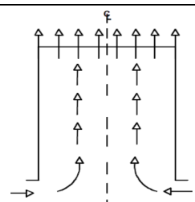	a) Verma and Selvam (C) - CFD b) Rotunno (1977) - CFD c) Verma and Selvam (2021) - CFD d) Ward (1972) - EXP e) Kashefizadeh et al. (2019) –CFD	a) 1 b) 1 c) 1 d) 1 e) 1	TFOS	a) 0.30 b) ≈0.40 c) 0.45 d) 0.48 e) 0.50
3	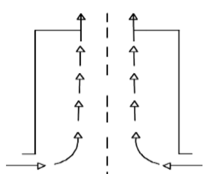	a) Church et al. (1977) – EXP b) Verma and Selvam (C)-CFD c) Gillmeier (2019) - EXP d) Verma and Selvam (C) - CFD e) Liu and Ishihara (2015) – CFD	a) 0.89 b) 0.75 c) ≈ 0.32 d) 0.50 e) 0.67	TPOS	a) 0.34 b) 0.45 c) 0.50-0.69 d) 0.60 e) 4.42
4	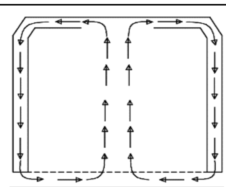	a) Yuan et al. (2019) - CFD b) Haan et al. (2008) – EXP	a) 0.376 b) 0.375	ISU	a) 1.46 b) 2.23
5	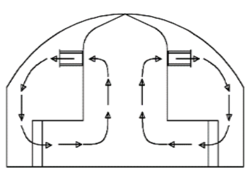	a) Karami et al. (2019)- EXP ; Refan and Hangan (2018) – EXP	a) 0.064-0.18	WindEEE	a) 1.96

*Note:- In 3rd column, 'C' indicates CFD simulation from current work; EXP: Experimental; CFD : CFD simulation

Table 2. Comparison of total computation (CPU) time of Tornado Chambers with different S_T

S.N.	Tornado chamber	S_T	Total Grid points & simulation type	Total computation time (minutes)
1	SOS (a = 1.0)	0.22	75 x 75 x 70 (Transient)	460
2	TFOS (r_{out}/r_{up} = 1.00)	0.40	75 x 75 x 70 (Transient)	2136
3	TPOS (r_{out}/r_{up} = 0.75)	0.45	75 x 75 x 70 (Transient)	3655
4	TPOS (r_{out}/r_{up} = 0.50)	0.60	75 x 75 x 70 (Transient)	6778

In Table 2, the aspect ratio of SOS type chamber is used rather than r_{out}/r_{up} (= 0.18 from Table 1) ratio because the reported value of $S_T = 0.22$ corresponds to configuration of tornado chamber at aspect ratio of unity. For the same tornado chamber but with aspect ratio of 0.5, touchdown was observed at 0.36. As aspect ratio of tornado chamber can influence the value of S_T, the aspect ratio of the reported case is explicitly stated for SOS in Table 2. Besides, the total number of grid points used to discretize the computational domain is stated in 4th column of Table 2 and all the simulation work in Table 2 are transient calculations.

3. CONCLUSIONS

Using a single consistent definition of swirl ratio, the touchdown swirl ratio of different TCs are compared. Different flow structures of tornado vortices exist in different tornado chambers at similar swirl ratio as each tornado chamber has different value of S_T (Refer Table 1). Due to differences in flow structure of tornado vortices from different tornado chambers, tornado forces and pressures on buildings are also likely to differ from one tornado chamber to another. This is due to the fact that different flow structures of tornado vortices have different wind profiles and pressure distribution and thus their interaction with buildings is likely to produce different impacts resulting in different force and pressure coefficients. Similarly, it can be observed from Table 2 that the TCs that have higher S_T takes longer computation time for completion of simulation, so, the TC with comparatively low values of S_T are more efficient than those with higher S_T. From Table 2, it is concluded that the tornado chambers with side openings (SOS type TCs) are more efficient in producing a stationary touched-down tornado vortex than others.

ACKNOWLEDGEMENTS

The authors acknowledge the support received from National Science Foundation (NSF) under award number CMMI-1762999.

REFERENCES

Church, C.R.., Snow, J.T. and Agee, E.M., 1977. Tornado Vortex Simulation at Purdue University, Bulletin American Meteorological Society, 58, 900-909.

Gillmeier, S., 2019. An investigation concerning the simulation of tornado-like vortices, PhD dissertation, University of Birmingham.

Haan, F.L., Sarkar, P.P and Gallus, W.A. 2008. Design, construction and performance of a large tornado simulator for wind engineering applications, Engineering Structures, 30, 1146-1159.

Harlow, F.H., and Stein L.R., 1974. Structural Analysis of Tornado-like Vortices, Journal of Atmospheric Sciences, 31, 2081-2098.

Karami, M., Hangan, H., Carassale, L. and Peerhossaini, H., 2019. Coherent structures in tornado-like vortices, Physics of Fluids 31, 085118.

Kashefizadeh, M.H., Verma, S. and Selvam, R.P., 2019. Computer modelling of close-to-ground tornado wind-fields for different tornado widths, Journal of Wind Engineering & Industrial Aerodynamics, 191, 32-40.

Liu, Z. and Ishihara, T., 2015. A study of tornado induced mean aerodynamic forces on a gable-roofed building by the large eddy simulations, Journal of Wind Engineering & Industrial Aerodynamics, 146, 39-50.

Refan, M. and Hangan, H., 2018. Near surface experimental exploration of tornado vortices, Journal of Wind Engineering & Industrial Aerodynamics., 175, 120-135.

Rotunno, R.. 1977, Numerical simulation of a laboratory Vortex, Journal of Atmospheric Sciences., 34, 1942–1956.

Tang, Z., Feng, C., Wu, L., Zuo, D. and James, D.L. 2018. Characteristics of tornado-like vortices simulated in a large scale ward type simulator, Boundary-Layer Meteorology, 166, 327-350. Ward N.B. (1972), The exploration of certain features of tornado dynamics using a laboratory model, Journal of Atmospheric Sciences, 29, 1194-1204.

Verma, S. and Selvam, R.P., 2020. CFD to VorTECH pressure field comparison & roughness effect on flow, Journal of Structural Engineering, 146, 04020187-1 to 12.

Verma, S. and Selvam, R.P., 2021. Effect of height of the tornado chamber on vortex touchdown, In: Rushi Kumar B., Sivaraj R., Prakash J. (eds) Advances in Fluid Dynamics. Lecture Notes in Mechanical Engineering. Springer, Singapore.

Yuan, F., Yan, G. and Honerkamp, R. 2019. Numerical simulation of laboratory tornado simulator that can produce translating tornao-like wind flow, Journal of Wind Engineering & Industrial Aerodynamics, 190, 200-217.

Large-eddy simulations of combined wind and buoyancy driven ventilation in a slum house in Dhaka, Bangladesh

Yunjae Hwang [a*], Catherine Gorle [b]

[a]*Stanford University, Stanford, CA, US, yunjaeh@stanford.edu*
[b]*Stanford University, Stanford, CA, US, gorle@stanford.edu*

ABSTRACT:
A previous study in Bangladesh indicated that there might be an association between the incidence of childhood pneumonia and ventilation in low-income houses. To support further investigation of this relationship, our study aims to establish a validated computational framework that can accurately estimate household ventilation rates. To achieve this objective, high-fidelity large-eddy simulations are performed under various weather conditions, and the simulation results are validated against field measurements of the ventilation rate and temperatures.

Keywords: Natural ventilation, Computational Fluid Dynamics(CFD), Large Eddy Simulation(LES)

1. INTRODUCTION

Pneumonia is the leading cause of death in children under five, accounting for one-sixth of total mortality in this age group (Unicef, 2016). In Bangladesh, one of the top 15 countries accounting for 70% of total pneumonia deaths, a preliminary study indicated that there might be an association between the occurrence of the respiratory disease and ventilation status in a low-income house: "households where pneumonia occurred were 28% less likely to be cross-ventilated." (Ram, et al. 2014) Our study aims to establish a validated computational framework to precisely estimate ventilation rates and to support the further investigation of the relationship. We perform high-fidelity computational fluid dynamics (CFD) simulations to accurately quantify ventilation rates driven by buoyancy and turbulent wind in urban settings. The simulations are conducted for two different thermal boundary conditions, representing either day or night, as well as two cross-ventilation layouts with different sized openings, to investigate a variety of temperature patterns and ventilation scenarios. The results of these computationally demanding large-eddy simulations (LES) are validated against field measurements of the ventilation rate and indoor temperatures, and analyzed to identify robust ventilation solutions that will work under a variety of weather and housing conditions.

Figure 1. Configuration of the target house (left), bird-eye view of the urban-slum area (center), and the computational representation of the buildings in the area (right)

* Lead presenter

2. TARGET HOUSE AND MEASUREMENT

We rented a representative single-room house in one of the urban slums in Dhaka, where Figure 1 depicts the detailed floor plan of the house and the slum neighborhood. In the target house, we measured indoor air and wall surface temperatures, as well as ventilation rates in terms of air changes per hour (ACH) using a tracer concentration decay technique. In addition to these indoor measurements, we collected outdoor air temperature, and free-stream wind speed and direction data at the tallest building in the slum area. The measured data at both locations are used either to define boundary conditions for our simulations or to validate the simulation results.

3. COMPUTATIONAL FLUID DYNAMICS SIMULATION

Our LES simulations are performed using CharLES, a commercial CFD package developed by Cascade Technologies, Inc. LES solves the filtered Navier-Stokes equation; the subgrid scale motions are modeled with the Vreman model. Considering the small temperature variation in our simulations, the Boussinesq approximation is adopted to incorporate buoyancy effects. As our region of interest is the indoor environment and the vicinity of the target house, the geometries close to the house are precisely represented, while more remote buildings are modeled as rectangular blocks. For the turbulent wind inflow condition, we employ a gradient-base optimization technique coupled with a digital filter method to achieve the target turbulence characteristics at the location of the house (Lamberti, et al. 2018). To reproduce the buoyancy effects, constant temperature boundary conditions are specified at the inlet and at the walls of the target house, using the measured outdoor and wall surface temperatures. Figure 2 shows the significant variability in the indoor flow and temperature patterns obtained for the different ventilation scenarios under different wind and temperature boundary conditions; this variability translates into ACH values ranging from 6.7 to 24.0. Future research aims to further characterizing the ventilation rate variability, such that it can accounted for when analysing the relationship between health outcomes and ventilation rate measurements, which provide a single data point.

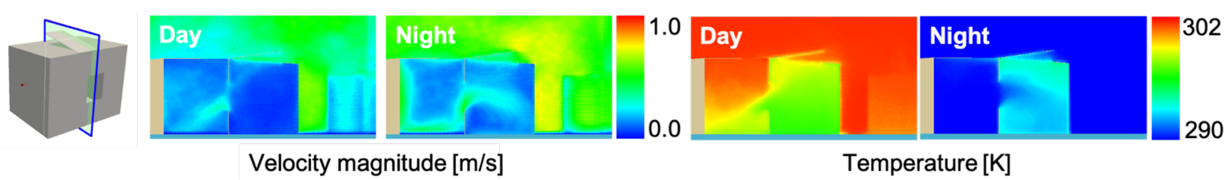

Figure 2. Comparison of velocity and temperature patterns between two simulations with different temperature boundary conditions

ACKNOWLEDGEMENTS

This research is supported by an Environmental Venture Projects Grant from the Stanford Woods Institute for the Environment.

REFERENCES

Lamberti, G., García-Sánchez, C., Sousa, J. and Gorlé, C., 2018. Optimizing turbulent inflow conditions for large-eddy simulations of the atmospheric boundary layer. Journal of Wind Engineering and Industrial Aerodynamics, 177, pp.32-44.

Ram, P., Dutt, D., Silk, B., Doshi, S., Rudra, C., Abedin, J., Goswami, D., Fry, A., Brooks, W., Luby, S. and Cohen, A., 2014. Household air quality risk factors associated with childhood pneumonia in urban Dhaka, Bangladesh. The American journal of tropical medicine and hygiene, 90(5), pp.968-975.

Unicef, 2016. One is too many: ending child deaths from pneumonia and diarrhoea. New York: UNICEF

Critical Evaluation of Roof Pressure Statistics over an Isolated Low-rise Building using NIST and TPU Aerodynamic Databases

Erick Shelley *, Erin Hubbard, Wei Zhang

Mechanical Engineering, Cleveland State University, Cleveland, Ohio, U.S.,
erick.shelley@gmail.com, erin.p.hubbard@nasa.gov, w.zhang13@csuohio.edu

ABSTRACT:
Roof pressure statistics, as the foundation of the ASCE wind-loading design provision, are usually obtained from boundary-layer (BL) wind-tunnel tests. However, a long-standing issue has been acknowledged -- the inconsistency of results reported from different BL wind tunnels. Note that, these BL wind-tunnel tests tend to follow the standard set-up, use established instrument and equipment to measure flow and pressure over scaled-down building models, and process the data with common methodology. What are dominant factors that cause the non-negligible differences in the reported pressure statistics? Considering the wind-tunnel data's increasing role in serving as the reference cases for CFD tool validation, it is imperative to critically evaluate existing wind-tunnel pressure data and seek insights into this outstanding issue of the wind engineering community. This work will focus on time-series of roof pressure data of selected cases for the isolated low-rise building model subjected to simulated BL inflows archived in the NIST and TPU aerodynamic databases. Results include histogram of the instantaneous pressure, mean and RMS surface pressures, and peak pressure estimated by the Gumbel model in terms of the pressure tap location over the roof and the wind directions. We hope to identify the dominant factors in the wind-tunnel tests that cause differences in the results and help address this issue.

Keywords: Wind-tunnel tests, data inconsistency, NIST aerodynamic database, TPU aerodynamic database

1. INTRODUCTION

Wind-tunnel tests create a controlled, desirable, simulated boundary-layer flow condition and scaled building models are used to reproduce the wind structure interaction that is of interest. For wind load tests, primary measurement quantities include local surface pressure and/or overall forces and moments, as well as the inflow properties (wind speed profiles, turbulence level and spectrum) that a model is subjected to. Boundary-layer wind tunnel tests have advanced the wind loading design in an enormous way. However, the inconsistency among wind-tunnel test results has been a long-standing issue recognized by the wind engineering community. For example, the variability of wind pressure data from six well-known wind tunnel laboratories were compared, yielding a coefficient of variation in the results ranging from 10 to 40% (Fritz et al, 2008).

The discrepancies of wind-tunnel results can be attributed to multiple aspects in wind load measurements and estimation. A wind tunnel could be limited by the capability to realize the full-spectra of the ABL wind (cut-off large and small scales of turbulent structures due to the physical size and missing roughness details), relatively low Re-number range and uncertainties associated with a particular piece of equipment. In terms of the low-rise building models, the ratio of height to the boundary layer aerodynamic roughness (H/z_0 Jensen number) is very challenging to be practical. Architecture features and surface textures are difficult to model, which may considerably affect the flow separation, reattachment and vortex development that are key to the surface

* Lead presenter

pressure.

This work will seek the dominant factors that cause the non-negligible differences in the wind-tunnel pressure statistics, by evaluating time-series of roof pressure data of comparable cases for an isolated low-rise building model archived in the NIST and TPU aerodynamic databases. The NIST aerodynamic database collected by the University of Western Ontario (UWO) includes time series of surface pressures over low-rise building of various geometry and inflow conditions in boundary-layer wind tunnels along with the metadata. The quantities of interest include the histogram of instantaneous pressure, mean, RMS and peak pressures over the model low-rise building from the UWO and TPU wind-tunnel data. The results are expected to reveal how similarities/differences between these two public databases and identify which factors may play significant roles in causing the differences. Associated with this comparison, uncertainty quantification is being conducted in another work.

2. METHODOLOGY

2.1. Low-rise Building Model, Inflow Conditions and Terrain Exposure

Several publications documented the comprehensive wind-tunnel study of pressure distribution on variations of building model scale, wind directions, leakage condition and terrain type (Ho 2005). An isolated low-rise building of a nearly-flat roof (1:100 scaled, 1:12 roof pitch, no leakage model) is selected as the target building model. Only test cases for a suburban terrain of roughness length of zo = 0.3 m will be considered, to enable the comparison with that in the TPU database. We will summarize the characterization of the inflow conditions in terms of mean wind profiles (power-law or log-law formulation), turbulence intensity profiles, boundary-layer description. Wind direction is one of the key parameters to determine the flow development and pressure distribution. We will focus on the normal wind direction of 270° (90° equivalent) and two oblique wind directions of 315° (45° equivalent) and 325° (35° equivalent).

2.2. Methodology to Process Pressure Statistics

Wind pressure studies often focus on mean, root-mean-square (RMS), and peak values of the pressure coefficients. While computation of mean and RMS pressures using the sampled time-series of pressure is standard, variations in the methods to estimate the peak pressure coefficient and its interpretation are reported in Peng et al. (2014). There are two approaches to process the pressure data: (1) determining a single peak value or the mean of several observed maximum from peaks recorded in the sample (observed peak method); (2) Gumbel method (Cook and Mayne, 1980; Ho et al. 2005). The Gumbel model appears to maintain accuracy and precision regardless Gaussian or non-Gaussian data (Peng et al. 2014). Moreover, the TPU aerodynamic database includes pressure coefficients obtained by the Gumbel method, which is to be used to process the data in the NIST database to ensure a meaningful comparison.

3. RESULTS AND DISCUSSION

Results will be presented in the following aspects: 1) BL inflow characteristics; 2) histogram of C_p of the sampled periods at selected locations for a specific wind direction; 3) Contour map of the mean C_p (as shown in Fig. 1), RMS C_p and peak C_p for a wind direction. 4) Comparison the results of the NIST database with that from the TPU aerodynamic database.

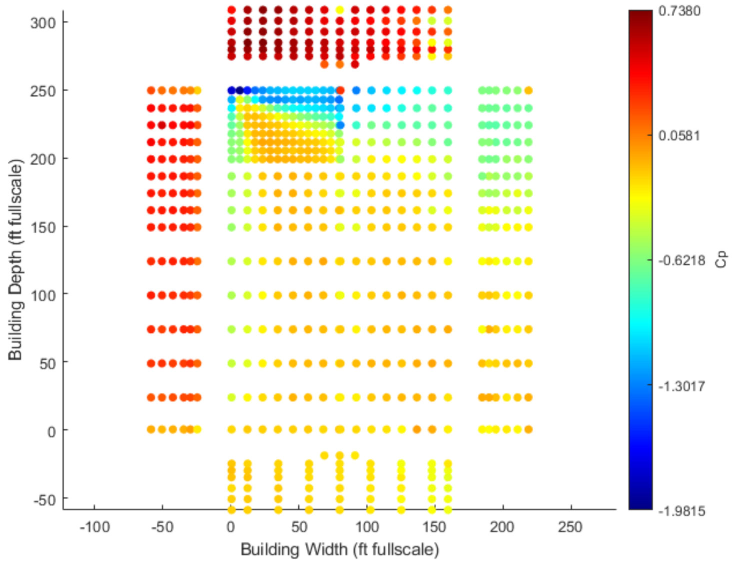

Figure 1. Mean pressure coefficient (C_p) over a low-rise building model at the pressure tap locations (no leakage, suburban terrain conditions and wind direction of 45°).

4. CONCLUSIONS AND OUTLOOK

Boundary-layer wind tunnel tests have significantly advanced the wind loading design of the built environment, however, the inconsistency among wind-tunnel results has been a long-standing issue. This work critically evaluates time-series of roof pressure data for an isolated low-rise building model archived in the public NIST and TPU aerodynamic databases. We hope to identify the dominant factors that cause differences in the results and help address this issue.

ACKNOWLEDGEMENTS

E. Shelley acknowledges the support of the Ohio Space Grant Consortium (OSGC) university internship. E. Hubbard acknowledges the generous support of the OSGC Master's Fellowship. W. Zhang acknowledges the NSF CAREER grant (Award# 1944776) and the OSGC Faculty Research Initiation Grant Project (FRIGP).

REFERENCES

Cook, N.J., and Mayne, J.R., 1980. A Refined Working Approach to the Assessment of Wind Loads for Equivalent Static Design. Journal of Wind Engineering and Industrial Aerodynamics, vol. 6, pp. 125-137, 1980.

Fritz, W.P., Bienkiewicz, B., Cui, B., Flamand, O., Ho, T.C.E., Kikitsu, H. Letchford, C.W., and Simiu, E., 2008. International Comparison of Wind Tunnel Estimates of Wind Effects on Low-Rise Buildings: Test-Related Uncertainties. Journal of Structural Engineering, ASCE 134(12): 1887-1890.

Ho, T.C.E., Surry, D., Morrish, D., and Kopp, G.A., 2005. The UWO Contribution to the NIST Aerodynamic Database for Wind Loads on Low Buildings: Part 1. Archiving Format and Basic Aerodynamic Data. Journal of Wind Engineering and Industrial Aerodynamics, 93(1):1-30.

Kumar, K.S., and Stathopoulos, T., 2000. Wind Loads on Low Building Roofs: A Stochastic Perspective. Journal of Structural Engineering, ASCE 126(8): 944-956.

Peng, X., Yang, L., Gavanski, E., Gurley, K., and Prevatt, D., 2014. A Comparison of Methods to Estimate Peak Wind Loads on Buildings. Journal of Wind Engineering and Industrial Aerodynamics, 126(2014):11-23.

A probabilistic composite resistance model for the vertical load path in typical residential construction

Brandon M. Rittelmeyer [a,*], David B. Roueche [b]

[a]Auburn University, Auburn, Alabama, United States, bmr0036@auburn.edu
[b]Auburn University, Auburn, Alabama, United States, dbroueche@auburn.edu

ABSTRACT:
Past failure risk studies of uplift resistance in wood-frame residential construction have tended to focus on a few key connections in isolation. Proposed here is a probabilistic modeling framework for evaluating uplift resistance in residential structures that (1) considers both the obvious connections and many of the less obvious connections in the vertical load path and (2) accounts for composite resistance of parallel elements in the load path. Connection capacities are based on applicable design provisions and cumulative dead load. Formulating connection capacity in units of force per unit length of wall permits direct comparison of relative connection strengths. System resistance is evaluated by Monte Carlo simulation using a weakest-link failure criterion, providing a way to assess the overall impact of different connection configurations.

Keywords: failure risk analysis, residential construction, uplift capacity, vertical load path

1. INTRODUCTION

Probabilistic modeling of the resistance of wood-frame residential structures to wind uplift forces has been the subject of many failure risk studies (Ellingwood et al, 2004; Masoomi et al, 2018; Standohar-Alfano et al, 2017). Often such analyses have focused on a few critical links in the vertical load path, such as the roof-to-wall connection. The present study proposes a more comprehensive modeling paradigm for the vertical load path that seeks to (1) represent both the primary and secondary connections and (2) approximate the composite resistance of parallel structural elements in the load path. For instance, nailed connections between the wall framing members act in series, but wall sheathing connections act parallel to the framing connections in a way that strengthens the wall system overall. A typical, single-story, exterior-wall load path observed during damage surveys conducted after the March 3, 2020 Nashville-Cookeville tornado is taken as a test case to illustrate the modeling framework, consisting of hurricane-clip roof-to-wall connections, fully-sheathed stud walls, and unreinforced masonry stem wall foundations.

2. COMPOSITE RESISTANCE MODEL

The connections considered in the illustrative model are noted on the left-hand side of Fig. 1. Following IRC 2012 prescriptions for connection design in non-high-wind regions, mean uplift capacities (in lb/ft. of wall) are computed from applicable design criteria for wood and masonry connections; design capacity variances are either conservatively assigned or drawn from published work where available. Total uplift capacity is the sum of the connection design capacity and the normally-distributed cumulative dead load. Depicting uplift capacities as in the left-hand plot in Fig. 1 affords direct visual comparison of the relatively strong and weak links in the load path.

* Lead presenter

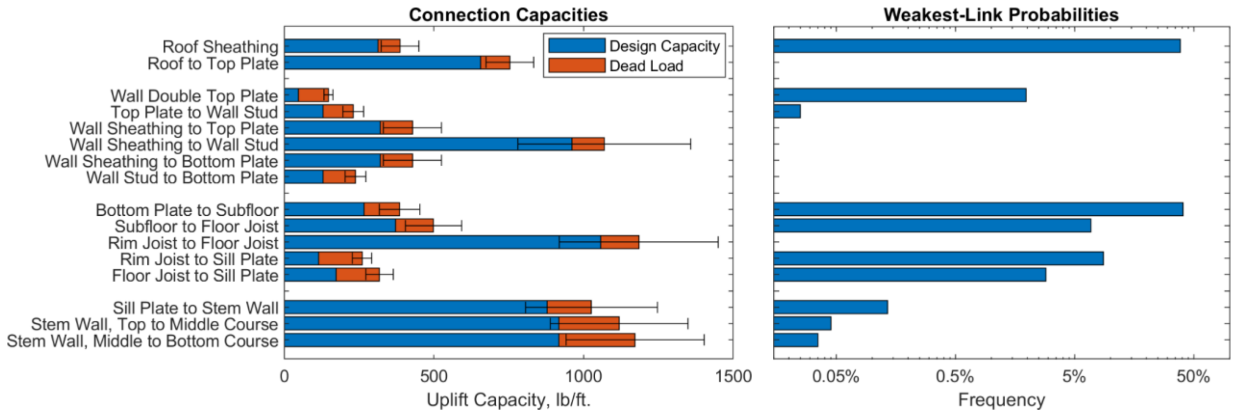

Figure 1. (L) Estimated mean uplift capacities for the connections in the vertical load path, visualizing the contribution of dead load at each point; error bars represent ±1 standard deviation. [Note: 1 lb/ft. = 14.59 N/m.] (R) Monte Carlo simulation results indicating how frequently each connection is found to be the weakest link in the system; frequency is plotted on a logarithmic scale for clarity.

The overall resistance of the load path is evaluated by Monte Carlo simulation, where system failure is based on failure of the weakest connection in series (i.e. capacities of parallel elements are summed to form a load chain composed only of connections in series). Simulation output takes the form of the right-hand plot in Fig. 1, which gives the results of a 20,000-run simulation of the system given the connection capacities plotted in Fig. 1. The “weakest-link probability” corresponds to the frequency with which each connection is the weakest in the series and thus triggers system failure; because the model aims to capture the composite behavior of parallel elements, the weakest link is not necessarily the connection with the least individual capacity.

3. CONCLUSIONS

By taking a higher-resolution view of the vertical load path, the composite-resistance modeling framework described here can be used to examine the relative strengths of connections in realistic vertical load paths and to explain why failure is far more likely to initiate at some points than at others. By providing a way to evaluate the impact of different connection configurations or retrofits to the overall system resistance, it can also be used to demonstrate why focusing attention on a single connection (e.g., hurricane clip) may not have a substantial effect on the system capacity.

ACKNOWLEDGMENTS

This work is supported by the National Science Foundation under Grant No. CMMI-1944149. Any opinions, findings, and conclusions expressed in this material are those of the authors and do not necessarily reflect the views of the National Science Foundation.

REFERENCES

Ellingwood, B., Rosowsky, D., Li, Y., and Kim, J., 2004. Fragility assessment of light-frame wood construction subjected to wind and earthquake hazards. Journal of Structural Engineering, ASCE 130, 1921-1930.

Masoomi, H., Ameri, M., and van de Lindt, J., 2018. Wind performance enhancement strategies for residential wood-frame buildings. Journal of Performance of Constructed Facilities, ASCE 32, 04018024.

Standohar-Alfano, C., van de Lindt, J., and Ellingwood, B., 2017. Vertical load path failure risk analysis of residential wood-frame construction in tornadoes. Journal of Structural Engineering, ASCE 143, 04017045.

Detection and classification of damages to civil infrastructure using a video-monitoring tool

Michael L. Whiteman [a], Pedro L. Fernández-Cabán [b], Claudia C. Marin [c,*], Jale Tezcan [d], Xinxing Wu [e], Qiang (Shawn) Cheng [f]

[a]*Howard University, Washington DC, DC, USA,* michael.whiteman@howard.edu
[b]*Clarkson University, Potsdam, NY, USA,* pfernand@clarkson.edu
[c]*Howard University, Washington DC, DC, USA,* cmarin@howard.edu
[d]*Southern Illinois University, Carbondale, IL, USA,* jale@siu.edu
[e]*University of Kentucky, Lexington, KY, USA,* xinxingwu@uky.edu
[f]*University of Kentucky, Lexington, KY, USA,* qiang.cheng@uky.edu

ABSTRACT
This study seeks to integrate recent advances in machine learning and pattern recognition disciplines with physics-based reasoning to develop a novel, accurate, field-calibrated computational platform for in-situ monitoring and damage detection of civil infrastructure under service loading and wind loading. Physics-informed machine learning models are developed to detect the existence, location, and severity of damage using video recordings of in-service structures. The procedure enables non-contact, full-field measurement of structural response with a high spatiotemporal resolution, enabling cost-effective monitoring of structures for which traditional sensor-based structural health monitoring technologies are often cost-prohibitive or impractical to implement. Proof-of-concept was demonstrated using available experimental data. Future studies will use the video-monitoring tool to monitor wind-loaded structures which are impractical for traditional sensor-based technologies.

Keywords: structural health monitoring; machine learning; civil engineering infrastructure;

1. INTRODUCTION

The most recent Infrastructure Report Card released by the American Society of Engineers in 2021 ranks the overall condition of the United States infrastructure as C-, with some categories scoring as low as D- and no category considered to be meeting capacity needs for the future (ASCE, 2021). The investment required to earn a grade indicating good to excellent condition for each infrastructure category has increased from \$2.1 trillion in 2017 (ASCE, 2017) to nearly \$2.59 trillion. Failure to address these infrastructure inadequacies will ultimately make utilities unreliable, increase the cost to manufacture and distribute goods, and lead to significant job loss. Reliable methods for evaluating structural health are critical in streamlining the decision-making process by classifying appropriate courses of action regarding maintenance, retrofit, or replacement, and prioritize decision-making and inform budget allocation.

Traditional sensor-based structural health monitoring techniques are often cost-prohibitive and impractical to implement for many classes of structures, including temporary structures, transmission towers, communication towers, residential and commercial buildings, and industrial chimneys. Practical applications of existing vibration-based damage detection methods have been limited due to the difficulty of accurately modeling real structures given uncertainties in material properties, support conditions, and variations in environmental and operational conditions. Additionally, the computational expense required makes traditional techniques impractical for real-time monitoring of civil engineering infrastructure.

2. BACKGROUND

Failure of many civil infrastructure structures (e.g., cantilevered light support structures) can often be attributed to fatigue. Sources most likely to induce vibration of high-mast luminaire structures have been identified, including buffeting winds, vortex-shedding, and truck-induced wind gusts (Chang et al., 2014; Giosan and Eng, 2013; Krauthammer, 1987; Zuo and Letchford, 2008). Buffeting winds tend to create vibrations in the along-wind direction, while vortex-shedding and truck-induced wind gusts create vibrations in the across-wind direction. Recent studies have shown that damage to high mast luminaire structures is mostly due to structural fatigue – long-term wind-induced vibrations accumulate fatigue damages and can ultimately result in cracking at high stress locations (Dexter, 2002; Phares et al., 2007). Examples of recent reports of failure and cracking of high mast luminaire structures include more than 20 lighting poles in Iowa in 2003 (Chang et al., 2009) and approximately 140 aluminum lighting poles in Illinois in 2003 (Caracoglia and Jones, 2004). In both instances, special inspections were prompted due to unexpected failure during a winter storm.

3. VIDEO MONITORING FRAMEWORK

In the absence of affordable, practical techniques, this study proposes a non-contact, non-destructive, fast, and cost-effective damage detection and load monitoring tool using video recording footage obtained by monitoring cameras. This tool can be used to detect the existence, location, and severity of damage, where damage is broadly defined as a change in the geometric or material properties adversely affecting the system's performance. Damage can occur as a result of instantaneous loading (e.g., impact, blast, or seismic loads), or as the result of cyclic loading (e.g., fatigue-induced cracking due to wind-induced or traffic-induced vibrations). Continuous monitoring enables the identification of changes in dynamic behavior (i.e., damage) and need for an appropriate inspection to be held.

Modern computer vision and video tracking techniques will be implemented to identify key feature points and extract corresponding displacements from video recordings. Different sized motions can be tracked, and damage features (e.g., strain-rotation relationships or varying instant effective stiffnesses) can be extracted. A novel implementation of Blind Source Separation based on Independent Component Analysis will be used to extract statistically independent components.

4. PROOF-OF-CONCEPT DEVELOPMENT

Existing experimental data from a five-story, full-scale building subject to applied seismic excitation is explored to demonstrate proof-of-concept. The points in red in Figure 1a are associated with instrument EL01E42 (M. C. Chen et al., 2016) for capturing relative displacement. The relative displacements for the red points of the beam in Figure 1a were extracted using video analysis for testing under Denali 100%. These displacements are then scaled considering the reference distance (21 in) of the instrumentation. Figure 1b shows the comparison of scaled video and experimental measurements. The relative displacement from the video reproduces the experimental measurements relatively well with slight differences in the trend and peak values. These differences could be attributed to the lack of correction for the shaking of the camera's support, or the lack of the depth to calculate the displacements between the two three-dimensional points with the video-measured two-dimensional data.

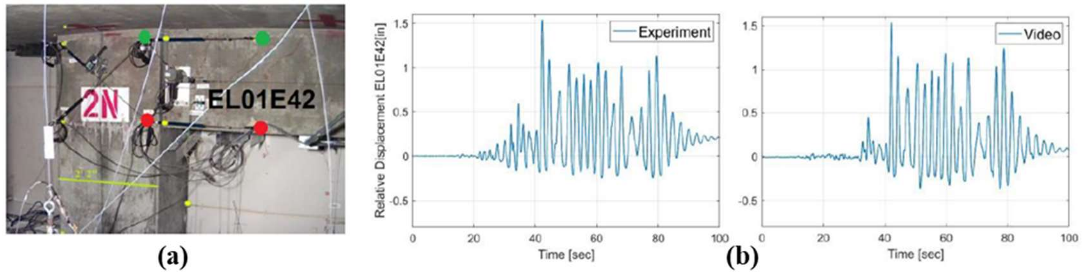

Figure 1. Beam in fixed base experiment under Denali 100%, tracking points for EL01E42 in red.

Multiple structures subject to wind loading will be monitored using the video-monitoring tool for a period of months to obtain field-data, including tall, slender high-mast luminaires, industrial masonry chimneys, and traffic and pedestrian bridges. These structures are depicted in Figure 2.

(a) (b) (c)

Figure 2. Structures for field monitoring: (a) High-mast luminaire; (b) Masonry chimney; (c) Pedestrian bridge.

These structures will be instrumented with accelerometers and crack monitoring devices to validate the video monitoring tool's accuracy of defect detection. The anticipated defects to be observed include the development and propagation of cracks and fatigue due to cyclic loading as summarized in Table 1. Monitoring these structures will provide a better understanding of their dynamic properties (e.g., natural frequencies and mode shapes) and behavior under service and extreme wind loading conditions.

Table 1. Summary of planned field-monitored structures.

Structure	Measurements Taken	Anticipated Defects
High-mast luminaire	Accelerations	Fatigue
Masonry chimney	Accelerations, crack lengths	Fatigue, crack propagation
Pedestrian bridge	Accelerations	Fatigue

ACKNOWLEDGEMENTS

This material is based upon work supported by the National Science Foundation (NSF) under Grant No. 2040665. Any opinions, findings, and conclusions or recommendations expressed in this material are those of the authors and do not necessarily reflect the views of NSF.

REFERENCES

American Society of Civil Engineers (ASCE), “A Comprehensive Assessment of America’s Infrastructure – Executive Summary”, 2017, [Online]. Available: https://infrastructurereportcard.org/wp-content/uploads/2017/04/2017-IRC-Executive-Summary-FINAL-FINAL.pdf

American Society of Civil Engineers (ASCE), “A Comprehensive Assessment of America’s Infrastructure – Executive Summary”, 2021, [Online]. Available: https://infrastructurereportcard.org/wp-content/uploads/2020/12/2021-IRC-Executive-Summary.pdf

Caracoglia, L., & Jones, N. (2004). Analysis of light pole failures in Illinois. Final report. Civil Engineering Studies, Structural Research Series, (635).

Chang, B., Neill, M., Issa, R., & Miller, A. (2014). Development of wind vortex shedding coefficients for a multisided cylinder structure. Wind and Structures, 18(2), 181-194.

Chang, B., Phares, B. M., Sarkar, P. P., & Wipf, T. J. (2009). Development of a procedure for fatigue design of slender support structures subjected to wind-induced vibration. Transportation research record, 2131(1), 23-33.

Dexter, R. J. (2002). Fatigue-resistant design of cantilevered signal, sign, and light supports (Vol. 469). Transportation Research Board.

Giosan, I., & Eng, P. (2013). Vortex shedding induced loads on free standing structures. Structural Vortex Shedding Response Estimation Methodology and Finite Element Simulation, 42.

Krauthammer, T. (1987). A numerical study of wind-induced tower vibrations. Computers & Structures, 26(1-2), 233-241.

M. C. Chen *et al.*, “Full-scale structural and nonstructural building system performance during earthquakes: Part I - Specimen description, test protocol, and structural response,” *Earthq. Spectra*, vol. 32, no. 2, pp. 737–770, 2016, doi: 10.1193/012414EQS016M.

Phares, B. M., Sarkar, P. P., Wipf, T. J., & Chang, B. (2007). Development of fatigue design procedures for slender, tapered support structures for highway signs, luminaries, and traffic signals subjected to wind-induced excitation from vortex shedding and buffeting (No. MTC Project 2005-2).

Zuo, D., & Letchford, C. (2008). Investigation of wind-induced highway lighting pole vibration using full-scale measurement (No. FHWA/TX-08-0-4586-5).

Aerodynamic testing and response evaluation of a large-scale high-rise building model at a high Reynolds number

Aly Mousaad Aly [a], Suvash Chapain [b, *]

[a] *WISE Research Lab, Louisiana State University, Baton Rouge, LA, USA, aly@lsu.edu*
[b] *WISE Research Lab, Louisiana State University, Baton Rouge, LA, USA, schapa3@lsu.edu*

ABSTRACT
In this paper, experimental investigations of a large-scale (1:50) high-rise building model are performed at a high Reynolds number (~21 million), to evaluate the wind loads and the corresponding structural responses. A total of 256 pressure taps are mapped on all sides of the building model, to determine dimensionless pressure coefficients on the surfaces. Wind loads at each floor are evaluated using the pressure integration technique. The dynamic properties of the full-scale building are obtained from a finite element model in ANSYS. The wind-induced responses are calculated by applying wind loads on an equivalent lumped mass model of the building derived from the finite element model. Excessive vibration occurred in the cross-wind direction that exceeds the serviceability requirements. To attenuate these vibrations, a pendulum pounding tuned mass damper (PTMD) based on Hertz contact law is proposed.

Keywords: High-rise buildings; Open-Jet; Large-scale testing; Wind loads

1. WIND LOADS ON TALL BUILDINGS

High-rise buildings are wind-sensitive structures, and usually, the lateral wind loads are a governing design factor. The pattern of wind flow around a building is distorted by the mean flow, flow separation, vortices formation, and wake development. These effects result in aerodynamic pressure on the structural system which imposes intense fluctuating forces on the facade and hence transferred to the main force resisting system with a potential to excite the whole building in the rectilinear directions and torsion. Crosswind responses can be significant for slender structures with low damping. Crosswind excitations are usually associated with "vortex shedding". A high crosswind response can be induced if the vortex shedding frequency resonates with the natural frequency of the structure. Wind tunnel testing is fundamental for the accurate estimation of wind effects on tall buildings (Mendis et al., 2007).

1.1. Open-Jet Testing

Wind-tunnel tests are generally carried out in a turbulent flow on scaled models of the structure at relatively low Reynolds numbers, compared to the actual Reynolds numbers of the prototype structure. The choice of testing at a low Reynolds number is related to cost consideration and the limited availability of large wind tunnels. In this study, aerodynamic testing is performed in the modern open -jet facility at the Windstorm Impact, Science and Engineering (WISE) laboratory, Louisiana State University (LSU). This facility provides a realistic simulation of wind loads, by reducing the scaling effects (Aly and Yousef, 2021). The building model, and the wind velocity and turbulence intensity profiles are shown in **Figure 1**. The building is placed at twice the height of the open-jet and the base is restrained against overturning.

* Lead presenter

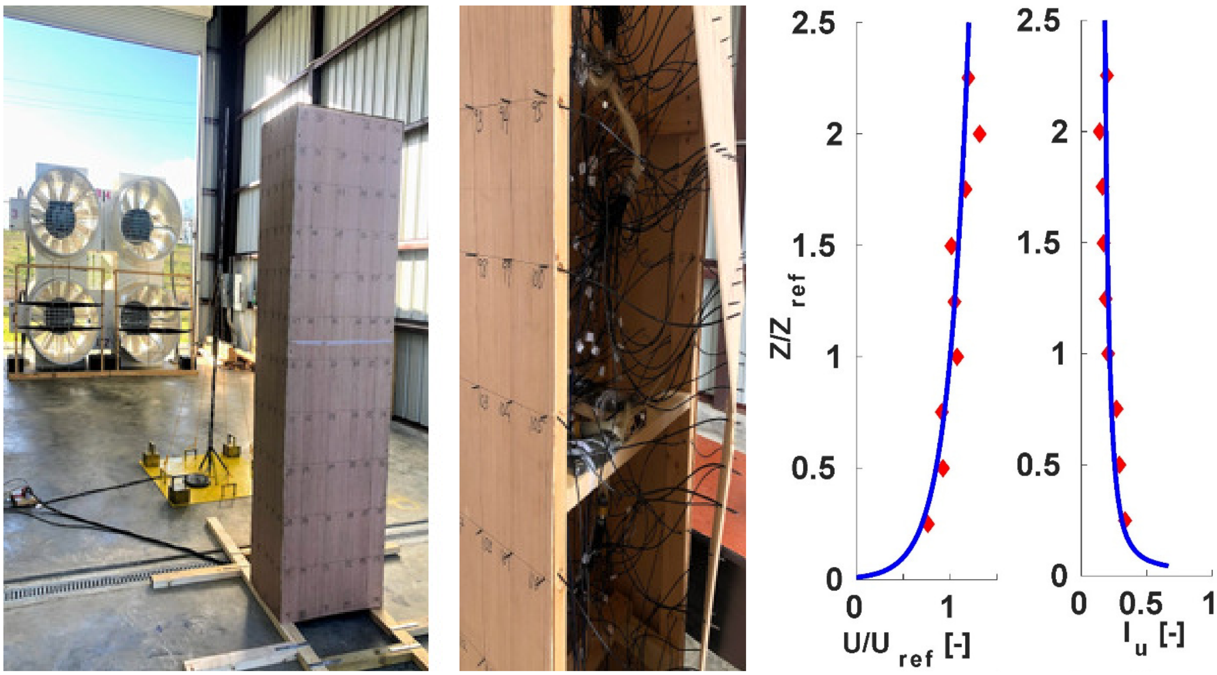

(a) **(b)**

Figure 1. Experimental setup: (a) aerodynamic test model and scanivalve pressure scanner arrangement inside it, and (b) along-wind normalized velocity profile and turbulence profile.

2. PRESSURE DISTRIBUTION

The time history of the wind forces at each story in the full scale is determined by scaling up the wind loads calculated using open-jet testing. The geometric scale of the model to prototype λ_L is 1:50. Assuming mean wind speed at 50 m in full scale to be 20 m/s and mean wind speed during open jet testing is 12.5 m/s.

This provides the velocity scale λ_V of 1:1.6. Based on that time scale becomes λ_T =1:31.25. Continuous-time series of pressure fluctuations were measured at a sampling frequency of 625 Hz using 256 taps installed in the building. The time history of dimensionless pressure coefficient is written as:

$$C_p(t) = \frac{P(t) - P_{ref}}{0.5\rho U^2} \tag{1}$$

Where, $P(t)$, ρ, and $U$are pressure time history, air density, and mean wind speed measure at reference height (1m corresponding to 50 m at full scale). Wind loads at any story in a given direction can be obtained by integrating pressure over the tributary area corresponding to that story and expressed as:

$$F(t) = \int P(t)\, dA \tag{2}$$

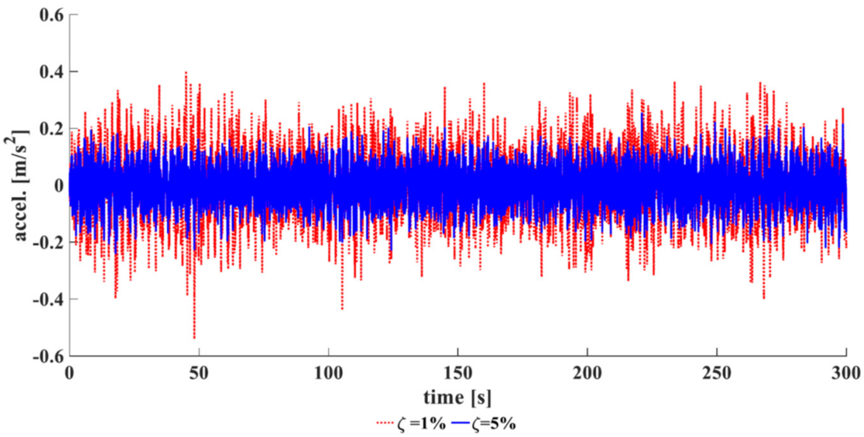

Figure 2. Controlled and uncontrolled acceleration response of floor 42.

2.1. Response Evaluation

Once the wind loads on each story are calculated using the pressure integration technique (Aly, 2013), the wind-induced responses in each direction are determined by solving the following equation of motion:

$$M\ddot{X} + C\dot{X} + KX = F(t) \tag{3}$$

where M, C, and K are the mass, damping, and stiffness matrix of the building. Since the pressure fluctuation in crosswind direction is relatively high, the crosswind responses of the building can be dominant over the along-wind response. **Figure 2.** shows the response of the building for two different values of damping (1% and 5%). To minimize the structural vibration in the crosswind direction, a pendulum pounding TMD is proposed. The pendulum PTMD has shown its effectiveness to mitigate vibrations (Chapain and Aly, 2021).

3. SUMMARY

A large-scale model of a high-rise building was tested to investigate its, in terms of aerodynamics and structural responses. The extensive hybrid experimental/computational framework enables the evaluation of the responses of tall buildings, under realistic wind simulation capabilities of open-jet testing. Excessive acceleration in crosswind direction exceeds the threshold of occupants' comfort. Performance-based design of a pendulum PTMD is proposed to attenuate excessive vibrations.

REFERENCES

Aly, A.M., 2013. Pressure integration technique for predicting wind-induced response in high-rise buildings. Alexandria Eng. J. 52. doi:10.1016/j.aej.2013.08.006

Aly, A.M., Yousef, N., 2021. High Reynolds number aerodynamic testing of a roof with parapet. Eng. Struct. 234. doi:https://doi.org/10.1016/j.engstruct.2021.112006

Chapain, S., Aly, A.M., 2021. Vibration Attenuation in Wind Turbines: A Proposed Robust Pendulum Pounding TMD. Eng. Struct. 233. doi:10.1016/j.engstruct.2021.111891

Mendis, P., Ngo, T., Haritos, N., Hira, A., Samali, B., Cheung, J., 2007. Wind loading on tall buildings. Electron. J. Struct. Eng. 3, 41–54.

Statistical Investigation of Wind Duration Using A Refined Hurricane Track Model

Haifeng Wang[a,*], Teng Wu[b]

[a]*Department of Civil, Structural and Environmental Engineering, University at Buffalo, Buffalo, New York, United States, hwang48@buffalo.edu*
[b]*Department of Civil, Structural and Environmental Engineering, University at Buffalo, Buffalo, New York, United States, tengwu@buffalo.edu*

ABSTRACT:
A complete characterization of the atmospheric boundary-layer winds essentially involves speed, direction and duration. While extensive statistical analyses have been carried out to determine wind speed and directionality for appropriate wind design of buildings, there is a lack of similar research effort for wind duration. Recent advances of performance-based wind design methodology allow the controlled nonlinear, inelastic deformation of buildings under strong winds, and hence place a demand on statistical investigation of wind duration. In this study, the wind duration is measured with the over-threshold method (i.e., uniform duration) using a refined hurricane track model. A statistical analysis framework is developed to jointly consider wind duration, speed and direction. A case study is conducted to demonstrate the efficacy of the proposed statistical analysis framework for characterization and quantification of wind duration.

Keywords: Wind duration, Performance-based wind design, Refined hurricane track model, Statistical Analysis

1. INTRODUCTION

The wind design of building is moving towards performance-based methodology, where it is important to consider duration effects on the strong wind-induced nonlinear, inelastic structural response (ASCE, 2019). The accurate and reliable characterization and quantification of wind duration is a critical step in advancing this consideration. To this end, the statistical investigation of wind duration is carried out in this study. The successful implementation of probabilistic hurricane duration analysis requires a large number of wind data using the Monte Carlo simulation method. This study employs a refined hurricane track model with improved modelling of hurricane movement for wind data preparation. It is noted that by itself the wind duration sheds little light on its effect on structural response. Actually, there is a difficulty in decoupling the wind duration consideration from the wind speed and direction. Accordingly, a statistical analysis framework is developed to jointly consider wind duration, wind speed and wind direction. The efficacy of the proposed statistical analysis framework for characterization and quantification of duration in wind climate consideration is demonstrated through a case study.

2. METHODOLOGY

2.1. Refined hurricane track model

Vickery et al. (2000) utilized the current-step longitude, latitude, translation speed and direction to get the next-step hurricane location. While the beta effect (controlled by both hurricane location and translation) may be well captured in their simulation, the environmental flow is not considered. To accurately assess the duration of hurricanes, an improved translation simulation scheme with

* Lead presenter

consideration of both the environmental flow and beta effect is proposed here:

$$u_{i+1} = a_1 + a_2\psi_{i+1} + a_3\lambda_{i+1} + a_4u_i + a_5U_{i+1,850} + a_6U_{i+1,250} + \varepsilon_a \quad (1)$$
$$v_{i+1} = b_1 + b_2\psi_{i+1} + b_3\lambda_{i+1} + b_4v_i + b_5V_{i+1,850} + b_6V_{i+1,250} + \varepsilon_b \quad (2)$$

where u and v are respectively the longitudinal and latitudinal storm translation speeds; subscripts i and $i+1$ are respectively the current and next time steps; ψ and λ are respectively the latitude and longitude of hurricane center; U and V are respectively the longitudinal and latitudinal environmental flow speed; the subscripts 850 and 250 respectively represent the heights at 850- and 250-hPa levels; $a_1, a_2, \cdots, a_6$ and $b_1, b_2, \cdots, b_6$ are coefficients obtained by linear regression; ε_a and ε_b are random error terms generated following Student's T distribution (Cui and Caracoglia, 2016). The coefficients $a_1, a_2, \cdots, a_6$ and $b_1, b_2, \cdots, b_6$ are estimated for 5°×5° grids over the Atlantic Ocean and the Gulf of Mexico.

2.2. Statistical analysis framework

A large number of wind data are generated using the refined hurricane track model, as well as the corresponding duration data based on the over-threshold method. To comprehensively investigate the characteristics of wind duration, a statistical analysis framework is proposed. Figure 1 depicts each component of the duration statistical analysis framework used in this study to comprehensively investigate wind duration effects on structural performance.

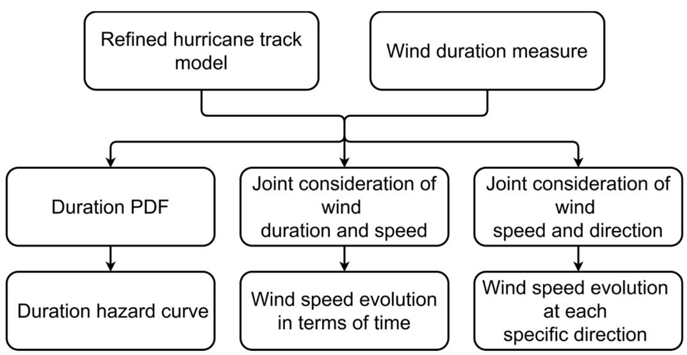

Figure 1. Statistical analysis framework of wind duration

3. CASE STUDY OF WIND DURATION

Orlando (28.55°N, 81.38°W), a hurricane-prone city in Florida, is selected as the site of interest. The wind duration with a threshold wind speed of 46.5 m/s, corresponding to a mean recurrence interval (MRI) of 50 years (ASCE, 2016), is obtained and analyzed. A total number of 2,160,000 hurricanes are simulated using the refined hurricane track model. Data preprocessing is performed to pre-select the hurricanes that affect the site of interest. There are 2517 hurricanes to be considered.

3.1. Duration statistical analysis

Based on the synthesized duration data, their distribution is estimated and presented in Fig. 2. As shown in the figure, the durations are randomly distributed with a mean value of five hours. The fitted Gamma distribution is also presented in Fig. 2. The good match indicates that Gamma distribution may be utilized for describing the duration distribution.

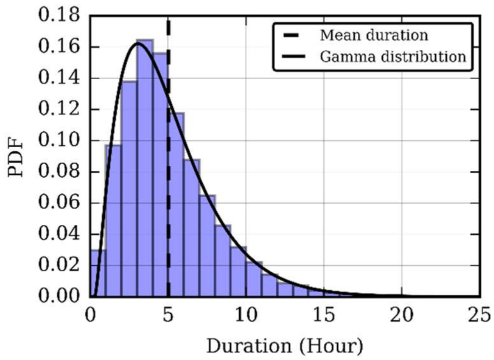

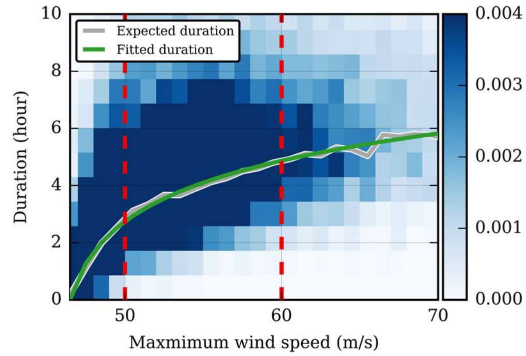

Figure 2. Duration distribution

Figure 3. Joint distribution of speed and duration

3.2. Joint consideration of wind speed and duration

The duration and the expected wind speed are simultaneously examined here. Figure 3 depicts the joint distribution of wind speed and duration. It is observed that the wind duration is positively related to wind speed. Due to the positive relation between the wind duration and speed, it is important to consider the long durations for extreme hurricane wind events. For the convenience of application, an empirical relation between wind duration and wind speed is fitted as:

$$D_T = a(U - U_T)^{\frac{1}{2}} \tag{3}$$

where a is the shape parameter set as 1.82 here; U is the wind speed; and U_T is the threshold wind speed. It is shown that the proposed empirical relation matches well with the duration expectation extracted from simulations. It is noted that the wind duration distributions conditional on wind speeds are also well fitted by Gamma distribution.

REFERENCES

ASCE, 2016. Minimum Design Loads for Buildings and Other Structures. Structural Engineering Institute of ASCE, Reston, VA.

ASCE, 2019. Prestandard for performance-based wind design. Structural Engineering Institute of ASCE, Reston, VA.

Cui, W. and Caracoglia, L., 2016. Exploring hurricane wind speed along US Atlantic coast in warming climate and effects on predictions of structural damage and intervention costs. Engineering Structures, 122, 209–225.

Vickery, P. J., Skerlj, P. F., and Twisdale, L. A., 2000. Simulation of hurricane risk in the U.S. using empirical track model. Journal of Structural Engineering, 126(10), 1222–1237.

Probabilistic Wind Hazard Analysis for Performance-Based Wind Design of Buildings: Hazard Curve, Wind Demand and Loading Protocol

Haifeng Wang[a,*], Teng Wu[b]

[a]*Department of Civil, Structural and Environmental Engineering, University at Buffalo, Buffalo, New York, United States, hwang48@buffalo.edu*
[b]*Department of Civil, Structural and Environmental Engineering, University at Buffalo, Buffalo, New York, United States, tengwu@buffalo.edu*

ABSTRACT:
The wind design of buildings is moving toward the performance-based methodology, where controlled nonlinear, inelastic wind-induced response of buildings is allowed. To ensure the structure satisfy the desired performance objectives, it is critical to examine the wind performance of structural members in both elastic and plastic deformation ranges. To this end, it is necessary to establish representative loading protocols for member tests. The wind loading protocol for the experimental qualification of structural members is currently lacking. In this study, the wind loading protocol design framework is proposed to facilitate the implementation of performance-based wind design. First, the wind hazard curve is extracted from available database. Then, the wind demand of members is determined using nonlinear time-history analysis with a finite element model and wind-tunnel aerodynamic data. At last, the wind loading protocol is set up based on the statistical analysis of wind demand on members.

Keywords: Performance-based wind design, Loading Protocol, Wind Demand, Hazard Curve

1. INTRODUCTION

The wind design of buildings is moving toward the performance-based methodology, where controlled nonlinear, inelastic deformation of buildings is allowed under strong winds (ASCE, 2019). To ensure the structure satisfy the desired performance objectives, it is critical to examine the wind performance of structural members in both elastic and plastic deformation ranges. As a result, it is necessary to establish representative loading protocols for component tests. Currently, the wind loading protocol for the experimental qualification of structural members is in lack. In this study, the wind loading protocol design framework for member performance test is developed.

The wind loading protocol design involves the statistical analyses of wind speed, wind duration, building aerodynamics, and structural response. In this study, the wind hazard curve is first revisited to generate the basic wind speed ratios of various mean return intervals (MRIs). Then, the wind duration statistics is obtained from meteorological stations data to achieve the wind speed histories. Based on the wind-tunnel aerodynamic data, the wind load on the structure is calculated. and the corresponding wind demand for target structural members is extracted from nonlinear time-history analysis results of the finite element model (FEM). Using the obtained statistics of structural member demand time history, the wind loading protocols for both alongwind and acrosswind responses are determined.

* Lead presenter

2. WIND LOADING PROTOCOL DESIGN FRAMEWORK

Loading histories involve the number, range, and amplitudes of all damaging cycles that a structural component may experience. Hence, the statistical analysis of the member wind demand histories is critical. In this study, the member wind demand history is obtained with FEMs, and the loading protocol design framework is composed of the following three parts.

2.1. Structural system modeling

Steel frame systems with various lateral load resisting systems are designed and modeled in this study. Figure 1 depicts the structural system with buckling-restrained braces (BRBs). Figure 2 schematically depicts the load-deformation hysteretic curve of BRB. The steel frame systems are designed to have elastic-limit wind speeds corresponding to different MRIs. The nonlinear dynamic analysis is conducted in OpenSees (Mazzoni et al., 2006).

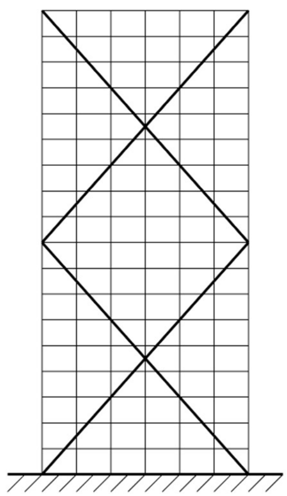

Figure 1. Structural system model

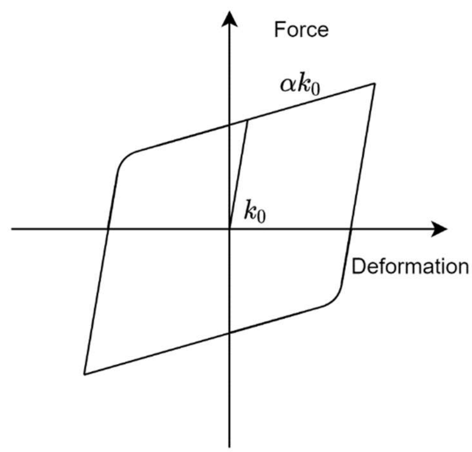

Figure 2. Hysteretic curve

2.2. Wind load history

To obtain realistic wind loading protocols, it is important to identify the relation between member wind demand and MRI. To achieve this goal, the wind hazard curves are first extracted from ASCE 7 Hazard Tool (https://asce7hazardtool.online) for the United States. Figure 3 presents the basic wind speed ratio of 3000-year MRI to 100-year MRI. It is observed that the basic wind speed ratios among various MRIs are site-dependent, and they are typically more significant in hurricane-prone regions. Due to the complex bluff body aerodynamics, it is actually inappropriate to simply approximate the wind load on buildings proportional to the square of the wind speed (quasi-static assumption). Accordingly, the building geometry-related wind loads of a series of generic building shapes corresponding to various MRIs are obtained based on available wind tunnel database to investigate the relation between the wind demand and MRI for various wind hazard curves.

Once the design wind speed is determined based on the extracted wind hazard curves, the wind speed variation trend and windstorm duration are extracted from meteorological station measurement data. Then, the wind load history is synthesized using aerodynamic data obtained from wind tunnel experiments and it can be used for the member demand history analysis.

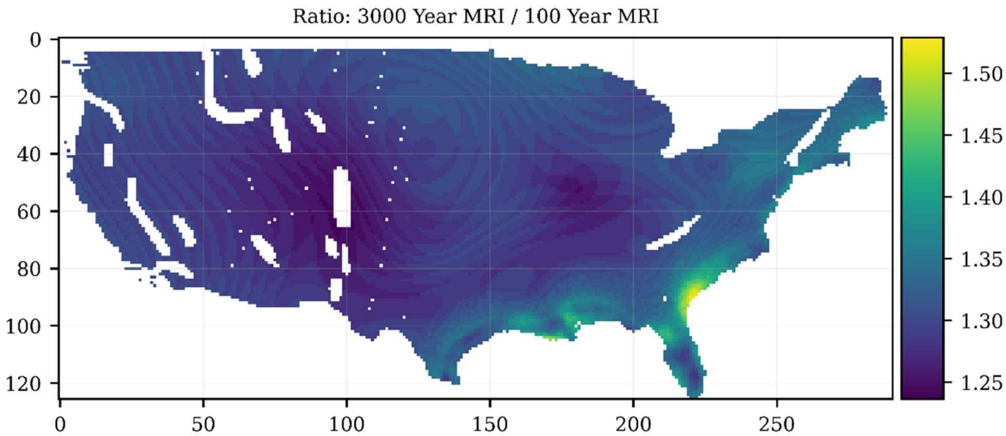

Figure 3. Basic wind speed ratio map

2.3. Member demand history, cycle counting and loading protocol

With the FEM and the wind load histories, the member demand histories are obtained. Accordingly, the loading protocol can be determined by statistical analysis of member demand histories. The designed loading protocol needs to have the equivalent cumulative damage of the member demand history. The cumulate damage is calculated as (Krawinkler et al., 2000):

$$D = C\sum \Delta d^{c} \quad (1)$$

where D is the cumulative damage; C denotes the structural performance parameter depending on the failure mode; Δd is the change in deformation; and c is another performance parameter always greater than unity.

The design of loading protocol involves the trade-off between the accuracy and practicability (Richards and Uang, 2006). On the one hand, one expects the loading protocol to realistically capture the wind load demand on members. On the other hand, the loading protocol needs to be practical in terms of experimental testing. To this end, the load levels is first reduced to an acceptable level (e.g., 15 load levels), and the rainflow counting method is utilized to obtain the number of cycles corresponding to each member load level.

REFERENCES

ASCE, 2019. Prestandard for performance-based wind design.

Krawinkler, H., Gupta, A., Medina, R., Luco, N., 2000. Development of loading histories for testing of steel beam-to-column assemblies. Stanford University.

Mazzoni, S., McKenna, F., Scott, M.H., Fenves, G.L., 2006. OpenSees command language manual. Pacific Earthquake Engineering Research (PEER) Center 264.

Richards, P.W., Uang, C.-M., 2006. Testing protocol for short links in eccentrically braced frames. Journal of Structural Engineering 132, 1183–1191.

Integrating survivor stories, tornado wind field models, and forensic investigations to reconstruct tornado events

Savannah Howie [a,*], David Roueche [b], Franklin Lombardo [c], Daphne LaDue [d], Lara Mayeux [e]

[a]Auburn University, Auburn, AL, United States, slh0111@auburn.edu
[b]Auburn University, Auburn, AL, United States, dbr0011@auburn.edu
[c]University of Illinois Urbana-Champaign, Champaign, IL, United States, lombaf@illinois.edu
[d]University of Oklahoma, Norman, OK, United States, dzaras@ou.edu
[e]University of Oklahoma, Norman, OK, United States, lmayeux@ou.edu

ABSTRACT:
The sequence of wind loading and ensuing damage to structures during the passage of a tornado is largely unknown, with most investigations focusing on the post-storm damage state. This study focuses on the 2019 EF4 Beauregard and 2020 EF3/EF4 Nashville/Cookeville tornados and integrates survivor stories, numerical tornado wind speed models, and directional damage patterns to reconstruct the sequence of events in these tornadoes for specific structures. This method of integrating multiple sources will allow for a more detailed understanding of what exactly occurs during a tornado, and it will provide improved guidance on sheltering locations to increase the occupant survivability.

Keywords: tornado, structures, field investigations, damage patterns

1. INTRODUCTION

Since 2008, nearly 71% of all tornado fatalities have occurred in permanent or mobile/ manufactured homes (SPC, 2021), with the southeast U.S. containing a higher proportion of these fatality locations relative to the rest of the country. The 2019 EF4 Beauregard tornado (Roueche et al, 2019) and the 2020 EF3/EF4 Nashville/Cookeville tornados (Wood et al, 2020) were two disastrous events that caused a total of 48 fatalities. Following these storms, the 2nd through 5th authors completed assessments of damage to structures and trees and conducted first-hand interviews with survivors. This study explores initial integrations of these multi-disciplinary data, aligning (1) directional damage patterns with (2) insights of the sequence of events gained from survivor interviews, and (3) velocity time histories from a numerical tornado wind field model.

2. ANALYSIS FRAMEWORK

The post-storm imagery captured of the residential homes (including on-site photographs, UAV imagery, and street-level panoramas) was used to determine the percentage of damage (0-100%) to the primary structural members, components, and cladding elements. These percentages were then used to assign an overall damage category to each elevation of the roof and walls (Figure 1). The damage patterns on the homes were then compared to a numerical wind speed model assuming a Rankine vortex conditioned to tree fall patterns to see if the direction and intensity of wind modeled was comparable to the physical damage. As indicated by the wind speed and direction time history plot in Figure 2, the strongest winds for this location were emanating from the westward direction. This correlates well with the damage patterns seen in Figure 1. Based on the

* Lead presenter

interviews, the occupants sheltered in the lower level of the southeast corner of their home. The windows in that corner blew in first followed by all the other windows in the home. Debris that blew into their home was funneled through an interior hallway from the southwest corner to northwest corner which would agree with the wind direction model for this location.

Similar analysis is being conducted for a collection of homes with corresponding survivor interviews. Integrating these data at larger scales deepens our understanding of tornado-induced wind loading with particular relevance to enabling more refined sheltering guidance to at-risk populations.

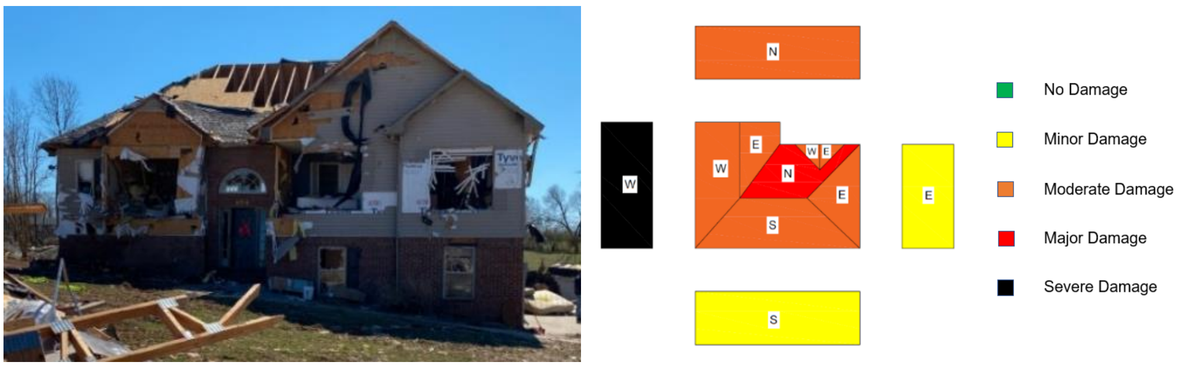

Figure 1. (Left) Tornado damage to North side of residential home in Cookeville, TN. (Right) An exploded view showing the direction and damage category of each roof and wall elevation.

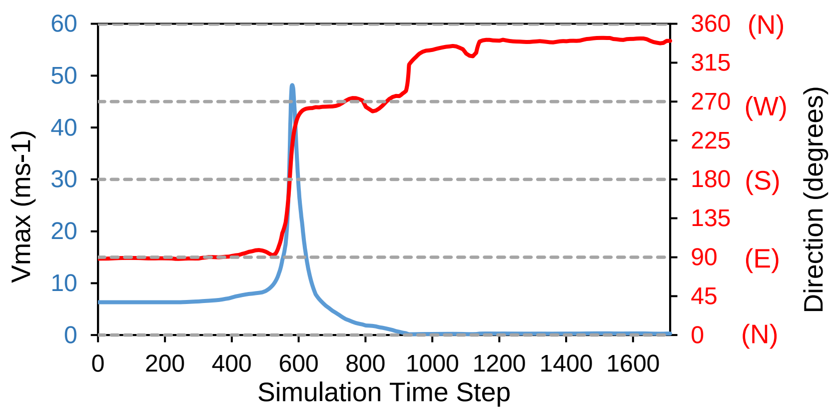

Figure 2. Wind speed and direction time history plot for the residential home shown in Figure 1.

ACKNOWLEDGEMENTS
This project was funded by the National Oceanic and Atmospheric Administration VORTEX-Southeast program under Grant No. NA19OAR4590212.

REFERENCES

Storm Prediction Center (SPC), 2021. Annual U.S. Killer Tornado Statistics. National Oceanic and Atmospheric Administration National Weather Service. Available at https://www.spc.noaa.gov/climo/torn/fatalmap.php.

Roueche, D.B. et al. (2019) "StEER - 3 March 2019 Tornadoes in the Southeastern US: Field Assessment Structural Team (FAST) Early Access Reconnaissance Report (EARR)." DesignSafe-CI.

Wood, R.. et al. 2020. "Early Access Reconnaissance Report (EARR)", in StEER - 3 March 2020 Nashville Tornadoes. DesignSafe-CI.

Multi-event comparative analysis of common wind damage patterns from recent windstorms

David B. Roueche [a], Jordan O. Nakayama [b*]

[a]*Auburn University, Auburn, AL, USA, dbr0011@auburn.edu*
[b]*Auburn University, Auburn, AL, USA, jon0003@auburn.edu*

ABSTRACT:
Data-driven analyses of windstorm building performance typically utilize reconnaissance data from a single event. The Structural Extreme Events Reconnaissance (StEER) network, funded by the National Science Foundation, has collected post-windstorm building performance data since 2017 using standardized methodologies, allowing for multi-event comparisons. This study analyses the damage patterns for various structure components and structure types using data from hurricanes Harvey (2017), Irma (2017), Michael (2018) and Laura (2020). Fragility analyses are performed highlighting regional differences in performance under similar hazard conditions.

Keywords: fragility, windstorm, hurricane, reconnaissance, multi-event

1. INTRODUCTION

Since 2018, the Structural Extreme Events Reconnaissance network (StEER), funded by the National Science Foundation, has conducted post-windstorm reconnaissance missions utilizing consistent methods and data standards, and unbiased sampling techniques. These efforts build on pilot studies by the first author (Roueche et al., 2018) and others in 2017 to demonstrate the feasibility of such approaches. In combination, the datasets produced in this manner allow for multi-event analyses of common wind damage patterns in the major building components, stratified by key factors such as hazard intensity, occupancy, year built, structural system, and more. This study highlights common component-level damage patterns in recent windstorms and presents illustrative fragility analyses of component damages.

2. METHODS

The combined dataset includes the following hurricanes: Harvey (2017), Irma (2017), Michael (2018), and Laura (2020). Within the combined dataset is included the building location, occupancy, relevant appraisal and structural attributes, as well as component-level damage assessments. This information, as well as estimated peak wind speeds for each building's location were used to evaluate the frequency of damage for each component and perform initial fragility analyses. In this preliminary analysis, frequency of damage for each component is quantified as follows:

$$\%\,Damage = 100\% * \frac{1}{N_c}\sum_{s=1}^{N_c} I_s \tag{1}$$

where N_C is the number of buildings in occupancy class C, and I_S is an indicator function with a value of 0 if the given component for building S has no evidence of damage, and 1 if any of the component is damaged. The fragility analysis was completed using maximum likelihood estimation (MLE) to condition lognormal cumulative distribution functions.

* Lead presenter

4. PRELIMINARY RESULTS

The pie charts depicted in Fig. 1 display the percent damage for each structural component stratified by the three broad occupancy classifications—single family residential, multi-family residential, and commercial/industrial.

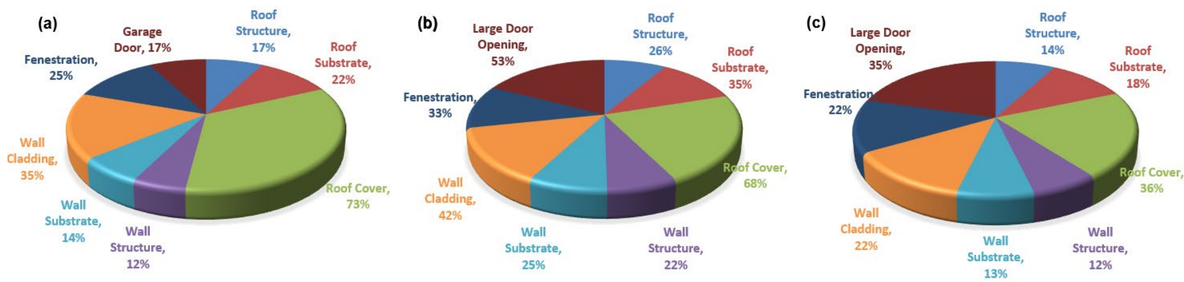

Figure 1. Frequency of damage type for windstorms with respect to (a) single family (N = 3813), (b) multi-family (N = 150), and (c) commercial structures (N = 284). Note: percentages do not sum to 100% because the component-level damages overlap.

The fragility analysis illustrate the probability of failure of the roof cover and structure with a limit state of greater than or equal to 25% and 5% damage respectively for all buildings in Figure 2.

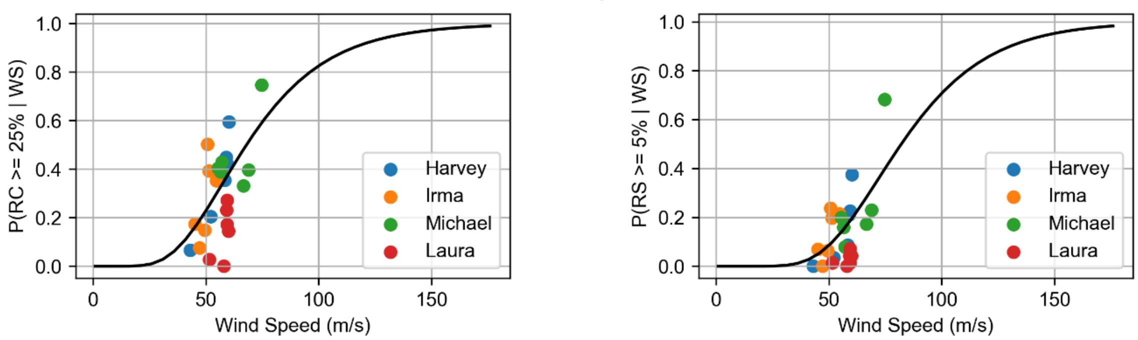

Figure 1. Multi-event fragility curves for all buildings considering (left) roof cover damage and (right) roof structure damage, with empirical failure rates stratified by hurricane event also shown.

Roof cover is by far the most damaged component. The multi-event analyses highlight the event-to-event variability, potentially indicative of regional differences in design wind speed and construction practices.

ACKNOWLEDGMENTS

This work is supported by the National Science Foundation under Grant No. CMMI-1944149. Any opinions, findings, and conclusions expressed in this material are those of the authors and do not necessarily reflect the views of the National Science Foundation.

REFERENCES

Roueche, D. B., Lombardo, F. T., Smith, D. J., & Krupar III, R. J. (2018). Fragility Assessment of Wind-Induced Residential Building Damage Caused by Hurricane Harvey, 2017. In *Forensic Engineering 2018: Forging Forensic Frontiers* (pp. 1039-1048). Reston, VA: American Society of Civil Engineers.

* Lead presenter

Automation of post-windstorm reconnaissance data enrichment using web scraping and machine learning

Hadiah Rawajfih [a,*], David B. Roueche [b]

[a]*Auburn University, Auburn, Alabama, USA, hzr0032@auburn.edu*
[b]*Auburn University, Auburn, Alabama, USA, dbr0011@auburn.edu*

ABSTRACT:
Post-windstorm field reconnaissance data are a valuable resource for understanding and improving the performance of buildings during extreme wind events. Datasets collected in the field are often fragmented and non-uniform, necessitating the development of data enrichment and quality control protocols to ensure datasets are accurate, complete, and standardized. If carried out manually, such processing can require months, considerably delaying data analysis. This work proposes a preliminary automation framework to accelerate an existing data enrichment and quality control process. Scripting and machine learning techniques are employed to automate building attribute retrieval, image collection and processing, and damage recognition and classification, illustrating how such methods can support and augment human-based approaches.

Keywords: automation, damage assessments, machine learning, reconnaissance

1. INTRODUCTION

Post-windstorm damage assessments conducted by field reconnaissance teams yield valuable data for understanding and ultimately improving the performance of structures subjected to extreme wind loads. Because practical constraints on field data collection often result in incomplete and non-standardized records, data enrichment and quality control (DE-QC) protocols, such as those developed by the Structural Extreme Events Reconnaissance (StEER) network (Roueche et al, 2019), are implemented to ensure accuracy, completeness, and consistency in the published datasets. Performed manually, DE-QC is time-intensive and can stall data analysis for months. Considering the StEER protocols specifically, this work presents a preliminary automation framework to expedite the DE-QC process by means of scripting and machine learning methods.

2. AUTOMATION METHODS

The automation framework is illustrated in Fig. 1. The current framework focuses on the following three essential tasks. (1) For a set of addresses or coordinates, basic building attributes are retrieved by scripted web scraping; these include “number of stories”, “year built”, “foundation type”, and “occupancy type”. The attribute list is then supplemented and enhanced using tools available in the open-source Building Recognition using AI at Large-Scale (BRAILS) and Spatial Uncertainty Research Framework (SURF) research applications developed and maintained by the NHERI SimCenter (Yu et al, 2019). BRAILS extracts building attributes from Google satellite and street-view imagery, and BRAILS classifiers identify additional attributes, such as roof shape, that cannot typically be obtained by web scraping. SURF infers attribute values from spatial relationships between points of interest. Applying these three methods in concert thus generates a

* Lead presenter

comprehensive attribute list for the building inventory under study. (2) Individual roof images are extracted from NOAA aerial imagery; these are processed to obtain a satisfactory balance between image resolution and data file size. (3) Lastly, a trained machine learning model evaluates the processed roof images and classifies each according to its damage state: undamaged, minor, moderate, severe, or destroyed. For this task, several machine learning algorithms have been tested, including support vector machines (SVM), stochastic gradient descent (SGD), and multi-layer perceptron (MLP). Of these, SVM is found to yield the greatest overall accuracy, with an average threefold cross-validation accuracy score of 62%.

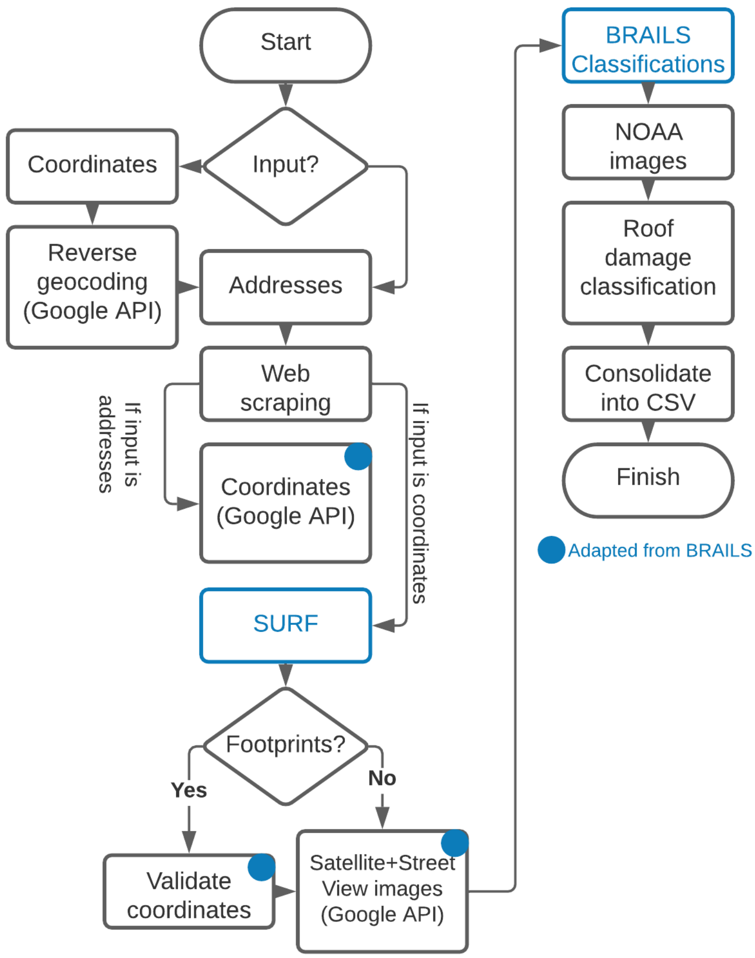

Figure 1. Flowchart illustrating the sequence of operations in the automation framework.

3. CONCLUSION AND SUMMARY

The proposed automation framework seeks to accelerate existing post-windstorm reconnaissance DE-QC protocols. Building attribute data are collected by means of scripted web scraping and tools provided in the open-source BRAILS and SURF applications. Roof damage detection and classification is performed using a trained machine learning model. Damage classification accuracy presently does not surpass 62%; this is to be improved in future work.

ACKNOWLEDGMENTS
This work is supported by the National Science Foundation under Grant No. CMMI-1944149. Any opinions, findings, and conclusions expressed in this material are those of the authors and do not necessarily reflect the views of the National Science Foundation.

REFERENCES

Roueche, D., Kijewski-Correa, T., Mosalam, K., Prevatt, D., and Robertson, I., 2019, Virtual Assessment Structural Team (VAST) Handbook: Data Enrichment and Quality Control (DE/QC) for US Windstorms, StEER, v. 2.0.

Yu, Q., Wang, C., Cetiner, B., Yu, S., McKenna, F., Taciroglu, E., and Law, K., 2019. Building information modeling and classification by visual learning at a city scale. arXiv preprint arXiv:1910.06391.

Wind-induced failures and structural modeling of large-volume buildings impacted by Hurricane Michael (2018)

Marshall, J.D. [a], Roueche, D.B. [b*], Berman, J.W.[c], Roberts, J.A.[d], Blue, C.B.[e]

[a]*Auburn University, Auburn, AL, USA, jdmarshall@auburn.edu*
[b] *Auburn University, Auburn, AL, USA, dbr0011@auburn.edu*
[c] *University of Washington, Seattle, WA, USA, jwberman@uw.edu*
[d]*Auburn University, Auburn, AL, USA, jar0070@auburn.edu*
[e]*Auburn University, Auburn, AL, USA, cbb0032@auburn.edu*

ABSTRACT: (10 pt)
This paper describes the forensic assessments and observed failure mechanisms to a collection of large-volume, low-rise buildings in Panama City, FL that failed during below-design conditions induced by Hurricane Michael (2018). The buildings represented multiple structural systems, including pre-engineered metal buildings, precast tilt-up concrete systems, and metal rack buildings, and represented a range of years of construction. Three case study buildings are studied in detail, informed by static and dynamic analysis of the structural systems through 3D, linear elastic finite element models developed from structural drawings and extensive reconnaissance data. The analysis demonstrates the critical importance of the longitudinal load path through the end bay of the windward wall in the observed collapse mechanisms.

Keywords: hurricane, industrial buildings, forensics, collapse

1. INTRODUCTION

The landfall of hurricanes producing design-level winds is a relatively uncommon occurrence in the United States, and so provides an important opportunity to evaluate structural performance at or near design limits. Hurricane Michael (2018) was one such event, making landfall on October 10, 2018 near Mexico Beach, FL with peak wind gusts estimated at just over 68 m/s (150 mph). This study specifically focuses on the performance of large-volume, low-rise buildings (LVLRB) during Hurricane Michael (2018), which is a class of buildings here loosely defined as buildings with heights less than 18 m (60 ft) above ground level, long-span structural systems, and large, mostly undivided interior volumes. Structural systems within LVLRB include pre-engineered metal building systems, precast concrete tilt-up systems, and steel braced frames.

Twenty-three buildings were assessed in total (all in locations experiencing below design-level wind speeds) using lidar, unmanned aerial systems, and high-resolution terrestrial photographs primarily using equipment from the NSF NHERI RAPID facility (Berman et al. 2020). Fifteen of the twenty-three buildings experienced partial or full collapse of the end bay, with the collapse typically propagating to successive interior bays. Damage mechanisms included buckled steel roof joists or roof purlins in the end and interior bays, removal of some steel roof decking, buckling of large rollup or panelized doors, and collapse of some columns and wall systems. Damage observed to the buildings was strongly directional in nature, with typically heavy damage on one side of the building but little to no evidence of damage on the opposite side. A few buildings suffered complete collapse. Three case study buildings are studied in detail from this dataset.

* Lead presenter

2. CASE STUDIES

The three case studies examined in more detail consist of (1) Watson's Marina, a 4000 m^2 footprint, steel rack marina building, (2) the Intermodal Distribution Center, a 14,000 m^2 footprint, tilt-up precast concrete building with steel joists and steel deck diaphragm, and (3) the Port of Panama City East Terminal, a 17,500 m^2 footprint, pre-engineered metal building. Failure mechanisms present in each are highlighted in Figure 1. 3D structural analysis models were generated for each building using the analysis software SAP2000, based on the reconnaissance data and structural drawings provided by the building owners. Nonlinear static and dynamic analyses were performed using ASCE 7 load cases and wind tunnel data from the NIST Aerodynamic Database (Ho et al. 2005). Wind loads were applied for both design conditions and best estimates of conditions during Hurricane Michael (peak wind speeds and directions adjusted for actual upwind terrain).

The analysis of these case studies suggests an end bay load path failure mechanism is at fault for many of the premature failures observed, but further exploration is needed. The study identified several possible contributing causes, including internal pressurization, failure of roof decking removing lateral support to framing members, and eccentricities in the lateral load path. The premature failures of these buildings, many of which served as critical facilities, warrants further investigation so that existing vulnerabilities can be identified and prevented in future designs.

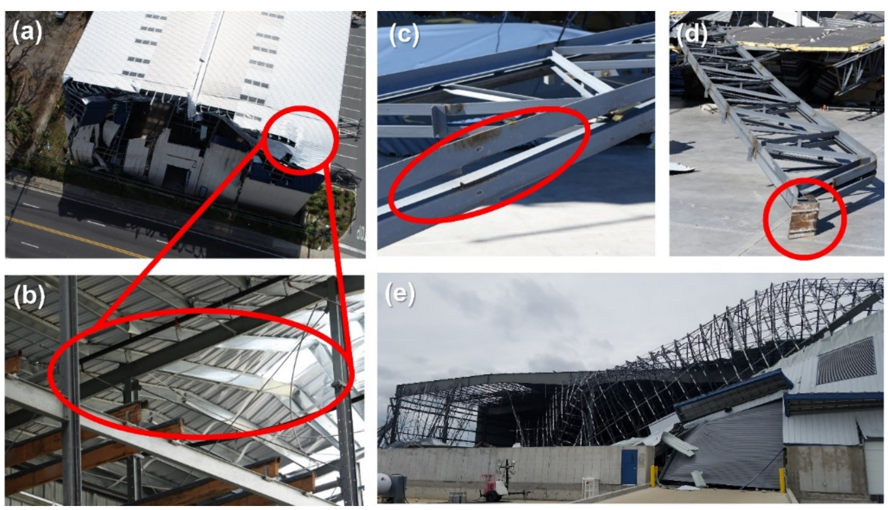

Figure 1. Specific failure mechanisms including (a), (b) purlin buckling in the end and interior bays of Watson's Marina, (c), (d) joist girder failures pullout and buckling in the Intermodal Distribution Center, and (e) end bay collapse of the Port of Panama City East Terminal.

ACKNOWLEDGEMENTS

This work was partially supported by the Metal Building Manufacturers Association and by the National Science Foundation under Grant No. 1904653. Any opinions, findings, and conclusions expressed in this material are those of the author(s) and do not necessarily reflect the views of the National Science Foundation.

REFERENCES

Berman, J. W., et al. "Natural hazards reconnaissance with the NHERI RAPID facility." *Frontiers in Built Environment* 6 (2020): 185.

Ho, T. C. E., et al. "The UWO contribution to the NIST aerodynamic database for wind loads on low buildings: Part 1. Archiving format and basic aerodynamic data." *Journal of Wind Engineering and Industrial Aerodynamics* 93.1 (2005): 1-30.

Field monitoring the wind-induced response of a large-area fabric membrane structure

Roueche, D.B. [a*], Marshall, J.D. [b], Stiles, J.W. [c], Jackson, D.T.[d], Anderson, J.B.[e], Davidson, J.S.[f]

[a]*Auburn University, Auburn, AL, USA, dbr0011@auburn.edu*
[b] *Auburn University, Auburn, AL, USA, jdmarshall@auburn.edu*
[c] *Air Force Civil Engineer Center, Tyndall Air Force Base, FL, USA, john.stiles.1@us.af.mil*
[d]*Auburn University, Auburn, AL, USA, dtj0003@auburn.edu*
[e]*Auburn University, Auburn, AL, USA, jba0005@auburn.edu*
[f]*Auburn University, Auburn, AL, USA, jim.davidson@auburn.edu*

ABSTRACT: (10 pt)
This paper provides preliminary observations on the structural wind-induced response of an in-service fabric structure located in a coastal environment near Panama City, FL. The structure was instrumented in July 2020 with 66 individual sensors. Between August 2020 and November 2020, the instrumented structure was affected by ten windstorm events with peak 3-second gust wind speeds of at least 15 m/s. The captured data provides insights on the lateral and vertical load paths through the structure, the dynamic response of the building to high winds, and the role of wind-induced internal pressurization.

Keywords: field-monitoring, fabric, wind loads, structural response

1. INTRODUCTION

Tensile fabric structures have historically served many purposes, including use in stadiums, airports, and outdoor pavilions where their light weight and varied form factors are ideally suited. However, these same factors make them dynamically sensitive to high winds, and several notable failures have occurred (e.g., the collapse of a professional football team's practice facility in 2009). This sensitivity is particularly a risk in temporary fabric structures, which are often employed in mining and military operations, as the necessary cost-efficiency prioritizes design based on simplified static loads that ignore dynamic and aeroelastic effects. The objective of this study is to explore the wind-induced response of a temporary fabric membrane structure through in-situ monitoring of an in-service structure located near the coast in Panama City, FL.

2. METHODS

The LAMS is a temporary, enclosed building consisting of T6160 aluminium frames and a stretched fabric membrane envelope as shown in Figure 1. It is located in flat, rough terrain per the Davenport terrain classes but with large open patches from 0°-180°. A weather station is located approximately eight roof heights from the LAMS, measuring wind velocity at 10 m above ground at 1 Hz. A suite of 66 sensors were installed in the LAMS to measure strain, displacement of the frames and fabric membrane, internal forces, and acceleration in key locations within the longitudinal and transverse load path, and internal pressure within the enclosed interior volume. Between 1 August 2020 and 31 January 2021, 451 10-minute segments were measured at the

* Lead presenter

LAMS site with peak 3-second wind gusts of 11.5 m/s (25 mph) or higher, representing 27 different storm events. The storms included two hurricane events—Hurricane Sally (2020) and Hurricane Zeta (2020)—both of which tracked north of the LAMS site but were close enough to subject the LAMS to wind speeds as high as 22 m/s (50 mph) over a wide swath of wind directions. A sample segment with illustrative structural response is shown in Figure 2.

Figure 1. Exterior view of the LAMS.

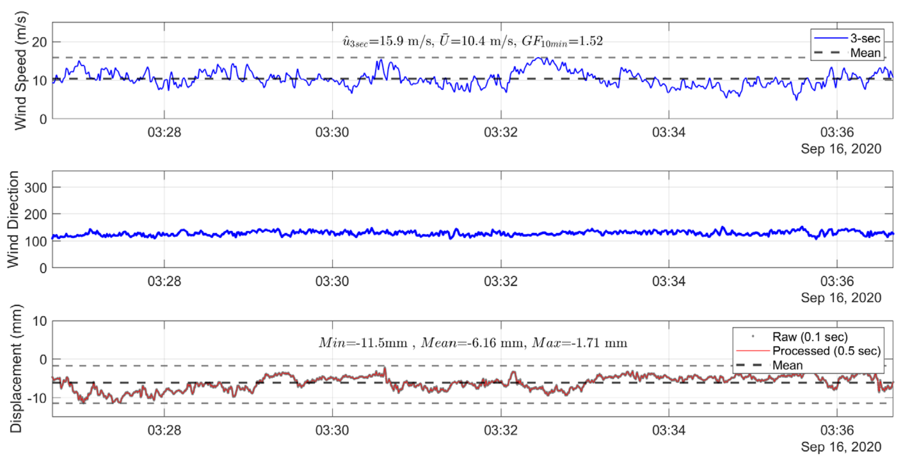

Figure 2. Illustrative 10-minute segment showing wind speed, wind direction, and longitudinal displacement response for a frame line.

2. PRELIMINARY RESULTS

Preliminary data show stresses in the frames and bracing cables that, when scaled to represent design conditions (assuming linear elastic response), are higher than those being designed for as provided by the manufacturer. The data also suggests that wind loads acting in the longitudinal axis of the building are disproportionately being carried by the purlins/struts in the first bay, with the tension cables in the roof not being engaged as much as expected. Further, secondary loading effects are noted, including loose fabric transferring wind loads into (what are designed to be) two-force elements as bending stresses. This paper will present these amongst other findings and highlight some of the challenges encountered in monitoring the structural response of structures to wind in a remote environment using a self-contained monitoring system.

ACKNOWLEDGEMENTS

This project was supported by the Air Force Civil Engineer Center (AFCEC) through Battelle Memorial Institute, Airbase Technologies II: Airfield Protection, Installation Resiliency & Blast (APIRB) Subcontract No. 764992.

6th American Association for Wind Engineering Workshop (online)
Clemson University, Clemson, SC, USA
May 12-14, 2021

Aerodynamics of low-rise buildings: large-scale open-jet testing to address Reynolds number effects

Aly Mousaad Aly[a,*], Md Faiaz Khaled[b]

[a]WISE Research Lab, Louisiana State University, Baton Rouge, LA, USA, aly@lsu.edu
[b]WISE Research Lab, Louisiana State University, Baton Rouge, LA, USA, mkhale7@lsu.edu

ABSTRACT:
Wind flow over low-rise buildings in the atmospheric boundary layer (ABL) is accompanied by some complex flow physics such as flow separation and generation of vortices in the shear layer. The uncertainties associated with such complex flow mechanisms make the case-by-case experimental or numerical investigation of buildings' aerodynamic behavior fundamental. Engineers have aspired to replicate the full-scale real wind behavior in wind-tunnels to create more resilient infrastructures. Traditional wind-tunnel experiments struggle to accurately predict surface pressures despite being widely embraced by the structural engineering community. This limitation is attributed to the lack of large-scale turbulence and low Reynolds numbers in wind-tunnels. Such drawbacks prompted the consideration of aerodynamic testing by the open-jet concept. Open-jet experiments of building models with higher Reynolds numbers reveal the generation of higher mean and peak pressure coefficients, compared to those obtained from wind-tunnels; the findings reinforce the initial hypothesis.

Keywords: Bluff body, Atmospheric boundary layer (ABL), Wind-tunnels, Open-jet, Turbulence, Reynolds number.

1. INTRODUCTION

The human activity-induced phenomenon, global warming, is indirectly making powerful hurricanes more frequent in the South-Eastern coast of the United States. Hurricanes are the costliest natural disasters in the United States. The most common source of economic losses stems from widespread damages to low-rise buildings. An estimated gross economic loss worth up to $265 billion was recorded due to hurricanes Irma, Maria, and Harvey [1]. In the majority of the cases, damages initiate from the building's envelope, especially, the roof. Roofs experience extreme negative pressures as strong winds separate at or near buildings' leading edges, corners, and ridges. The partial or total failure of the roof and its components leave the entire building extremely vulnerable to powerful winds by allowing internal pressure to increase. Therefore, accurate estimation of surface pressures is crucial to improve buildings' resiliency against powerful windstorms. The unpredictable and complicated nature of turbulent winds makes aerodynamic loads' prediction a challenging task. The accuracy of such load prediction depends on the exactness of replicating the turbulence intensity, integral length scale, and Reynolds numbers. The ideal scenario is to reproduce the features of full-scale real-wind in the laboratory. Furthermore, for precise load-prediction, it is important to ensure small and large-scale turbulence in the incident flow. In other words, the laboratory should be able to reproduce both low-frequency (large-scale) and high-frequency (small-scale) velocity fluctuations with adequate energy. In wind-tunnels, the low-frequency turbulence does not possess sufficient energy; consequently, such experiments fail to produce large-scale turbulence in the laboratory. This limitation contributes to the difference in the estimation of peak pressure coefficients from wind-tunnels and the

* Lead presenter

corresponding full-scale scenario [2]. Aerodynamic testing at higher Reynolds numbers employing the open-jet concept is expected to improve the capability of generating turbulence over the entire frequency range. Thus, open-jet facilities are expected to produce higher peak aerodynamic loads than those from wind-tunnels. The Windstorm, Impact, Science, and Engineering (WISE) research group at Louisiana State University (LSU) aims to employ open-jet testing to reproduce real-wind in the laboratory; thus, facilitating the prediction of accurate aerodynamic loads on low-rise buildings. The authors tested two cubic models, at scales 1:13 and 1:26, in the open-jet and compared the roof pressure coefficients with those from a 1:100 scale wind-tunnel model.

2. METHODOLOGY IN BRIEF

The LSU open-jet is capable of large-scale testing at high Reynolds numbers along with destructive testing. Two cubic building models of 1:13 and 1:26 scale were constructed out of wooden members and sheets; the full-scale height of the cubic model is 16 m. The velocity measurements were taken at different along-wind locations in the jet facility and at different heights to choose an appropriate scale and location for testing. Besides, the mean and peak pressures are statistically computed after recording pressure-time history using pneumatic tubes and Scanivalve pressure scanners. The sensitivity of surface pressures in regards to Reynolds numbers is assessed as well.

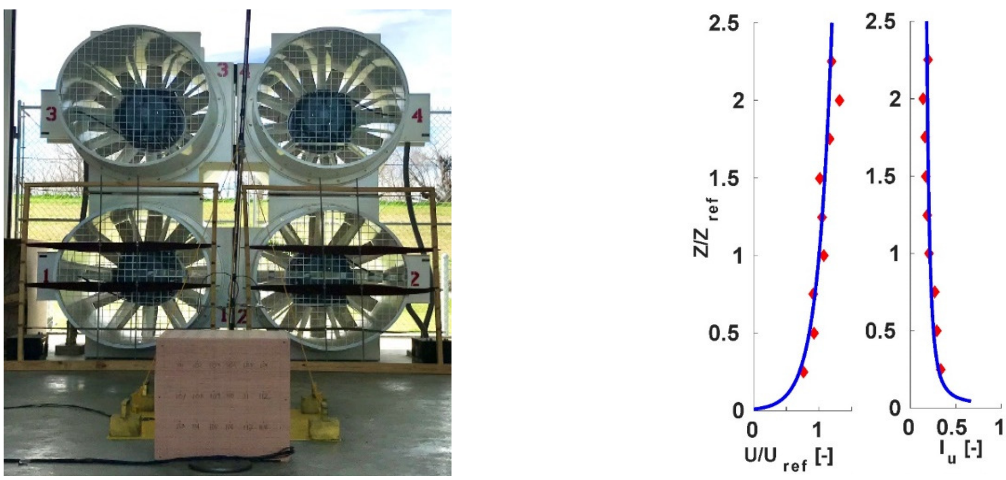

(a) (b)

Figure 1. Large-scale open-jet testing at LSU: (a) 1:26 scale cube, and (b) along-wind normalized velocity profile and turbulence profile.

3. FINDINGS AND CONCLUSION

Figure 1 (a) introduces the LSU open-jet blowers with an adjustable flow management device placed in front. The flow management device facilitates generation of appropriate mean velocity and turbulence intensity profile corresponding to sub-urban terrain in the open-jet facility. Figure 1 (b) shows the along-wind normalized velocity profile and turbulence profile. The open-jet generated small and large-scale turbulence are in compliance with the theoretical spectra from Von-Karman, and ESDU formulations [3]. This is a momentous finding in experimental building aerodynamics. Testing in the open-jet concept assists in producing large-scale turbulence in the facility.

Table 1. Computed Reynolds numbers for different scales.

Scale	1:100 (TPU WT)	1:26 (LSU OJ)	1:13 (LSU OJ)
Reynolds number	$4.9 * 10^4$	$0.34 * 10^6$	$0.8 * 10^6$

Table 1 presents the corresponding Reynolds numbers for different scales. Figure 2 and Figure 3 manifest the trend of increase in mean and 95% quantile peak pressure coefficients along with the increase in Reynolds numbers. Besides, results demonstrate existence larger separation bubble in open-jet compared to wind-tunnels causing a gradual pressure drop downstream on the cube's roof. These encouraging results evidently bring aerodynamic testing of low-rise buildings closer to full-scale scenario. Testing of such large-scale buildings at higher Reynolds numbers in the open-jet has proven to produce higher local peak pressures. The results can have far-reaching impact in updating the existing building standards.

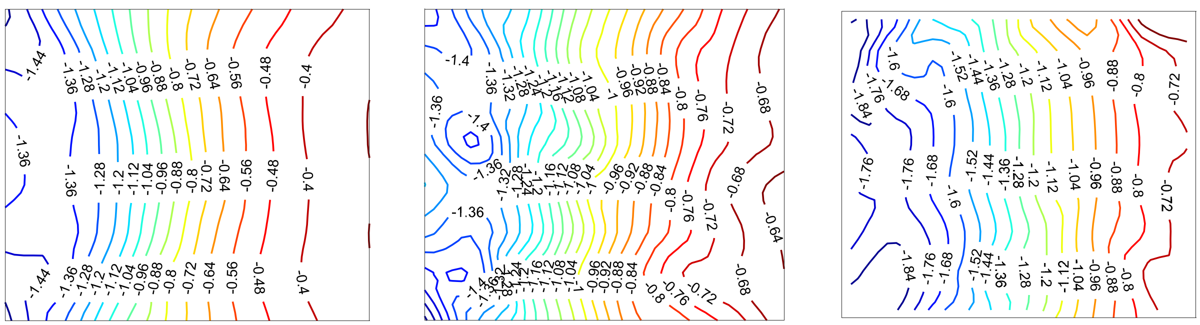

(a) (b) (c)

Figure 2. Mean pressure coefficients (a) 1:100 TPU Wind-tunnel, (b) 1:26 LSU open-jet, (c) 1:13 LSU open-jet

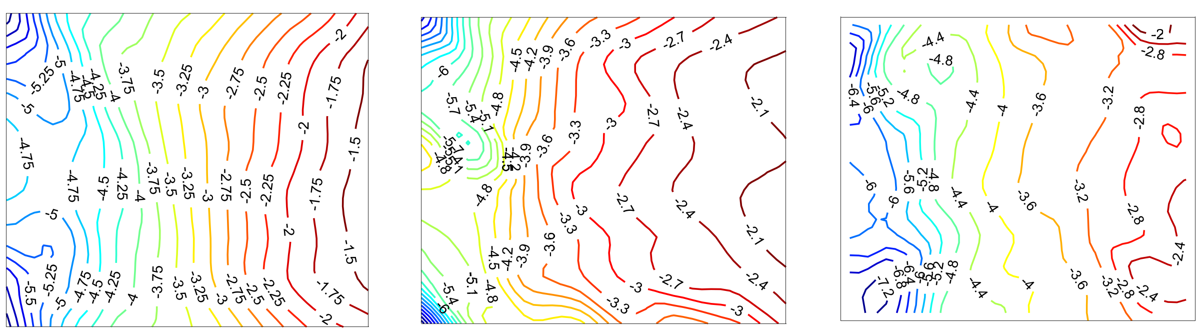

(a) (b) (c)

Figure 3. 95% quantile minimum pressure coefficients (a) 1:100 TPU Wind-tunnel, (b) 1:26 LSU open-jet, (c) 1:13 LSU open-jet

References

[1] U S Federal Emergency Management Agency. 2017 Hurricane Season, FEMA After-Action Report. 2018. doi:https://www.fema.gov/media-library-data/1531743865541-d16794d43d3082544435e1471da07880/2017FEMAHurricaneAAR.pdf.

[2] Aly AM, Khaled F, Gol-Zaroudi H. Aerodynamics of Low-Rise Buildings: Challenges and Recent Advances in Experimental and Computational Methods. Aerodynamics, 2020, p. 1–22. doi:10.5772/intechopen.92794.

[3] Aly AM, Yousef N. High Reynolds number aerodynamic testing of a roof with parapet. Eng Struct 2021;234. doi:https://doi.org/10.1016/j.engstruct.2021.112006.

Wind speed maximum sustained, mean and gust factor comparison using publicly available H*WIND and Texas Tech University Hurricane Research Team data

Joseph B. Dannemiller [a,*], Douglas A. Smith [b], Stephen Morse [c]

[a]*Texas Tech University, Lubbock, TX, USA, joseph.b.dannemiller@ttu.edu*
[b] *Texas Tech University, Lubbock, TX, USA, doug.smith@ttu.edu*
[c]*Michigan Tech University, Houghton, MI, USA, smmorse@mtu.edu*

ABSTRACT:
Peak wind speeds (maximum sustained), mean wind speeds and gust factors are computed from Texas Tech University Hurricane Research Team (TTUHRT) platform deployments in 10-min windows to facilitate comparison with publicly available data from the National Oceanic and Atmospheric administration (NOAA) Hurricane Research Division (HRD) HWIND hindcasting model. The wind data comparison uses wind data gathered by 5 TTUHRT observation platform deployments during the landfall of six hurricanes. The magnitude in m/s and percent differences are computed for maximum sustained and mean wind speeds for all 10-min windows where the TTUHRT platforms were in the NOAA HRD HWIND hindcast wind fields. The distribution of gust factors computed using TTUHRT data in 7,915 10-min windows is compared with a computed gust factor of 1.18 used to compute maximum sustained wind speeds reported in NOAA HRD HWIND hindcast wind fields. This three-part comparison shows the differences between the TTUHRT wind data used in the creation of NOAA HRD HWIND hindcasts, and the data reported in the hindcasts themselves.

Keywords: TTUHRT, HWIND, gust factor, maximum sustained, mean wind speed

1. INTRODUCTION

The National Oceanic and Atmospheric administration (NOAA) Hurricane Research Division (HRD) HWIND hindcasting model used data from many sources to seed simulations of hurricane wind fields and report maximum sustained winds over open exposure. One of the sources used to seed simulations was data gathered by the Texas Tech university Hurricane Research Team (TTUHRT). This study examines the differences between the wind speed values reported by NOAA HRD HWIND between 1998 and 2005, and the wind speed values computed directly from the TTUHRT time histories. TTUHRT 10-min windows are disaggregated into smooth, open and rough regimes to illustrate differences between the NOAA HRD HWIND and TTUHRT values.

The TTUHRT began deploying atmospheric measurement platforms in the path of landfalling hurricanes in 1998 during the landfall of Hurricane Bonnie. This study uses data gathered by three platforms that each gathered wind speed and direction data at 10m. The three TTUHRT platforms are the Wind Engineering Mobile Instrumented Tower Experiment (WEMITE) #1, WEMITE #2, and three Portable Mesonet Tower (PMT) towers named “Black,” “White” and “Clear.” All five TTUHRT platforms gathered wind data at frequencies of either 5Hz or 10Hz. The data gathered by the TTUHRT platforms is compared to the publicly available wind

* Lead presenter

hindcasting data from NOAA HRD HWIND model for the 1998 landfall of Hurricane Bonnie, the 2003 landfall of Hurricane Isabel, the 2004 landfall of Hurricane Frances, and the 2005 landfalls of Hurricanes Dennis, Katrina and Rita. The NOAA HRD HWIND hindcasts report maximum sustained wind speeds over open exposure computed using a mean wind speed multiplied by a gust factor equal to 1.18 in a 10-min window (Powell et al, 2010; Vickery and Skerlj, 2005). The TTUHRT time histories for all six hurricanes is therefore split into 10-min windows, centered around the middle of the NOAA HRD HWIND hindcast 10-min windows. During time histories of all six storms, the TTUHRT platform deployment locations were in the NOAA HRD HWIND hindcast field a total of 106 times. During the data processing of all TTUHRT 10-min window time histories any window exhibiting non-stationarity, using the Run Test (RunT) and the Reverse Arrangement Test (RAT) (Bendat and Piersol, 1986), was excluded from further comparison. No 10-min window exhibiting non-stationarity occurred during the same 10-min window where a NOAA HRD HWIND hindcasts are reported.

A mean wind speed is computed for each NOAA HRD HWIND hindcast 10-min window by dividing the maximum sustained wind speed reported by the NOAA HRD HWIND utilized gust factor 1.18. An analytical comparison is presented here between the mean wind speeds reported in the NOAA HRD HWIND hindcasts and the TTUHRT platforms. All TTUHRT data is corrected for exposure using aerial imagery captured as close to the landfall of each storm, in each 30-deg wind direction bin, over the full 360-deg range of possible wind directions. Surface roughness values where roughness transitions exist upwind in a 30-deg bin are computed using methods in (Deaves and Harris, 1981; Simiu and Scanlan 1996). The differences are reported in both m/s and percent differences against the TTUHRT computed data.

A comparison between the maximum sustained wind speeds reported by NOAA HRD HWIND and the TTUHRT data would require selective disqualification of all TTUHRT data not captured over open exposure limiting the comparison. Therefore, the mean wind speeds in the 104 10-min windows where the TTUHRT platforms were in the NOAA HRD HWIND hindcasts, already corrected to open exposure, were multiplied by the NOAA HRD HWIND utilized gust factor of 1.18. This facilitates a direct comparison of the maximum sustained wind speeds computed using the TTUHRT mean data versus the values reported in HWIND hindcasts. The differences in all 104 comparisons are reported in both m/s and as percent differences.

Last, the gust factors are computed for all 10-min windows in the time histories recorded by the TTUHRT platforms. The total number of 12,906 10-min windows were recorded by TTUHRT platforms during the landfalls of all six hurricanes. Of these 4,991 were removed from further analysis. Some of the 4,991 were removed due to errors during data capture, but most were removed as they were recorded well after a storm made landfall but before TTUHRT scientists could retrieve one of the TTUHRT platforms. This leaves a total of 7,915 10-min windows for the gust factor comparison. The TTUHRT 10-min windows are separated into three roughness regimes, smooth (z_0<0.03m), open (0.03m≤z_0≤0.07m), and rough (z_0>0.07m) and the distribution of gust factors computed for each roughness regime is provided. The NOAA HRD HWIND utilized gust factor 1.18 is then superimposed on the distribution of each TTUHRT computed gust factor distribution for the three roughness regimes. The location of the NOAA HRD HWIND utilized gust factor 1.18 is then assessed based on its quantile location in each distribution and its probability of exceedance for each roughness regime.

On the computational efficiency of LES and hybrid RANS-LES models in building aerodynamics

Md Faiaz Khaled[a,*], Aly Mousaad Aly[b]

[a]*WISE Research Lab, Louisiana State University, Baton Rouge, LA, USA, mkhale7@lsu.edu*
[b]*WISE Research Lab, State University, Baton Rouge, LA, USA, aly@lsu.edu*

ABSTRACT:
Large-eddy simulation (LES) has proven to offer superior accuracy in regards to predicting surface pressures compared to the Reynolds-averaged Navier Stokes (RANS) models. However, the primary impediment is the high computational cost associated with LES. The authors attempt to investigate the computational cost and accuracy by employing different sub-grid scale (SGS) models in LES and hybrid RANS-LES models. One of the prerequisites of accurate pressure estimations is to ensure a horizontally homogeneous empty computational domain. This study aims to compare the computational competence qualitatively and quantitatively using an empty domain in regards to the ability to maintain horizontal homogeneity. The Wall-adapting eddy viscosity (WALE) SGS model in LES exhibits a significant reduction in computational time. Moreover, the application of detached eddy simulation (DES) and its modified versions manifest encouraging results in reducing computational time and retaining accuracy.

Keywords: Large-eddy simulation (LES), horizontal homogeneity, sub-grid scale (SGS), Detached eddy simulation (DES), computational cost, Wall-adapting eddy viscosity (WALE).

1. INTRODUCTION

Improving buildings' resiliency against frequently occurring powerful windstorms is becoming more critical with evolving demands rooted in climate change. Computational fluid dynamics (CFD) has a growing reputation in the engineering community as a robust tool to model wind flow around a built environment. The performances of CFD applications vary with the turbulence model that is being employed. Reynolds-averaged Navier Stokes (RANS) models are commonly used by CFD practitioners to model and predict mean flow variables. In one of their previous studies, the authors demonstrated the superior performance of $k-\omega\, SST$ model in estimating mean surface pressures in the zone of flow separation. However, local peak pressures are considered to cause extreme suction on roofs leading to considerable damage to buildings' envelope. The large-eddy simulation (LES) model has attained the reputation of offering better accuracy while modeling mean and instantaneous flow fields around bluff bodies than RANS models. However, LES is computationally expensive for near-wall complex flow problems [1]. Besides, some studies have identified discrepancies while predicting peak pressure coefficients with LES. A few of them scrutinized the efficacy of LES in building aerodynamics and highlighted the importance of precise replication of turbulence intensity and length scales in the inflow [2]. Therefore, estimating peak surface pressures and high computational cost are the two core impediments for LES. Furthermore, ensuring minimum artificial acceleration in the computational domain is critical to predicting atmospheric flow fields accurately, which is a commonly encountered challenge in CFD [3].

One of the objectives of this study is to prepare an empty domain with acceptable horizontal

* Lead presenter

homogeneity and integral length scale of turbulence, which are fundamental for the precise prediction of surface pressures. Another side of the study deals with the comparison of computational times to achieve the desired computational domain. LES is accompanied by the application of subgrid-scale (SGS) models. LES can generate dissimilar flow fields even with a similar grid system depending on the SGS model; moreover, the computational time varies with the change in SGS models. Different SGS models are proposed based on the way subgrid eddy viscosity, ν_{SGS}, is computed. As for the hybrid RANS-LES models, three versions of detached eddy simulation (DES)s are used in this study; apart from DES, delayed detached eddy simulation (DDES), and improved delayed detached eddy simulation (IDDES) are adopted. The hybrid models combine the favorable features of RANS and LES, depending on the requirement; also, they use a different transport equation to compute the eddy viscosity. Moreover, the filter width and length scale terms are defined uniquely in different versions of DES. The computational time and accuracy in regards to maintaining horizontal homogeneity are investigated for the hybrid models.

2. METHODOLOGY IN BRIEF

All the simulations are conducted using OpenFOAM 5.0 with identical hardware configurations. The simulations are initiated with LES accompanied by a dynamic one-equation eddy viscosity model as the SGS model. A grid independence study was conducted with this numerical setup. The conditions for accuracy and computational cost in any LES study are closely associated but paradoxical. Finer cell distribution near the walls is necessary for achieving horizontal homogeneity and precise pressure predictions. However, such an arrangement of smaller control volumes adds to the computational cost of LES. The time step was kept constant at 0.004 sec. The upper limit of maximum Courant number ($\cong$ 1.3) was settled by balancing between acceptable accuracy and stability of the investigated flow problem.

The optimal grid is employed to investigate the efficacy of different SGS and hybrid models. Velocities are recorded at five streamwise locations identified in Figure 1 (a). The mean velocity and turbulence intensity profiles obtained from the measured data are compared for different SGS and hybrid models; concurrently, the computational durations are recorded. The qualitative comparisons are made based on figures of vertical profiles and the quantitative comparisons are done based on four validation metrics. A Factor of 2 (FAC2), modified normalized mean bias (MNMB), fractional gross error (FGE), and linear correlation coefficient (R) are the four validation metrics. Moreover, the qualitative analysis is reinforced in the form of scatter plots. The qualitative comparison is made with respect to the profile at the inlet and theoretical profiles. However, the quantitative one is done relative to the inlet profile for investigating homogeneity.

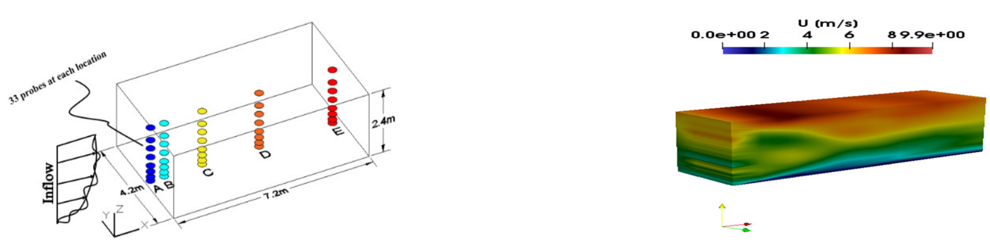

(a) (b)

Figure 1. (a) Computational domain, (b) Instantaneous velocity field at 132 seconds.

3. FINDINGS AND CONCLUSION

The comparative study reveals that LES (LES-7) with the one-equation eddy viscosity (SGS) model fails to offer adequate horizontal homogeneity. LES produces better homogeneity with the wall-adapting eddy viscosity (WALE) (LES-6) SGS model and the dynamic one-equation eddy viscosity (SGS) model (LES-3 and LES-5). However, the latter demands finer near-wall meshing to achieve the level of accuracy offered by the WALE SGS model with a relatively lower cell count. Figure 2 (a) demonstrates the superior performance of LES-3, LES-5, and LES-6 in maintaining the consistency of mean velocity profiles. WALE SGS model offers a reduction in computational time of 35% to 64% while comparing with the two cases of dynamic one-equation eddy viscosity dynamic model. Figure 1 (b) presents the turbulence observed in the instantaneous flow field at 132 seconds for the case LES-6.

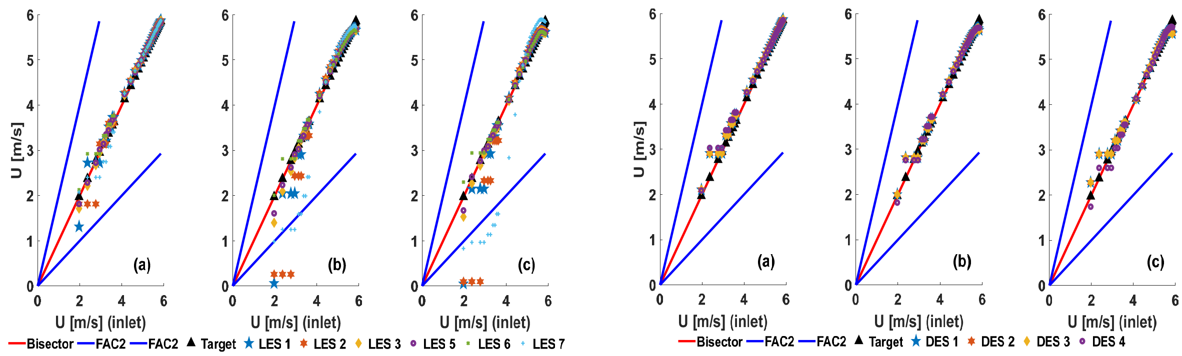

(a) (b)

Figure 2. Scatter plots for comparison of mean velocities at locations A, C, and E; (a) LES cases, (b) DES cases

The scatter plots for the DES cases look much improved when compared with all the LES cases (Figure 2 (b)). The DES cases, with the Spalart-Allmaras (SA) URANS model, yield accuracy comparable to LES, with the WALE SGS model, and LES, with dynamic one-equation eddy viscosity SGS model within Y^+ of 130. DES cases are computationally faster (40%) than LES with a dynamic one-equation eddy viscosity model (Y^+=48); on the contrary, DES cases are time-consuming (40%) than LES, with the WALE SGS model, of almost identical accuracy. Therefore, it can be concluded that LES combined with the WALE SGS model, and DES, DDES, IDDES combined with the SA URANS model can model atmospheric boundary layer (ABL) flow with better accuracy consuming lower computational resources. The next phase of research will involve a similar study with the building inside and the influence of these models on surface pressure predictions.

References

[1] Gopalan H, Heinz S, Stöllinger MK. A unified RANS-LES model: Computational development, accuracy and cost. J Comput Phys 2013;249:249–74. doi:10.1016/j.jcp.2013.03.066.

[2] Ricci M, Patruno L, de Miranda S. Wind loads and structural response: Benchmarking LES on a low-rise building. Eng Struct 2017;144:26–42. doi:10.1016/j.engstruct.2017.04.027.

[3] Blocken B, Stathopoulos T, Carmeliet J. CFD simulation of the atmospheric boundary layer: wall function problems. Atmos Environ 2007;41:238–52. doi:10.1016/j.atmosenv.2006.08.019.

Fragility analysis framework for transmission tower systems subjected to straight line winds

Saransh Dikshit [a*], Alice Alipour [b]

[a] *PhD Candidate, Iowa State University, Ames, Iowa, USA, saransh@iastate.edu (12pt)*
[b] *Associate Professor, Iowa State University, Ames, Iowa, USA, alipour@iastate.edu (12pt)*

ABSTRACT:

Electrical transmission tower systems are an integral part of the electric power network (EPN). These systems are a complex and dynamic system which are vulnerable to natural hazards. Failures associated with these systems can lead to massive blackouts which can severely disrupt the everyday life of the societies that depend on them. In this study, we present a framework for assessing the vulnerability of these systems under wind events through development of fragility functions. Initially, a finite element model for a line of transmission towers, insulators, and conductors is developed in ANSYS and validated with the available test-to-failure data. The models consider the effect of material and geometric nonlinearity. A pushover analysis for the tower of interest is conducted to understand the structural response, select modes of failure, and associated structural parameters. This model is then used to develop a realistic but computationally cost-effective solution to represent the boundary condition of the tower as represented by the adjacent conductors and towers. With the established simplified model, a nonlinear buckling analysis is performed for the tower of interest for straight line winds. This analysis helps with establishing the limit states for the transmission tower. For considering the uncertainty in wind loading, two different wind models are considered which consider the horizontal and vertical coherence associated with straight line winds. These wind models include the wave superposition method and the frequency wavenumber spectrum method. For considering uncertainty in the material properties, two variables which influence the structural response of the tower are selected. These variables include the yield stress and Youngs Modulus for the material composing the transmission tower. Finally, dynamic analysis is carried out for the simplified transmission tower system where the failure criteria is defined by a combination of three conditions which include: failure of the tower, failure of the conductors and the tower and conductors failing together. For applying realistic dynamic wind loads on the system using the two wind models, drag coefficients for the transmission tower and conductors are determined in wind tunnel tests for different orientations for the tower and conductors. The probability of failure for the simplified model is combined for different uncertain models to get a final probability of failure value for the simplified system. This procedure provides a detailed understanding of the behavior of transmission tower system under wind loads. It can also help us in better designing these tower cable systems which can make them more reliable in nature and less susceptible to failure due to wind loads.

Keywords: fragility framework, nonlinear buckling analysis, dynamic wind analysis

* Lead presenter

Drag Coefficients and Wind Loads of Retrofitted Pipe Racks with High Blockage Ratios

S. Ou[1,*], W. Pang[2], M. Stoner[3]

[1]*Clemson University, Clemson, SC, USA, Sovanro@clemson.edu*
[2]*Clemson University, Clemson, SC, USA, wpang@clemson.edu*
[3]*Clemson University, Clemson, SC, USA, mwstone@clemson.edu*

ABSTRACT:
While relatively rare, the failures of steel structures occasionally occur due to extreme wind events such as hurricanes and tornadoes, especially at the erection stage. The American Society of Civil Engineers (ASCE) provides well defined guidelines for determining wind loads for regular buildings; nonetheless, the actual wind loads for complex open frame steel structures is not as clearly understood for practicing engineers. Pipe bridges and pipe racks are open frame structures commonly used in many petrochemical plants. Over the years, additional pipes and cables, in excess of the initial planned number of pipes, are often added to existing pipe racks (or bridges) to accommodate changes in operation needs of the petrochemical plant. This study investigates (1) the influence of adding extra pipes and cable trays on the wind load of pipe rack using a wind tunnel, and (2) strategies to retrofit the pipe rack to accommodate increased wind load due to high blockage ratio. Using the force balance technique in the wind tunnel, this study determines drag coefficients for pipe racks and discusses the changes in wind loads during various stages of construction and retrofit.

Keywords: Drag Coefficient, W Section Beam, Wind Tunnel Test, Pipe Racks, Retrofit

1. INTRODUCTION

Once properly designed and constructed, steel frame is one of the most reliable and resilient structural system. The Canadian Architect (2017) published an article, claiming that steel offers consistency, precision, durability, and guaranteed strength in the most challenging environments. For this reason, there have been many applications for steel frame; one of which is the pipe racks. In the industrial plant, there are occasionally necessities for expansion which results in additional mass on the rack system. Instead of constructing new ones, retrofitting existing pipe racks to accommodate more pipes is often done. ASCE 7 has well defined guidelines for determining wind loads for regular buildings. The actual wind load and drag coefficients for open frame steel structure such as pipe racks are less well understood for practicing engineers. In 1989, the Australia Standards (AS) provided sets of drag coefficients for various sectional shapes, including the optimized shape such as W section, in part 2 of AS 1170. As of 2011, the ASCE Task Committee on Wind-Induced Forces published guidelines for determining drag coefficients for open frame structures (ASCE 2011).

While guidelines for designing new pipe racks and bridges are available, there is a scant body of knowledge on how to consider wind loads on retrofitted open frame steel structure. This paper presents and discusses responses of wind loads for retrofitted pipe racks, along with a series of drag coefficients for W section steel members, and a method for determining drag coefficients for open frame steel structures.

2. METHODS

In this paper, a pipe rack is selected to represent the open frame steel structure, shown in **Figure 1**. A 3D model of the pipe rack is created and properly scaled down for printing using a 3D printer. The printed model is then placed inside a wind tunnel for force balance test with multiple load cells placed at the base to capture the forces during the test. The forces measured in the principal directions (F_i) is used to determine the drag coefficients (C_{di}) using Eq. (1).

$$F_i = \frac{1}{2}\rho V^2 A C_{di} \tag{1}$$

In this equation, ρ, V, and A are the air density, wind velocity, and cross-sectional area, respectively.

Figure 1. Isometric view of pipe racks

A single W section steel column with various flange width to depth ratios is tested in the wind tunnel to verify and extend on the series of drag coefficients provided in AS 1170. To increase the number of pipes that can be carried by an existing pipe rack, one may add extenders as short cantilever beams (see **Figure** 2). A series of force balance tests is conducted on the various configurations shown in **Figure 2** to simulate the different stages of retrofitting. The effect of retrofits on both the change in the magnitude of the load and the path is also investigated.

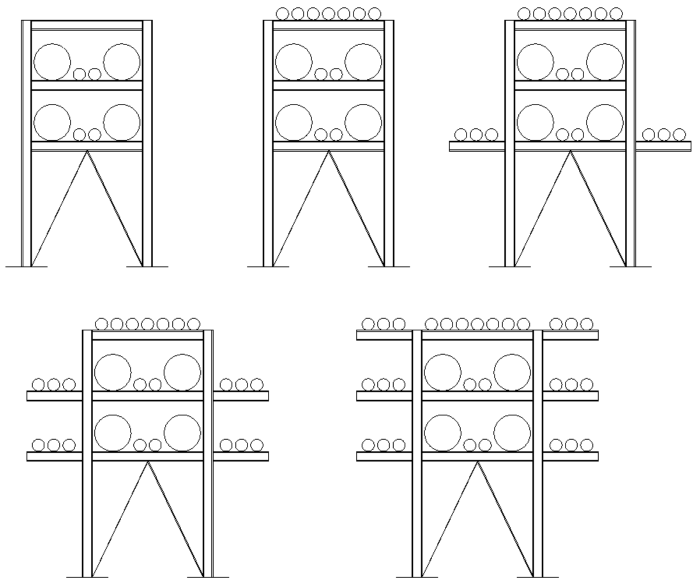

Figure 2. Stages of retrofitted pipe racks

3. RESULTS AND DISCUSSION

While AS 1170 provides drag coefficients for W section shape with the width to depth ratio of 0.48 and 1, this paper is able to expand upon that and provide drag coefficients for the ratio of 0.3, 0.5, 0.7, 0.9, and 1. From comparing the response of wind loads during various stages of retrofit, the resulting impact is identified and discussed. Additionally, the data obtained from the fully constructed pipe racks is used to compare with the force coefficient equation (Eq. 5B.2), provided by the ASCE Task Committee.

4. CONCLUSION

The provided series of drag coefficients for the steel W sections will be useful for practicing engineers to compute the actual wind loads for new or retrofitting of existing pipe racks in industrial facilities. It is anticipated that this study will provide new information and knowledge to engineers for safely retrofitting existing pipe racks and bridges to accommodate increased number of pipes in petrochemical and other similar plants.

ACKNOWLEDGEMENTS

The experiments and analyses presented herein are supported by Clemson Civil Engineering Department and Virginia Carolinas Structural Steel Fabricators Association (VCSSFA). Any opinions, findings, and conclusions presented in this paper are those of the authors and do not necessarily reflect the Clemson Civil Engineering Department and VCSSFA's views.

REFERENCES

AS, 1989. AS 1170: Structural Design Actions. Australian Standard.
ASCE, 2011. Wind Loads for Petrochemical and Other Industrial Facilities. American Society of Civil Engineers.
Canadian Architect. (2017). Design Versatility, Ease of Installation and Resilience. *Canadian Architect, 49*(1), 1-2.

6th American Association for Wind Engineering Workshop (online)
Clemson University, Clemson, SC, USA
May 12-14, 2021

High-Fidelity Probabilistic Collapse Assessment of Tall Steel Buildings under Extreme Winds

Srinivasan Arunachalam [a, *], S.M.J. Spence [b]

[a]*Department of Civil and Environmental Engineering, University of Michigan, Ann Arbor, MI, USA, sriarun@umich.edu*
[b]*Department of Civil and Environmental Engineering, University of Michigan, Ann Arbor, MI, USA, smjs@umich.edu*

ABSTRACT:
To further the knowledge required to implement performance-based wind engineering (PBWE), this study proposes a general framework for the probabilistic collapse assessment of tall steel buildings based on an uncertain fiber-based nonlinear modeling environment driven by wind tunnel informed stochastic wind loads calibrated to site-specific wind data. The fiber-based nonlinear modeling environment provides a means to explicitly simulate potential collapse from yielding, buckling, low-cycle fatigue, and fatigue-induced fiber fracture. For efficient estimation of rare events, e.g. collapse, the modeling environment is housed in a stochastic simulation framework that makes use of an Optimal Stratified-sampling based Monte Carlo Simulation (OSMCS) scheme that minimizes the variance of a target failure probability of interest. The effectiveness of the proposed framework is demonstrated on a 45-story steel braced archetype building.

Keywords: Reliability analysis, Nonlinear modeling, Probabilistic collapse assessment, Monte Carlo methods

1. INTRODUCTION

To cater to the growing interest to migrate from current design practices for wind that are based on elastic analysis and equivalent static loads to performance-based design techniques, there is a need for general performance-based wind engineering (PBWE) frameworks that are applicable to a wide range of structures. Previous studies have proposed frameworks based on incremental dynamic analysis (e.g., Judd and Charney, 2015), nonlinear time history analysis (NLTHA), and dynamic shakedown (Chuang and Spence, 2020), notably, using a range of complexity of numerical structural models to investigate performance under service loads, at first yield, and near collapse. However, they have not explicitly addressed the pressing need to efficiently estimate collapse-level reliability in the face of high-dimensional uncertainties and investigate the relative distance between the reliabilities associated with different limit states of interest. To address these knowledge gaps, a fully probabilistic collapse assessment framework is proposed in this work for assessing collapse probabilities/reliabilities through the adoption of an uncertain high-fidelity fiber-based structural modeling environment that is embedded in an efficient Monte Carlo Simulation (MCS) framework, referred to as the Optimal Stratified-sampling based Monte Carlo Simulation (OSMCS) scheme. The proposed framework is illustrated on a 2D braced steel frame extracted from a fully 3D archetype building.

2. RELIABILITY ASSESSMENT FRAMEWORK

Dynamic analysis of a structural system with material and geometric nonlinearities included, requires solving the following equation of motion:

* Lead presenter

$$\mathbf{M}\ddot{\boldsymbol{u}}(t) + \boldsymbol{f}_D\big(\boldsymbol{u}(t), \dot{\boldsymbol{u}}(t)\big) + \boldsymbol{f}_r\big(\boldsymbol{u}(t)\big) = \boldsymbol{f}_{\bar{v}_H,\alpha}(t) \tag{1}$$

where $\boldsymbol{u}$, $\dot{\boldsymbol{u}}$ and $\ddot{\boldsymbol{u}}$ are the vector of displacements, velocities and accelerations at the discretized degrees of freedom at any time t and $\mathbf{M}$ is the mass matrix, $\boldsymbol{f}_D$ and $\boldsymbol{f}_r$ are the vectors of damping and restoring forces that have nonlinear dependence on $\boldsymbol{u}$, and $\boldsymbol{f}_{\bar{v}_H,\alpha}$ is the stochastic wind load vector for wind direction α and hourly mean wind speed at the building top $\bar{v}_H$. A high-fidelity fiber-based modeling environment with the corotational formulation is used to estimate $\boldsymbol{f}_D$ and $\boldsymbol{f}_r$, such that they account for behaviour such as stiffness degradation, fatigue-induced fiber damage, progressive plastification, and damping. A Rayleigh damping model, as recommended for use in nonlinear analysis (Charney, 2008), is adopted. Each compression member is modeled using two inelastic elements with random initial camber to trigger flexural buckling. The Menegotto-Pinto material model is adopted to simulate the cyclic behaviour of steel along with low-cycle fatigue and potential fiber fracture (Karamanci and Lignos, 2014).

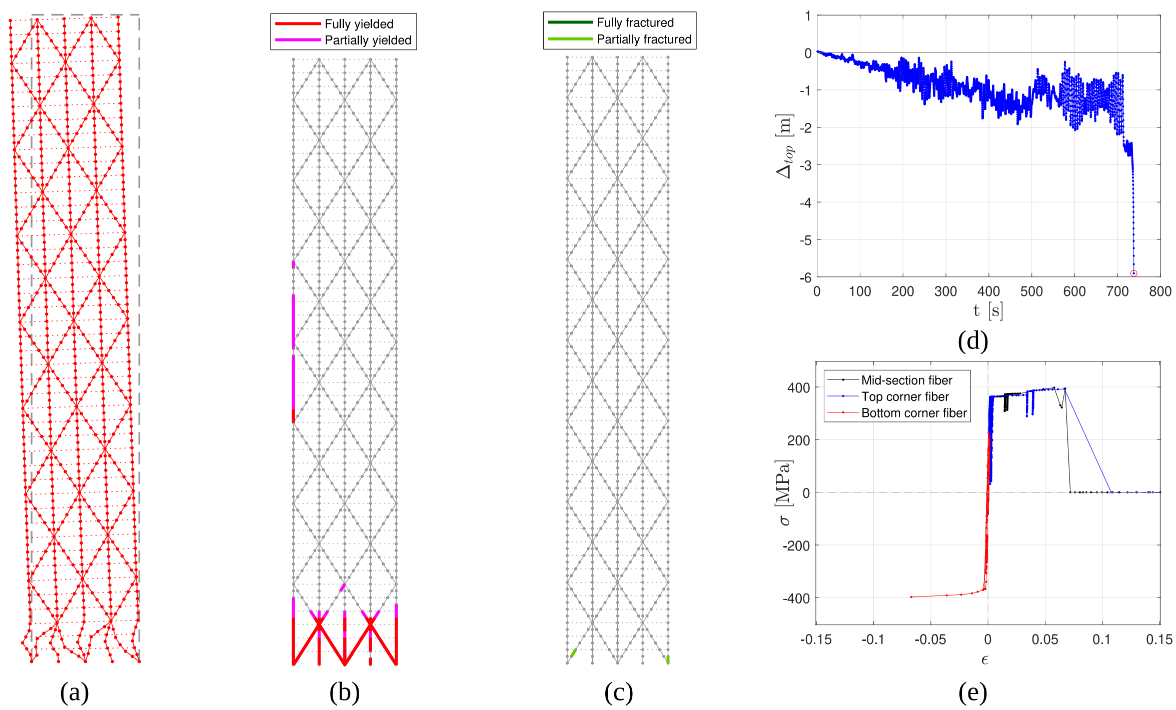

Figure 1. Illustration of a collapse scenario: (a) Deformed shape at collapse; (b) Partially (fiber level) and fully (sectional) yielded components; (c) Partially (fiber level) and fully (sectional) fractured components; (d) Roof displacement history; (e) Stress-strain history of fibers in an end section of the partially fractured base column

The stochastic wind load vector, $\boldsymbol{f}_{\bar{v}_H,\alpha}$, is generated using a peak elastic load effect-based hazard curve and spectral proper-orthogonal decomposition (SPOD) based stochastic wind load model. The hazard curve uses a simplified elastic model, and site-specific wind data to jointly model $\bar{v}_H$ and α. A kernel density copula is utilized to jointly model the wind speed and direction (Ouyang and Spence, 2020). The SPOD model captures complex aerodynamic phenomena on account of calibration to the cross-power spectral density matrix of the building-specific aerodynamic loads, as informed by wind tunnel data. A full range of code-consistent uncertainties in the structure (e.g., damping, material properties, initial imperfections) and loads (e.g., gravity loads, uncertainties associated with the use of wind tunnel data) are propagated through the system using limited sample sets. This is achieved using the OSMCS scheme, a modified version of the conditional simulation scheme (Ouyang and Spence, 2020), in which MCS samples are optimally allocated to wind speed subevents to minimize the estimator variance.

3. CASE STUDY

A 2D steel braced frame extracted from a 45-story archetype building assumed to be located in New York City is used to demonstrate the proposed framework. To implement OSMCS, the hazard curve was partitioned into 10 mutually exclusive and collectively exhaustive wind speed intervals and a total of 1000 MCS samples were utilized. The optimal allocation was based on variance minimization for collapse probability. Fig. 1 shows a collapse mechanism together with component yielding, fracture, displacement history, and stress-strain histories illustrating fiber fracture. Table 1 summarises the failure probabilities expressed as annual exceedance probabilities (AEP) and 50-year reliability indices, β_{50}, for four limit states of interest. The efficiency of the OSMCS scheme in comparison to crude MCS is also shown. From Table 1, it is clear that: 1) the probability of component failure, in terms of fracture, is significantly lower than the probability of component-level first yield; and 2) the probability of system collapse is not significantly lower than the probability of component-level first yield, illustrating the importance of explicit collapse analysis if wind excited structures are to be allowed to experience inelasticity during design.

Table 1. Failure probabilities and 50-yr reliability indices

Limit State	System Collapse	System First Yield	Component First Yield	Component Fracture
AEP	6.83×10^{-5}	7.04×10^{-4}	6.58×10^{-4}	7.13×10^{-6}
COV (MCS)	211%	66%	68%	654%
COV (OSMCS)	13%	36%	38%	39%
β_{50}	2.71	1.82	1.85	3.38

4. CONCLUSION

A general framework for high-fidelity probabilistic collapse assessment of steel structures subjected to extreme wind loads was developed. The need to explicitly evaluate collapse if inelasticity is to be allowed in design was illustrated.

ACKNOWLEDGEMENTS

The research effort was supported in part by the National Science Foundation (NSF) under Grant No. CMMI-1750339.

REFERENCES

Charney, F.A., 2008. Unintended consequences of modeling damping in structures. Journal of structural engineering, 134(4), pp.581-592.

Chuang, W.C., and Spence, S.M., 2020. Probabilistic performance assessment of inelastic wind excited structures within the setting of distributed plasticity. Structural Safety, 84, p.101923.

Judd, J.P. and Charney, F.A., 2015. Inelastic behavior and collapse risk for buildings subjected to wind loads. In Structures Congress 2015 (pp. 2483-2496).

Karamanci, E. and Lignos, D.G., 2014. Computational approach for collapse assessment of concentrically braced frames in seismic regions. Journal of Structural Engineering, 140(8), p.A4014019.

Ouyang, Z. and Spence, S.M., 2020. A Performance-Based Wind Engineering Framework for Envelope Systems of Engineered Buildings Subject to Directional Wind and Rain Hazards. Journal of Structural Engineering, 146(5), p.04020049.

Peak Wind Effects on Low-Rise Building Roofs and Rooftop PV Arrays

R. Braun[a], D. Chen[a], A. Chowdhury[b], J. Estephan [b,*], C. Gordon[a], P. Irwin[b], G. Johnson[a], B. Kennedy[a], G. Lyman[a], E. Raney[a], D. Reed[c], R. Sanford[a], S. Wang [c]

[a]*Central Washington University, Ellensburg, WA, USA*
[b]*Florida International University, Miami, FL, USA,*[b,*] *jeste059@fiu.edu*
[c]*University of Washington, Seattle, WA, USA*

ABSTRACT:
This paper describes a combined experimental-numerical investigation into the estimation and prediction of peak wind pressure loadings on the roofs and roof-top appurtenances of low-rise buildings. Preliminary results for the appurtenance examined here, a rooftop photovoltaic (PV) array, located on the top of the Hogue Technology Center (HTC) at Central Washington University (CWU) in Ellensburg, Washington will be discussed. These include numerical results from finite element models as well as from the pressure sensor, accelerometer, and strain gauge time series data. Designs of physical models of the full-scale and proposed 1:20 and 1:100 scale wind tunnel tests of the array and the building rooftop to be performed at the NSF NHERI Wall of Wind Experimental Facility (WOW EF) at Florida International University (FIU) will be presented.

Keywords: Peak winds, field measurements, wind tunnel testing, photovoltaic array

1. BACKGROUND

There are two major gaps in the estimation of peak wind effects on low-rise structures and their appurtenances. The first is aerodynamic in nature: the scales of traditional wind tunnel testing for low-rise buildings are mostly accurate except for peak negative pressures or suctions. Large-scale wind tunnel results do not account for energy-containing low-frequency eddies (Mooneghi et al., 2016; Moravej, 2018). One of the goals of the investigation described here is to use full-scale measurements in-situ and in the wind tunnel to account for the “missing” low-frequency turbulence and to develop robust hybrid simulation techniques. The second gap is dynamic: ASCE7-16 (ASCE 7, 2016) limits the investigation of structural dynamic effects to 1 Hz natural frequency and lower. Yet many appurtenances on rooftops, such as photovoltaic arrays, have displayed wind-induced vibrations with natural frequencies at 15 Hz (Moravej et al., 2015; Naeiji, 2017).

The research described here addresses these two gaps through field investigations, large-scale boundary layer wind tunnel testing, and small-scale dynamic modelling. Field measurements are underway on the Hogue Technology Center (HTC) at Central Washington University (CWU) to obtain time series data for comparison with upcoming large- and small-scale wind tunnel testing at Florida International University (FIU). This comparison will be used to determine transfer functions to account for low-frequency turbulence results missing in large-scale testing and subsequently improve the estimation of peak wind loads on low-rise buildings and their appurtenances. The details of the field measurements and numerical modelling are presented in the next section.

* Lead presenter

2. METHODS
2.1 Field investigations
The rooftop PV array, previously investigated by Bender et al. (2018), is arranged in landscape format with three rows of sensors in two sections. The end of the array is subject to an approximately N-S dominant wind in a suburban boundary layer. Figure 1 shows a close-up of the rooftop instrumentation of the anemometers, the array, and the modular pressure systems.

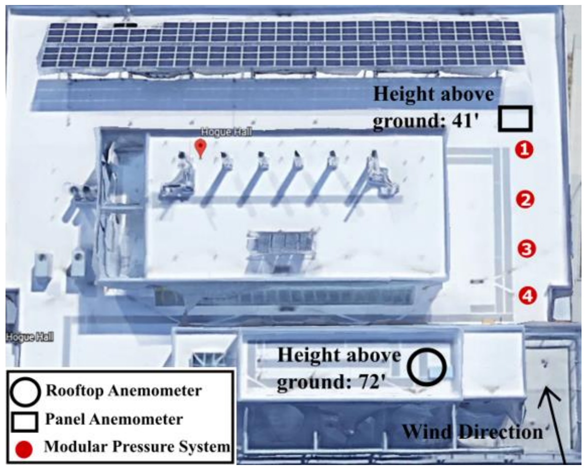

Figure 1. CWU rooftop instrumentation

The rooftop and panel ultrasonic anemometers Model 85000 and 86000, respectively, are manufactured by R.M. Young. The two anemometers collect wind speed and direction data at a sampling rate of 500 Hz. The modular pressure systems were designed by the research group for this project. Figure 2 shows a detailed depiction.

Figure 2. Modular pressure system

The modular pressure system is used to measure net rooftop pressures. Details of the instrumentation will be provided in the final paper. Ten pressure sensors have been installed at the end of the array as shown in Figure 3. These measure the net pressures on the panel at a point. The Setra pressure transducers were installed in the aluminum framing of the panels to prevent damage to their PV properties. The sensor locations for this investigation were based on the largest pressure loadings obtained in the previous study in addition to expanding the instrumentation to the cantilevered panels at the very end of the array. Accelerometers and strain gauges have been attached to the panels, as shown in Figure 3.

Figure 3. PV array sensor locations.

2.2. Numerical investigations

A modal analysis using Finite Element Modelling (FEM) was performed on SAP2000® to obtain the dynamic properties of the PV array. The estimated FEM natural frequencies of the panels were compared with those using the hammer test. Sample hammer test results for the PV panels are given in Figure 4.

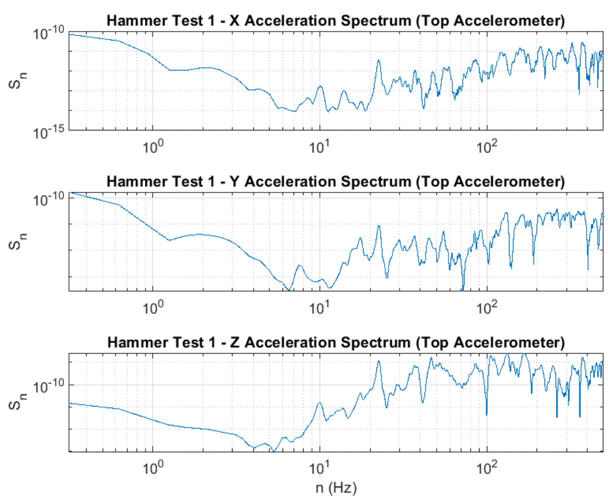

Figure 4. Sample hammer test results for a PV panel

3. RESULTS

Preliminary results suggest the following:

a. A transfer function can be used to incorporate low-frequency turbulence effects (Estephan & Chowdhury, 2020);
b. Wind-induced dynamic effects can be incorporated using the mechanical admittance function; and

c. Long-term outdoor data measurements are limited by equipment durability issues.

4. REFERENCES

ASCE 7. (2016). *Minimum Design Loads and Associated Criteria for Buildings and Other Structures*. Reston, VA: ASCE/SEI 7–16.

Bender, W., Waytuck, D., Wang, S., & Reed, D. A. (2018). In situ measurement of wind pressure loadings on pedestal style rooftop photovoltaic panels. *Engineering Structures*, *163*, 281–293. https://doi.org/10.1016/j.engstruct.2018.02.021

Estephan, J., & Chowdhury, A. (2020). Incorporating low-frequency gusts and dynamic effects for small structures tested at large scales. *AAWE Newsletter*, *August*. www.aawe.org

Mooneghi, M. A., Irwin, P., & Chowdhury, A. G. (2016). Partial turbulence simulation method for predicting peak wind loads on small structures and building appurtenances. *Journal of Wind Engineering and Industrial Aerodynamics*, *157*, 47–62. https://doi.org/10.1016/j.jweia.2016.08.003

Moravej, M. (2018). Investigating Scale Effects on Analytical Methods of Predicting Peak Wind Loads on Buildings. *FIU Electronic Theses and Dissertations*. https://doi.org/10.25148/etd.FIDC006834

Moravej, M., Chowdhury, A., Irwin, P., & Zisis, I. (2015). Dynamic effects of wind loading on photovoltaic systems. *Proceedings of the 14th International Conference in Wind Engineering*.

Naeiji, A. (2017). *Wind Loads on Residential Rooftop Solar Photovoltaic Panels* [FIU Electronic Theses and Dissertations, Florida International University]. https://doi.org/10.25148/etd.FIDC006588

ACKNOWLEDGEMENTS

The authors would like to acknowledge the National Science Foundation (NSF) financial support for a collaborative project (Award No. 1824995 and 1825908). They take sole responsibility for the views expressed in this paper, which may not represent the position of NSF or their respective institutions.

Numerical modeling of debris flight in a one-cell tornado wind field

Ali Tohidi [a]

[a] *Mechanical Engineering Department, San José State University, San José, CA, USA.*
ali.tohidi@sjsu.edu

ABSTRACT:
The windborne debris flight in strong wind fields of tornados is known to contribute significantly to the incurred damages. Previously, there has been a considerable amount of work done on the flight trajectory and impact of compact and plate-like debris in such wind fields. However, less attention has been paid to the flight path of rod-like debris. This study numerically models the trajectory of rod shape debris in the a one-cell tornado wind field and compares the results with trajectories of mass equivalent particles with different shapes, that is compact, and plate shapes. The preliminary results show the importance and effects of rotational motion on the flight path of rod-like debris compared to the mass equivalent compact debris with the same initial conditions. The present work conducts a set of stochastic simulations and characterizes the effects of shape on the flight path, landing distribution, and energy of impact upon landing.

Keywords: Wind-borne, debris, Tornado, Flight Path, Stochastic, Deterministic

1. INTRODUCTION

Tornados present a powerful whirling column of air that is bounded by the surface of the earth at the bottom and, usually, cumulonimbus clouds at the top. Each year in the United States more tornadoes occur than in any other country (Dotzek, 2003). NOAA's Storm Prediction Centre, reported 1,053 tornados in 2020, which is over three times the average of the reported cases in Europe (Dotzek 2003 & NOAA 2021). Most tornados generate wind speeds between 15-50 m/s but, in extreme cases, the velocity can reach more than 100 m/s (Baker & Sterling, 2017). Such winds not only cause different loading mechanism on the structures (Baker & Sterling, 2017), that may lead to structural damages, but also loft debris that is often visible as a rotating cloud around the tornado base. The impact energy of the lofted debris and their subsequent penetration to the structural elements are recognized to contribute significantly to the incurred damages (Grayson et al., 2012). For instance, the January 2020 tornados in the U.S., caused substantial property loss across multiple states and led to numerous injuries, and 10 fatalities (Smith, 2021). Thus, in order to better estimate the risks from tornados and, devise and improve on the existing tornado preparedness plans, it is important to characterize the amount of energy and radius of impact from lofted debris to the built environment during such wind events.

To this end, the flight path of debris needs to be resolved in the tornado-generated velocity field. The trajectories depend on the physical properties of the particles such as density, initial mass, geometric characteristics, namely shape and aspect ratio, initial release angles, and the turbulence characteristics of the ambient wind field (Kordi & Kopp, 2011). Previous studies have mostly investigated the trajectories of compact debris (Karimpour & Kaye, 2011; Liu et al., 2021) and plate-like debris (Kordi & Kopp, 2011) and little attention has been paid to the dispersion of rod-like debris in wind events. The existing literature on tornado wind fields, however, is rich; there is a large volume of published studies on the velocity field description and its turbulent characteristics. In the present work, we study the effects of particle geometry (shape and aspect ratio), and the initial release angles on the trajectories of rod-like debris compared to the

* Ali Tohidi

compact and plate-like ones with the same mass. Since the aim of the study is to investigate the effects of shape and initial release angles on the flight path, the ambient tornado-generated wind field is modelled using a simple one-cell tornado model proposed by (Baker & Sterling, 2017) without considering any turbulence effects.

2. TORNADO WIND FIELD AND DEBRIS TRANSPORT MODELS

Although multi-cell tornados are more common than one-cell tornados (Baker & Sterling, 2017), one-cell model is adopted to reduce the complications that multi-cell tornado velocity field may induce in the resolved trajectories. The model efficiently simulates the tangential, radial, and axial velocity profiles for both forced and free-vortex regions and is validated against experimental data (Refan et al., 2014). **Figure 1-(a)**, shows the wind velocity profiles of a one-cell tornado over open/grass land.

The trajectory of non-compact particles is often complicated which subsequently affects their flight range and landing distribution. Thus, a transport model that solves the governing equations of motion for non-compact particles in a fully deterministic 3D 6-degrees-of-freedom (DOF) mode is adopted; refer to (Grayson et al., 2012) for details. Also, the transport model incorporates the experimentally measured steady aerodynamic force and moment coefficients of (Richards et al., 2008). In a more recent study (Tohidi & Kaye, 2017b), modified the model to conduct stochastic simulations of the rod-like particles and experimentally validated the results (Tohidi & Kaye, 2017a). The transport model uses a one-way coupling approach to extract ambient velocity components, i.e., (U, V, W), from the tornado wind field.

3. SIMULATIONS AND RESULTS

The modelled tornado wind has maximum tangential velocity of 50 m/s at the core radius of 50 m with swirl ratio, $S = V_m/U_m$, one; where V_m and U_m are, respectively, the maximum tangential and radial velocities that occur at the core radius. The boundary layer thickness is calculated, based on the method of (Gjøsund, 2012) and data provided in (Baker & Sterling, 2017), for surface roughness of $z_0 = 0.03$ which corresponds to open flat terrain or grass land with few obstacles (Cermak & others, 1999). The initial release position is considered to be at the core radius, i.e. $(x_0 = 50\ m, y_0 = 0)$, and well over the boundary layer thickness $(z_0 = 10\ m)$. The rest of the initial conditions for the simulation are shown in Table 1.

Table 1. Initial conditions of the simulations. Here, $(\boldsymbol{\theta_x}, \boldsymbol{\theta_y}, \boldsymbol{\theta_z})$ are Tait–Brayan angles of the particles.

Debris geometry	Density $[\frac{kg}{m^3}]$	Aspect ratio, L_{max}/L_{min}	Characteristic length $[m]$	Tait-Brayan angles $(\theta_x, \theta_y, \theta_z)\ [rad]$	
				Deterministic	Stochastic
Compact	320	1	0.05	0, 0, 0	N/A
Plate	320	4	0.02	0, 0, 0	random~$[0, 2\,\pi]$
Rod	320	16	0.02	0, 0, 0	random~$[0, 2\,\pi]$

It should be noted that the physical properties of debris are chosen such that they have the same mass. Simulations are conducted with time interval of 0.01 s until the particle contact the ground. The time integration is done using modified Euler method introduced in (Grayson et al., 2012). **Figure 1- (b, c)**, respectively, shows the resolved trajectories for a compact and rod-like debris that are release from the same position, i.e. $(x_0 = 50\ , y_0 = 0\ \ , z_0 = 10)$, with the same random release angles.

The preliminary results show the importance of rotational effects on the trajectory of the rod shape particles. We propose to conduct a comprehensive stochastic simulation in order to capture the average behavior of the flight path of rod-like debris compared to the compact and plate-like ones in one-cell tornado wind field.

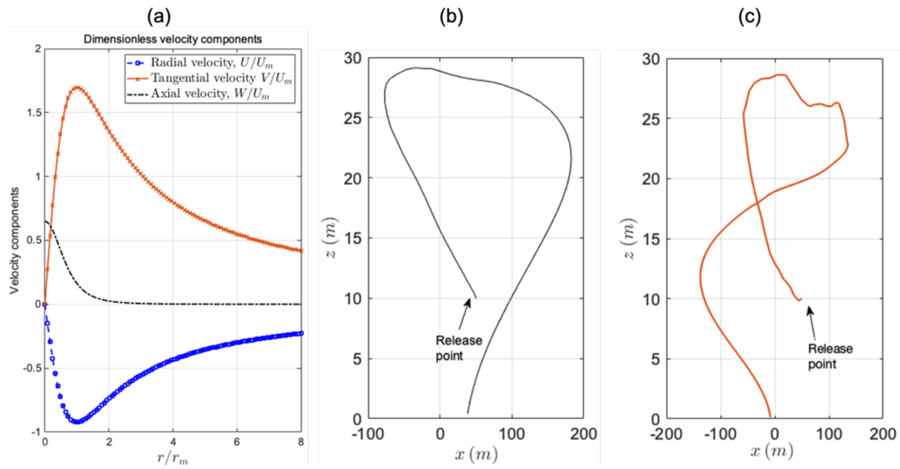

Figure 1. Shown are (a) dimensionless velocity field of the one-cell tornado and, trajectory of a compact (b) and rod-like (c) debris that are release from the same release position with random initial release angles.

REFERENCES

Baker, C. J., & Sterling, M. (2017). Modelling wind fields and debris flight in tornadoes. *Journal of Wind Engineering and Industrial Aerodynamics*, *168*(February), 312–321. https://doi.org/10.1016/j.jweia.2017.06.017

Cermak, J. E., & others. (1999). *Wind tunnel studies of buildings and structures*.

Dotzek, N. (2003). An updated estimate of tornado occurrence in Europe. *Atmospheric Research*, *67–68*, 153–161. https://doi.org/10.1016/S0169-8095(03)00049-8

Gjøsund, S. H. (2012). Simplified Approximate Expressions for the Boundary Layer Flow in Cylindrical Sections in Plankton Nets and Trawls. *Open Journal of Marine Science*, *02*(02), 66–69. https://doi.org/10.4236/ojms.2012.22009

Grayson, M., Pang, W., & Schiff, S. (2012). Three-dimensional probabilistic wind-borne debris trajectory model for building envelope impact risk assessment. *Journal of Wind Engineering and Industrial Aerodynamics*, *102*, 22–35. https://doi.org/10.1016/j.jweia.2012.01.002

Karimpour, A., & Kaye, N. B. (2011). *On the stochastic nature of compact debris flight*. https://doi.org/10.1016/j.jweia.2011.11.001

Kordi, B., & Kopp, G. A. (2011). Effects of initial conditions on the flight of windborne plate debris. *Journal of Wind Engineering and Industrial Aerodynamics*, *99*(5), 601–614. https://doi.org/10.1016/j.jweia.2011.02.009

Liu, Z., Cao, Y., Yan, B., Hua, X., Zhu, Z., & Cao, S. (2021). Numerical study of compact debris in tornadoes at different stages using large eddy simulations. *Journal of Wind Engineering and Industrial Aerodynamics*, *210*, 104530. https://doi.org/10.1016/j.jweia.2021.104530

Refan, M., Hangan, H., & Wurman, J. (2014). Reproducing tornadoes in laboratory using proper scaling. *Journal of Wind Engineering and Industrial Aerodynamics*, *135*, 136–148. https://doi.org/10.1016/j.jweia.2014.10.008

Richards, P. J., Williams, N., Laing, B., McCarty, M., & Pond, M. (2008). Numerical calculation of the three-dimensional motion of wind-borne debris. *Journal of Wind Engineering and Industrial Aerodynamics*, *96*(10–11), 2188–2202. https://doi.org/10.1016/j.jweia.2008.02.060

Smith, A. B. (2021). *U.S. Billion-Dollar Weather and Climate Disasters, 1980 - Present*. NOAA National Centers for Environmental Information (NCEI). https://doi.org/10.25921/stkw-7w73

State of the Climate: Tornadoes for Annual 2020. (2021). Information, NOAA National Centers for Environmental. https://www.ncdc.noaa.gov/sotc/tornadoes/202013

Tohidi, A., & Kaye, N. B. (2017a). Aerodynamic characterization of rod-like debris with application to firebrand transport. *Journal of Wind Engineering and Industrial Aerodynamics*, *168*(June), 297–311. https://doi.org/10.1016/j.jweia.2017.06.019

Tohidi, A., & Kaye, N. B. (2017b). Stochastic modeling of firebrand shower scenarios. *Fire Safety Journal*, *91*(March), 91–102. https://doi.org/10.1016/j.firesaf.2017.04.039

Characterization of surface roughness from LIDAR and anemometer measurements of near-surface storm winds.

H. Besing[a,*], S. Lazarus[a], S. Sridhar[a], J. Wang[a], C.S. Subramanian[a], J-P Pinelli[a], J. Zhang[a], J. Sun[b]

[a] *Florida Institute of Technology, Melbourne, Florida, US, hursensors@lists.fit.edu*
[b] *Shanghai, China, sun128764@gmail.com*

ABSTRACT:

Assessing the impact of a landfalling tropical cyclone (TC) can be challenging due to the lack of a coherent surface wind analysis. Albeit intermittent, surface winds over the ocean are still measured via in-situ dropsondes, SFMR, etc. Unfortunately, surface data (e.g., Automated Surface Observing Systems, ASOS) are more problematic as power outages are typically widespread during high impact events. In terms of spatial and temporal coverage, Doppler Radar is a useful tool, but the dual-Doppler analyses generally do not extend below a few hundred meters and thus must be extrapolated downward in order to estimate the near surface wind. In the case of a single radar – a VAD approach is generally necessary, but challenging, in the presence of deep convection. In either case, this requires knowledge of surface roughness and an assumption that the log law relationship is valid. However, even under neutral conditions, the latter is not a certainty – especially in the TC environment. Conversely, ground-based LIDAR systems can reliably be used to provide high resolution profiles of the three- dimensional wind field – however they do so only at a single point. The estimation of surface winds during a storm are generalized over large areas, and often do not represent the true winds experienced at a location. Local effects are dependent on the upwind surface elements at a given location, and thus the use of surface roughness is great way to incorporate local effects in the estimate of near surface wind speeds.

Winds from the Florida Tech LIDAR are combined with those from our Wireless Sensor Network (WSN) and R.M. Young anemometer during the passage of tropical storm Isaias on 2 August 2020. A conically scanning ZephIR Z300 LIDAR (Campbell Scientific, 2012) was sited at 28.177°N, -80.590 °W on the coast in east-central Florida and had an open fetch with respect to the on-shore flow. Wind profiles were sampled at approximately 20 s intervals at 10 vertical range gates (from 11-to-150 m above ground level (AGL)). As the outer rainbands of Isaias moved across the east-central Florida coast over 2000 vertical profiles were recorded during an 11-h window. The R.M. Young anemometer was located inland, approximately 0.36 km from the lidar , mounted at 7.3 m AGL. The wind data was collected over a 48-h period, before, during, and after the passage of Isaias off the east-central Florida coast, at a temporal resolution of 6s. Using representative surface roughness estimates and the log law, the LIDAR measurements are compared with those of the anemometer. The impact of the dynamic ocean surface with respect to the upstream roughness, are also examined.

To estimate dynamic oceanic roughness lengths, 20 s data from the LIDAR was averaged over 10 min periods. To estimate $z_{o,}$ the turbulence intensity was calculated using the LIDAR average 10m winds for each period. The TI responds to the passage of rainbands and the associated convection as changes in the wind speed impact the ocean surface. The passage of the rainband is accompanied by higher wind speeds which temporarily result in a rougher surface. . These fluctuations in z_o in the coastal zone are an important aspect in characterizing the land- falling tropical cyclone environment.

Our work includes an approach to determine z_o values using land cover and QGIS, an open-sourced geographic information systems software. A 'wedge' tool of variable angular width, based on upwind direction from a given location has been developed. The tool is used to extract a slice of 30 m resolution National Land Cover Database (NLCD) data. A look-up table that assigns z_o values (Markert et al., 2019; Nicholas & Lewis Jr., 1980; Wiernga, 1993), to land cover types and is functionally weighted based on distance from the location will be tested using the

*Lead Presenter, hbesing2018@my.fit.edu

LIDAR and anemometer data. When appropriate, the NLCD database may be modified in order to account for the classification of surfaces such as highways, airports, etc., that are currently labeled as high intensity developed areas even though they are relatively smooth surfaces when compared to commercial/industrial buildings also in this category.

In previous work Besing et al. (2021) compared dual-Doppler Analysis (DDA) winds from the University of Oklahoma SMART Radar (Biggerstaff et al., 2005) and the National Weather Service WRS-88D radar located in Melbourne, Florida with data collected from the FIT LIDAR during the passage of Hurricane Dorian on 2 September 2019. Using ocean based roughness estimates obtained from the TI calculations, a log-law relationship was used to "connect" winds between the lowest DDA level (500 m) to the LIDAR top range gate (150 m). In cases where winds at 500 m were a greater magnitude than those at 150 m, the log-law relationship yielded estimates frequently within +/- 1 standard deviation of the observed winds at that height. In cases where winds aloft were less than those at 150 m, the log-law relationship largely underestimated wind speeds. Even with improved surface roughness estimates, the reconstruction of the surface wind field within a tropical cyclone environment is a challenge and will likely require a more statistical approach.

Keywords: Wireless Sensors Network, Hurricane deployment, LIDAR, Young Anemometer, Surface Roughness

ACKNOWLEDGEMENTS
The National Science Foundation (NSF) financially supports this project under grants CMMI-1520817 and 2022469. In addition, the National Institute of Standards and Technology (NIST) supports the development and deployments of the WSN under grant 70NANB19H088. These supporters are gratefully acknowledged.

REFERENCES

Besing, H., Lazarus, S., Sridhar, S., Subramanian, C. S., & Pinelli, J.-P. (2021, January 12). *A Combined LiDAR and Dual-Doppler Assessment of the Near Surface Wind Field in East-Central Florida During Hurricane Dorian (2019)*. 101st American Meteorological Society Annual Meeting.

Biggerstaff, M. I., Wicker, L. J., Guynes, J., Ziegler, C., Straka, J. M., Rasmussen, E. N., Doggett, A., Carey, L. D., Schroeder, J. L., & Weiss, C. (2005). The Shared Mobile Atmospheric Research and Teaching Radar: A Collaboration to Enhance Research and Teaching. *Bulletin of the American Meteorological Society*, *86*(9), 1263–1274. https://doi.org/10.1175/BAMS-86-9-1263

Campbell Scientific. (2012). *Operations& Maintenance Manual*.

Markert, A., Griffin, R., Knupp, K., Molthan, A., & Coleman, T. (2019). A Spatial Pattern Analysis of Land Surface Roughness Heterogeneity and its Relationship to the Initiation of Weak Tornadoes. *Earth Interactions*, *23*, 1–28. https://doi.org/10.1175/EI-D-18-0010.1

Nicholas, F. W., & Lewis Jr., J. E. (1980). *Relationship Between Aerodynamic Roughness and Land Use and Land Cover in Baltimore, Maryland* (The Influence of Land Use and Land Cover in Climate Anlaysis) [Geological Survey Professional Paper 1099-C].

Wiernga, J. (1993). Representative roughness parameters for homogeneous terrain. *Boundary-Layer Meteorology*, *63*(4), 323–363. https://doi.org/10.1007/BF00705357

6th American Association for Wind Engineering Workshop (online)
Clemson University, Clemson, SC, USA
May 12-14, 2021

Wireless Sensor Network System Data Acquisition and Analysis using DesignSafe-CI

S. Sridhar[a] *, J.-P. Pinelli [a], J. Zhang [a], C.S. Subramanian[a], J. Wang[a], J. Sun[b], S. Lazarus[a], H. Besing[a]

[a]*Florida Institute of Technology, Melbourne, Florida, US, hursensors@lists.fit.edu*
[b] *Shanghai, China, sun128764@gmail.com*

ABSTRACT:
Florida Tech's Wireless Sensor Network (WSN) system consists of pressure and temperature sensors, and anemometer. The objective of the WSN is to collect data to measure wind loads on a variety of components on residential houses, such as roof, walls, windows, fascia, soffits, and shingles. The WSN system is generally deployed in the field on residential houses during tropical storms or hurricanes, while in laboratory tests the WSN system is deployed on a full- or large-scale model house in the Wall of Wind (WoW) at Florida International University (FIU). The WSN system collects data and communicates wirelessly to a local laptop. The system has the capability to upload the collected data in quasi- realtime to a cloud data storage by public Wi-Fi. This article describes how to synchronize the WSN system operations with the NSF-NHERI (National Science Foundation – Natural Hazards Engineering Research Infrastructure) cloud platform DesignSafe-CI for data uploading, processing, analysis, and visualization.

Keywords: Wireless Sensor Network, DesignSafe, Data Processing & Analysis, Jupyter Notebooks

1. INTRODUCTION

The FIT's WSN system (Subramanian et al.,2012) is deployed on residential homes during tropical cyclones or other high- impact wind events to measure pressure, wind speed, and wind direction. A remote laptop collects sensor data and uploads it to DesignSafe using a Wi-Fi hotspot device. Scripts embedded in Jupyter Notebooks process the raw data and convert it into meaningful information such as pressure, wind speed, and wind direction in their physical units. The analysis tools allow user-interactive applications to calculate and visualize specific information and plots. Figure 1 shows the generic process to access and analyse both field and experimental data.

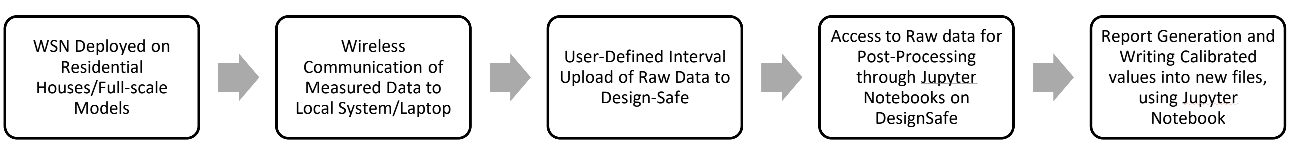

Figure 1. Data Flow Process from WSN Deployment to DesignSafe's Jupyter Notebooks

The following sections provide further details about this process.

1.1.Tapis for uploading raw data to DesignSafe-CI

DesignSafe offers Tapis (an open-source API) for uploading large amounts of data to a user-

* Lead presenter

defined project folder on the same cloud platform. The lack of manual uploading of data, decreases the chance of missing any important raw data file. Tapis is initiated before every measurement by signing into user's DesignSafe account through Windows Power Shell and creating a token. Figure 2 shows an example token which refreshes itself timely to enable continuous uploading of raw data from remote laptop to DesignSafe project folder.

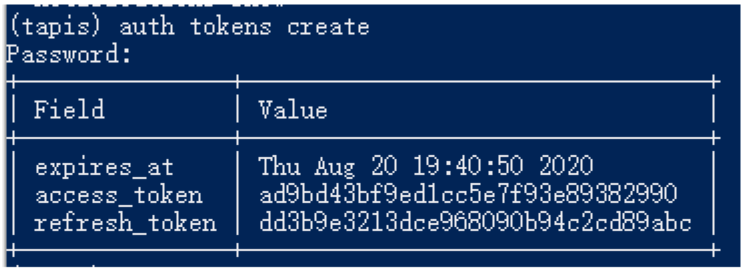

```
(tapis) auth tokens create
Password:
+---------------+--------------------------------+
| Field         | Value                          |
+---------------+--------------------------------+
| expires_at    | Thu Aug 20 19:40:50 2020       |
| access_token  | ad9bd43bf9ed1cc5e7f93e89382990 |
| refresh_token | dd3b9e3213dce968090b94c2cd89abc|
+---------------+--------------------------------+
```

Figure 2. Token created on Tapis that connects remote laptop and DesignSafe to upload raw data

1.2. Jupyter Notebooks for post-processing

Jupyter is an open-source application that also acts as an Integrated Development Environment (IDE). It is a useful tool for developing interactive documents that contain live code, images and information, with the biggest advantage being it is integrated within DesignSafe. The notebooks in this project convert raw data to meaningful information and provide a user-interactive platform for generation of report and a variety of visualizations. For older WSN deployments, MATLAB scripts (Gurram et al., 2016, 2017) performed similar data processing tasks. The post-processing details for field and experimental testing will be covered in two sections below.

1.2.1. Field Testing – Isaias, August 2020

Maximum wind speeds measured by the WSN reached between 11 and 12 m/s, in Satellite Beach, Florida, on the evening of 2 August, 2020, while then tropical storm Isaias was off the east coast of Florida.. The WSN sensors with 2 anemometers, 18 pressure sensors and 1 reference pressure sensor, collected pressure, wind speed, and wind direction data, on the rooftop of a house. Two Jupyter Notebooks converted the raw data values in different formats into their respective physical units. The first Jupyter Notebook asks the user to define sensor numbers, column numbers in the data file for essential raw data categories (pressure, temperature, time, and wind data), and time stamp format. This notebook enables different datafiles of any format to be processed and output in a standardized format. The second Jupyter Notebook applies calibration constants to the raw data thereby creating new csv files and so-called Pandas DataFrames. Figure 3 shows the change in data from raw data to values with physical units when using Jupyter Notebooks for post-processing.

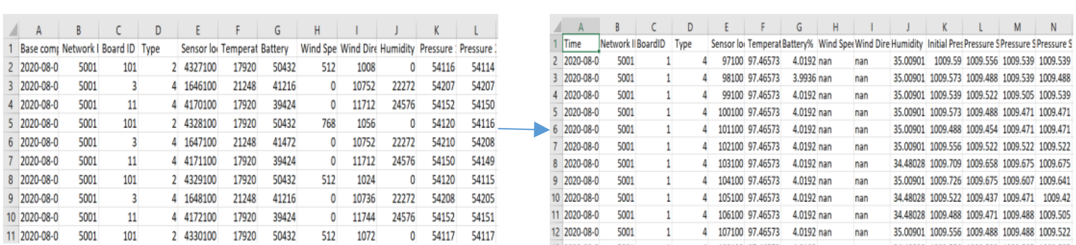

	A	B	C	D	E	F	G	H	I	J	K	L
1	Base comp	Network I	Board ID	Type	Sensor lo	Temperat	Battery	Wind Spe	Wind Dire	Humidity	Pressure	Pressure
2	2020-08-0	5001	101	2	4327100	17920	50432	512	1008	0	54116	54114
3	2020-08-0	5001	3	4	1646100	21248	41216	0	10752	22272	54207	54207
4	2020-08-0	5001	11	4	4170100	17920	39424	0	11712	24576	54152	54150
5	2020-08-0	5001	101	2	4328100	17920	50432	768	1056	0	54120	54116
6	2020-08-0	5001	3	4	1647100	21248	41472	0	10752	22272	54210	54208
7	2020-08-0	5001	11	4	4171100	17920	39424	0	11712	24576	54150	54149
8	2020-08-0	5001	101	2	4329100	17920	50432	512	1024	0	54120	54115
9	2020-08-0	5001	3	4	1648100	21248	41216	0	10736	22272	54208	54205
10	2020-08-0	5001	11	4	4172100	17920	39424	0	11744	24576	54152	54151
11	2020-08-0	5001	101	2	4330100	17920	50432	512	1072	0	54117	54117

	A	B	C	D	E	F	G	H	I	J	K	L	M	N
1	Time	Network I	BoardID	Type	Sensor lo	Temperat	Battery%	Wind Spe	Wind Dire	Humidity	Initial Pre	Pressure S	Pressure S	Pressure S
2	2020-08-0	5001	1	4	97100	97.46573	4.0192	nan	nan	35.00901	1009.59	1009.556	1009.539	1009.539
3	2020-08-0	5001	1	4	98100	97.46573	3.9936	nan	nan	35.00901	1009.573	1009.488	1009.539	1009.488
4	2020-08-0	5001	1	4	99100	97.46573	4.0192	nan	nan	35.00901	1009.539	1009.522	1009.505	1009.539
5	2020-08-0	5001	1	4	100100	97.46573	4.0192	nan	nan	35.00901	1009.573	1009.488	1009.471	1009.471
6	2020-08-0	5001	1	4	101100	97.46573	4.0192	nan	nan	35.00901	1009.488	1009.454	1009.471	1009.471
7	2020-08-0	5001	1	4	102100	97.46573	4.0192	nan	nan	35.00901	1009.556	1009.522	1009.522	1009.522
8	2020-08-0	5001	1	4	103100	97.46573	4.0192	nan	nan	34.48028	1009.709	1009.658	1009.675	1009.675
9	2020-08-0	5001	1	4	104100	97.46573	4.0192	nan	nan	35.00901	1009.726	1009.675	1009.607	1009.641
10	2020-08-0	5001	1	4	105100	97.46573	4.0192	nan	nan	34.48028	1009.522	1009.437	1009.471	1009.42
11	2020-08-0	5001	1	4	106100	97.46573	4.0192	nan	nan	34.48028	1009.488	1009.471	1009.488	1009.505
12	2020-08-0	5001	1	4	107100	97.46573	4.0192	nan	nan	35.00901	1009.556	1009.488	1009.488	1009.522

Figure 3. Post-processing using Jupyter Notebooks demonstrates how raw data is transformed to values with physical units.

1.2.2. Experimental Testing – Wall of Wind, September 2020

The Wall of Wind (WoW), a (NHERI) facility, is a hurricane simulator research facility at Florida International University (FIU) in Miami, Florida. To test the WSN pressure sensors performance, a full-scale gable roof house was placed on a rotating table that enabled collection of wind load data at different wind speeds and wind directions. The main objective of the project was to compare the performance of the WSN vs. the WoW Scanivalve (SCV) pressure taps. The SCV pressure taps are commonly used for wall of wind tests and can be positioned anywhere on the model house. The taps are flushed with the test surface and are connected to the SCV pressure scanner, with long tubes 1 to 2 metres in length.

Post-processing of WSN lab data is the same for field data as described in *section 1.2.1*. A new Jupyter Notebook post-processed the SCV raw data, which contained only differential pressure values with no information on pressure tap numbers or timestamps. The processed files have the essential information such as timestamps, pressure tap numbers, and their respective differential pressure values. Figure 4 shows the raw SCV data on the left, and the data after the post-processing on the right.

	A	B	C	D	E	F
1	-0.01413	-0.01265	-0.01021	-0.00664	-0.01606	-0.01452
2	-0.0156	-0.01434	-0.00863	-0.00778	-0.00143	-0.01456
3	-0.01992	-0.00972	-0.01338	-0.00493	-0.00724	-0.00125
4	-0.01358	-0.01291	-0.00388	-0.01404	-0.0093	-0.01673
5	-0.01134	-0.01251	-0.01678	-0.00102	-0.0057	-0.0008
6	-0.01714	-0.01768	-0.00573	-0.00886	-0.01156	-0.01453
7	-0.01351	-0.01183	-0.01423	-0.00434	-0.003	-0.0053
8	-0.01437	-0.01693	-0.00633	-0.01117	-0.01289	-0.00929
9	-0.01374	-0.01148	-0.00495	-0.00451	-0.00376	-0.00814
10	-0.01212	-0.01367	-0.01085	-0.00842	-0.00892	-0.01686
11	-0.01338	-0.01036	-0.01538	-0.00677	-0.00591	-0.01108

	A	B	C	D	E	F
1	Time	Press_Tap11	Press_Tap	Press_Tap	Press_Tap	Press_Tap
2	2020-09-0	-1.051926775	-0.88873	-0.71954	-0.54443	-0.57112
3	2020-09-0	-1.201255865	-0.99032	-0.94796	-0.721	-0.82836
4	2020-09-0	-1.31022042	-1.03926	-0.87924	-0.71364	-0.82473
5	2020-09-0	-1.203397728	-0.97243	-1.07966	-0.8425	-0.92102
6	2020-09-0	-1.25157857	-0.98644	-1.06224	-0.8393	-0.89515
7	2020-09-0	-1.41459915	-1.04317	-1.01384	-0.90875	-0.97902
8	2020-09-0	-1.456547855	-1.18255	-0.97751	-0.79118	-0.95625
9	2020-09-0	-1.378393525	-1.11389	-1.01665	-0.89698	-0.89411
10	2020-09-0	-1.3160907	-1.00924	-0.92634	-0.70726	-0.80346

Figure 4. Transformation of SCV files to contain timestamps and pressure tap values.

1.3. Jupyter Notebooks for Quasi-Realtime Monitoring

Thanks to the continuous quasi-realtime uploading of the data on DesignSafe, during a deployment, users can run the post processing notebook to visualize user-selected time windows for pressure, wind speed, and wind direction information, as it is being collected. Quasi-realtime monitoring allows users to check on the quality of the data, the proper functioning of the WSN, at anytime, and take remedial action if needed. Figure 5 shows a 9-hour time window of pressure data from different sensors during Isaias, 2-3 August, 2020. The figure shows a gap in data where one of the systems stopped working. The quasi-realtime monitoring allowed us to trouble shoot and get the system back online.

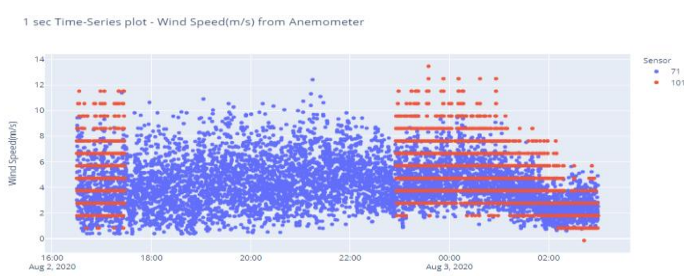

Figure 5. Isaias data from 2 anemometers.

2. USER-INTERACTIVE ANALYSIS FOR FIELD TESTING – ISAIAS, AUGUST 2020

Section 1.2.1 covers the deployment of the WSN system on a residential house in Satellite Beach, Florida during Isaias. The 18 pressure sensors (out of which 3 were from the new WSN and the rest were from an older WSN) were all installed on the shingle roof and 1 reference pressure sensor from the WSN was installed on the ground (away from any open area susceptible to changes in wind speed).

2.1. Sensor Performance and Critical Time Window Determination

WSN deployment collects data for two to three days and often only a few hours are of real interest to study the interaction of hurricanes with residential houses. To help identify the time window of interest, a Jupyter Notebook creates a 2D animation frame, not to scale, with the sensor locations. Figure 6 shows a side-by-side comparison of the sensor locations and the corresponding animation. Each sensor is color-coded according to its 1-hour average pressure value, which varies over time, as the animation plays. That way, a user can identify the time windows with higher pressures (warmer colors).

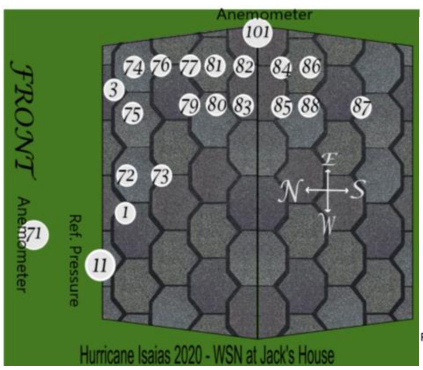

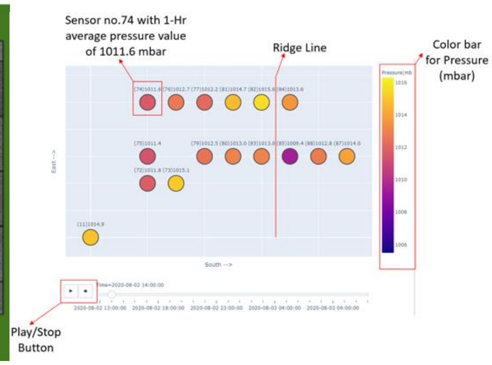

Figure 6. WSN deployment sensor location drawing (left) and Jupyter Notebook animation of 1-Hr averaged pressure values (right)

2.2. Anemometer data

Wind data can come from multiple anemometry (Lidar, one or more R.M. Young anemometer, Kestrel meter, etc.). An additional script in the Jupyter Notebook allows the user to plot the time history from any of the anemometry one at a time, or compare them. Figure 7 shows data from the anemometer of the newest WSN system for a 1-hour time window. Below the plot, an adjustable time scale can increase or decrease the time window of the plot.

Figure 7. Wind data from the new WSN's anemometer

2.3. Lidar Data

Florida Tech's conically scanning infrared Lidar (Besing et al., 2021) was deployed on the coast of Satellite Beach approximately half a mile from the WSN deployment. As the outer rainbands of Isaias moved across the east-central Florida coast, it measured the unobstructed on-shore flow and recorded over 2000 vertical profiles during a 11-hour window. It collected reference pressure at 1m level height and wind data at 10 different user defined vertical range gates (11m to 150m), sampled every 20 seconds. Lidar is useful to study how the wind changes as it moves inland to a residential area. The wind speed data plot at 11m from the Lidar in Figure 8 shows a gust around 8:40PM UTC.

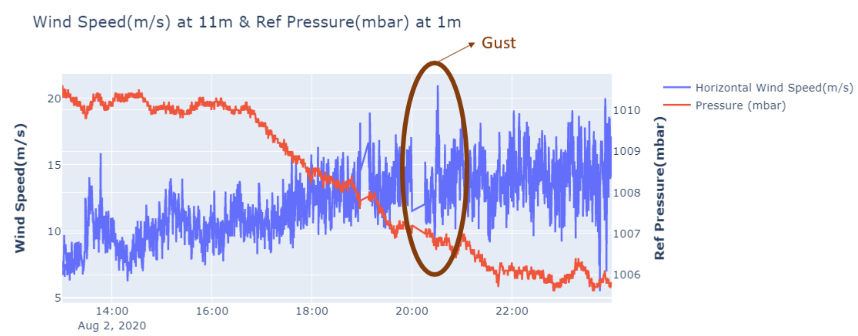

Figure 8. Lidar 11m wind speed and 1m barometric pressure indicating an upshoot in windspeed – Gust

3. USER-INTERACTIVE ANALYSIS FOR EXPERIMENTAL TESTING – WALL OF WIND, SEPTEMBER 2020

Section 1.2.2 covers the WSN deployment in the Wall of Wind experiment. One of the main differences between WSN and SCV is that the former has an aerodynamic casing with a large footprint and sits above the test surface with a small tube connecting the pressure port to the pressure sensor inside the casing, while the SCV tap sits flush to the test surface, and a long tube connects the pressure tap to the pressure scanner. The casing might influence the pressure readings and may disturb the accuracy of the reading. The test compared the accuracy of the WSN measurements against the SCV, to quantify the effect of:

(1) Tubing.
(2) Casing. To study this effect, a WSN sensor without the casing was installed on the roof of the test model.
(3) Wind Speeds at different Wind Directions.

The next two separate sections present two different scripts in the interactive analysis and visualization Jupyter Notebook to study the above. Additional functionalities exist which are not presented here for lack of space.

3.1. Differential Pressure and Pressure Coefficients

While the SCV samples differential pressure at 520 Hz, the WSN collects absolute pressure values at 10Hz. In order to compare the two, the WSN absolute pressure values are converted to differential pressure by subtracting from the absolute pressure of any selected pressure sensor the absolute reference pressure (from the barometric pressure sensor inside the house model), and the SCV data is resampled at 10 Hz. Then the pressure values are converted into pressure coefficients, according to Eq. (1), where p is the static pressure at the sensor location, p_∞ is freestream static pressure and V_∞ is the freestream velocity:

$$C_p = \frac{p - p_\infty}{\frac{1}{2}p_\infty V_\infty^2} \quad (1)$$

Figure 9a shows the time histories of two pressure sensors, while Figure 9b shows a plot of pressure coefficients.

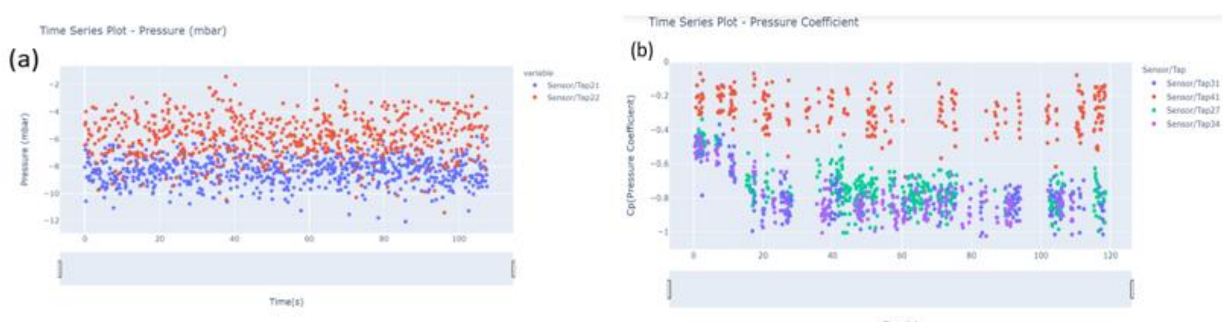

Figure 9. (a) Differential Pressure Plot for WSN, (b) Pressure Coefficient Plot

3.2. Tabular Results – Comparison of any 2 sensors

The Jupyter Notebook also provides statistical tabular results for any set of two selected pressure sensors. The results can be saved as csv files. Figure 10 shows the tabular comparison for two WSN pressure sensors at different wind speeds, where their percentage differences (in the last three columns) increase with increasing wind speed.

	Wind Speed [MPH]	MeanPress_WSN31	STDdev_WSN31	MeanPress_WSN41	STDdev_WSN41	First-Second	%diff_dynp	%diff_noflow
0	30	-1.500501	0.156368	-1.614136	0.164802	0.113635	10.291711	0.011173
1	60	-4.194786	0.467346	-2.596819	0.650091	-1.597967	-36.181103	-0.157118
2	90	-8.609218	0.945588	-3.846551	1.082407	-4.762668	-47.927177	-0.468283
3	120	-13.589064	2.503153	-5.118905	1.720759	-8.470159	-47.945259	-0.832816
4	145	-21.467660	1.804235	-6.062300	2.177243	-15.405360	-59.724488	-1.514710

```
Do you want to save this as a csv file? (Y/N)
```

Figure 10. Statistical Tabular Results comparing two WSN sensors.

4. CONCLUSION

This paper demonstrates how DesignSafe-CI (Pinelli et al., 2020; M. Rathje et al., 2017) facilitates the workflow for field deployments and lab experiments. Quasi-real time uploading of the data, allows for instant monitoring of the data collection and remedial action when a problem is encountered in a deployment. In addition, the platform offers analytical tools, including Jupyter Notebooks, which facilitate the processing, analysis, and visualization of the data.

The paper presents three notebooks for format standardization, post-processing of the raw data, and data analysis and visualization. The notebooks can process both field and laboratory data. Due to page limitation, analysis such as spectral analysis, correlation heatmaps and Lidar data analyses were not explained but were an integral part for data analysis and reporting.

The WSN pressure data collected during Isaias deployment amounted to 1GB in size, making the post processing tasks memory intensive and time consuming. Thus, it was important to separate the post-processing and analysis into different notebooks. Saving the processed data as Pandas DataFrame and pickling it, allowed the python scripts to load data easily, and perform slice and dice tasks. The visualizations were enabled by a Plotly package that was installed on DesignSafe's Jupyter hub and pulled data from smaller Pandas DataFrames. A good practice established in all the notebooks was to delete the non-essential DataFrames as and when they were finished executing. This technique saves memory, thereby reducing compilation time. Installing packages on Jupyter hub is not as straight forward as installing them on a local Jupyter Notebook. The Jupyter hub on DesignSafe requires the user to either submit a ticket and wait for a few days to have it installed or use a 'pip install' command every time the server is started (once every 3 days). The latter is a tedious process which adds to the compilation time of the notebooks. The biggest issue faced during the Isais and WoW deployments was the unpredictability of access to the Jupyter Notebooks. The server was down multiple times due to technical issues that the DesignSafe team was working on, which did not help for quasi-realtime analysis. In the case of data analysis after the completion of deployments, a work around to that problem was to simply download the pickled files and the Jupyter notebooks to a local desktop and run the Jupyter Notebook application locally. DesignSafe has improved the stability of Jupyter hub in recent times and increased their memory limit, making our experience with data processing and analysis smoother and more reliable.

Since the WSN pressure data collected from previous field and experimental deployments have sizes ranging between 0.5 and 1 GB, we are looking to improve on our data storage techniques and further reduce compilation time. Apart from Jupyter, DesignSafe also provides the option of using HPC (High Performance Computing) Jupyter which can perform memory intensive tasks better, but this tool is not available to the community yet. We are currently familiarizing ourselves with HPC Jupyter by attending DesignSafe workshops so we can transition when the tool is open. Another idea being worked on is to build multi-relational databases containing all data collected during the different field and experimental deployments. Python scripts in Jupyter Notebooks can connect to the database for pulling data and performing data analysis. Building a database however requires resources and training.

Eventually, the authors will publish the data, Jupyter Notebooks, and reports on DesignSafe so that they will be available to the research community. .

ACKNOWLEDGEMENTS

The National Science Foundation (NSF) financially supports the DesignSafe project under grants CMMI-1520817 and 2022469. In addition, the National Institute of Standards and Technology (NIST) supports the development and deployments of the WSN under grant 70NANB19H088. These supports are gratefully acknowledged.

REFERENCES

H. Gurram, C. Subramanian, J.-P. Pinelli and R. Basu., 2017. Processing Data from Hurricane Matthew in DesignSafe-ci, in 13th American Conference on Wind Engineering, Gainesville, Florida.

H. Gurram, C. Subramanian and J. -P. Pinelli., 2016. Hurricane Data Management using the DesignSafe-CI Workspace, in 4th American Association of Wind Engineering, Miami, Florida.

Besing, H., Lazarus, S., Sridhar, S., Subramanian, C. S., & Pinelli, J.-P., 2021. A Combined LiDAR and Dual-Doppler Assessment of the Near Surface Wind Field in East-Central Florida During Hurricane Dorian (2019), in 101st American Meteorological Society Annual Meeting.

Chelakara Subramanian, Jean-Paul Pinelli, Ivica Kostanic, Gabriel Lapilli. Design, 2012.Development and Testing of a Wireless Multi-sensors Network System, Journal of Mechanics Engineering and Automation, David Publishing Co., Inc., Libertyville, IL, 2, P169-183.

Ellen Rathje, Clint Dawson, Jamie E. Padgett, Jean-Paul Pinelli, Dan Stanzione, Pedro Arduino, Scott J. Brandenberg, Tim Cockerill, Maria Esteva, Fred L. Haan, Jr., Ahsan Kareem, Laura Lowes, Gilberto Mosqueda. Enhancing Research in Natural Hazards Engineering through the DesignSafe Cyberinfrastructure, Frontiers in Built Environment, section Wind Engineering and Science, https://doi.org/10.3389/fbuil.2020.547706.

Jean-Paul Pinelli, Maria Esteva, Ellen M. Rathje, David Roueche, Scott J. Brandenberg, Gilberto Mosqueda, Jamie Padgett, Frederick Haan, 2020. Disaster Risk Management through the DesignSafe Cyberinfrastructure, International Journal of Disaster Risk Science, DOI 10.1007/s13753-020-00320-8

Ellen M. Rathje, Clint Dawson, Jamie Padgett, Jean-Paul Pinelli, Dan Stanzione, Pedro Arduino, Scott Brandenberg, Tim Cockerill, Maria Esteva, Frederick Haan, Matthew Hanlon, Ahsan Kareem, Laura Lowes, Steve Mock, Gilberto Mosqueda, 2017. DesignSafe: A New Cyberinfrastructure for Natural Hazards Engineering," ASCE *Natural Hazards Review*, Volume 18 Issue 3; doi: 10.1061/(ASCE)NH.1527-6996.0000246.

Performance-Based Wind Design of Tall Buildings Considering the Nonlinearity in Building Response

S. Preetha Hareendran [a*], A. Alipour [b], B. Shafei [c], P. P. Sarkar [d]

[a]PhD Candidate, Department of Civil, Construction and Environmental Engineering, Iowa State University, Ames, IA, United States, smrithi@iastate.edu
[b]Associate Professor, Department of Civil, Construction and Environmental Engineering, Iowa State University, Ames, IA, United States, alipour@iastate.edu
[c]Associate Professor, Department of Civil, Construction and Environmental Engineering, Iowa State University, Ames, IA, United States, shafei@iastate.edu
[d]Professor, Department of Aerospace Engineering, Iowa State University, Ames, IA, United States, ppsarkar@iastate.edu

ABSTRACT:

Tall buildings exhibit complex structural responses under dynamic loads such as the actions of wind. In addition to the dependence on complex and dynamic nature of wind actions, the responses are influenced by numerous characteristics of the buildings itself such as its shape, height, and setback and tapering along the height etc. Difficulty in transferring the complex nature of wind and interaction it's with buildings led to the development of mathematical models and analysis techniques defining minimum design requirements to ensure safety of the occupants during specific design events. Progressive research and increased computational efficiency over the past couple of decades has produced more elegant solutions to the analysis and design of buildings such as Performance Based Design (PBD). PBD proposes that the structure be designed to meet specific performance objectives set forth by the stakeholders. PBD has become a mainstream approach to assess and reduce the risks in rehabilitation of existing structures. Application of PBD philosophy for design of tall buildings and other structures excited by wind loads has received much attention recently. The significant wind related economic losses incurred every year around the world has prompted the researchers to develop methods to reframe wind engineering to fully embrace the concepts of PBD. The main objective of Performance Based Wind Engineering (PBWE) is to assess the adequacy of a structure in terms of the decision variables (DVs) set forth by the stakeholders. Each DV is defined to satisfy specific performance levels such as operational, immediate occupancy, life safety, and collapse prevention. The performance levels are defined based on acceptable levels of strength and serviceability requirements of both structural and non-structural components. They also reflect the probable levels of damage, casualties, downtime, and costs of repair.

With the advancements in the computational capacity available, this study implements the proposed PBWE methodology by following the true nature of the PBD philosophy considering the nonlinearity in response of buildings and associated uncertainties in the wind loading. Furthermore, the study makes contributions to the field of PBWE by providing prediction of turbulent wind loads at each level of the building and also by developing the formulation to account for along- across- and torsional- wind loading along the height of the building. The aerodynamic load coefficients and aeroelastic load functions are obtained from wind tunnel experiments conducted on a scaled section model in the AABL Wind and Gust Tunnel at the Wind Simulation and Testing (WiST) laboratory at Iowa State University. The aerodynamic load (drag, lift and moment) coefficients and their derivatives with respect to angle of attack are obtained for three different mean angles of attack of wind (0^o, 34^o and 90^o) using section model tests in a wind tunnel. The aerodynamic load coefficients and their derivatives are then used to calculate buffeting load time histories for the building based on Quasi-Steady formulation, corresponding to synthetically generated wind speed time histories that are based on empirical Power Spectral Density (PSD) functions (Kaimal Spectra).

The wind hazard for a specific site is defined in terms of maximum wind velocity experienced at the specified height of the building over the given averaging time (i.e. gust) while accommodating the factors accounting for terrain roughness and other topographic factors. For a given body immersed in wind flow, the wind velocity fluctuations are to be converted into time varying forces to be able to conduct nonlinear time history analysis in such a way that decision variable (*dv*) can be generated to ease communications with stakeholders and owners. Tall buildings are subjected to non-uniform time varying wind loads along their height which vibrates at random frequencies. The winds

* Lead presenter

fluctuate about a mean wind speed corresponding to the height at which it acts. The wind models based on straight-line conditions cannot predict the structural response beyond the fundamental mode of vibration. The design wind speed specific to Miami-Dade County (130 mph) given by ASCE -07 was taken as the mean wind speed and a normal wind speed distribution was developed to identify the range of wind speeds in which the performance of building was to be analyzed. In this study, these parameters that are required for generating the wind-load time histories for various locations of the building along its height are extracted from wind tunnel experiments. For this purpose, the aerodynamic properties of the section model of example tall building that is subject to a two-dimensional smooth flow were extracted and applied to predict the wind loads on the tall building in time domain, where the variations of wind velocities (mean and fluctuating) in a typical atmospheric boundary-layer wind along its height were considered. A section model (1:400 scale) of the CAARC Standard tall building with a rectangular cross section was tested in the aerodynamic test section of the wind tunnel in uniform and smooth flow to obtain the static mean load coefficients. The wind acting on a tall building excites it under the action of a mean wind speed $U(z)$ at elevation z from the ground and time varying or turbulence components, $u(z,t)$ and $v(z,t)$ in the along- wind and across- wind directions about the mean wind speed, $U(z)$. The turbulent time histories are generated based on the algorithm proposed by Deodatis 1996.

A 44-story steel moment frame building under the wind load actions is designed for this study. The building is 528 ft. (161 m) tall and has a plan aspect ratio (B/D) of 1.5:1. The steel frames are composed of beams made from wide flanged I-sections and columns of cross rectangular sections built-up with wide flanged I sections. The steel beams in the frame have a span of 26.25 ft. (8 m) with 6 spans along the longer direction and 4 spans in the perpendicular direction. The 3-D and plan views of the model is shown in Figure 1. The building was designed under static loads based on the provisions of AISC 360 and ASCE 7-16 for a design wind speed of 130 mph (58 m/s) for Miami Dade County in Florida. The static analysis, and design was conducted in SAP2000 and frame sections were chosen that satisfy the structural requirements.

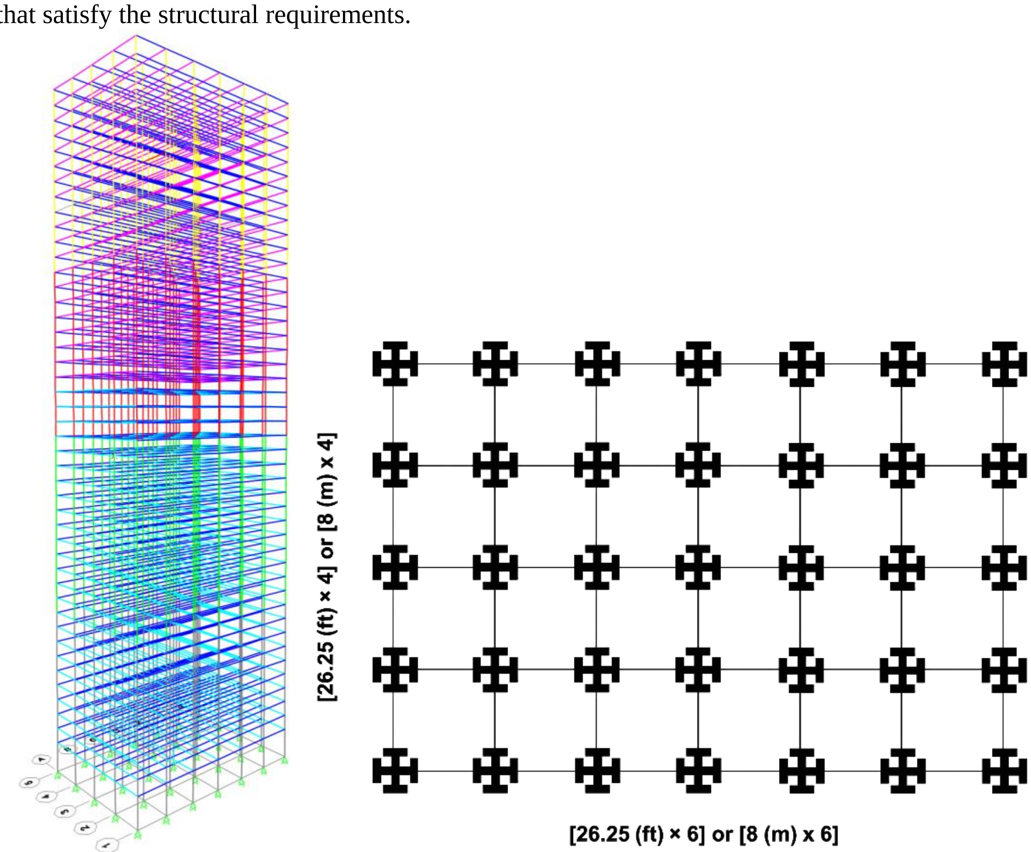

(a) (b)

Figure 1: 44-story steel frame building (a) 3D view of the SAP model and (b) Plan view with column sections along beam lines

To understand the structural response under long duration wind loads, the building was subjected to randomly varying

wind loads for a duration of 30 minutes. Different time history analyses were performed with wind speeds varying between 100 and 180 mph. The building responses recorded include acceleration and displacement time histories at every floor level. The member forces were recorded to identify the locations of plastic hinges and also to interpret any unusual variations in the recorded accelerations and displacements in the building. Multiple iterations of analyses for each set of wind speeds were used to develop fragility curves for different structural/non-structural components in the building. The fragility curves maybe used in the loss analysis of the structure. This study provides an effective method to understand the non-linear behaviour of tall buildings under high velocity long duration wind loads. The fragility curves also offer an attractive methodology to optimize the design of non-structural components of wind-sensitive high-rise buildings.

Keywords: Performance-based wind design, tall buildings, nonlinear response, performance objectives

Full Scale Wind Testing to Determine the Role of Vertical Protrusions on Curtainwall Performance

Kehinde J. Alawode [a*], Krishna Sai Vutukuru [a], Amal Elawady [a, b], Arindam Gan Chowdhury [a, b] and Guido Lori [c]

[a] *Florida International University, Miami, FL, United States, kalaw003@fiu.edu*
[b] *Florida International University, Miami, FL, United States, kvutu001@fiu.edu*
[c] *Florida International University, Miami, FL, United States, aelawady@fiu.edu*
[d] *Florida International University, Miami, FL, United States, chowdhur@fiu.edu*
[e] *Permasteelisa S.p.A., Vittorio Veneto, Treviso, Italy, g.lori@permasteelisagroup.com*

ABSTRACT:
Vertical protruding elements have been commonly used for building aesthetics and reduction of the energy demand. However, design code guidance for these types of curtainwalls are not currently available. This study investigates the effect of vertical protruding elements installed on a single skin façade system on the overall wind actions on the façade using full scale wind experiments. The results show that vertical protrusions can increase the pressure loads on the building surface (as evidenced by increased Cp) by as much as 30% for the condition covered in this study.

Keywords: vertical projections, curtain walls, wind effects, aerodynamic loading

1. INTRODUCTION

Glazed curtain walls or façades are a type of building envelope that primarily serve the purpose of separating the interior of the building and its contents and/or occupants from the exterior environment. Architects have increasingly used glass curtainwalls as facades in mid-and high rise structures for many reasons, including enhancing the resistance to corrosion, recyclability of glass, reduction of building energy consumption as it provides natural lighting, and recent improvements in glass coating technology (Pariafsai, 2016). With the growing need for energy-efficient buildings, the adoption of shading devices on buildings with glazed façades is increasing. Shading devices are usually projecting out of the curtain wall (vertical or horizontal), hereby reducing the amount of sunlight getting into the building. These devices could also have some aesthetic appeal.

A study focused on assessing wind actions on buildings with vertical projections was carried out by Stathopoulos and Zhu (1991) which experimentally simulated both open and urban terrain exposures using a model with an adjustable height, representing tall buildings and low rise buildings. Their results indicated that the effects of vertical projections are adverse and more pronounced at the edges. Also, the change in terrains had little to no effect on the Cps measured on walls with fins.

Chand and Bhargava (1997) considered the effects of both vertical and horizontal projections on wind pressure coefficients. They concluded that the effect of vertical projections on wind pressure distribution on a wall depends on the distance from the projection to the edge of the wall. With

* Lead presenter

projections at the wall edge increasing wind pressures at the corners while projections at a distance from the wall edge reduce pressures at points between the projection and the wall edge.

More recent studies on the effects of vertical projections such as Yang, et al (2020) have majorly focused on the effects of vertical projections on the aerodynamic loads (i.e Base moments and Across and Along Wind forces) on tall buildings. There are also a few numerical studies on the effect of wall projections on wind pressure coefficient such as Zheng et al, (2020).

This research project was motivated by the lack of guidance in major wind loading standards (e.g. Eurocode EN 1991-1-4:2005 and ASCE 7-16) regarding the effect of adding vertical projections on curtain walls on the overall wind actions on the system. This paper therefore presents a comparative experimental study on the wind pressures acting on a full-scale glazed curtainwall panels with and without vertical projections. Section 2 provides details of the experimental setup, materials and methodology, section 3 is a discussion of the results from the experimental study while section 4 summarizes the major findings of the study.

2. METHODOLOGY

2.1. Experimental Setup

The experimental study was carried out at the Wall of Wind (WOW) Experimental Facility (EF) at Florida International University. The WOW EF is an open jet wind tunnel with a 2 x 6 array of fans. The facility is capable of testing large and full scale models up to and at category 5 hurricane wind speeds of ∼70m/s (Gan Chowdhury et al. 2017). Wind speed and turbulence characteristic measurements at the center of the turntable were measured with Cobra probes. The mean wind speed at the center of the turntable and roof height (3.2m) of the test building was ∼21.97m/s. The roughness length z_0 was at 0.08m, which falls within the range of open-terrain exposure.

2.2. Model Configurations

The model used in this study is a full scale, a 3.65m by 1.83m rectangular building with a 3.2m height and a flat roof with 0.41m overhang. Figure 1 shows the plan of the model with vertical projections and the wind directions. The tests were carried out from 0° to 345° wind directions in 15° increments.

Two test configurations were tested in this study, a reference model 'Without Vertical Projections' configuration (*Model A*) and a 'With Vertical Projections" configuration (*Model B*) which had 2 protruding V-shaped fins. On both configurations, the walls on one of the 3.65m length sides of the building were made from three glazed single-skin unitized façade units supported on rigid steel frames. The second wall was constructed from three sections of clear polycarbonate plates mounted on a wooden frame. A wooden vertical projection matching those on the glazed side was added to the wooden frame for Model B. The polycarbonate wall side has a dimension of 3.65m by 3.2m and its main purpose was to provide a similar geometric surface as the actual glazed façade that can be drilled to allow for the fixing of pressure taps. Figure 2 shows *Model A and Model B* configuration on the turntable at the WOW. The other two walls on the 1.83m length side of the building were made from wood, with a door structure at one of the walls to provide access to the inside of the model to allow for instrumentation of the model. During tests, the door was sealed. All the walls were fixed to a steel frame bolted to the turntable. The steel frame provided high rigidity, as needed for running high wind velocity tests.

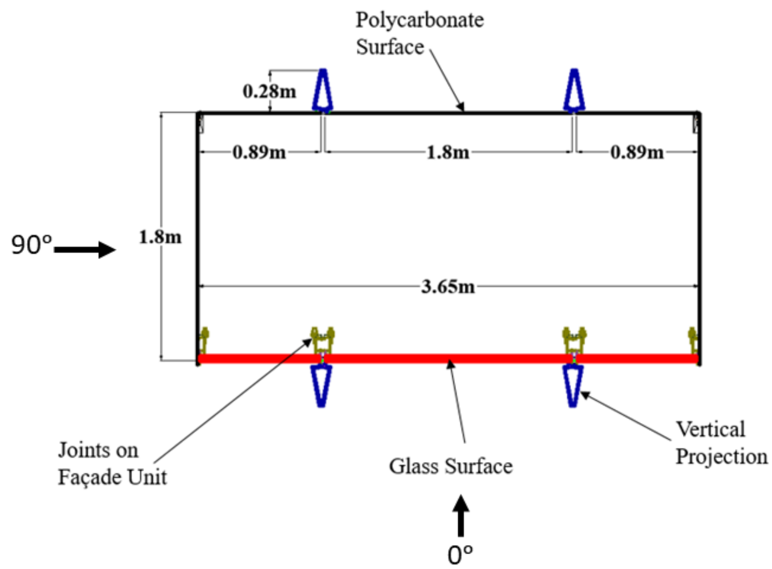

Figure 1. Schematic Plan of Test Model (Model B) and Wind Direction

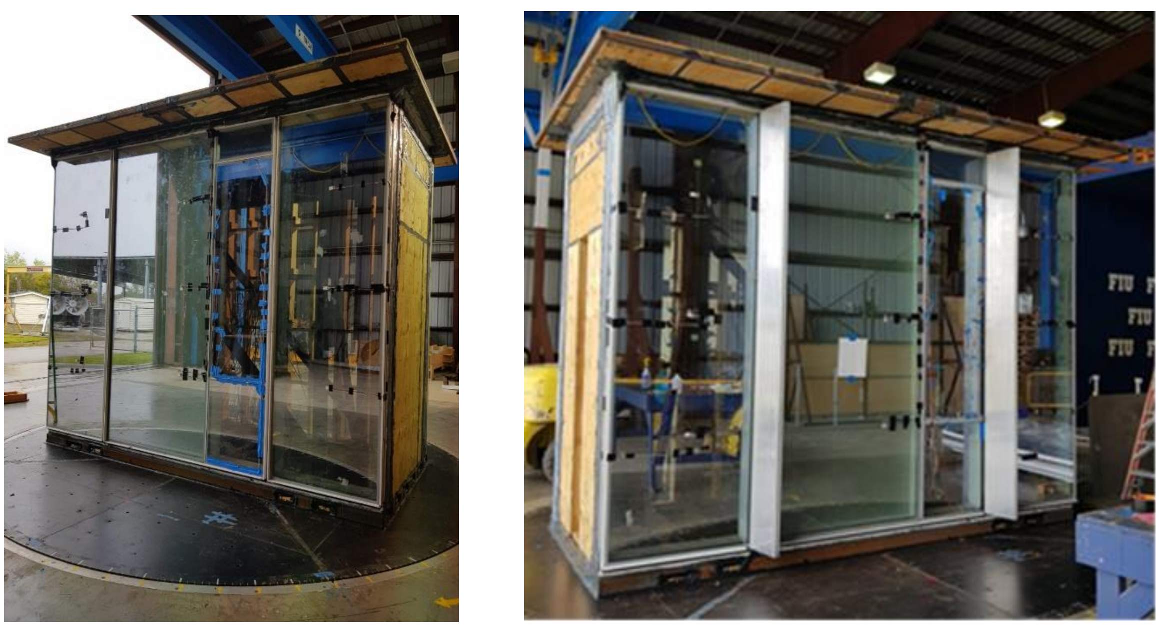

(a) (b)

Figure 2. Test Model on the Turn Table at WOW (a) Model A (b) Model B

2.4. Instrumentation

Pressure on the polycarbonate wall of the model, the wooden fins, and inside the test building were measured using a total of 128 pressure taps (110 taps on walls, 16 taps on the fins and 2 taps inside the test building). The pressure taps had a denser resolution at the edges to ensure that the variation of pressure at those edges are captured appropriately. Figure 3 shows the tap locations on the polycarbonate wall. Each tube was connected to the ZOC33 Scanivalve pressure scanner module. Wind pressure data was acquired at 512Hz sampling frequency for a 1 min window. A tubing transfer function by Irwin et al. (1979) was used in the analysis given the long length of tubes used due to the size of the model. Wind directions were varied from 0° to 345° at 15° increments by rotating the automated turntable.

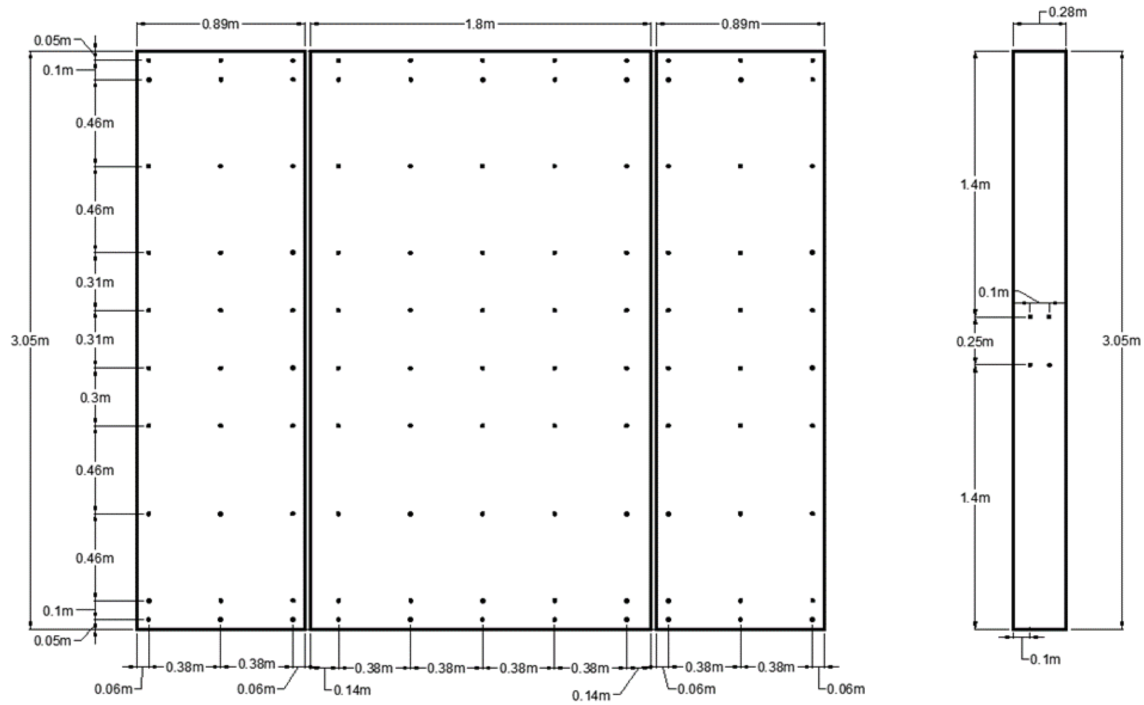

(A) (B)

Figure 3. Pressure Tap Layout on (A) Polycarbonate wall and (B) Wooden Vertical Projection

2.3. Data Analysis Method

The peak Cp values were estimated using the Partial Turbulence Simulation (PTS) method which was developed and validated at the WOW (Mooneghi, et al , 2016) to provide the missing data of low-frequency turbulence which is not obtainable at a large scale testing.

The pressure coefficients, both mean Cp_{mean} and peak Cp_{peak} values are defined by Equation 1 and 2:

$$Cp_{mean} = \frac{P_{mean}}{\frac{1}{2}\rho U_{mean}^2} \quad (1)$$

$$Cp_{peak} = \frac{P_{peak}}{\frac{1}{2}\rho U_{3s}^2} \quad (2)$$

In Equation 1 and 2, U_{mean} and U_{3s} are the mean and peak 3s wind speeds at the roof height of the model, ρ is the air density while P_{mean} and P_{3s} are the differential mean and peak pressures. The area-averaged pressure coefficients presented were computed using Equation 3;

$$Cp_{avg.,peak} = \frac{\frac{\sum P_{k,peak}(t).A_k}{\sum A_k}}{\frac{1}{2}\rho U_{3s}^2} \quad (3)$$

In Equation 3, $P_{k,peak}(t)$ is the pressure time history at pressure tap k. A_k is the tributary area of pressure tap k. Most of the data analysis and plots were carried out on MATLAB (2020) software.

3. RESULTS AND DISCUSSION

The distribution of the peak pressure coefficients (Cp) on the walls of Model A and Model B are compared in this section. The envelope (from all wind directions) of the Cp max and Cp min values on Model A and B is presented in Fig. 4. The results show a concentration of 30% higher Cp max at the positions of the vertical projections on Model B in comparison with model A. Cp min values are also higher on Model B in comparison with Model A across the wall.

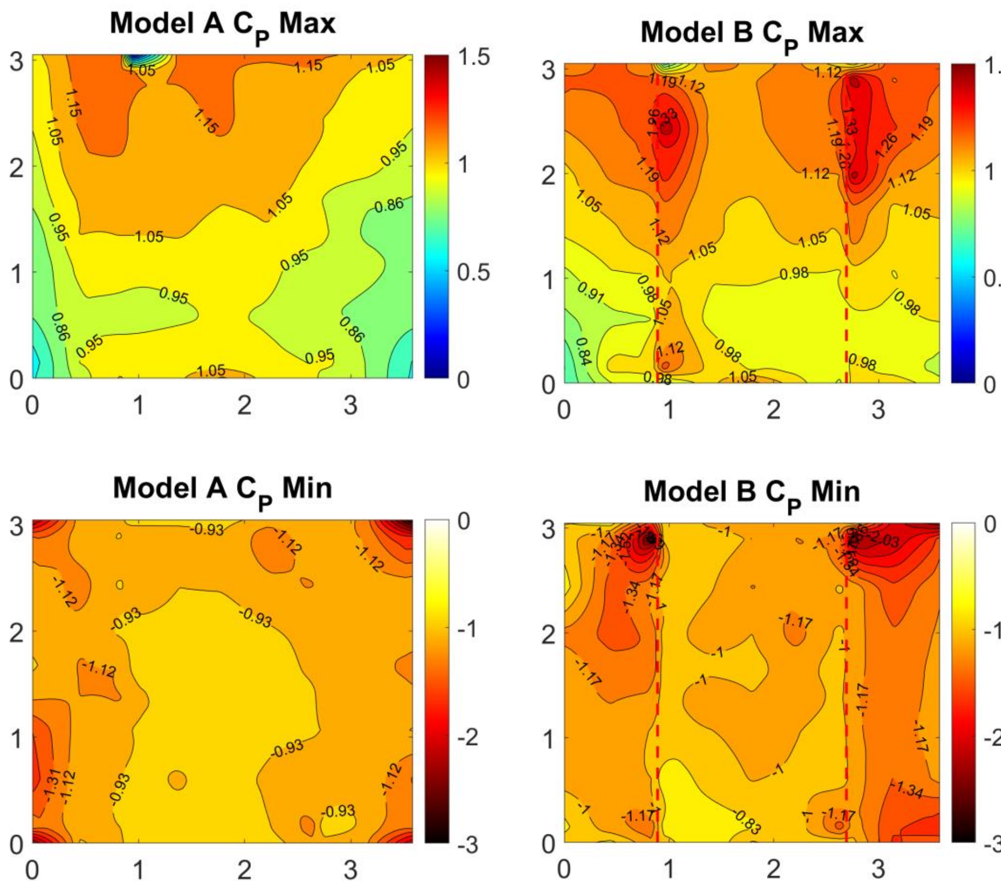

(A) (B)

Figure 4. Envelope of Max Cp and Min Cp on (A) Model A and (B) Model B

At 0° wind angle, Cp peak at the edge of the walls are about 10% higher in Model B compared with those on Model A as shown in Fig 5. However, the central panel experienced about 12.5% higher Cp peak values in Model A compared to walls of Model B. This is similar to the observation by Stathopoulos and Zhu (1991). Also, on walls of Model B, Cp values in the vicinity of the vertical projections are much lower than those at the same positions on walls of Model A. A similar observation was made by Chand and Bhargava (1997).

At 45°, there is a lower Cp peak values on Model B at the left and middle panel in comparison with Model A. Also, the right panel of Model B indicate suction in comparison with positive pressure on Model A. This is due to the flow-impedance effect of the first and second vertical projection.

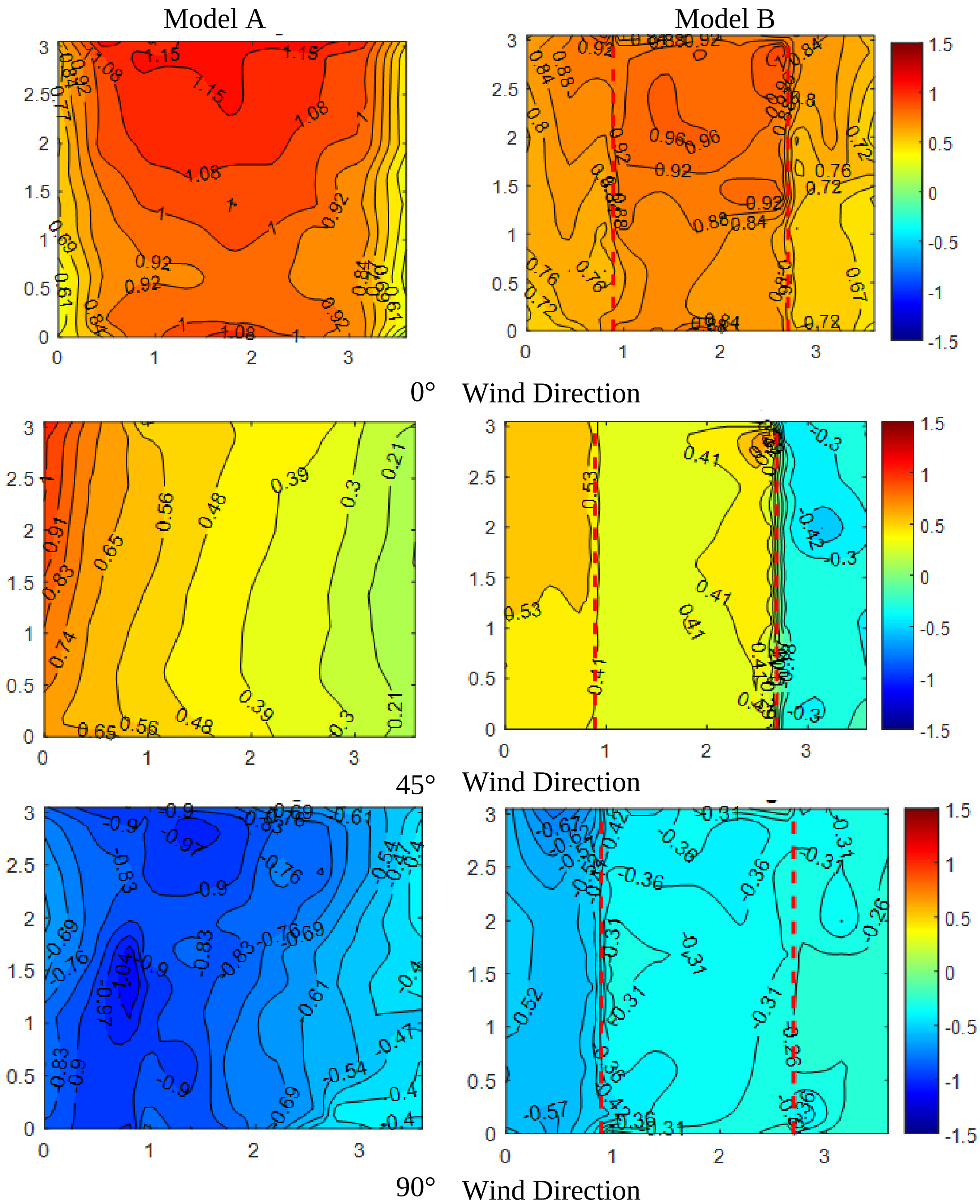

Figure 5. Cp Peak Contour plots for Model A and Model B at varying wind directions

At 90° wind direction, when the wind is parallel to the curtainwall, the suction across the wall of Model A is higher at the left and middle panel in comparison with those on Model B. The reason for this could be the formation of recirculation vortices behind the left vertical projection which reduce the suction. This observation at 90° (as shown in Fig 5) is contrary to the observation of

Stathopoulos and Zhu (1991), where suction increased (Cp mean) in the presence of vertical projections. The difference in the proximity of the projections to the wall edges in both studies, and differences in the number and depth of vertical projections used, could be the cause of the observed difference, as Stathopoulos and Zhu (1991) opined that the distance of the first projection from the edge of the wall plays a significant role in the measured Cp values.

Comparison of the area averaged ‘envelope Cp max’ from this experimental study, with ASCE 7-16 recommendation for components and cladding is presented in Table 1. The results indicate that the ASCE 7-16 underestimates the positive Cps on both models at Zone 4 and 5 and the negative Cps on both models at Zone 4. It was however conservative with the negative Cps at zone 5 in both models. Consequently, more experimental and numerical investigations are urged to complement available data on the wind actions on façade structures with projections.

Table 1. ASCE 7-16, Model A and Model B GCp Values

Zone	ASCE 7-16	Model A	Model B
4 (Positive)	0.8637	0.9651	1.0724
(Negative)	-0.9637	-1.0728	-1.2773
5 (Positive)	0.9179	1.0451	1.0708
(Negative)	-1.2358	-0.9291	-0.9879

4. CONCLUSION

Vertical projections influence the pressure values and pattern on claddings as they increase the overall positive Cp (by as much as 30%) at regions close to the projections and increase negative Cp (by as much as 26%). Further tests and numerical studies with different geometry and different projection configurations is recommended for future studies.

ACKNOWLEDGEMENTS

This paper is based upon work sponsored by the US National Science Foundation under the awards IIP 1841503 and I/UCRC Wind Hazard and Infrastrture Performance (WHIP) project # 2019-04. The authors also would like to thank Permasteelisa group for providing the curtain wall specimen. The opinions, findings, conclusions, or recommendations expressed in this article are solely those of the authors and do not represent the opinions of the funding agencies

REFERENCES

Chand, I., & Bhargava, P. K. (1997). Laboratory studies on the effect of external projections on wind pressure distribution on low-rise buildings. *Architectural Science Review*, *40*(4), 133–137.

Gan Chowdhury, A., Zisis, I., Irwin, P., Bitsuamlak, G., Pinelli, J. P., Hajra, B., & Moravej, M. (2017). Large-scale experimentation using the 12-fan wall of wind to assess and mitigate hurricane wind and rain impacts on buildings and infrastructure systems. *Journal of Structural Engineering (United States)*, *143*(7).

Irwin, H. P. A. H., Cooper, K. R., & Girard, R. (1979). Correction of distortion effects caused by tubing systems in measurements of fluctuating pressures. *Journal of Wind Engineering and Industrial Aerodynamics*, *5*(1), 93–107.

Mooneghi, A. M., Irwin, P., & Gan Chowdhury, A. (2016). Partial turbulence simulation method for predicting peak wind loads on small structures and building appurtenances. In *Journal of Wind Engineering and Industrial Aerodynamics* (Vol. 157).

Pariafsai, F. (2016). A review of design considerations in glass buildings. *Frontiers of Architectural Research*, *5*(2),

171–193.
Stathopoulos, T., & Zhu, X. (1991). Wind Pressures on Buildings with Mullions. *Journal of Structural Engineering*, *116*(8), 2272–2291.
Yang, Q., Liu, Z., Hui, Y., & Li, Z. (2020). Modification of aerodynamic force characteristics on high-rise buildings with arrangement of vertical plates. *Journal of Wind Engineering and Industrial Aerodynamics*, *200*(March), 104155.
Zheng, J., Tao, Q., & Li, L. (2020). Wind pressure coefficient on a multi-storey building with external shading louvers. *Applied Sciences (Switzerland)*, *10*(3).

Development of a Wireless Sensor Network for Hurricane Monitoring

J. Wang[a], J. Sun[b], C.S. Subramanian[a], J-P Pinelli[a], S. Lazarus[a]

[a]*Florida Institute of Technology, Melbourne, Florida, US, hursensors@lists.fit.edu*
[b]*Shanghai, China, sun128764@gmail.com*

1 INTRODUCTION

The object of the WSN is to characterize the wind effects on the surface of residential houses. The fully developed system contains hardware and software subsystems. The hardware measures data and transfers it through the Zigbee network. The base unit of the hardware subsystem gathers data from all sensors and transfers it to the terminal computer through Universal Serial Bus (USB). The support system such as the charging system and solar system are included in the hardware subsystem. The onboard pressure transducer and temperature sensor enable the board to measure pressure and temperature without any independent electronics. The software subsystem consists of the firmware programed on the sensor board chip and enables the software graphical user interface (GUI) to calibrate the data and output as comma-separated values file (CSV file).

Calibration generates the transfer function to convert digital data to physical measurements such as the pressure in mbar and wind speed in m/s. The resolution of the sensor board is determined by that of the microcontroller (MCU) on the board, which has the original 12-bit analog-to-digital converter (ADC). With the oversampling function, this ADC resolution is increased to 16-bits.

2 SYSTEM DESCRIPTION (HARDWARE AND SOFTWARE)

2.1 Zigbee Network and sensor board

The Xbee modules generate a Zigbee network which allow communication between all nodes (sensors) and a coordinator (base unit). IEEE 802.15.4 standard network coexisting with 2.4 GHz Wi-Fi. The filtering of several Zigbee channels is used to avoid the interference with other Wi-Fi devices. Adding routers reduces the duty of the coordinator and increases the total number of knots.

The main controller unit (MCU) of the sensor board is ATSAM21 and is compatible with the Arduino IDE. The board connects to a 3.7V Li-ion battery power source. The board also supports solar panels to charge batteries for long-duration operations. The on/off port makes it possible to turn on or off the sensor using an on/off plug.

2.2 Measurement subsystem

A measurement system consists of total-pressure sensors, a reference-pressure box, and an anemometers box. A total- pressure sensor board is housed in a case, with a 3.7V 4000 mAh Li-ion battery. A 5 mm Tygon tube connects the pressure transducer with the outside port. The 4000 mAh battery powers the board for up to 48 hours. The combination of the disk probe and the reference pressure box, which includes a 4000 mAh Li-po battery and the censor board, is used for measuring reference pressure. The Young's Anemometer with its own box is used for the wind speed and direction. All the sensors transfer the data packages through the Zigbee network.

2.3 Firmware and software

The firmware programmed in the board chip controls all tasks of measurement, including regular(pressure), wind speed, and anemometer. The software program runs in the Window 10 environment and monitors the activity of the remote sensors. The sensor data is transmitted to the USB port of a laptop computer so that the monitor can show the real-time plot of measurements. Both firmware and software provide the cyclic redundancy check-32 (CRC-32) and detect any error data received in the network. The causes of the error data might be the noise of the decoding process when the Xbee module packages the data or the disturbances from other signal sources. The error data package will not be accepted as a useful value and will not be stored. The program organizes the CRC-32 passed packages to the cluster of CVS files and uploads them to the project storage in DesignSafe through the public internet. This uploading function is optional. Users can save the data locally and upload the files later if there is no internet service available.

2.4 Performance benchmarking and calibration

With the oversampling method, the resolution of the readings is maintained at 16 bits for temperature, wind speed, wind direction, humidity, air pressure, and battery level. The resolution for ADC is $3.3V/2^{16}bit = 0.05\,mV/bit$. The overall resolution of the measurement for air pressure, humidity, temperature, wind speed, and wind direction are 0.1mbar, 0.03%RH, $0.05°C$, 0.05m/s, 0.005 degrees, respectively. The calibration for the anemometer and pressure sensor is necessary for reliability data. The Compact pressure calibrator is used to calibrate the pressure sensor. The wind tunnel, pitot tube, and pressure manometer are used to calibrate the anemometer. The zero-offset correction modifies the offset of the pressure transfer function and is necessary before every measurement job. Ideally, the number limitation of the sensors within one system is 50, which is determined by the capacity of the Zigbee network. Now the number of sensors in one system is 26, including 24 normal-pressure sensors, a reference pressure sensor, and an anemometer. Users can burn the firmware in one minute to create a new sensor in the system. The wireless transfer test shows that the maximum connection range of Zigbee modules under open air and complex in-house conditions are 179m and 35m. The tests were done in Murano Drive Melbourne, FL, and Olin Engineering Complex, Florida Institute of Technology, Melbourne, FL.

The previous field (Hurricane Eta) and experimental (Wall of Wind Test) test show that it cost 2 hours on average to deploy a system on a residential house. The combination of Velcro™ and epoxy enable the normal-pressure sensor to attach to the surface temporally and keep the strength under 90m/s, and the combination of Dual Lock™ and epoxy enhance the attachment, which the quantized maximum wind speed is to be determined in the future experience. The advantage of using Dual lock™ and Velcro™ is that users take the sensors off the surfaces without damaging the house. The M5 flanges provide the most strength of attachment but damage the house surface significantly.

Keywords: Wireless Sensors Network, Pressure Sensor, Wind Sensors, Anemometer, Design-Safe, Hurricane, Zigbee, Xbee.

ACKNOWLEDGMENTS

The National Science Foundation (NSF) financially supports the DesignSafe project under grants CMMI-1520817 and 2022469. In addition, the National Institute of Standards and Technology (NIST) supports the development and deployments of the WSN under grant 70NANB19H088. These supports are gratefully acknowledged.

Performance Testing and Calibration of the Generation –IV Wireless Sensor Network System

J. Zhang[a,*], S. Sridhar[a], C.S. Subramanian[a], J-P Pinelli[a], S. Lazarus[a], J.Wang[a], J.Sun[b], H.Besing[a]

[a]Florida Institute of Technology, Melbourne, FL, U.S., hursensors@lists.fit.edu
[b]Shanghai, China, sun128764@gmail.com

Keywords: Wireless Sensors Network, Pressure Sensor, Wind Sensors, WoW testing, Scannivalve Sensor

1. BACKGROUND AND HARDWARE

To measure wind loads on structural and non-structural components of low-rise buildings, the researchers developed a new Generation-IV wireless sensor network (WSN). With a smaller size, faster sampling rate and better communication range than the previous generation of the WSN, these sensors measure pressure, temperature, wind direction, and wind speeds under tropical wind conditions.

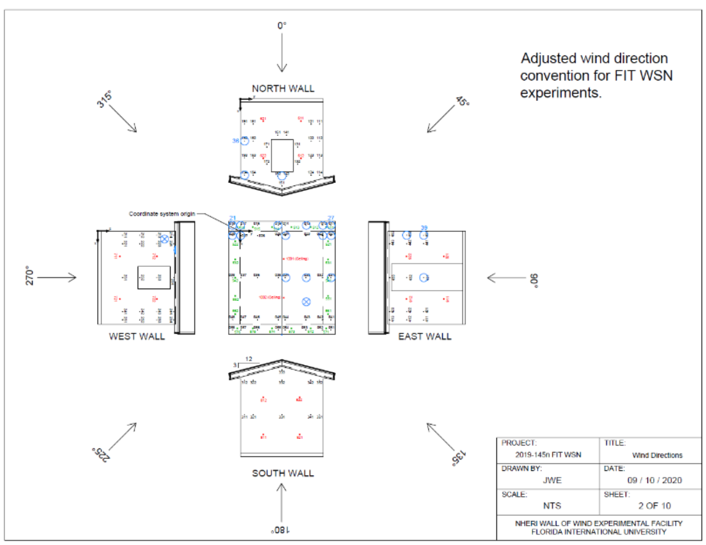

Figure 1. Deployment Setup

The authors deployed the WSN System on a 10'x10'x10' house model for testing in the Florida International University (FIU) Wall of Wind (WoW). For wind speeds ranging from 30 mph to 145 mph, the System performance and calibration were compared against a traditional surface tap Scannivalve measurement system. The WSN pressure sensors were compared to pressure taps connected to the Scannivalve system, located at symmetrical or similar positions for wind directions 0 to 270 degrees in 45 degrees increments. The pressure readings from both sources were analyzed using Matlab and Python scripts, embedded into Jupyter notebooks, and compared

* Lead presenter

to each other. The tubing effect of the Scannivalve pressure sensors, the casing effect for portable sensors, and the sensor accuracy at different locations for different wind speeds and wind directions were studied using control variable analysis.

2. DATA ANALYSIS

The deployment protocol in the WSN data-acquisition software allows for the uploading of the data in quasi-real-time to the DesignSafe cyber-infrastructure on the cloud.

Once in DesignSafe, the data are processed using a combination of Matlab scripts or Python scripts embedded in Jupyter notebooks. In the analysis process, the code is automated to effectively identify the test period, wind direction, wind speed information for each sensor. The code then compares the pressure readings from WSN sensors with the Scannivalve system's results at the exact or symmetric location, with a pre-defined mapping table.

3. RESULTS

The differential pressure difference between the two systems is compared, and the percentage of difference against dynamic pressure estimated from test wind speed is calculated.

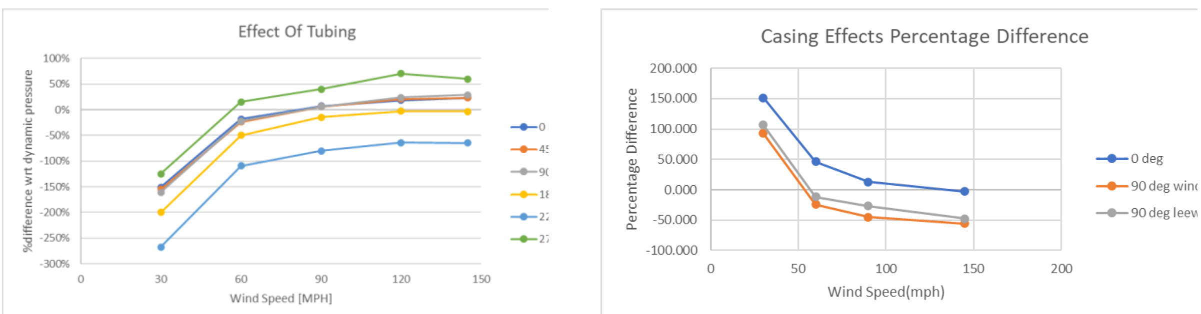

Figure 2. Effect of Tubing and Casing respectively

From research, both the tubing effect of Scannivalve sensors and the casing effect reduces as the wind speed increased. Percentage difference for tubing effects decreases with wind speed, with the minimum percentage difference ranging from 50% to 70% for 225 and 270 deg and a smaller range of 3% to 29% for 0,45,90 and 180 deg wind direction. The percentage difference of WSN sensors with and without a casing is decreasing with high wind speeds. Under crosswinds, the pressure measurements with casing are more negative than expected, which needs to be improved for future experiments.

The performance analysis of the WSN sensor indicates an improved resolution of 0.1 millibars ocf measurements at all locations, as the wind speed increased from 30 mph to 145 mph. Pressures measured on the north wall are slightly more negative than expected. At a 45-degree headwind, the calculated results are not converging on high wind speeds. On the East wall and the roof, a more significant difference is found at a 90-degree crosswind. At higher wind speeds, the sensors deployed under the soffit show trends of improving accuracy, with the differences ranging from 1% to 17% at 145Mph.

ACKNOWLEDGEMENTS
The National Institute of Standards and Technology (NIST) supported the development and deployments of the WSN under grant 70NANB19H088. The National Science Foundation (NSF) financially supports the DesignSafe project under grants CMMI-1520817 and 2022469. These supports are gratefully acknowledged.

Addressing Turbulence Model Form Uncertainty

M. F. Ciarlatani [a*], Z. Hao [b], C. Gorlé [c]

[b]*Stanford University, Stanford, California, US, mattiafc@stanford.edu*
[a]*University of Cambridge, Cambridge, UK, zh343@eng.cam.ac.uk*
[c]*Stanford University, Stanford, California, US, gorle@stanford.edu*

ABSTRACT

The aim of the present work is to investigate different strategies to reduce RANS model form uncertainty. We investigate if using (1) accurate knowledge on the normalized Reynolds stress anisotropy tensor, (2) a double scale turbulence model that can quantify uncertainty in the dissipation, or (3) a combination of both, can improve RANS predictions of the flow around a bluff body representative of a high rise building. Our quantities of interest are the mean velocity field and the mean pressure field on the surface of the building. An LES simulation of the flow is performed to generate a high-fidelity data set that can provide information on the anisotropy tensor and serve as a reference when comparing the three RANS predictions. The results show that correctly quantifying RANS model form uncertainty requires addressing uncertainty in both the normalized anisotropy tensor and the dissipation.

Keywords: Turbulence model form uncertainty, Bluff body, High-Rise building.

1. INTRODUCTION

RANS simulations are frequently used for flow simulations of engineering complexity. However, the turbulence model required to close the RANS equations introduce a significant amount of uncertainty in the results. The ability to quantify and reduce this uncertainty is key to supporting the use of RANS as a source of information for engineering decisions. Quantifying turbulence model form uncertainty is a challenging task, as there is no straightforward way to estimate it. However, one can reduce the model uncertainty by embedding more physics into the turbulence model equations. The aim of the present work is to investigate multiple strategies for reducing turbulence model form uncertainty, focussing on the k-ω SST model. The first strategy considers informing the production term of the k-ω SST model with the LES-computed anisotropy. The second strategy considers the adoption a double scale version the k-ω SST model, which is equivalent to introducing uncertainty in the dissipation. The third and final strategy considers the combination of the two previous techniques, i.e. it informs the double scale version of the k-ω SST with the LES-computed normalized anisotropy. To perform this study, we consider the case of the flow around a bluff body representative of a high rise building. Our Quantities of Interest (QoIs) are the mean velocity field and the mean pressure field on the surface of the building. Three RANS simulations of the flow around the high rise building are performed to assess the success of the three aforementioned strategies. The results are then compared against predictions from an LES simulation of the same flow.

* Lead presenter

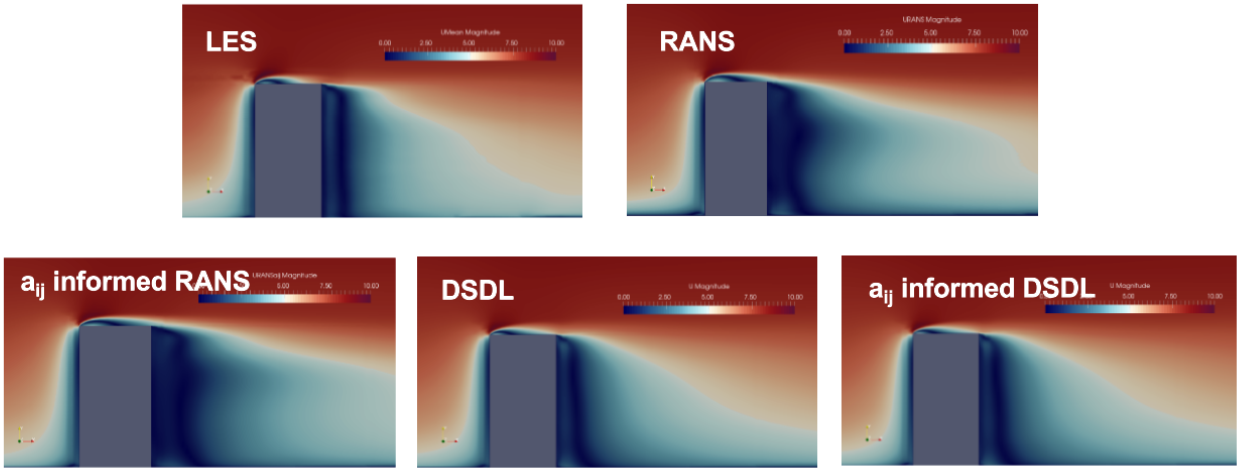

Figure 1. Comparison between the velocity field obtained computed by the LES, the informed RANS, the DSDL, and the informed DSDL.

2. A HIGH-FIDELTY ANISOTROPY TENSOR INFORMED MODEL

The first strategy informs the turbulence model with accurate knowledge on the Reynolds Stress tensor anisotropy. Specifically, the normalized anisotropy tensor

$$a_{ij} = \frac{R_{ij}}{k} - \frac{2}{3}\delta_{ij} \tag{1}$$

computed from an LES simulation is used to compute the production term of the k-ω SST model. The comparison of the prediction of the informed model with the standard k-ω SST and the LES predictions indicates that this approach is not sufficient to increase RANS model accuracy; Figure 1 shows that the size of both the separation region on the roof and the building wake remain significantly overpredicted.

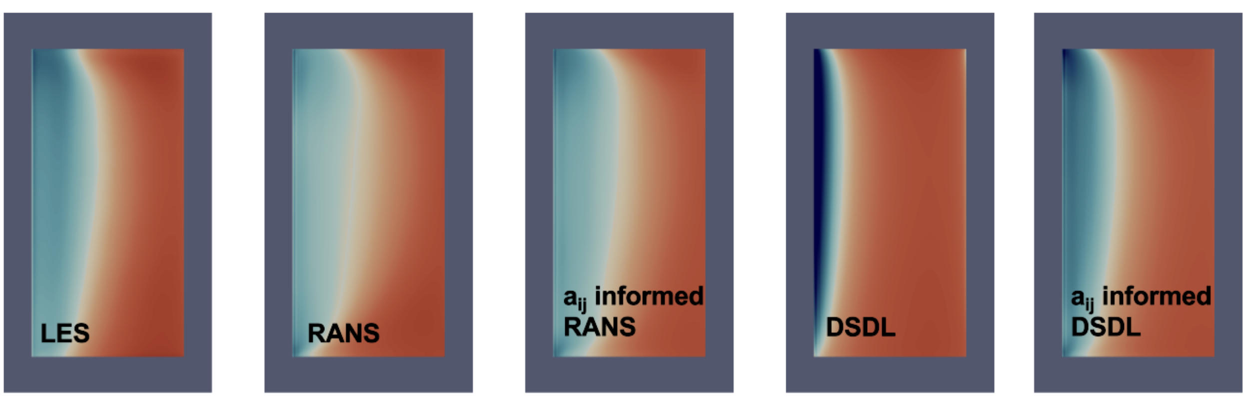

Figure 2. Comparison between the pressure over the surface of the building predicted by the LES, the informed RANS, the DSDL, and the informed DSDL.

3. A DOUBLE SCALE APPROACH TO TURBULENCE MODELING

The second strategy adopts a double scale (DSDL) version of the k-ω SST model. As noted by many authors, the existent of coherent structures (CS) within a stochastic turbulence field (ST), such as vortex shedding or VITA events, exposes an important problem with traditional RANS modeling, i.e. the existence of multiple length and velocity scales within the same flow field. To address this problem, a double scale approach as proposed by Hao 2020 can be explored. This approach consists in splitting the contribution to the velocity fluctuations between different length scales, i.e. CS and ST, and model their associated turbulent kinetic energy (TKE) separately. The TKE associated to the larger length scales (i.e. CS) flows to the smaller length scale (i.e. ST) according to a modelled energy transfer rate. In a fashion similar to the turbulence cascade, dissipation only acts on the TKE stored at the smaller length scales. In this model, uncertainty can be introduced in the energy transfer rate, which is equivalent to introducing uncertainty in the dissipation rate. The results show that the DSDL can generate remarkably good predictions for the velocity field; Figure 1 visualizes the improved predictions of the separation region on the roof and the building wake. However, when considering the pressure, the model does not provide an accurate representation of the LES solution.

4. INFORMING A DOUBLE SCALE TURBULENCE MODELING

The third strategy combines the two aforementioned techniques by informing the DSDL model with the LES-computed anisotropy tensor. This strategy provides a similar prediction for the mean velocity field as the DSDL model, with a more accurate prediction of the separation and wake region. However, it also significantly improves the prediction of the pressure on the building surface.

5. SUMMARY AND FUTURE WORK

The results of this study indicate that quantifying and reducing turbulence model form uncertainty requires an uncertainty estimate or more accurate information on both the normalized anisotropy tensor and the dissipation rate. In ongoing work we are performing this analysis for additional wind directions, and we are using the insights obtained from this study to develop multi-fidelity simulation strategies that can reduce turbulence model form uncertainty.

ACKNOWLEDGEMENTS

This research has been funded by a CIFE seed award.

REFERENCES

Hao, Z., 2020.Physics-based uncertainty quantification of Reynolds-averaged-Navier-Stokes models for turbulent flows and scalar transport, PhD thesis.

Hurricane Maria Hindcast Using WRF-LES: A Preliminary Comparison of Topographic Wind Speed-Up

Luis D. Aponte-Bermúdez, Ph.D., P.E [a*], Forrest J. Masters, Ph.D., P.E. [b], Jorge X. Santiago-Hernández [c], and Edward L. Cruz-García [c]

[a]*Professor, University of Puerto Rico Mayagüez, Mayagüez, PR, USA, luisd.aponte@upr.edu*
[b]*Professor and Associate Dean for Research and Facilities, University of Florida, Gainesville, FL, USA, masters@ce.ufl.edu*
[c]*Ph.D. Graduate Student, University of Florida, Gainesville, FL, USA, jxavier.santiago@ufl.edu*
[c]*Graduate Student, University of Puerto Rico Mayagüez, Mayagüez, PR, USA, edward.cruz1@upr.edu*

EXTENDED ABSTRACT:
Hurricane Maria was a strong category 4 hurricane with sustained winds of 155 mph when it struck Puerto Rico in the morning of September 20, 2017, making landfall in the coastal municipality of Yabucoa with damage estimates of approximately $100 billion. Like other tropical island or Appalachians, Puerto Rico's complex terrain causes a considerable topographic speed-up effect resulting in stronger winds over hilly or mountainous terrain than flat terrain. The Federal Emergency Management Administration (FEMA), thru its Mitigation Assessment Team (MAT) Report FEMA P-2020 Hurricanes Irma and Maria in Puerto Rico, recommended the development of new design guidance for wind speed-up in Puerto Rico to produce guidance or wind maps similar to what was produced for Hawaii. Such maps were developed under the Strategic Alliance for Risk Reduction (STARR II), and Technical Services Architectural and Engineering contracted Applied Research Associates (ARA) to create a special wind region map for the mountainous areas in Puerto Rico, as defined by Section 26.5.2 in the ASCE 7-16 Standard *Minimum Design Loads and Associated Criteria for Buildings and Other Structures* (aka. Microzonation). The University of Florida (UF) supported this effort by experimentally characterizing speed-up on the main island of Puerto Rico and the municipal Island of Vieques and Culebra in the boundary layer wind tunnel (BLWT) using Cobra probes to collect data for ARA to validate wind speed-up predictions informed by studies of geographic regions outside of Puerto Rico. The outcome of such study is the new Wind Maps currently adopted in the 2018 Puerto Rico Building Code, which had been incorporated into the Applied Technology Council (ATC) *Hazard by Location* web tool and are currently under consideration for adoption in ASCE 7-22. The work that will be presented in this paper is part of an on-going investigation between UF and the University of Puerto Rico Mayagüez funded by the National Science Foundation (NSF) EAGER program. One of the EAGER project's main goals is to elucidate multiscale atmospheric simulations' capability using numerical weather prediction (NWP) framework to assess their potential for prediction wind speed-up in mountainous areas and other regions with steep slopes. Besides, speed-up under the EAGER project was under investigation using other numerical and experimental studies conducted using computational fluid dynamics (CFD) using OpenFOAM®, Machine Learning (ML), and collecting new wind tunnel data at UF's BLWT using stereoscopic PIV measurements under instrument control.

Furthermore, this paper will present the insight of the NWP framework configuration using the Weather Research and Forecasting (WRF) Model Advanced Research WRF (ARW) version 4.2.2 from the National Weather Service (NWS) Science and Training Resource Center's (STRC) Unified Environmental Modeling System (UEMS) version 21.1.2. The NWP simulation had been developed using UPRM in-house and the computational capabilities of the Texas Advanced Computing Center (TACC) of The University of Texas at Austin. A hindcast of Hurricane Maria over Puerto Rico had been conducted using WRF-ARW in LES mode for domains with a horizontal resolution less than 1 km. The WRF model configuration consists of six (6) one-way nesting domains ranging from a 12.15 km course horizontal resolution down to 50 m using a 1/3 ratio, with 61 vertical levels and a large time step of 40 seconds corresponding to the parent domain. The Timestep is also to scale down using a 1/3 ratio. The model boundary and initial conditions were obtained from the Global Forecast System Analysis (GFS-ANL) data set of 0.5° (~55.6 km), and Sea Surface Temperature (SST) data were obtained from 8.33 km Global data set. The speed-up comparison present will consist of ratios obtained from (i) FEMA-UF-BLWT-Cobra, (ii) ARA-model, (iii) EAGER-ML, (iv) EAGER-CFD-OpenFOAM®, (v) EAGER-UF-BLWT-PIV, and (vi) EAGER-NWP.

* Lead presenter

Keywords: NWP, WRF-LES, Topographic Speed-up, wind field modeling

ACKNOWLEDGEMENTS
NSF NHERI Experimental Facility at UF: Award No. 2037725. Natural Hazards Engineering Research Infrastructure: Experimental Facility with Boundary Layer Wind Tunnel 2021-2025; Award No. 1520843. Natural Hazards Engineering Research Infrastructure: Experimental Facility with Boundary Layer Wind Tunnel, Wind Load and Dynamic Flow Simulators, and Pressure Loading Actuators NSF Award No. 1841979. EAGER: Exploring Machine Learning and Atmospheric Simulation to Understand the Role of Geomorphic Complexity in Enhancing Civil Infrastructure Damage during Extreme Wind Events. FEMA-4336-DR-PR & FEMA-4339-DR-PR Modelling of Wind Speed Up for Microzoning of Design Wind Speeds in Puerto Rico under Strategic Alliance for Risk Reduction (STARR II)

Large-eddy Simulation of Wind Loads on a Roof-mounted Cube: A Means to Interpolate Experimental Data

Abiy F. Melaku [a,*], Lakshmana S. Doddipatla [b], Girma T. Bitsuamlak [a]

[a] *Civil and Environmental Engineering Department, WindEEE Research Institute/Boundary Layer Wind Tunnel Laboratory, Western University, London, ON, Canada.*
[b] *FM Global, Research Division, Norwood, MA, USA.*

ABSTRACT:
Large-eddy simulations (LES) have been conducted in OpenFOAM to estimate wind loads on 3 m cube shaped roof-mounted equipment for seated and three elevated configurations. The study aims to interpolate existing experimental data for different equipment elevations. The LES results were first validated against wind tunnel data using mean as well as fluctuating pressure and force coefficients for a few representative cases. The results from the simulations suggest that the uplift wind loads can be reduced by up to 50% (approximately) for elevated equipment in general. In contrast, the drag wind loads remain relatively unchanged.

Keywords: Large-eddy simulation (LES); roof-mounted equipment; wind loads; low-rise building.

1. BACKGROUND

Recent Federal Emergency Management Agency (FEMA) damage surveys conducted in the aftermath of major hurricanes indicate widespread failure to rooftop equipment. Failure of rooftop equipment due to wind have several consequences. Notably, displaced equipment tears up the roof membrane and creates a large opening on the roof, allowing water to infiltrate the building envelope. In some cases, blown-up equipment becomes high-momentum windborne debris, damaging the roof and the surrounding buildings located downwind (Reinhold, 2006). An accurate estimation of the wind loads on these kinds of equipment is essential to minimize wind related damage.

ASCE 7-16 (2017) addresses the wind loads for rooftop equipment; it outlines the procedure for calculating drag and uplift force coefficients. However, the recommendations in ASCE 7-16 (2017) do not explicitly differentiate between seated and elevated rooftop equipment. A recent study conducted by Doddipatla and Kopp (2021) suggested revising ASCE 7-16 (2017) guidelines to account for size and elevation of the rooftop equipment. The study considered equipment with different elevations (C) mounted on an industrial building with height (h) and showed that, for $C/h \geq 0.15$, the variation in the wind loads was not significant. Nevertheless, it was not clear if the wind loads would be similar for lower elevations ($0 < C/h < 0.15$), a question which forms the main objective of this study. To investigate this issue in detail, large-eddy simulations were conducted in OpenFOAM for different equipment elevations with the aim of complementing the available experimental data.

* Lead presenter

2. NUMERICAL MODEL

The simulations were performed at a model scale of 1:50, matching that of the experimental prototype. A cube-shaped piece of equipment with a full-scale side length, S = 3 m mounted on an industrial building with dimensions ($L \times B \times h$) of 45.6 m x 30.4 m x 9.8 m, where B is the width, L is the length, and h is the height of the building, is modeled following Doddipatla and Kopp (2021). The equipment was placed at four different locations on the roof, representing the corner, perimeter, and field zones. Four elevations (C) were studied, including seated (C/h = 0) and elevated (C/h = 0.03, 0.09, and 0.15). Ten wind directions from 0^0 to 90^0 at 10^0 increments were considered, counting to a total of 160 simulation cases. The approaching inlet turbulence for LES was generated using the CDRFG (Aboshosha et al., 2015) method for an open terrain exposure condition with aerodynamic roughness height z_0= 0.02 m. A transient solver based on the PIMPLE algorithm was adopted with the standard Smagorinsky sub-grid scale model in OpenFOAM.

3. RESULTS AND CONCLUSION

The pressure and force coefficients found from LES generally matched reasonably well the experimental data for representative benchmarking cases (C/h = 0, 0.15), as shown in Fig. 1 (a,b). The LES results suggested that the uplift wind loads are generally reduced by about 50% for all elevated cases ($C/h \geq 0.03$), as depicted in Fig. 1c. However, the drag loads remain relatively unchanged between seated and elevated cases. Details of the results and observations from the current study will be presented at the workshop.

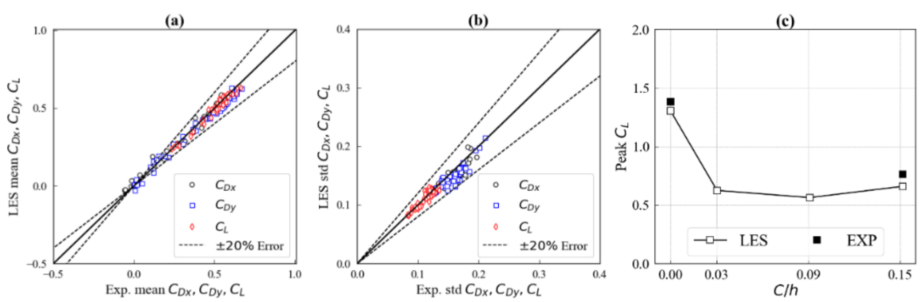

Figure 1 Statistical comparison of the lateral (C_{Dx}, C_{Dy}) and uplift (C_L) force coefficients from LES with experiment: (a) mean; (b) standard deviation; (c) peak uplift (C_L) force coefficient

ACKNOWLEDGEMENTS

The first author is thankful for the internships at FM Global in 2017 and 2019 when this work was conducted.

REFERENCES

Aboshosha, H., Elshaer, A., Bitsuamlak, G.T. and El Damatty, A., 2015. Consistent inflow turbulence generator for LES evaluation of wind-induced responses for tall buildings. J. Wind Eng. Ind. Aerodyn., 142, p. 198.

ASCE 7-10, 2010. Minimum Design Loads for Buildings and Other Structures. American Society of Civil Engineers, Reston, VA.

Doddipatla, L.S. and Kopp, G.A., 2021. Wind loads on roof-mounted equipment on low-rise buildings with low-slope roofs. Journal of Wind Engineering and Industrial Aerodynamics, 211, 104552.

Reinhold, T.A., 2006. Wind loads and anchorage requirements for rooftop equipment. ASHRAE Journal, 48(3), p. 36.

Model for simulating extreme wind speed distribution parameters for hurricane winds

J.B. Dannemiller [a,*], D.A. Smith [b], S.M. Morse [c]

[a]*Texas Tech University, Lubbock, TX, USA, joseph.b.dannemiller@ttu.edu*
[b] *Texas Tech University, Lubbock, TX, USA, doug.smith@ttu.edu*
[c]*Michigan Tech University, Houghton, MI, USA, smmorse@mtu.edu*

ABSTRACT:
A model is developed to simulate distributions of extreme wind speeds to be used in structural performance analysis post hurricane landfall. Texas Tech University Hurricane Research Team (TTUHRT) wind data gathered by 15 observations platforms during the landfall of 9 hurricanes is used to compute summary statistics for parent wind fields and extreme value distribution parameters fitting the distributions of extreme winds. Linear relationships and conditional probability tables are computed to use a mean wind speed and one of three roughness regimes to simulate distributions of extreme value distribution location and scale parameters utilizing wind data from 12906 600s wind speed records netting 1591 600s stationary records with mean winds above 15m/s. Conditional tables are presented to facilitate simulation of extreme wind speed distributions for use in scientific and engineering endeavours.

Keywords: TTUHRT, extreme wind distribution, simulation, conditional probabilities

1. METHODS

To facilitate simulating distributions of extreme wind speeds that occur during hurricane landfall wind speed time histories gathered by Texas Tech University Hurricane Research Team (TTUHRT) Wind Engineering Mobile Instrument Tower Experiment (WEMITE) and Portable Mesonet Tower (PMT) platforms, at 10m height, during the 1998 landfall of Hurricane Bonnie, the 2003 landfall of Isabel, the 2004 landfall of Frances, and the 2005 landfalls of Dennis, Katrina and Rita are investigated. Aerial imagery captured close to the landfall of each storm is used to classify the upwind surface roughness regimes in 30-degree directional bins at all TTUHRT platform deployment locations. The TTUHRT wind time histories are broken into 600s windows, checked for stationarity using the Run Test (RunT) and the Reverse Arrangement Test (RAT) (Bendat and Piersol, 1986), and any 600s window with a wind speed below 15m/s is discarded to focus on wind speed records that could lead to significant damage to the built environment. Of the total 12,906 complete 600s windows captured by TTUHRT platforms, 7,915 exhibited no errors during data capture and not well after a storm’s landfall. Out of the 7,915 a total of 1,613 recorded a mean wind speed above 15m/s. Out of the 1,613 a total of 22 failed either the RunT or the RAT for stationarity were disqualified leaving a total of 1,591 complete 600s windows across 6 hurricane landfalls. Numerical software is used to compute the location and scale parameters of the distributions of extreme wind speeds mapping the upper tails of the 1,591 600s windows for the raw wind speed time histories, as well as time histories computed by applying a 3s and 60s moving average (MA) to the raw time history. The distributions of location and scale parameters for the raw, 3s MA and 60s MA data are fit using a three parameter General Extreme Value Distribution (GEV). The 1,591 600s windows are then broken into three surface roughness regimes using the aerial imagery assigned surface roughness

* Lead presenter

regimes and the wind direction recorded by TTUHRT platforms. The linear relationship between the parent wind field mean wind speeds and the extreme wind field location parameters is quantified and a model for simulating distributions of location and scale parameters is presented using the raw, 3s MA and 60s MA wind data. The model uses the TTUHRT data to quantify GEV parameters for distributions of extreme wind location and scale parameters conditional upon mean wind speed and surface roughness regime. The model is presented in tabular form making the identification of conditional GEV parameters easy for any scientist or engineer needing to simulate extreme wind fields occurring during hurricane landfall.

Time Variant Hurricane Modeling in Performance-based Wind Engineering

Zhicheng Ouyang [a], Seymour M.J. Spence [b,*]

[a]*University of Michigan, Ann Arbor, MI, USA, ouyangzc@umich.edu*
[b]*University of Michigan, Ann Arbor, MI, USA, smjs@umich.edu*

ABSTRACT:
Over the past decades, significant research effort has been put into the development of frameworks for the performance assessment of engineered buildings in wind engineering. However, there is still a significant lack of frameworks for the envelope systems of this class of buildings. In order to address this issue, this paper proposes a performance-based assessment framework based on full hurricanes, where probabilistically continuous wind speed, wind direction, and rainfall intensity are captured with random event durations through a set of computational models. An innovative non-stationary/-straight/-Gaussian wind pressure model is introduced to model the full hurricane induced pressure. To illustrate the framework, 45 story archetype building in downtown, Miami, FL, is studied. A full range of probabilistic performance metrics in terms of the amount of damages, losses, and water ingress are evaluated and compared with the same metrics estimated for nominal hurricanes.

Keywords: Performance-based Wind Engineering, Envelope Systems, Wind Driven Rain, Hurricane Modelling.

1. INTRODUCTION

Performance-based wind engineering (PBWE) is becoming accepted as a rational way to assess risks associated with building systems subject to extreme winds. Even though multiple frameworks have been developed for the performance assessment of structural systems of engineered buildings and the envelope systems of low-rise buildings, limited frameworks exist for evaluating the envelope performance of engineered buildings. While the methodology outlined in (Ouyang and Spence, 2020) does explicitly focus on the performance evaluation of the envelope system, it is based on a classic nominal representation of the wind hazard, in which hurricanes are simulated as 1-hour events with constant mean wind speed, wind direction, and rainfall intensity. However, hurricanes will in general have various event durations as well as continuously varying wind speed, wind direction, and rainfall intensities. The adequacy of the adoption of a nominal representation of hurricanes in estimating the envelope system performance has not been studied. To fill this gap, synthetic hurricane-based hazard analysis is suggested in this work, where the envelope and structural system response are evaluated through hurricanes with full evolutions of wind speed, wind direction and rainfall intensity.

The characteristics of full hurricanes necessitate a new set of models to simulate the non-stationary/-straight/-Gaussian wind pressure processes and the transient wind-driven rain intensity field. Herein, an innovative wind-tunnel informed proper orthogonal decomposition (POD)-based nonstationary simulation framework with a non-Gaussian translation model is introduced to simulate the full hurricane induced wind pressures. To enable efficient simulation of the evolution of wind-driven rain, a CFD-based interpolation-enabled simulation strategy is proposed.

* Lead presenter

2. PERFORMANCE-BASED WIND ENGINEERING SETTING

The evaluation of envelope system performance consists of the three analysis steps of: hazard analysis; system analysis; and loss analysis. In the hazard analysis, uncertainties in the hurricane hazard climate are modelled through a set of parametric models of the hurricane track, wind field, and filling rate (Vickery and Twisdale, 1995b). In the system analysis, the aerodynamic response of the system is modelled through a non-stationary/-straight/-Gaussian wind pressure model that is calibrated to classic wind tunnel data and ensures efficiency through the use of spectral proper orthogonal decomposition. System measures associated with damages are evaluated for each envelop component considering both structural and net pressure demands through adopting the progressive damage model recently introduced in (Ouyang and Spence, 2020). In the loss analysis, approaches based in consequence functions are used to translate damages into losses. Through a conditional stochastic simulation framework, general model and load uncertainties are propagated to the system responses therefore enabling the estimation of probabilistic performance metrics related to total loss (e.g. monetary loss or downtime) and the total amount of water ingress. Mathematically, the proposed hurricane framework can be expressed through the following integral:

$$\lambda(dv) = \iiint G(dv|sm)|G(sm|\Theta)||G(\Theta|\bar{v}_H)||d\lambda(\bar{v}_H)| \tag{1}$$

where $\bar{v}_H$ is the maximum hourly-mean wind speed measured at the building top, Θ is a vector collecting the hurricane model parameters, sm is the vector of system measure variables (e.g. the number of damaged components and the volume of water ingress), and dv is the decision variable of interest to the stakeholders, e.g. repair costs.

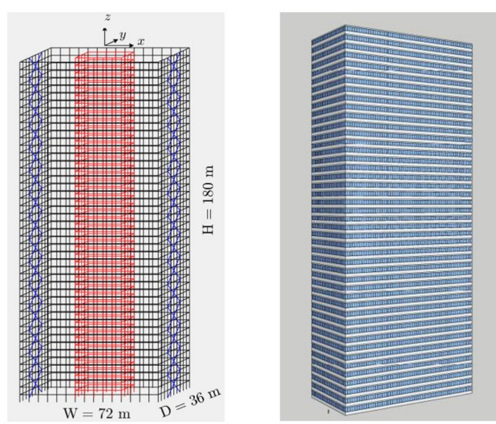

(a) (b)

Figure 1. The building archetype: (a) a 3-D view of structural system (b) cladding system layout

4. CASE STUDY

The building archetype defined in (Ouyang and Spence, 2020), and shown in Fig. 1, was considered for illustrating the framework. This building consists of a 45 story steel structure with 8100 dual pane laminated glass units defining the envelope. The glass units are considered as the only damageable components, which are modelled through fragility functions associated with two drift induced damage states $DS_{D_r,1}$ and $DS_{D_r,2}$ and one pressure induced damage state $DS_{P_{60}}$. The hurricane hazard environment at the building site was calibrated through the HURDAT database reported by Vickery and Twisdale (1995b). In calibrating the non-stationary/-straight/-Gaussian wind pressure, building specific wind tunnel data is used. Subset simulation is implemented to estimate the hazard curve through a set of sub-events. The sub-events samples are subsequently used in the stochastic simulation algorithm proposed by Ouyang and Spence (2020) to evaluate the probabilistic envelope performance of the case study structure. The resulting performance metrics, in terms of the total number of damaged components, total repair cost, and total volume of water ingress, are reported in Table 1.

Table 1. System measure and decision variables for different mean recurrence intervals (MRI).

Performance metrics	MRI = 500	MRI = 1000	MRI = 10^4	MRI = 10^5	MRI = 10^6
Number of components in $DS_{Dr,1}$	0	3	29	137	177
Number of components in $DS_{Dr,2}$	0	4	33	138	216
Number of components in DS_{P60}	1	55	215	409	651
Total loss [million US dollars]	0.0041	0.13	0.81	2.24	3.0
Total loss* [million US dollars]	0.0047	0.063	0.48	1.5	3.8
Total volume of water ingress [m^3]	3	270	2800	5300	5800
Total volume of water ingress* [m^3]	0.3	230	200	700	1200

* Nominal hurricane results

The results of Table 1 show that the pressure induced damages have dominated over the drift induced damages. The total losses estimated through adopting a nominal hurricane setting are underestimated, as compared to a full hurricane setting, for nearly all MRIs. In particular, underestimations of up to 52% are seen. The total volume of water ingress estimated by nominal hurricanes is underestimated for all MRIs with maximum underestimations exceeding 90%. These results illustrate the importance of considering a full hurricane representation during the application of PBWE.

5. CONCLUSIONS

In this paper a performance-based wind engineering framework for building envelope systems subject to full hurricanes was introduced. Through a conditional stochastic simulation approach, the framework is capable of evaluating the probabilistic metrics associated with envelope system of engineered buildings under full hurricanes. A case study of a 45 story archetype building has shown that the damages and losses estimated by nominal hurricanes will in general be underestimated for mean recurrence intervals of less than 10^6 years while estimates of water ingress will be underestimated by up to an order of magnitude.

ACKNOWLEDGEMENTS

The research effort was supported in part by the National Science Foundation (NSF) under Grant No. CMMI-1562388.

REFERENCES

Ouyang, Z. and Spence, S.M., 2020. A Performance-Based Wind Engineering Framework for Envelope Systems of Engineered Buildings Subject to Directional Wind and Rain Hazards. Journal of Structural Engineering, 146(5), p.04020049.

Vickery, P.J. and Twisdale, L.A., 1995a. Wind-field and filling models for hurricane wind-speed predictions. Journal of Structural Engineering, 121(11), pp.1700-1709.

Vickery, P.J. and Twisdale, L.A., 1995b. Prediction of hurricane wind speeds in the United States. Journal of Structural Engineering, 121(11), pp.1691-1699.

Vulnerability Assessment of Structural Insulated Panels Subjected to Windborne Debris Impact

Dikshant Saini [a,*], Behrouz Shafei [b]

[a]*Graduate Research Assistant, Dept. of Civil, Construction, and Environmental Engineering, Iowa State University, Ames, IA, USA, dikshant@iastate.edu*
[b]*Associate Professor, Dept. of Civil, Construction, and Environmental Engineering, Iowa State University, Ames, IA, USA, shafei@iastate.edu*

ABSTRACT:
This study investigates the damage to structural insulated panels (SIPs) under windborne debris hazards. For the SIPs, a high-fidelity finite element (FE) framework is developed to evaluate the perforation resistance. In this study, SIPs consisting of expanded polystyrene (EPS) sandwiched between two metal skin layers are investigated. The simulation approach is validated with the impact tests performed on the SIPs. Upon validating the models, the performance of SIPs is investigated using several parameters, including deformation pattern, critical and residual velocity, and energy absorption. The vulnerability of the SIPs is determined by evaluating the critical velocity, which is defined as the maximum velocity at which no perforations occur. Furthermore, a parametric study is conducted to study the influence of mechanical and structural properties of face sheets and foam core on the perforation resistance of SIPs used in high wind hazard regions.

Keywords: Structural Insulated Panels, Windborne Debris, Impact Simulation, Damage Assessment.

1. INTRODUCTION

Windborne debris hazard is a significant source of damage to residential and commercial buildings, resulting in billions of dollars of property loss over the past few decades. The creation of openings from impact damage will change the building's internal pressure, which would trigger further damage to structural and non-structural components. Among common types of buildings walls, structural insulated panels (SIPs) have received growing attention, owing to their high energy efficiency and reduced construction time. A typical SIP consists of polymeric foam sandwiched between two structural sheets of steel, aluminium, glass fiber reinforced polymer (GFRP), and oriented strand board (OSB). Although SIPs are considered to have superior strength, the impact resistance of such class of wall panels against windborne debris hazard has not been investigated. In this study, the performance of SIPs subjected to windborne debris impact using high-fidelity finite element (FE) models. For that purpose, a set of representative numerical models are developed, which are calibrated with impact tests from the literature (Chen and Hao, 2014). In this study, the SIPs with a height of 2.4 m, a width of 1.2 m, and a total thickness from 50 mm to 150 mm, are investigated. Based on the developed models, a parametric study is conducted to investigate the effects of a wide range of parameters (e.g., debris mass, impact velocity, mechanical and structural properties of face sheets and foam core) on the energy absorption of SIPs during the impact process. Finally, a set of vulnerability curves are developed as a function of debris mass and debris velocity to predict the perforation resistance of SIPs.

2. METHODOLOGY

To investigate the perforation resistance of SIPs subjected to windborne debris impact, a set of explicit FE simulations are performed in LS-DYNA (Saini and Shafei, 2020). The developed

* Lead presenter

models for SIPs consist of a 100 mm thick expanded polystyrene (EPS) foam core sandwiched between two 0.4 mm metal sheets made up of zincalume G300 steel. A timber projectile of a mass 4.1 kg and 100 mm × 50 mm in cross-section is modelled to simulate the windborne debris impact. This satisfies the impact test requirements prescribed for extreme conditions, per Florida Building Code (2017). The face sheets are modeled using an elastic-plastic material model, capturing the strain rate effects using Cowper and Symonds model. The EPS foam core is modeled using a modified crushable foam model that models the yield stress as a function of volumetric strain and volumetric strain rate. As observed in the past experiments, the hardwood projectile commonly experiences no deformation and mass loss during impact. Thus, it is modeled as a rigid object. The interaction between the projectile and SIPs is captured by using appropriate contact algorithms.

3. RESULTS

In this study, the perforation resistance of SIPs is evaluated by calculating the critical velocity. Critical velocity is defined as the maximum velocity of debris below which the full penetration does not occur. To capture the critical velocity, a set of simulations are conducted at sufficiently high velocities, in which the debris passes through the SIPs. After recording the residual velocities from the FE simulations with increasing initial debris impact velocities, the expression proposed by Ipson and Recht (1975) is employed for fitting the curve. Figure 1(a) illustrates how the fitted curve can be utilized to obtain the critical velocity. To obtain a vulnerability curve, the process is repeated for different debris masses from 2.0 kg to 8.0 kg. The relationships obtained for the debris mass and corresponding critical velocities can be expressed as vulnerability curves (Figure 1(b)). The curve illustrates that the SIPs will not experience perforation when the combination of design wind speed and the debris mass falls under the curve.

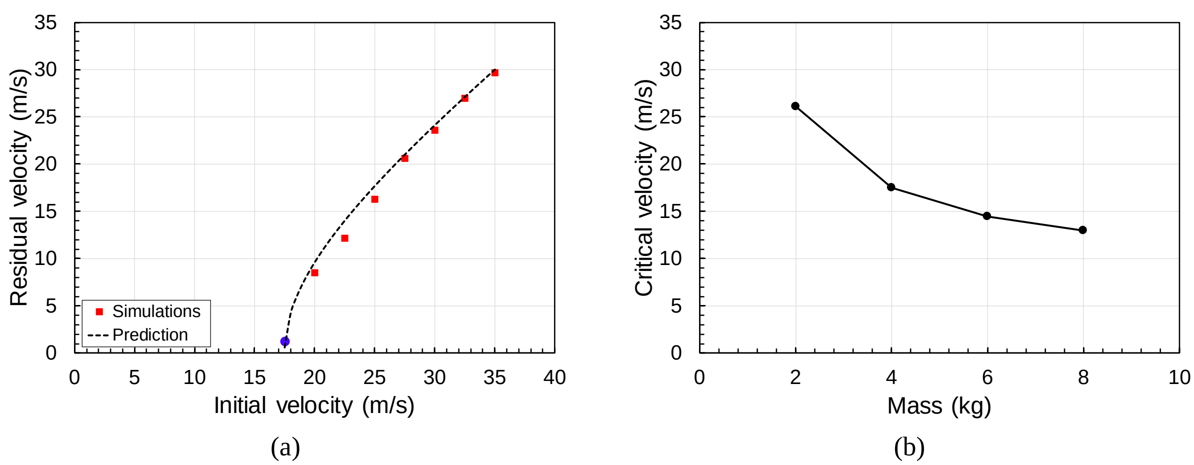

Figure 1. Development of vulnerability curve: (a) relationship between residual velocity and initial velocity, and (b) vulnerability curve.

REFERENCES

Chen, W., Hao, H., 2014. Experimental and numerical study of composite lightweight structural insulated panel with expanded polystyrene core against windborne debris impacts. Mater. Des. 60, 409–423.

Florida Building Commission, 2017. Florida Building Code, USA: International Code Council, Inc. Tallahassee, FL.

Ipson, T.W., Recht, R.F., 1975. Ballistic-penetration resistance and its measurement. Exp. Mech. 15, 249–257.

Saini, D., Shafei, B., 2020. Damage assessment of wood frame shear walls subjected to lateral wind load and windborne debris impact, Journal of Wind Engineering and Industrial Aerodynamics, 198, 104091, pp. 1–13.

A probabilistic loading model including the vertical angle of attack to estimate tornado loading

Antonio Zaldivar de Alba [a,*], Franklin T. Lombardo [b], David J. Bodine[c], Anthony E. Reinhart[d]

[a]University of Illinois at Urbana-Champaign, Urbana, IL, U.S.A., zldvrdl2@illinois.edu
[b]University of Illinois at Urbana-Champaign, Urbana, IL, U.S.A., lombaf@illinois.edu
[c]University of Oklahoma, Norman, OK, U.S.A., bodine@ou.edu
[d]NOAA National Severe Storms Laboratory, Norman, OK, U.S.A., anthony.reinhart@noaa.gov

ABSTRACT:
This presentation will detail the development of a probabilistic loading model that includes the effects of the vertical angle of attack and its use to estimate loading during tornadoes. The loading model is built using full-scale data from the Wind Engineering Research Field Laboratory (WERFL) building at Texas Tech University. Extreme value analysis is performed, separating the data depending on time-averaged values of the horizontal and the vertical angles of attack. This analysis results in distribution parameters that depend on both angles of attack. The probabilistic model is then used to estimate the loading during tornadoes using Monte Carlo (MC) simulations. The MC uses an actual tornado record captured by an anemometer and Large Eddy Simulations (LES) of tornadoes in different terrains. Tornado loading is generated with and without the vertical angle of attack to estimate its effects in loading. The simulations are done for different building positions and orientations to the simulated tornadoes. In the end, the results of multiple simulations are compared, and a factor to include the effects of the vertical angle of attack (Fv) in loading during tornadoes is proposed.

Keywords: full-scale, vertical angle of attack, tornado, wind loading

1. TORNADO LOADING, AN EXISTING PROBLEM

Tornadoes have caused significant damage for many years in the United States. In 2020 three tornado events surpassed the one billion dollars of losses threshold (NOAA 2021). Given the current demographic trends, tornado risk is expected to increase (Strader et al. 2017). Critical infrastructure is unprepared to deal with tornadoes (Kuligowski et al. 2014), and design procedures for tornadoes are needed (van de Lindt et al. 2012). Despite the multiple unknowns, progress has been made. The ASCE 7-16 commentary includes design procedures for tornadoes, and ASCE 7-22 is likely to include a Chapter dedicated to tornado loading (ASCE 2017). However, tornado loading remains an open question, and current research is proposing ways of dealing with it (Kopp and Wu 2020; Roueche et al. 2020).

1.1.The vertical angle of attack in tornadoes and building loads

Other than the extreme wind speeds during tornadoes, an essential difference between them and atmospheric boundary layer winds is their high vertical angle of attack correlated with high wind speeds (Lombardo 2017). The high values of the vertical angle of attack are important because there is full-scale evidence that peak suctions beneath conical vortices are correlated with high values of the vertical angle of attack (Wu 2000). Kopp and Wu used a loading model that included the vertical angle of attack (Wu and Kopp 2016) and developed a new framework that proposes that tornado loads can be estimated by handling the aerodynamic loads and the static load effects

* Lead presenter

separately (Kopp and Wu 2020). In line with this framework, the current work focuses on the aerodynamic difference caused by the vertical component of the wind.

This presentation will detail the development of a probabilistic loading model based on extreme pressures accounting for horizontal and vertical angles of attack. The model will be used to estimate loading during tornadoes, and a factor (Fv) to account for the effects of the vertical angle of attack during tornadoes will be proposed.

2. PROBABILISTIC LOADING MODEL DEVELOPMENT

The loading model was developed using full-scale data from the Wind Engineering Research Field Laboratory (WERFL) at Texas Tech University (Levitan et al. 1990; Smith et al. 2018). A total of 144 15-min stationary records were used. First, the pressure coefficients are normalized by the wind speed recorded at a sonic anemometer located at 30ft height at the geometric center of the building. The wind speed is averaged using an averaging time calculated using Eq. 1. Eq. 1 is derived from the finding that 5H is the smallest length scale of turbulence for which the pressure fluctuations can be explained by the quasi-steady theory (Wu and Kopp 2018).

$$\overline{WS_{T(t)}}(t) \times T(t) = 5 \times H \qquad (1)$$

In Eq. 1 $\overline{WS_{T(t)}}(t)$ is the time-averaged wind speed using the moving averaging time $T(t)$ at a time t, and H is the height of the building. The resulting pressure coefficients are declustered to guarantee independence between the peaks (Duthinh et al. 2017). The process to generate the loading model is similar to Guo et al. but using full-scale data (Guo et al. 2019). The extreme value analysis was performed by fixing the percentile threshold for peaks to be considered and their number. In this case, the number of peaks used is 35 peaks exceeding the 95th percentile value of the declustered data. This selection resulted in dividing the data into segments of 2100 declustered peaks sorted by their value of time-averaged horizontal angle of attack. Then, these segments were divided into three pieces depending on their value of the time-averaged vertical angle of attack. Gumbel parameters were obtained for all pieces of all segments for the 35 peaks of each. As a result, the current model has Gumbel parameters that depend on both angles of attack.

3. ESTIMATION OF TORNADO LOADING AND PRELIMINARY CONCLUSIONS

A series of Monte Carlo (MC) simulations were performed using the loading model developed and a full-scale tornado record (Lombardo 2017). The simulations included different building orientations, and tornado loading was generated with and without the vertical angle of attack to estimate its effects in loading. A vertical angle of attack factor (Fv) was calculated by dividing the maximum tornado load with the vertical angle of attack by the one without it. Figure 1 shows the median Fv factor for a corner tap for each building orientation. An Fv greater than 1 means the loading is increasing by including the effects of the vertical angle of attack.

Future work includes MC simulations using Large Eddy Simulations (LES) of tornadoes in different terrains. The simulations will vary the orientation and position of the building with respect to the tornado center. The current model is developed for single pressure taps, but future work includes the development of an area-averaged loading model and its corresponding analysis.

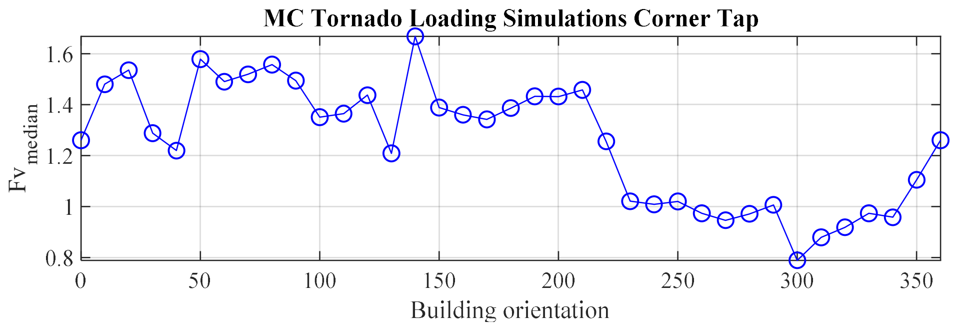

Figure 1. Median Fv resulting from MC simulations using full-scale tornado record for a corner pressure tap.

ACKNOWLEDGEMENTS

The authors gratefully acknowledge the Wind Engineering Research Field Laboratory (WERFL) at Texas Tech University for the valuable data provided. The first author acknowledges CONACYT and Alianza FiiDEM for their financial support during his Ph.D. studies and ASCE and SEI for their support with the 2020 O.H. Ammann Research Fellowship in Structural Engineering.

REFERENCES

ASCE. (2017). "ASCE 7-16: Minimum Design Loads and Associated Criteria for Buildings and Other Structures." American Society of Civil Engineers, Reston, Virgina.

Duthinh, D., Pintar, A. L., and Simiu, E. (2017). "Estimating peaks of stationary random processes: A peaks-over-threshold approach." *ASCE-ASME Journal of Risk and Uncertainty in Engineering Systems, Part A: Civil Engineering*, 3(4), 04017028.

Guo, Y., Wu, C.-H., and Kopp, G. A. "A conditional-averaging method to estimate peak pressures onlow-rise building." *The 15th International Conference on Wind Engineering*, Beijing, China.

Kopp, G. A., and Wu, C.-H. (2020). "A framework to compare wind loads on low-rise buildings in tornadoes and atmospheric boundary layers." *Journal of Wind Engineering and Industrial Aerodynamics*, 204, 104269.

Kuligowski, E. D., Lombardo, F. T., Phan, L. T., Levitan, M. L., and Jorgensen, D. P. (2014). "Final report, National Institute of Standards and Technology (NIST) technical investigation of the May 22, 2011, tornado in Joplin, Missouri."

Levitan, M. L., Mehta, K. C., Chok, C. V., and Millsaps, D. L. (1990). "An overview of Texas Tech's wind engineering field research laboratory." *Journal of Wind Engineering and Industrial Aerodynamics*, 36, 1037-1046.

Lombardo, F. T. (2017). "Engineering Analysis of a Full-Scale High-Resolution Tornado Wind Speed Record." *Journal of Structural Engineering*, 144(2), 04017212.

NOAA. (2021). "U.S. Billion-Dollar Weather and Climate Disasters ", National Centers for Environmental Information (NCEI).

Roueche, D. B., Prevatt, D. O., and Haan, F. L. (2020). "Tornado-induced and straight-line wind loads on a low-rise building with consideration of internal pressure." *Frontiers in built environment*, 6, 18.

Smith, D., Mehta, K., and Morse, S. (2018). "Wind Engineering Research Field Laboratory Selected Data Sets for Comparison to Model-Scale, Full-Scale and Computational Fluid Dynamics Simulations." DesignSafe-CI

Strader, S. M., Ashley, W. S., Pingel, T. J., and Krmenec, A. J. (2017). "Observed and projected changes in United States tornado exposure." *Weather, climate, and society*, 9(2), 109-123.

van de Lindt, J. W., Pei, S., Prevatt, D. O., Dao, T., Coulbourne, W., Graettinger, A. J., and Gupta, R. "Dual objective design philosophy for tornado engineering." *Structures Congress 2012*, 965-976.

Wu, C.-H., and Kopp, G. A. (2016). "Estimation of wind-induced pressures on a low-rise building using quasi-steady theory." *Frontiers in built environment*, 2, 5.

Wu, C.-H., and Kopp, G. A. (2018). "A quasi-steady model to account for the effects of upstream turbulence characteristics on pressure fluctuations on a low-rise building." *Journal of Wind Engineering and Industrial Aerodynamics*, 179, 338-357.

Wu, F. (2000). "Full-scale study of conical vortices and their effects near roof corners," Texas Tech University.

Tornado Wind Speed Estimation Methods in Rural Forested Regions: The Alonsa, MB Tornado

Daniel M. Rhee [a,*], Sarah Stevenson [b], Franklin T. Lombardo [c], Greg Kopp [d]

[a]*University of Illinois at Urbana-Champaign, Urbana, IL, USA, rhee16@illinois.edu*
[b]*University of Western Ontario, London, ON, Canada, ssteve72@uwo.ca*
[c]*University of Illinois at Urbana-Champaign, Urbana, IL, USA, lombaf@illinois.edu*
[d]*University of Western Ontario, London, ON, Canada, gakopp@uwo.ca*

ABSTRACT:
Wind speed estimation of a tornado is exceptionally difficult in forested regions where minimal structural damage is observed. Instead, tornadoes inflict extensive tree damage. This tree damage can be used to estimate the near-surface wind field by analyzing the fall patterns (i.e., tree-fall analysis). Aerial imagery was collected following the EF-4 rated Alonsa, MB by the Northern Tornadoes Project (NTP). The necessary tree characteristics were extracted from aerial photographs using image processing tools, and other tornado properties such as the damage path and width were acquired by the NTP. The tree-fall analysis showed the evolution of tornado growing in both intensity and size with an overall maximum wind speed of 88 m/s (195 mph). Debris flight analysis and detailed structural analysis were also carried out and compared as independent wind speed estimates.

Keywords: Tornado, Near-surface Wind Speed, Tree-fall Pattern, Debris Flight

1. INTRODUCTION
According to Sills et al. (2020), more tornadoes are believed to occur than currently reported, especially in the northern part of Canada where majority of the land is heavily forested and uninhabited. However, near-surface wind speed estimation of a tornado is often difficult in these regions using conventional methods (i.e., structural damage). Tree-fall analysis is a tool that utilizes the fall pattern of trees to estimate the near-surface wind field of a tornado (Lombardo et al., 2015; Rhee and Lombardo, 2018) and is particularly useful in forested regions.

In August 2018, a violent tornado developed near Alonsa, MB, which caused significant tree (and forest) damage. The tree-fall pattern was acquired by Rhee et al. (2021) using computer vision and image processing tools and the near-surface wind field was estimated by tree-fall analysis based on the acquired tree-fall pattern and the estimated critical wind speed of tree-fall V_c. Independent wind speed estimations were also made by the NTP using structural damage and debris flight analysis and compared to the wind field estimation from the tree-fall analysis.

2. WIND FIELD ESTIMATION BASED ON TREE-FALL PATTERNS
2.1. Critical Wind Speed of Tree-fall
Through the use of computer vision and image processing tools, the dimensions of tree can be estimated from an aerial photo with a known resolution and estimated tree pixels. An example sampled from the Alonsa, MB tornado aerial photograph with a resolution of 5-cm is shown in Figure 1. First, an RGB color-filter that depicts the tree pixels is applied and converted into a

* Lead presenter

binary image (Figure 1(b)). Second, the object detection algorithm is applied to remove noise (Figure 1(c)) and separate the tree pixels (Figure 1(d)). Multiplying the resolution scale to the number of pixels (5-cm/pix for length and 25-cm^2/pix for area), the actual dimensions of tree can be estimated. In the HWIND model (Peltola et al., 1999), a wind-induced force is exerted on the tree, which is governed by the frontal area. Herein, the area of tree estimated from the aerial photo using image processing tool is used. A total of 41 trees are sampled and their mean V_c was estimated to be 47.5 m/s (106 mph).

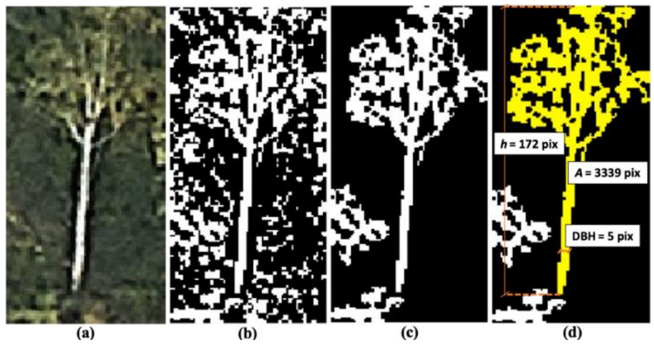

Figure 1. Extraction of tree pixels using image processing tools

2.2. Near-surface Wind Field Estimation

Tree-fall patterns acquired by a semi-automated tree-fall identification technique (Rhee et al., 2021) were used to estimate Rankine vortex (RV) parameters and recreate the near-surface wind field of the Alonsa tornado. A total of six transects at different locations along the tornado track were selected and analyzed to capture the evolution of the tornado. With an assumed translational speed (V_T) of 18 m/s (COD, 2018) and the average V_c (48 m/s) estimated in section 2.1, tree-fall analysis was carried out for each transect, in which the wind speed contour lines are shown in Figure 2. The overall maximum wind speed from the "best-match" RV parameters was estimated at 88 m/s (195 mph) with an uncertainty range of 71-97 m/s (160-215 mph).

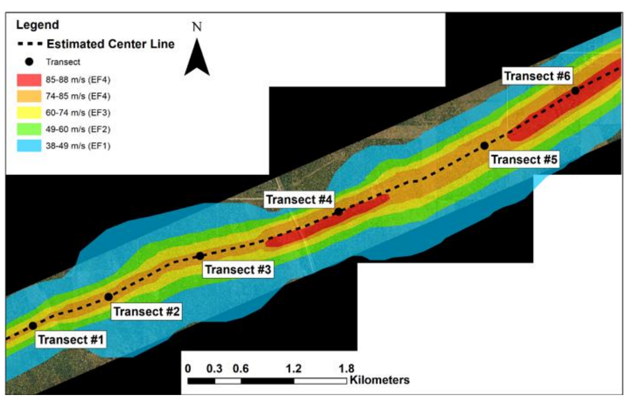

Figure 2. Estimated near-surface wind field of the Alonsa tornado

3. WIND SPEED ESTIMATION BASED ON OTHER DAMAGE INDICATORS

3.1. Structural Analysis

A ground-based damage survey was also conducted by the NTP. Two members of the NTP assessed the site and determined an EF4 damage (DOD 9) for One- and Two-Family Residences (FR12) and several EF2 and EF3 damages of FR12 and Small Barns and Farm Outbuildings. A more detailed structural analysis can provide more accurate wind speed estimates by inspecting the weak links between structural components. In the Alonsa tornado, wall baseplate failures due to nail withdrawal from the plywood floor were observed in the EF4 and one of the EF3 damaged FR12. The strength required to cause the wall baseplate failure was estimated by Stevenson et al. (2020). The 3-s gust wind speed to cause the same failure for the damaged FR12 was estimated at 67 m/s (150 mph), confirming an at least EF3 wind speed.

3.2. Debris Flight Analysis

Ground observations also showed evidence of debris flight where large haybales and vehicles were lofted from the ground and traveled mid-air. The threshold wind speed to loft an industrial haybale was estimated at 75 m/s (170 mph) using a debris flight model (Wills et al., 2002). However, the lofted haybales were found near the shore of Lake Manitoba, traveling at least 1.5 km and indicating that the wind speed may have been significantly higher than the debris threshold wind speed. Although debris flight analysis was carried out for the lofted vehicles, wind tunnel and tornado simulator experiments performed by Haan et al. (2017) suggest that debris threshold wind speed for lofting of vehicles tends to occur in wind speed of high-end EF3 to low-end EF4 range.

4. COMPARISON

The preliminary analysis suggests that the independent wind speed estimates using different damage indicators show reasonable agreement with one another. The tree-fall analysis estimated the maximum wind speed in the high-end EF4 range (195 mph), and the other damage indicators estimated the wind speed to be at least high-end EF3 (150-165 mph), and possibly EF4 wind speed (170 mph or higher). A more detailed spatial comparison is yet to be performed.

REFERENCES

Haan Jr, F. L., Sarkar, P. P., Kopp, G. A., and Stedman, D. A., 2017. Critical wind speeds for tornado-induced vehicle movements. Journal of Wind Engineering and Industrial Aerodynamics, 168, 1-8.

Lombardo, F. T., Roueche, D. B., and Prevatt, D. O., 2015. Comparison of two methods of near-surface wind speed estimation in the 22 May, 2011 Joplin, Missouri Tornado. Journal of Wind Engineering and Industrial Aerodynamics, 138, 87-97.

Peltola, H., Kellomäki, S., Väisänen, H. and Ikonen, V. P., 1999. A mechanistic model for assessing the risk of wind and snow damage to single trees and stands of Scots pine, Norway spruce, and birch. Canadian Journal of Forest Research, 29(6), 647-661.

Rhee, D. M. and Lombardo, F. T., 2018. Improved near-surface wind speed characterization using damage patterns. Journal of Wind Engineering and Industrial Aerodynamics, 180, 288-297.

Rhee, D. M., Lombardo, F. T. and Kadowaki, J., 2021. Semi-automated tree-fall pattern identification using image processing technique: Application to Alonsa, MB tornado. Journal of Wind Engineering and Industrial Aerodynamics, 208, 104399.

Sills, D. M., Kopp, G. A., Elliott, L., Jaffe, A. L., Sutherland, L., Miller, C. S., Kunkel, J. M., Hong, E., Stevenson, S. A. and Wang, W., 2020. The Northern Tornadoes Project: Uncovering Canada's True Tornado Climatology. Bulletin of the American Meteorological Society, 101(12), E2113-E2132.

Stevenson, S. A., Kopp, G. A. and El Ansary, A. M., 2020. Prescriptive Design Standards for Resilience of Canadian Housing in High Winds. Frontiers in Built Environment, 6, 99.

Wills, J. A. B., Lee, B. E., and Wyatt, T. A., 2002. A model of wind-borne debris damage. Journal of Wind Engineering and Industrial Aerodynamics, 90(4-5), 555-565.

Computational methods of windborne debris trajectories in a near-surface tornadic field

Guangzhao Chen [a*], Franklin T. Lombardo [a]

[a]University of Illinois at Urbana-Champaign, Urbana, IL, USA, gc4@illinois.edu
[a]University of Illinois at Urbana-Champaign, Urbana, IL, USA, lombaf@illinois.edu

ABSTRACT:
In a tornado, windborne debris is the main source of residential building envelope damage. In an estimated tornadic field based on post-damage survey data, the windborne debris can act as a particle in the pressure field. To consider the debris risk analysis, the flying trajectories of the debris need to be analyzed for a specific tornado scenario. This paper raises a novel model which simulates compact, rod-like, and plate-like windborne debris trajectories with a simplified coupled computational fluid dynamics rigid body (CFD-RBD) method. A translational vortex field generates a windborne debris distribution map around the target building. Thus, the in-situ debris distribution map, which can be accessed from the post damage survey, will be compared with the CFD-RBD result and then provides the estimation of the tornadic wind and pressure fields. An example of a windborne debris distribution map is given to demonstrate the whole method by using the post damage survey data of the 2011 Joplin, MO tornado.

Keywords: Tornado, Debris, Near-surface, post-disaster data, Trajectories

1. INTRODUCTION

A tornado is an extreme and complex wind event that is composed of a violently rotational wind field and a persistently translational wind field, and it cause nearly one-fifth of all-natural hazard fatalities based on 10-year average data in the United States (NWS Analyze, 2020). To understand and replicate the complex near-surface tornadic field, some numerical vortex models have been proposed such as Rankine vortex model (Rankine, 1882, p. 1), Burgers-Rott Model (Burgers, 1948; Rott, 1958), and Baker-Sterling model (Baker and Sterling, 2017). These models have been proposed for use in numerous actual tornadoes (Refan and Hangan, 2018; Bluestein et al., 2018, Chen and Lombardo, 2019) based on radar data and tree-fall/damage patterns as *in-situ* data are challenging to obtain.

In a tornado, windborne debris is commonplace. The debris will obtain massive kinetic energy as missiles during the motion in the near-surface tornadic field (Lin et al., 2007). Hence, it is possible to consider the windborne debris landing points as evidence for evaluating the near-surface tornadic field. Thus, this paper puts forward a method for applying translational numerical vortex models into a real tornado event by adopting the windborne debris distribution map around the damaged building to replicate the near-surface tornadic field in the real case.

As for replicating the near-surface tornadic field from previous tornado cases, this paper adopting the estimated tornado path from satellite images and applying a translational vortex model with pre-set parameters combination along the path. Then, the computed debris flying trajectories in the replicated tornadic field can be described through theoretical formula results (Twisdale et al., 1979) and the fitting aerodynamic coefficient result from CFD-RBD test data.

* Lead presenter

Then, The estimated landing points of windborne debris generated from the footprint of the damaged building during a tornado case are recorded to generate a distribution cluster map. Comparing the cluster with the real debris landing point from post damage survey data, an evaluation score for the matching degree between the numerical replicated near-surface tornadic field and the in-situ situation is given, and the best-fit model parameters combination can be found.

In this paper, Section 2 introduces the acquisition process of the in-situ debris distribution data from post damage survey as the source data of this method; Section 3 introduces the numerical models of a translational one-cell vortex and plate debris trajectories in the simulated wind field coupled with CFD-RBD simulation for wind coefficient; the model fitting and approximation process with the 2011 Joplin, MO tornado is shown in Section 4 and the possible improvement is developed in Section 5.

2. DATA COLLECTION

During a post damage survey, orthogonal photos containing building damage and windborne debris are generated from aerial imagery. As an illustration, Figure 1 shows an extracted building footprint and nearby windborne debris from that footprint. After the image analysis process, the coordinates of debris landing points and the aspect ratio for each piece of debris are recorded as the input data.

Figure 1. An aerial photo of a rectangular residential building with yellow marked plate debris and blue marked rod debris

3. MODELS

3.1. Estimated near-surface tornadic field

Considering the previously mentioned stationary vortex models along a tornado path to reproducing a real tornado case, a modified near-surface tornadic field can be generated as a combination of a numerical stationary vortex field and a translation field (Chen and Lombardo, 2019). To consider the debris flight trajectories in the estimated translational near-surface tornadic field, a three-dimensional vortex model (e.g. Burgers-Rott Model; Baker Sterling model) is able to describe the debris motion.

3.2. Computed trajectories in the estimated near-surface tornadic field

Previous studies have built exhaustive theoretical formulas to describe the aerodynamic behaviors of different types of debris. Windborne debris is classified into three types: compact, sheet, and rod based on its shape (Wills et al., 2002). In the beginning, basic equations of motion (EOM) for debris were established only considering the drag force of spherical particles (McDonald, 1976). Then, a three-dimensional trajectory model with lift, drag, and side force impact under relative wind vector was generated (Twisdale et al., 1979). Finally, a six-dimensional model with overall consideration of lift, drag, side force, pitch moment, rolling moment, and deflection torque coefficients is established (Redmann et al., 1978). The computed solution of debris flight trajectories matured gradually from the theoretical model to the wind tunnel test validation and modified models with considering Magnus and turbulence effects (Lin et al., 2007; Richards et al., 2008). Computational Fluid Dynamics (CFD) is also applied in recent studies of simulating the windborne debris trajectories, and unsteady/ quasi-steady flow methods are the two main simulation methods applied. In the unsteady flow simulation method, the debris motion in the wind field is considered as a Fluid-Structure Interaction (FSI) problem, and Large Eddy Simulation (LES) with dynamic mesh technique is applied for solving the time-varying debris spatial position (Liu et al., 2021). As for the quasi-steady simulation method, the debris aerodynamic force is assumed only related to the relative rigid body motion in the current time step, and RANS could be applied to solve the trajectories (Kakimpa et al., 2012). Since the traditional EOM method usually describes the specific debris used in wind tunnel experiment and inconvenient to be applied for the debris real cases, and the unsteady CFD method requires a huge computer source, this paper couples a 3-DOF debris EOM with a quasi-steady CFD method for determining the aerodynamic coefficient for the debris from the real case under the variance of wind attack angle and debris' aspect ratio. As an illustration, 3-DOF EOM under a steady flow (U and V are computed from the wind field model) for plate debris are shown in Eq (1)-(3), and the small-time step simulation method is shown in Eq (4)-(6):

$$\frac{d^2x}{dt^2} = \frac{dU_m}{dt} = \frac{\rho_a A\left[(U-U_m)^2+(V-U_m)^2\right](C_D\cos\beta - C_L\sin\beta)}{2m} \tag{1}$$

$$\frac{d^2z}{dt^2} = \frac{dV_m}{dt} = \frac{\rho_a A\left[(U-U_m)^2+(V-U_m)^2\right](C_D\sin\beta + C_L\cos\beta)}{2m} - \mathrm{g} \tag{2}$$

$$\frac{d^2\theta}{dt^2} = \frac{d\omega_m}{dt} = \frac{\rho_a A l\left[(U-U_m)^2+(V-U_m)^2\right]C_M}{2I_m} \tag{3}$$

$$x_i = x_{i-1} + U_{m,i-1}\Delta t + 0.5a_{x,i-1}\Delta t^2 \tag{4}$$

$$y_i = y_{i-1} + V_{m,i-1}\Delta t + 0.5a_{y,i-1}\Delta t^2 \tag{5}$$

$$\theta_i = \theta_{i-1} + \omega_{m,i-1}\Delta t + 0.5a_{\theta,i-1}\Delta t^2 \tag{6}$$

In these equations, C_D, C_L and C_M for a single time step with are determined by CFD under the wind attack angle β, which can be denoted by rotation angle θ as Eq (7):

$$\sin\beta = \frac{V_i - V_{m,i}}{\sqrt{\left(U_i - U_{m,i}\right)^2 + \left(V_i - V_{m,i}\right)^2}} \tag{4}$$

4. RESULTS

For the case shown in Figure 1, a plate debris with a length of 1.92 meters and a width of 0.84 meters, which were obtained from image analysis, is selected as the target plate. Then, the aerodynamic coefficients under different wind attack angles for this debris are simulated in ANSYS Fluent software with Spalart-Allmaras viscous equation under second-order upwind solution format. The source building footprints are meshed based on the debris area information and for each mesh grid point, flying debris is generated once a critical wind speed V_c=70 mph is reached. As for the illustration case, a Rankine vortex field with parameters ($\eta = 3.69$, $G_{max} = 5.13$, $\alpha = 24.9°$, R_{max}=380m, $\varphi = 0.821$) (Chen and Lombardo, 2019) is applied for the near-surface tornadic field.

Then for each piece of flying debris, a trajectory is computed under the pre-defined wind field model coupled with the 3-DOF equations with CFD-generated aerodynamic coefficients. As a result, the clustering degree of the simulated debris' landing points represents the accuracy of the whole model. As shown in Figure 2, the Euclidean Distance for the landing point cluster to the target plate debris is 7.07 meters.

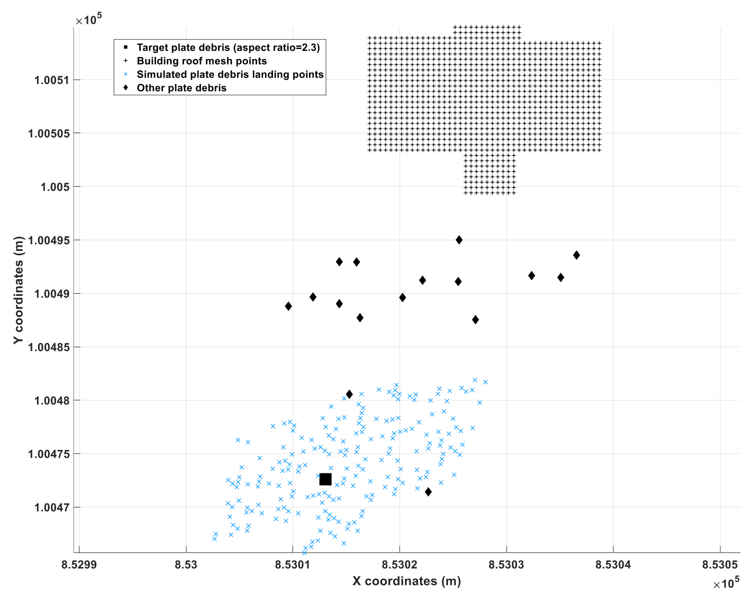

Figure 2. An illustration for simulated debris landing point cluster map

5. CONCLUSION AND IMPROVEMENT

This numerical debris model, which couples a tornado vortex model and 3-DOF equations with CFD-RBD simulated coefficients, makes it possible to rapidly simulate and evaluate the debris distribution from actual tornado cases. The estimated debris trajectories and distribution map will help to calibrate the near-surface wind field. As for improvements, a joint evaluation method for various debris with different types will be considered.

ACKNOWLEDGEMENTS
The authors gratefully acknowledge the financial support of the UIUC-ZJU grant and the members of the Wind Engineering Research Laboratory (WERL).

REFERENCES

Baker, C.J., Sterling, M., 2017. Modelling wind fields and debris flight in tornadoes. J. Wind Eng. Ind. Aerodyn. 168, 312–321. https://doi.org/10.1016/j.jweia.2017.06.017

Burgers, J.M., 1948. A Mathematical Model Illustrating the Theory of Turbulence, in: Von Mises, R., Von Kármán, T. (Eds.), Advances in Applied Mechanics. Elsevier, pp. 171–199. https://doi.org/10.1016/S0065-2156(08)70100-5

Kakimpa, B., Hargreaves, D.M., Owen, J.S., 2012. An investigation of plate-type windborne debris flight using coupled CFD–RBD models. Part I: Model development and validation. J. Wind Eng. Ind. Aerodyn. 111, 95–103. https://doi.org/10.1016/j.jweia.2012.07.008

Lin, N., Holmes, J.D., Letchford, C.W., 2007. Trajectories of Wind-Borne Debris in Horizontal Winds and Applications to Impact Testing. J. Struct. Eng. 133, 274–282. https://doi.org/10.1061/(ASCE)0733-9445(2007)133:2(274)

Liu, Z., Cao, Y., Wang, Y., Cao, J., Hua, X., Cao, S., 2021. Characteristics of compact debris induced by a tornado studied using large eddy simulations. J. Wind Eng. Ind. Aerodyn. 208, 104422. https://doi.org/10.1016/j.jweia.2020.104422

McDonald, J.R., 1976. Tornado-generated missiles and their effects, in: Proceedings of the Symposium on Tornadoes. pp. 331–348.

NWS Analyze, F. and S.O., n.d. NWS Analyze, Forecast and Support Office [WWW Document]. URL http://www.nws.noaa.gov/om/hazstats.shtml (accessed 11.12.18).

Rankine, W.J.M., 1882. A Manual of Applied Physics. Man. Appl. Phys.

Redmann, G., Radbill, J., Marte, J., Dergarabedian, P., Fendell, F., 1978. Wind field and trajectory models for tornado-propelled objects. Electr. Power Res. Inst. Rep. EPRI NP.

Richards, P.J., Williams, N., Laing, B., McCarty, M., Pond, M., 2008. Numerical calculation of the three-dimensional motion of wind-borne debris. J. Wind Eng. Ind. Aerodyn. 96, 2188–2202. https://doi.org/10.1016/j.jweia.2008.02.060

Rott, N., 1958. On the viscous core of a line vortex. Z. Für Angew. Math. Phys. ZAMP 9, 543–553. https://doi.org/10.1007/BF02424773

Twisdale, L.A., Dunn, W.L., Davis, T.L., 1979. Tornado missile transport analysis. Nucl. Eng. Des. 51, 295–308. https://doi.org/10.1016/0029-5493(79)90096-7

Wills, J.A.B., Lee, B.E., Wyatt, T.A., 2002. A model of wind-borne debris damage. J. Wind Eng. Ind. Aerodyn. 90, 555–565. https://doi.org/10.1016/S0167-6105(01)00197-0

Probabilistic assessment of the nonlinear response of the 20-story SAC building under extreme wind loads through collapse

Azin Ghaffary [a], Mohamed Moustafa [b]

[a]*University of Nevada Reno, Reno, Nevada, USA, aghaffary@nevada.unr.edu*
[b]*University of Nevada Reno, Reno, Nevada, USA, mmoustafa@nevada.unr.edu*

ABSTRACT
Recent advancements for performance-based design of buildings subjected to wind loads require incorporation of uncertainties in both loading and resistance into the nonlinear analysis procedures that are used for predicting wind-induced response of the buildings. While probabilistic analysis approaches are more commonly used for incorporation of uncertainties, their ability in simulating detailed nonlinear behaviour of the structures if often subject to limitations. Deterministic methods, on the other hand, are generally capable of simulating complex nonlinear behaviour of buildings such as stiffness and strength degradation and provide more accurate predictions of the nonlinear state of the structure such as yield and collapse points, with the expense of additional computational effort. In this study, uncertainties in wind loads subjected to the building as well as the building properties are included into the nonlinear deterministic simulation of the wind-induced response of the 20-story SAC frame all the way through collapse. WE-UQ tool developed by SimCenter is utilized for incorporating uncertainties into the deterministic model of the frame created in OpenSEES. The WE-UQ Application is an open-source software that provides researchers a tool to assess the performance of a building to wind loading. Nonlinear probabilistic/deterministic performance assessment of the building through collapse is then performed by incorporating uncertainties into the simulation of building-related and wind-related parameters, while incorporating the effects of wind directionality.

Keywords: Uncertainty quantification, nonlinear analysis, performance-based wind engineering

1. INTRODUCTION

Current practice in the wind design of the regular-shaped buildings that do not possess unstable response characteristics in the across-wind direction is the equivalent static design method (ASCE/SEI 2017). In this approach, the wind loads are applied to the building statically, and the response of the building remains linear elastic. More realistic methods have been proposed to date, such as the Data-Based Assisted Design (DAD) method proposed by (Park, Duthinh et al. 2019), in which a linear response history analysis approach is used. However, recently, researchers and practicing engineers have been interested in the development and utilization of performance-based wind design of the buildings. Although this approach has been well established in seismic applications, it is still undergoing developments in the field of wind engineering. The main objective of this study is to obtain an improved understanding of the probabilistic nonlinear response of the building structures subjected to strong wind loads all the way through collapse.

2. MTHODOLOGIES

The 20-story steel moment resisting frame, from the SAC project (SAC Joint venture 2000), is chosen for the purpose of the probabilistic nonlinear performance assessments in the current study. SAC is a joint venture between the Structural Engineers Association of California (SEAOC; the S in SAC), the Applied

Technology Council (ATC; the A in SAC), and California Universities for Research in Earthquake Engineering (CUREe; the C in SAC). The chosen building is located in Boston, USA and has a wind-governed design. Given the importance of detailed simulation of the nonlinear structural response in accurate prediction of different nonlinear states such as yielding and collapse, a complex nonlinear model of the frame is created in OpenSEES (McKenna 2000). This model includes detailed simulation of the beam, column, and panel zone nonlinear behavior including stiffness and degradation. The wind loading histories for the building are obtained from the Tokyo Polytechnic University database for high-rise buildings (TPU 2008). The OpenSEES model and the wind loading history from TPU database are then used as inputs to the WE-UQ tool (Frank McKenna 2019) developed by SimCenter for incorporating uncertainties into the deterministic simulation of the wind-induced response of the buildings. In the OpenSEES model, the building's inherent damping, the material's modulus of elasticity, and the parameters of the modified Ibarra-Medina-Krawinkler deterioration model for the beam (Lignos and Krawinkler 2010) and column (Lignos, Hartloper et al. 2019) elements are chosen as random variables with proper statistical distributions chosen according to the relevant literature (Kareem 1987, Lignos and Krawinkler 2010, Li and Hu 2014, Huang 2017, Lignos, Hartloper et al. 2019). In addition, the speed of the wind loading histories is also chosen as a random variable. Nonlinear probabilistic/deterministic performance assessment of the building through collapse is then performed using the Latin Hypercube Sampling (LHS) method chosen for the uncertainty quantification engine within the WE-UQ tool.

6. REFERENCES

ASCE/SEI (2017). "Minimum Design Loads and Associated Criteria for Buildings and Other Structures (ASCE 7-16)."

Frank McKenna, P. M.-H., Wael Elhaddad, Michael Gardner, Jiawei Wan, & Dae Kun Kwon (2019). "NHERI-SimCenter/WE-UQ: Version 2.0.0 (Version v2.0.0). Zenodo."

Huang, M. (2017). Performance-Based Design Optimization of Wind-Excited Tall Buildings. High-Rise Buildings under Multi-Hazard Environment, Springer**:** 157-185.

Kareem, A. (1987). "Wind effects on structures: a probabilistic viewpoint." Probabilistic engineering mechanics **2**(4): 166-200.

Li, G. and H. Hu (2014). "Risk design optimization using many-objective evolutionary algorithm with application to performance-based wind engineering of tall buildings." Structural Safety **48**: 1-14.

Lignos, D. G., A. R. Hartloper, A. Elkady, G. G. Deierlein and R. Hamburger (2019). "Proposed Updates to the ASCE 41 Nonlinear Modeling Parameters for Wide-Flange Steel Columns in Support of Performance-Based Seismic Engineering." Journal of Structural Engineering **145**(9): 04019083.

Lignos, D. G. and H. Krawinkler (2010). "Deterioration modeling of steel components in support of collapse prediction of steel moment frames under earthquake loading." Journal of Structural Engineering **137**(11): 1291-1302.

McKenna, F., Fenves, G. L., Scott, M. H., and Jeremic, B. (2000). Open System for Earthquake Engineering Simulation (OpenSees), Pacific Earthquake Engineering Research Center, University of California, Berkeley, CA.

Park, S., D. Duthinh, E. Simiu and D. Yeo (2019). "Wind Effects on a Tall Building with Square Cross-Section and Mid-Side Base Columns: Database-Assisted Design Approach."

SAC Joint venture (2000). Recommended seismic design criteria for new steel moment-frame buildings, Federal Emergency Management Agency.

TPU (2008). Wind Pressure Database for High-Rise Building. Tokyo Polytechnic University.

Using the Jupyter Notebooks as a tool for CFD simulations

Fei Ding [a,*], Ahsan Kareem [b]

[a]*NatHaz Modeling Laboratory, University of Notre Dame, Notre Dame, IN, US, fding@nd.edu*
[b]*NatHaz Modeling Laboratory, University of Notre Dame, Notre Dame, IN, US, kareem@nd.edu*

ABSTRACT:
The Jupyter Notebooks (www.jupyter.org) have been widely used in science and engineering communities as an open-source interactive literate programming paradigm. It has the capabilities of combining text, images or videos with research codes, and can easily document, share, and reproduce data analysis. As for computational fluid dynamics (CFD), an open-source software OpenFOAM is popularly used for computationally establishing wind effects on structures. To help beginners overcome the challenges of steep learning curve posed by OpenFOAM, we present the work to script the workflow for OpenFOAM simulations using the Jupyter Notebooks. The developed Jupyter Notebooks can aid in determining inflow conditions, creating mesh files for parameterized building geometries and running the selected solvers. This tool can also contribute to the education for CFD learning as online resources, which will be implemented in the DesignSafe cyberinfrastructure (CI) (www.designsafe-ci.org).

Keywords: Jupyter Notebooks, CFD, OpenFOAM, DesignSafe

1. INTRODUCTION

The Jupyter Notebooks has become an attractive venue for data processing, visualization and sharing due to its interactive feature with the code. The Jupyter Notebooks are composed of cells which can be categorized into three types: code, markdown and raw. A code cell can be executed, and a markdown cell contains text or images to illustrate the code. Tools that convert the Jupyter Notebooks into other formats can use raw cells for configuration (Pimentel et al., 2019). The Jupyter Notebooks can be accessed either through a local PC or through a web browser such as on the Jupyter Hub in the Discovery Workspace of DesignSafe CI (Rathje, et al. 2017). This makes it easy to use the same interface running on a remote server (Kluyver et al., 2016) to access and manipulate the files.

In the digital age, the burgeoning growth of computational resources to conduct numerical experiments have promoted the use of CFD to address the evaluation of wind effects on structures. Moreover, OpenFOAM is a CFD open-source code that is used to solve turbulent flows and other complex fluid flows. However, OpenFOAM as well as commercial CFD software requires the expertise in computational wind engineering (Ding et al., 2019), which may hinder their practical use for non-CFD-experts. For example, the engineers or researchers lacking the knowledge about the necessary precision regarding the grid size close to the building envelope could lead to the failure in CFD simulations (Tamura & Van Phuc, 2015). To address this issue, we developed the Jupyter Notebooks as an open-source project to directly execute the functions for mesh generation, inflow settings, etc. in a user-friendly and interactive coding environment, aiming at alleviating the sophistication in running CFD models in OpenFOAM. In particular, this developed Jupyter notebooks will be implemented in the Jupyter Hub in the DesignSafe CI to expand the user base and contribution to research, education and practical use in the area of computational wind engineering.

* Lead presenter

2. OPENFOAM WORKFLOW

The overall concept of the OpenFOAM workflow may be expressed as meshing-solution-analysis-optimization-visualization. In the input contexts, three folders named "0", "Constant" and "System" should be predefined by users, among which "0" contains initial and boundary conditions, "constant" involves physical properties and turbulence modelling properties, and "system" covers the run-time control and solver numeric (Jasak et al., 2007). The commonly used solvers for turbulent flows include PisoFoam which is a transient solver for incompressible and turbulent flows and simpleFoam as a steady-state solver. The parallel computation in OpenFOAM allows the simulation to run in the distributed processors simultaneously. In addition, flow simulations can also be set on the OpenFOAM interface on the website of Discovery Workspace in the DesignSafe CI. The job can be submitted to the HPC resources at TACC by simply clicking the *Run* button. The status of the job can be viewed through the *Job Status* on the right of the website. Simulation results are stored in the Data Depot and available to be post-processed by users.

3. DEVELOPMENT OF THE JUPYTER NOTEBOOKS CONNECTING OPENFOAM DICTIONARIES

To overcome the challenges of steep learning curve posed by OpenFOAM, an illustrative example for an end-to-end flow simulation as shown in Fig. 1 will be provided for a rectangular building in which its envelope is parameterized by the aspect ratio. OpenFOAM command lines for mesh generation and simulation in parallel are written in the code cells and executed using the kernel in the Jupyter Notebooks. We will also implement TAPIS which is a scriptable command line interface in Python to access to TACC HPC resources.

To introduce more flexibilities and bring the maximum automation in CFD modelling including parameterization of the building geometry and boundary conditions, an OpenFOAM library named PyFoam needs to be utilized. PyFoam is written in Python, therefore can be used in Jupyter Notebooks to execute OpenFOAM solvers and manipulate the parameter files in OpenFOAM. With the aid of PyFoam, the Jupyter Notebooks can manipulate the parameter files and dictionaries in OpenFOAM cases as regular Python dictionaries without looking into the OpenFOAM C++ libraries. In this study, the automated mesh generation and inflow configuration using the Jupyter Notebooks with the aid of PyFoam will be illustrated through wind flow simulations around rectangular buildings with various aspect ratios and inflow conditions.

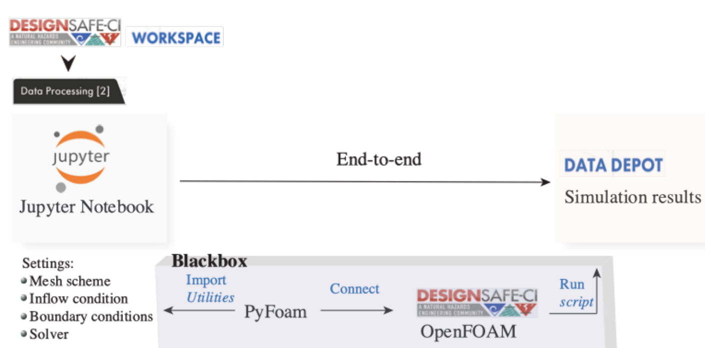

Figure 1. Schematic of an end-to-end flow simulation implemented in the Jupyter Notebooks

5. CONCLUSIONS

This study demonstrates the Jupyter Notebooks developed for scripting the OpenFOAM workflow for the wind flow simulation around a building. In particular, this tool is expanded to the direct use of the Jupyter Hub in the DesignSafe CI and HPC resources provided by TACC, through which the script can be easily published and shared with broader research communities and engineering groups.

ACKNOWLEDGEMENTS

Support for this work is in part provided by the NSF Grant # CMMI-2022469.

REFERENCES

Ding, F., Kareem, A. and Wan, J., 2019. Aerodynamic tailoring of structures using computational fluid dynamics. Structural Engineering International, 29(1), 26-39.

Jasak, H., Jemcov, A. and Tukovic, Z., 2007. OpenFOAM: A C++ library for complex physics simulations, Vol. 1000, 1-20. IUC Dubrovnik Croatia.

Kluyver, T., Ragan-Kelley, B., Pérez, F., Granger, B.E., Bussonnier, M., Frederic, J., Kelley, K., Hamrick, J.B., Grout, J., Corlay, S. and Ivanov, P., 2016. Jupyter Notebooks-a publishing format for reproducible computational workflows, Vol. 2016, 87-90.

Pimentel, J.F., Murta, L., Braganholo, V. and Freire, J., 2019. A large-scale study about quality and reproducibility of jupyter notebooks. In 2019 IEEE/ACM 16th International Conference on Mining Software Repositories (MSR), 507-517. IEEE.

Rathje, E. M., Dawson, C., Padgett, J. E., Pinelli, J-P, Stanzione, D., Adair, A., Arduino, P., Brandenberg, S. J., Cockerill, T., Dey, C., Esteva, M., Haan Jr, F. L., Hanlon, M., Kareem, A., Lowes, L., Mock, S. and Mosqueda, G., 2017. DesignSafe: new cyberinfrastructure for natural hazards engineering, Natural Hazards Review 18(3), 06017001.

Tamura, Y. and Van Phuc, P., 2015. Development of CFD and applications: Monologue by a non-CFD-expert. Journal of Wind Engineering and Industrial Aerodynamics, 144, 3-13.

Impact of Extreme Wind Loads on Sliding Glass Doors

M. Moravej[a*], B. Arya[b], C. Simsir[c], A. Jain [d]

[a]*Forensic Engineer, Walker Consultants, Los Angeles, California, USA, mmoravej@walkerconsultants.com*
[b]*Senior Consultant, Walker Consultants, Los Angeles, California, USA, barya@walkerconsultants.com*
[c]*Senior Consultant, Walker Consultants, Los Angeles, California, USA, csimsir@walkerconsultants.com*
[d]*Vice President, Walker Consultants, Los Angeles, California, USA, ajain@walkerconsultants.com*

ABSTRACT:
Performance of building envelope components during extreme wind events can substantially affect the overall performance of a building and the level of damage it sustains. The authors of this paper have been extensively involved in investigations to determine the type and level of wind damage incurred to building envelope components and more specifically, sliding glass doors and windows. A damage type that we frequently observe is the rotation and separation of the door and window panel framing joints that is indicative of wind-induced stresses transmitted through the door and window components. To numerically study the impact of extreme wind pressures on the sliding glass doors, a detailed three-dimensional finite element model was developed, and a static nonlinear analysis was conducted. Analysis results show that the panel framing joints bend out of frame and the element stresses at the panel joints exceed the elastic limit, indicating a permanent deformation. The obtained results were consistent with the field observations.

Keywords: wind damage, fenestration, reconnaissance, forensic engineering, wind simulation, hurricane loss

1. INTRODUCTION

Sliding glass doors (SGDs) are widely used in various types of buildings to provide access to the exterior spaces such as balconies, lanais, terraces, and patios. SGDs are also sometimes used to enclose the balconies or lanais. SGDs can span a wide opening as they are installed in a multi-panel setting, hence providing an ample amount of natural light and ventilation. However, when such a large size opening is breached during a wind or storm event, it can lead to widespread interior damage caused by debris impact, water intrusion and rapid alteration of interior pressures. The change in the building interior pressure can even lead to catastrophic cascade failure in low-rise buildings. Fig. 1 shows the displacement of internal partition walls in a reinforced concrete building where window and door openings were compromised during Hurricane Maria.

Besides the apparent damage types such as broken glass and blown out frame, which constitute a total system failure, sliding glass doors can also sustain a wide range of other damage types that often remain unnoticed by inexperienced eyes. Separation at the door frame joineries and rotation of panel joints are damages that frequently occur when the wind induced loads approach and exceed the rated capacity of the system and can be identified through a careful inspection. Detection of these types of damages is critical as they impair the structural integrity of the door

* Lead presenter

system, leading to lower-than-expected performance or possible failure in future wind and rain events. Fig. 2a and 2b display some examples of these damage types. For a better understanding of the damage mechanism and to complement our field observations, we performed a finite element simulation of a sliding glass door system subjected to a static load. The following sections describe the methodology, results, and conclusions.

Figure 1. Displacement of an internal wall due to excessive internal pressures

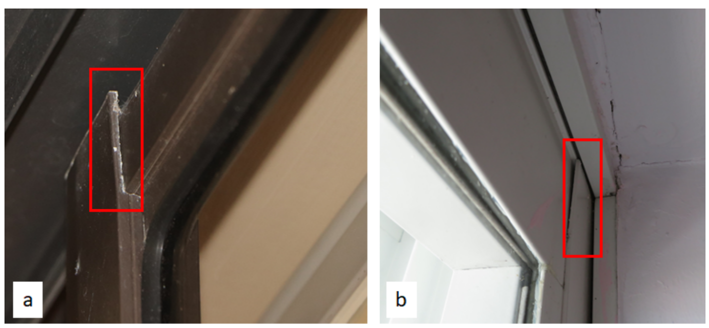

Figure 2. Rotation and separation of panel framing joints of sliding glass doors

2. METHODOLOGY

The sliding glass door chosen for this study was a 200 Series Aluminum Sliding Glass Door manufactured by NuAir Aluminum Windows & Doors, with a 4ftx8ft dimension and pressure rating of 30psf (NUAIR, 2005). This model was selected as it is similar to the glass doors typically found during our investigations, in terms of the capacity, framing structure and profile. Fig. 3a shows an overall view of the finite element model created in CSI SAP2000® software. Fig. 3b and 3c display the level of details incorporated into the model at the top and bottom rails, respectively. The analysis model consists of nonlinear shell elements with nonlinear material properties to represent the inelastic behavior of the framing components, and nonlinear spring elements to model the boundary conditions at the interface between the frame and the glass. The material used to create the frame sections in the model was 6063 Aluminum alloy (as specified in the drawings) with a yield stress of 25 ksi and ultimate stress of 30 ksi. Linear shell elements were used to model the glass panes.

The analysis approach consisted of a nonlinear static analysis of the system subjected to a load monotonically increasing up to a target pressure of 60 psf. This analysis helped to study the overall behavior of the system as well as a detailed study of the deformations and the stresses developed in the framing elements. The following calculations show the basis for selecting the 60 psf target pressure and provide a better understanding of the magnitude of wind induced pressures that these glass door systems may undergo during an event like Hurricane Irma. Peak gust wind speeds recorded in Collier County, Florida, ranged from 129 to 142 mph during Hurricane Irma (National Hurricane Center, 2018). Based on provisions of Chapter 30 of ASCE 7-16 (ASCE, 2017), the following wind load calculations were performed for a representative mid-rise building with a height of 120 ft and a surrounding suburban terrain (Exposure B), subjected to a 3-s gust wind speed of 135 mph:

K_z=1.04, K_d=1 (wind direction is determined), GC_{pi}=-/+0.18
For corner zones with GC_p=-1.8 : $P=0.00256\times1.04\times1\times135^2\times(-1.8-0.18)=-96$ psf
For inner zones with GC_p=-0.9 : $P=0.00256\times1.04\times1\times135^2\times(-0.9-0.18)=-52$ psf

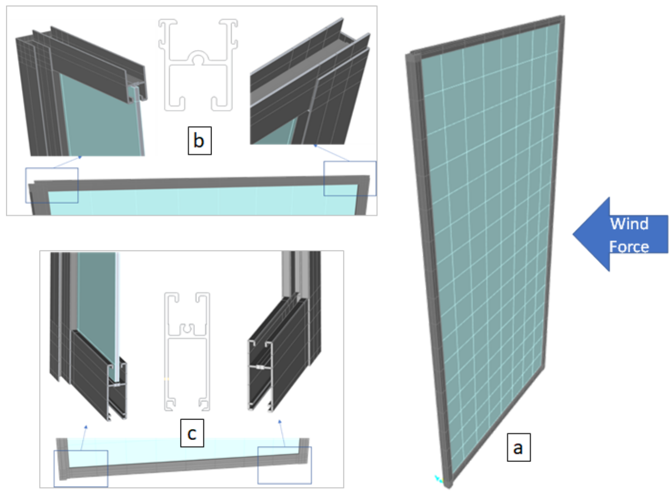

Figure 3. Detailed 3D model of the sliding glass door: (a) overall view, (b) top panel joints, (c) bottom panel joints

3. RESULTS AND DISCUSSION

The deformed shape of the structure is shown in Fig. 4. As observed in this figure, the top and bottom rails have rotated causing deformation and rotation at the panel joints at the intersection of horizontal and vertical panel frame members, leaving behind gaps at the joints. The deformation shape and magnitude are similar to the damages observed in the field shown in Fig. 2. The extent of this damage varies based on the rated capacity of the door and the intensity of the applied load. Boundary conditions and technical details of the joint assembly can also affect the profile of the deformed shape and size of the gap. To understand whether these deformations are elastic or permanent, the level of normal stresses developed in the elements surrounding the joint gap were investigated. Fig. 5a displays the stress contours at two of the panel joints. The stress diagram shows that at the locations where the rotated horizontal rail pushes against the vertical panel, an area of stress concentration has developed with stress levels exceeding the yield stress of aluminium alloy. In addition to overall stress distribution, stress-strain relations of the panel joint shell elements were also examined. Fig. 5b illustrates the stress-strain curve for an element located on the horizontal bottom rail in a panel framing joint (marked with red square). Comparison of the element stresses (blue dots) with the nonlinear material curve (dashed line) indicates that the stresses developed in the element exceed the yield stress, leading to inelastic deformations leaving behind residual permanent gaps at the panel joint.

4. CONCLUSIONS

Results obtained from the nonlinear finite element analysis of the sliding glass door model confirm that the panel framing joints likely experience permanent deformations when applied wind loads exceed the rated capacity of the door. Deformation modes and mechanisms observed in the analytical model are consistent with the damage types observed in the field. As the next step of the study, authors plan to conduct a nonlinear dynamic analysis to incorporate the dynamic characteristics of the wind load and the time variant characteristics of the system response. In addition, the result of the analysis will be compared against the data to be obtained from a laboratory experiment on a full-scale specimen.

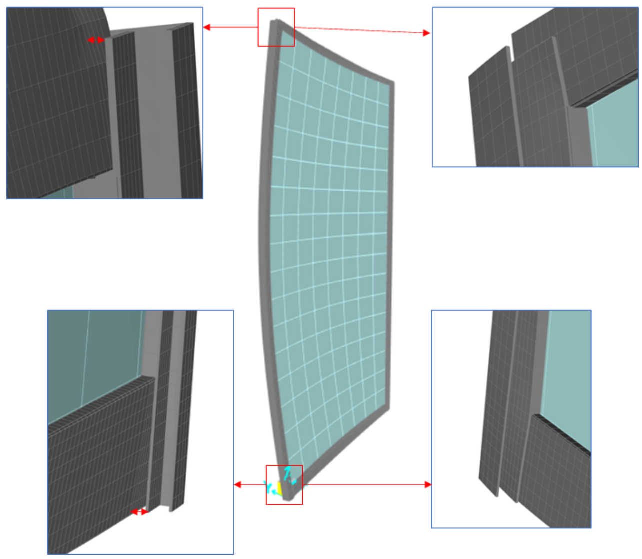

Figure 4. Deflected shape of the door panel under the applied pressure

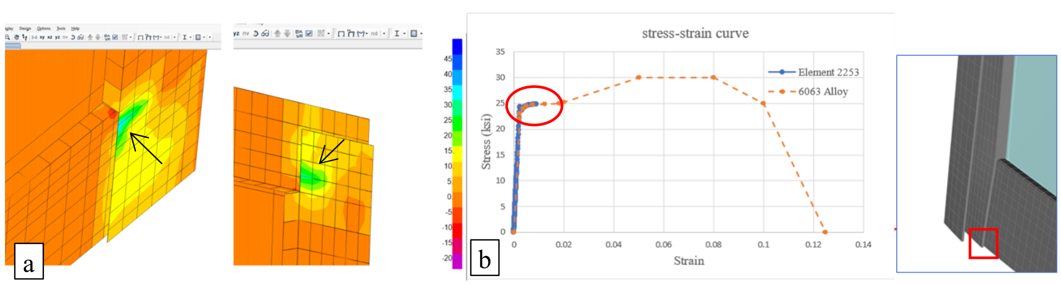

Figure 5. (a) Stress distribution in the panel joint zones (b)Stress-strain curve of a panel joint shell element indicating that the aluminium alloy at panel joint has yielded

REFERENCES

NUAIR Sliding Glass Doors Series 200, Drawings & Technical Specifications, NUAIR Windows and Doors, September 2005.

National Hurricane Center, 9 March 2018, Tropical Cyclone Report: Hurricane Irma (AL112017), 30 August-12 September 2017.

American Society of Civil Engineers, Minimum Design Loads and Associated Criteria for Buildings and Other Structures (ASCE/SEI 7-16), 2017.

Generation of inflow velocity field for CFD analyses using GPUs

Fei Ding [a,*], Ahsan Kareem [b]

[a]NatHaz Modeling Laboratory, University of Notre Dame, Notre Dame, IN, US, fding@nd.edu
[b]NatHaz Modeling Laboratory, University of Notre Dame, Notre Dame, IN, US, kareem@nd.edu

ABSTRACT:
Generation of appropriate inflow boundary conditions satisfying prescribed statistical properties is essential for running a successful CFD simulation in a turbulent flow. With the advances in HPC, parallel programming can be explored to generate turbulent velocity fields on the inlet patch by harnessing the power of the computer's graphics process unit (GPU). The time sequence of the velocity vector at each grid point on the inlet patch is computed by executing the kernel function on an allocated thread of a GPU. As a result, the entire inflow velocity field can be computed by running on thousands of threads in parallel. The proposed GPU programming in inflow generation has the promise to enhance the computational performance by orders of magnitude, and then be integrated into the real-time CFD simulation carried out using open-source software OpenFOAM.

Keywords: Inflow generation, GPU programming, CFD simulation

1. INTRODUCTION

Generation of inflow turbulence satisfying prescribed statistical properties such as turbulence intensity, integral scale and turbulence spectra is of great importance in CFD analyses. Numerous studies have been contributed to developing the methodologies to produce the appropriate inflow boundary conditions, which can be classified into three categories: precursor simulation methods, recycling methods and synthesis methods (Ding et al., 2019; SimCenter, 2019). The synthesis methods generally offer a relatively efficient and convenient approach to generate inflow turbulence compared to the other two categories. These synthesis methods include the synthetic random Fourier method, synthetic digital filtering method, and synthetic eddy method (SimCenter, 2019). Among these, the modified discretizing and synthesizing random flow generation (DSRFG) approach (Castro and Paz, 2013) consisting of applying the spectrum of the wind velocity fluctuations to building a trigonometric series with Gaussian random coefficients is employed in this study.

Concerning inflow turbulence generation in CFD simulations, the time sequences of the velocity vector containing three-directional components need to be computed at all the grid points on the inlet patch and at each simulation time step. In comparison to the traditional data processing pipeline that involves the use of a single CPU processor to generate the turbulence velocity field, performing computations on GPUs is a new concept. The GPUs were originally designed to produce a color for every pixel on the screen and have evolved so that the input "color" can be any type of data (Sanders and Kandrot, 2010). The emergence of GPU programming has proven to speed up data processing in orders of magnitude. Moreover, it is suitable to solve the inflow generation problem as a grid point on the inlet surface can be treated as a pixel on the graph.

* Lead presenter

To take advantage of the GPU programming, at each grid point on the inlet patch, the time sequence of the velocity vector is computed by implementing the modified DSRFG approach through the kernel function on an allocated thread of a GPU. To organize the architecture of the GPU threads to allow the velocity field on the inlet patch to be computed in parallel, multiple 2D blocks are designed to be consistent with the configuration of the grid points on the inlet patch. Section 2 will be devoted to the detailed discussion of GPU programming for inflow velocity generation.

2. PARALLEL COMPUTING USING GPUS

In some CFD applications that require the real-time processing of the information from the instantaneous flow field by tuning inflow parameters such as separation control, control of boundary layer thickness, and inflow uncertainty quantification, there is a strong desire for the improvement of the computational performance for inflow velocity generation by taking advantage of the advanced high-performance computing techniques. In this study, the introduction of the GPU programming based on the CUDA architecture brings significant performance improvement over the traditional central processing technologies.

The GPU consists of multiprocessor elements that can run under hundreds or thousands of parallel execution units known as threads (Sanders and Kandrot, 2010) as shown in Fig. 1. To implement the modified DSRFG approach in the GPU, the kernel function is coded based on the selected inflow generation approach and executed on the allocated threads to generate the time sequence of inlet velocity at each grid point on the inlet patch. Considering the correlated inflow velocity field, it can be first decoupled into an uncorrelated one based on some decomposition techniques such as Cholesky decomposition (Li and Kareem, 1993), and the uncorrelated flow field data can then be directly generated using GPU threads. The sketch of the proposed methodology is shown in Fig. 1. On each thread, the input of the kernel function is the coordinates of a grid point, and the output will be the time-history velocity data at that grid point. The computed velocity data on all the threads will be collected and copied to the CPU host to generate the inlet output files compatible with running a CFD simulation in open-source software OpenFOAM (Jasak et al., 2007). The initial investigation shows that the extremely rapid computation over traditional CPU processing has been delivered by GPU-powered parallel computing.

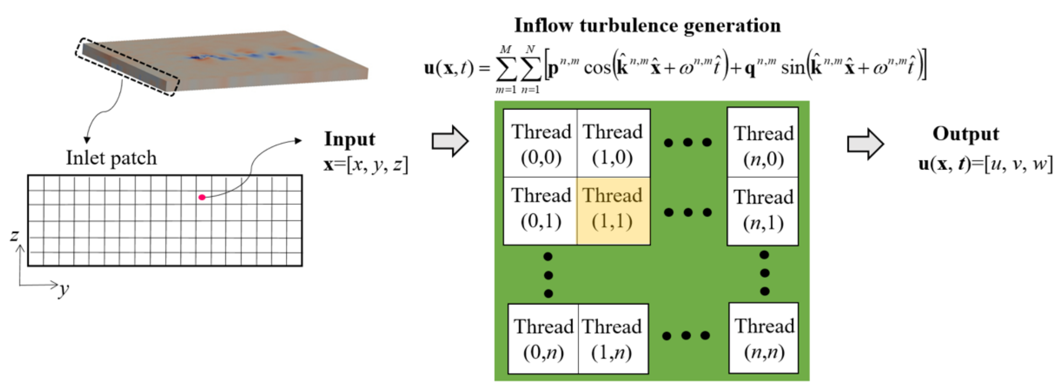

Figure 1. Schematic of the implementation of inflow velocity generation using GPUs

3. CONCLUSIONS

In summary, the synthesis inflow generation methods are implemented using GPUs in this study to achieve superior computational performance over traditional methodologies that are built on central processing technologies. The proposed parallel programming technique for the inflow generation will serve as a useful tool in many CFD applications that require a very short period to process feedback information including real-time or near real-time flow control.

ACKNOWLEDGEMENTS

Support for this work is in part provided by the NSF Grant # CMMI-1612843 under the NSF NHERI Center for Simulation and Modeling (SimCenter).

REFERENCES

Castro, H.G. and Paz, R.R., 2013. A time and space correlated turbulence synthesis method for Large Eddy Simulations. Journal of Computational Physics, 235, 742-763.

Ding, F., Kareem, A. and Wan, J., 2019. Aerodynamic tailoring of structures using computational fluid dynamics. Structural Engineering International, 29(1), 26-39.

Jasak, H., Jemcov, A. and Tukovic, Z., 2007. OpenFOAM: A C++ library for complex physics simulations. Vol. 1000, 1-20. IUC Dubrovnik Croatia.

Li, Y. and Kareem, A., 1993. Simulation of multivariate random processes: hybrid DFT and digital filtering approach. Journal of Engineering Mechanics, 119(5), 1078-1098.

Sanders, J. and Kandrot, E., 2010. CUDA by example: an introduction to general-purpose GPU programming. Addison-Wesley Professional, Boston, MA, USA.

SimCenter, University of California at Berkeley, 2019. The Turbulence Inflow Tool (TInF). GitHub repository, https://nheri-simcenter.github.io/TinF-Documentation/about.html.

6th American Association for Wind Engineering Workshop (online)
Clemson University, Clemson, SC, USA
May 12-14, 2021

Wind-induced response of buildings incorporating nonlinear fluid-structure interaction effects

Azin Ghaffary [a], Mohamed Moustafa [b]

[a]*University of Nevada Reno, Reno, Nevada, USA, aghaffary@nevada.unr.edu*
[b]*University of Nevada Reno, Reno, Nevada, USA, mmoustafa@nevada.unr.edu*

ABSTRACT
The wind-induced response of tall buildings and flexible slender structures can be adversely affected by instabilities which might be introduced into the system as a result of fluid-structure interaction (FSI) effects. These effects can be captured using aeroelastic wind tunnel tests, assuming a linear-elastic behaviour for the building. Meanwhile, there is growing interest among the wind engineering community on understanding nonlinear buildings response under extreme wind loads, which cannot be experimentally captured yet. Thus, there is no good understanding yet of the possible effects of nonlinear structural response, if any, on the wind-induced vibration of buildings. This study aims at employing computational fluid dynamic (CFD) simulations to investigate the effects of nonlinear structural response on the aerodynamic feedback (e.g. damping) of tall buildings under extreme wind loads, if any, especially as the flexibility of the building increases. For this purpose, multi-physics simulations of a low-rise, mid-rise, and high-rise moment frame with aspect ratios of 1:2, 1:5, and 1:10 respectively is performed through a two-way coupled simulation approach. In this method, the 3D wind flow and the building surrounding environment are simulated in ANSYS Fluent, while the building dynamics are modeled in OpenSEES. The interaction between the two processes is configured using an iterative procedure. Both linear and nonlinear models of the buildings with different dynamic characteristics are created in OpenSEES. Then, coupled simulation results using these OpenSEES models are compared to examine the extent of the effects that the nonlinear FSI, e.g. aerodynamic damping, might have on the overall response of the structure and induced wind forces.

Keywords: nonlinear wind-structure interaction, computational fluid dynamics (CFD), aerodynamic instability

1. INTRODUCTION

Aerodynamic instability evaluation of high-rise buildings is gaining increased attention among the wind engineering/structural engineering community to the point that the Architectural Institute of Japan incorporated such evaluations in their recent guidelines (Hasama, Saka et al. 2020). One of the major reasons causing instabilities the wind-induced response of tall buildings is vortex induced resonance of the building, especially in the cross-wind direction. This happens when the frequency of the shedding vortices generated by the wind loads applied to the structure is close to the natural frequency of the structure, which happens around a critical wind speed specified by the Strouhal number, St and continues in a limited range of wind velocities. This usually happens at relatively low wind velocities within some narrowly limited ranges, and can cause a response amplification, called vortex induced vibration (VIV) which should carefully be detected and controlled (Zhou, Ge et al. 2019, Gao, Zhu et al. 2020, Wijesooriya, Mohotti et al. 2020). Tall slender buildings are especially prone to transverse aerodynamic instabilities such as VIV. It should be noted that VIV is a nonlinear self-excited vibration. Even though, as mentioned earlier, it stems from the resonance between vortex shedding and body vibration, the forced vibration by pure vortex shedding force is negligible during the build-up process and nonlinear self-excited vibration plays a major role during VIV (Gao, Zhu et al. 2020). Therefore, to better understand the

* Lead presenter

wind-induced instabilities of high-rise buildings, it is critical to study the fluid-structure interaction (FSI) of building structures which undergo nonlinear when subjected to wind loads.

Traditional wind tunnel tests using rigid models are incapable of capturing the FSI effects. This can significantly alter the design and lead to more conservative designs or result in under-designed buildings in case large vortex shedding effects at higher wind speeds are neglected. Therefore, when there is a dire need for including the FSI effects in predicting the response of the building, single-degree-of-freedom (SDOF) or multi-degree-of-freedom (MDOF) aeroelstic wind tunnel tests are usually used. However, aeroelastic tests are generally more expensive, time consuming, and harder to calibrate for the required stiffness, natural frequency, and damping ratio. Therefore, such tests in previous studies were mainly conducted for the research purpose based on simple models. As a result, the conclusions drawn through limited aeroelastic model experiments of simple prisms with conventional cross-sections may not be directly used for future engineering applications (Zheng, Liu et al. 2019, Ghaffary, Bas et al. 2020). Analytical methods of predicting wind induced response of the buildings using statistical approaches for modeling the effects of the wind loads as well as the properties of the building have gained popularity in the wind engineering field due to their computational efficiency. Simulation of the nonlinear FSI effects have been successfully implemented using these approaches by (Feng and Chen 2017). However, simulation of the wind loads and building's properties through deterministic and/or experimental methods is a critical requirement for more detailed prediction of the nonlinear building response subjected to strong wind loads which should inevitably be implemented for improving the accuracy of the stochastic methods. This is where advanced computational methods such as combined Finite Element (FE) and Computational Fluid Dynamics (CFD) methods followed by combined computational/experimental techniques such as wind real-time hybrid simulation (wRTHS) emerge to facilitate the prediction of the wind-induced response of the buildings incorporating FSI effects.
Combined computational/experimental techniques such as the wRTHS approach have shown to be promising in the simulation of complex wind-induced behavior of the buildings (Kanda, Kawaguchi et al. 2003, Kato and Kanda 2014), avoiding the higher costs of aeroelstic wind tunnel tests and prestigious CFD models, while preserving accuracy and proper inclusion of FSI effects. However, combined FE/CFD simulations are imperative for proper development of wRTHS methods, especially where wind tunnel testing facilities are not available.

To the best of the authors' knowledge, the above mentioned literature on wRTHS or combined CFD/FE methods have all investigated the wind-induced response of the structure, assuming the structure would remain linear elastic during the wind event. Hence, there is no knowledge available on the effect of nonlinear FSI on the response of the building structures. However, given the recent advances in performance-based design concepts in the field of wind engineering, it is crucial to have a clear understanding of the nonlinear behavior of building structures subjected to strong wind loads, including nonlinear FSI (Ghaffary and Moustafa 2021). The importance of such nonlinear analyses are more highlighted by the recent ASCE/SEI pre-standard for performance-based wind design (ASCE/SEI (Structural Engineering Institute) 2019), stating that linear analysis procedures can lead to localized damage, residual deformations, loss of element or connection stiffness and/or capacity. Hence, advanced nonlinear analysis procedures, which are very scarce in the field of wind engineering as opposed to earthquake engineering, are crucial for wind performance assessment of the buildings. Thus, the knowledge gained from the rapidly developing field of nonlinear wind engineering is expected to introduce modifications to the design guidelines provided by ASCE.

The objective of this paper is to investigate the effect of nonlinear FSI in the wind-induced response of high-rise buildings with special attention to the possible effects on intensifying the the VIV effects. For this purpose, the response of three building models with width:breadth:height ratios of 1:1:2, 1:1:5, and 1:1:10 are simulated through an iterative system coupling approach. In the utilized simulation procedure, the dynamic response of the buildings is simulated in two uncoupled transverse directions using OpenSEES (McKenna 2000), while the aerodynamic response of the buildings is simulated using a validated ANSYS Fluent (ANSYS Inc 2020) model. The overall response of the buildings, including nonlinear FSI effects, is then calculated using the proposed two-way system coupling approach in an iterative manner. Such analysis is performed for predicting the wind-induced response of the previously mentioned buildings with a linear-elastic behavior and an inelastic bilinear behavior. The results are then compared to quantify the extent of the effects of nonlinear FSI on the response of the described buildings subjected to strong winds.

2. SIMULATION STRATEGY

In order to incorporate the effects of Fluid-Structure-Interactions (FSI) into the simulation of the wind-induced response of the buildings, Computational Fluid Dynamics (CFD) simulation of the wind flow around the building should be coupled with the Finite Element (FE) simulation of the structural stiffness and damping. In this study, an iterative approach is utilized to conduct the coupled CFD/FE simulations that incorporates the FSI effects. In this method, the flow around the building is first simulated using a stand-alone CFD model in ANSYS/Fluent. The resulting aerodynamic forces are then transferred to OpenSEES, where a linear or nonlinear response history analysis is performed. The building deformations from OpenSEES are then recorded and incorporated into the CFD model. The CFD model is then run for the second time, this time allowing the mesh to be updated during the simulation based on the deformations obtained from OpenSEES. This procedure is repeated until convergence is achieved for the building forces and deformations recorded from Fluent and OpenSEES.
In the following sections, first, the configuration of the FE models and the CFD models are described in detail, followed by the simulation results and discussions.

2.1. FE model description

The stiffness and the inherent structural damping of the buildings is simulated using FE software OpenSEES. To investigate a wide range of structural response, three different building models with aspect ratios (breadth:depth:height) of 1:1:2, 1:1:5, and 1:1:10, representing low-rise, mid-rise, and high-rise buildings are considered in this study. The buildings are assumed to be of risk category II, located in Miami, Florida. To limit the number of the parameters under investigation, the behavior of the buildings is simulated using a simple two-degree-of-freedom (2-DOF) model. The two simulated DOFs are the first two translational DOFs, neglecting the torsional and other higher modes of vibration, as well as the coupling between the DOFs. The building model geometries are symmetric. Therefore, the simulation properties are the same in both directions. The models are created in small scale to match the length scale used in the CFD models described in section 2.2. All the simulation parameters used for the small-scale linear and nonlinear models are shown in Table 1 and Table 2, respectively. The inherent damping of the buildings is incorporated into the models using one percent Rayleigh damping applied to the first and second modes of vibration. Nonlinear building behavior is simulated using a simple bilinear material.

Table 1. OpenSEES model parameter settings for linear simulations

Model name	Stiffness (N/s)	Mass (kg)	Damping (%)	Frequency (Hz)
Low-rise-lin-1	7183.0	0.123	1	38.5
Mid-rise-lin-1	4352.0	0.307	1	18.6
High-rise-lin-1	2824.0	0.612	1	10.81
High-rise-lin-2	2824.0	0.612	0	10.81

Table 2. OpenSEES model parameter settings for nonlinear simulations

Building name	Fy (N)	Strain hardening ratio	Damping (%)
Low-rise-nonlin-1	1.0	0.041	1
Mid-rise-nonlin-1	4.0	0.078	1
High-rise-nonlin-1	12.0	0.27	1
High-rise-nonlin-2	10.0	0.05	1
High-rise-nonlin-3	10.0	0.05	0

2.1. CFD model description

The flow around the building is simulated using the commercial CFD code ANSYS Fluent 20.2. CFD models are also created in small scale. The utilized dimensions of the computational domain for the three buildings, chosen based on the recommendations found in the best practice guidelines (Tominaga, Mochida et al. 2008, Dagnew and Bitsuamlak 2013), are shown in Fig. 1. A structured meshing scheme is found to provide the highest mesh quality for all the models. In order to achieve this, the domain is divided into two regions. The inner region in the vicinity of the building, 1cm away from each building surface, is defined with a refined mesh. The size of the elements in this region is chosen to be equal to 4 mm. The power law vertical velocity profile is chosen for the simulation of the atmospheric boundary layer (ABL). Given the comparative nature of the study, the accuracy of the predictions on the magnitude of the oscillations is not a concern. Also, the simulation of flutter and galloping is not the focus of this study and is avoided by eliminating the coupling between the DOFs and keeping the velocities small. On the other hand, VIV effects which are of concern for this study, can be properly captured using the unsteady RANS models. Therefore, $k-\omega$ SST is chosen as the turbulence model. A second order implicit method is used for temporal discretization. All the discretized equations are solved using the SIMPLE algorithm for updating the pressure and velocity. Scaled normalized residuals are set to 10^{-4} for continuity, x, y, and z momentums, and for turbulent kinetic energy (k) and the specific energy dissipation rate (ω) (Tominaga, Mochida et al. 2008, Franke, Hellsten et al. 2011, Meng, He et al. 2018). A fixed time step equal to 0.001 sec is used for performing the transient analyses.

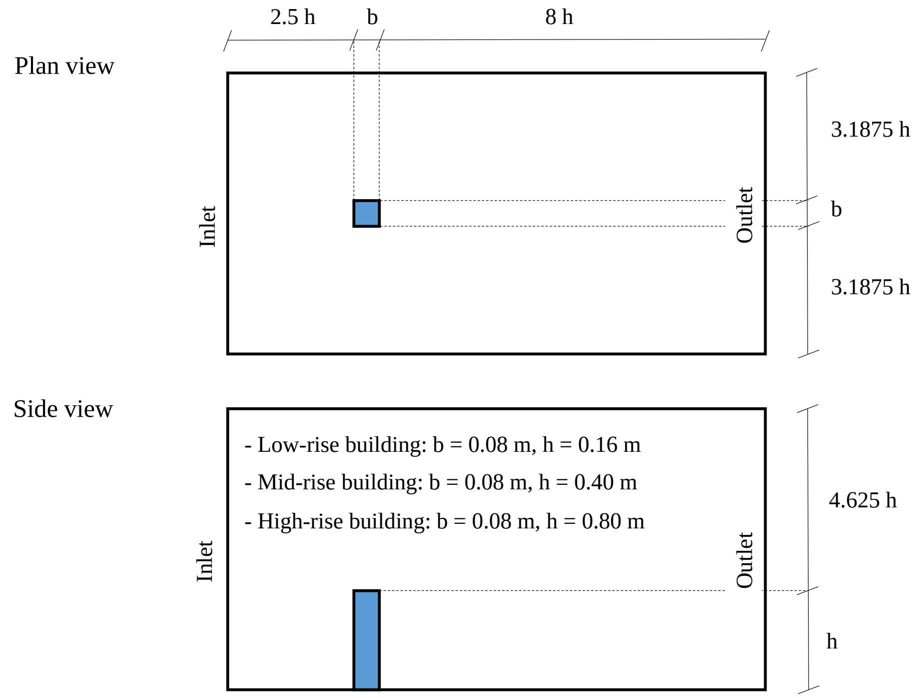

Figure 1. Computational domain dimensions and boundary conditions (dimensions are not to scale)

3. SIMULATION RESULTS AND DISCUSSIONS

Results of the converged coupled simulations for the models shown in Table 1 and Table 2 are reported in this section. Fig. 2 shows the comparison between the lift forces obtained from linear and nonlinear coupled simulation results for the low-, medium-, and high-rise buildings. As can be seen from Fig. 2 (a) to Fig. 2 (c), the linear and nonlinear aerodynamic force feedback for the low-, mid-, and high-rise buildings are almost identical. However, the nonlinear buildings models used in Fig. 2 (a) to Fig. 2 (c) only poses mild levels of nonlinearity, leading to drift ratios of 0.19%, 0.35%, and 0.56% for the low-, mid-, and high-rise buildings, respectively. In order to understand the possible effects that high levels of building deformation can have on the aerodynamic feedback, coupled simulations are performed for the high-rise building with severe nonlinear behavior leading to 2.5% drift ratio. The results of this analysis are shown in Fig. 2 (d). As can be seen, the nonlinear model results in slightly smaller aerodynamic feedback compared to the linear model. This indicates that the presence of large nonlinear deformations does not intensify the aerodynamic feedback. On the other hand, it has a positive effect on reducing the aerodynamic force through the hysteretic damping effects caused by structural nonlinearity. The results also suggest that structural damping, either in the form of inherent damping or nonlinear hysteretic damping has the ability to significantly confront the negative aerodynamic effects caused by the VIV effects.

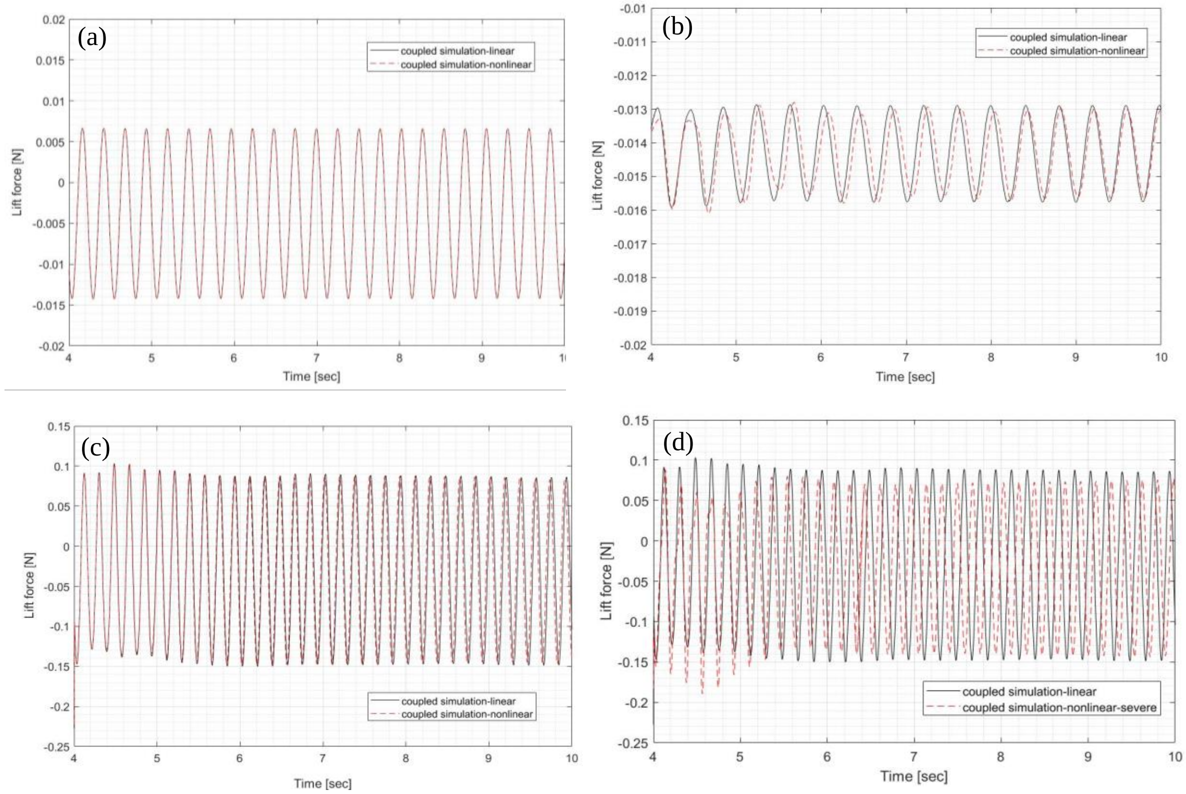

Figure 2. Comparison of the lift force feedback from Fluent for: (a) the Low-rise-lin-1 model containing linear FSI effects and Low-rise-nonlin-1 model containing mild nonlinear FSI effects; (b) Mid-rise-lin-1 model containing linear FSI effects and the Mid-rise-nonlin-1model containing mild nonlinear FSI effects; (c) high-rise building for model containing linear FSI effects and model containing mild nonlinear FSI effects; (d) high-rise building for model containing linear FSI effects and model containing severe nonlinear FSI effects.

4. CONCLUSIONS

In this study, possible effects of nonlinear structural behavior on the aerodynamic feedback of the buildings subjected to wind loads are investigated. The investigations are done through a comparative approach, looking at the stand-alone CFD simulations that do not incorporate FSI effects, and the linear as well as the nonlinear coupled simulation results, incorporating linear and nonlinear FSI effects, respectively. The results indicated that the nonlinear behavior of the building, depending on the extent of the nonlinearity and the value of the inherent structural damping of the building, can have no effect or slight decrease in the aerodynamic force feedback. The decrease in the response is associated to the presence of hysteretic damping caused by nonlinear behavior. This is an unused capacity of the elements that can be used like a hysteretic damper in order to reduce the adverse effects of instabilities such as VIV and galloping. Additionally, it was shown that the post-yield frequency does not lead to the occurrence of nonlinear VIV effects, and does not amplify the effects of the existing elastic VIV effects.

6. REFERENCES

ANSYS Inc (2020). "ANSYS FLUENT 20.1 User's Guide."

ASCE/SEI (Structural Engineering Institute) (2019). "Prestandard for Performance-Based Wind Design." Reston, VA: ASCE.

Dagnew, A. and G. T. J. W. S. Bitsuamlak (2013). "Computational evaluation of wind loads on buildings: a review." **16**(6): 629-660.

Feng, C. and X. Chen (2017). "Crosswind response of tall buildings with nonlinear aerodynamic damping and hysteretic restoring force character." Journal of Wind Engineering and Industrial Aerodynamics **167**: 62-74.

Franke, J., A. Hellsten, K. H. Schlunzen and B. Carissimo (2011). "The COST 732 Best Practice Guideline for CFD simulation of flows in the urban environment: a summary." International Journal of Environment and Pollution **44**(1-4): 419-427.

Gao, G., L. Zhu, J. Li and W. Han (2020). "Modelling nonlinear aerodynamic damping during transverse aerodynamic instabilities for slender rectangular prisms with typical side ratios." Journal of Wind Engineering and Industrial Aerodynamics **197**: 104064.

Ghaffary, A., E. E. Bas and M. A. Moustafa (2020). "A hybrid simulation approach for aeroelastic wind tunnel testing: challenges and foundational work." International Journal of Lifecycle Performance Engineering **4**(1-3): 46-79.

Ghaffary, A. and M. A. Moustafa (2021). "Performance-Based Assessment and Structural Response of 20-Story SAC Building under Wind Hazards through Collapse." Journal of Structural Engineering **147**(3): 04020346.

Hasama, T., T. Saka, Y. Itoh, K. Kondo, M. Yamamoto, T. Tamura and M. Yokokawa (2020). "Evaluation of aerodynamic instability for building using fluid–structure interaction analysis combined with multi-degree-of-freedom structure model and large-eddy simulation." Journal of Wind Engineering and Industrial Aerodynamics **197**: 104052.

Kanda, M., A. Kawaguchi, T. Koizumi and E. Maruta (2003). "A new approach for simulating aerodynamic vibrations of structures in a wind tunnel—development of an experimental system by means of hybrid vibration technique." Journal of Wind Engineering and Industrial Aerodynamics **91**(11): 1419-1440.

Kato, Y. and M. Kanda (2014). "Development of a modified hybrid aerodynamic vibration technique for simulating aerodynamic vibration of structures in a wind tunnel." Journal of Wind Engineering and Industrial Aerodynamics **135**: 10-21.

McKenna, F., Fenves, G. L., Scott, M. H., and Jeremic, B. (2000). Open System for Earthquake Engineering Simulation (OpenSees), Pacific Earthquake Engineering Research Center, University of California, Berkeley, CA.

Meng, F.-Q., B.-J. He, J. Zhu, D.-X. Zhao, A. Darko and Z.-Q. Zhao (2018). "Sensitivity analysis of wind pressure coefficients on CAARC standard tall buildings in CFD simulations." Journal of Building Engineering **16**: 146-158.

Tominaga, Y., A. Mochida, R. Yoshie, H. Kataoka, T. Nozu, M. Yoshikawa and T. Shirasawa (2008). "AIJ guidelines for practical applications of CFD to pedestrian wind environment around buildings." Journal of wind engineering and industrial aerodynamics **96**(10-11): 1749-1761.

Wijesooriya, K., D. Mohotti, A. Amin and K. Chauhan (2020). An uncoupled fluid structure interaction method in the assessment of structural responses of tall buildings. Structures, Elsevier.

Zheng, C., Z. Liu, T. Wu, H. Wang, Y. Wu and X. Shi (2019). "Experimental investigation of vortex-induced vibration of a thousand-meter-scale mega-tall building." Journal of Fluids and Structures **85**: 94-109.

Zhou, R., Y. Ge, Y. Yang, S. Liu, Y. Du and L. Zhang (2019). "A nonlinear numerical scheme to simulate multiple wind effects on twin-box girder suspension bridges." Engineering Structures **183**: 1072-1090.

Data-driven simulation of asymmetric hurricane wind fields for community resilience planning

Yanlin Guo [a,*], John W. van de Lindt [b]

[a] *Colorado State University, Fort Collins, CO, USA, yanlin@colostate.edu*
[b] *Colorado State University, Fort Collins, CO, USA, John.van_de_Lindt@colostate.edu*

ABSTRACT:
In community resilience planning, a hurricane wind field of a desired intensity for a community of interest can be used to study the effects on the community infrastructure. This necessitates simulation of the hurricane wind field of a specified intensity with a landfall location specific to that community, even though the community may not yet have experienced a similar event. In this context, this paper proposes a data-driven simulation technique to simulate the temporally and spatially varying hurricane wind fields for the purposes of hindcasting and synthetic scenario analysis based on integrated asymmetric Holland models. The proposed technique successfully overcomes two shortcomings of the existing Holland-type models, i.e. poor representation of wind field in the inner core and the inability to model surface wind speed change due to roughness changes. The performance of the proposed data-driven simulation technique is illustrated in examples of simulations for both historical and synthetic hurricanes.

Keywords: Data-driven hurricane simulation, backward and forward Holland models, inner and outer cores

1. INTRODUCTION

In the context of community resilience planning, typically a scenario (or portfolio of scenarios) analysis is carried out, which eventually facilitates better risk communication with decision-makers and planners. In general, two types of scenario analyses are used, i.e., hindcast analysis and synthetic scenarios analysis. Hindcast analysis uses data from past events to validate the models (e.g. damage and recovery) used in resilience analysis. However, measurements from past events may not include wind field data at a tight enough temporal resolution, while such information may be needed when carrying out time-dependent analysis, e.g. wind, wave, and/or surge for damage and response and early recovery. Whereas, for synthetic scenario analysis, a synthetic hurricane event with a specified strength passing close to the community of interest is needed. This will provide a mechanism for researchers and others to answer the common question that arises: What if hurricane XYZ of a certain strength and duration struck our community? Therefore, wind field modeling with a focus on both historical and synthetic events is needed to enable accurate modelling of the accumulated damage from a hurricane making landfall to the physical infrastructure at the community scale.

In the literature, the axially symmetric parametric vortex models, such as the Holland and Georgiou model (Georgiou, 1985; Holland, 1980), are widely used in engineering applications, due to their high computational efficiency. Recently, researchers have improved these models to capture the asymmetric structure of actual hurricanes (Hu et al., 2012). Despite these improvements, there are still two remaining shortcomings. First, the generalized exponential pressure field model used to drive the parametric wind model may provide a poor approximation of the radial profile in the inner core of some storms, resulting in a less accurate estimation of the wind field in the inner core region. Second, these parametric models cannot model the sudden change of wind field due to the roughness change which occurs when going from water to land.

* Lead presenter

To overcome the aforementioned shortcomings of the existing parametric hurricane models, this paper proposes a novel data-driven simulation technique to simulate the temporally and spatially varying hurricane wind fields. The performance of the proposed data-driven simulation technique is illustrated in wind field simulations for both historical and synthetic hurricanes.

2. METHODOLOGY

This technique is developed based on the Holland-type model (forward Holland model),

$$V_g = \sqrt{\frac{B}{\rho_a}\left(\frac{R_m}{r}\right)^B \left(p_n - p_c\right) e^{-(R_m/r)^B} + \left(\frac{rf}{2}\right)^2} - \frac{rf}{2} \tag{1}$$

The parameters of the Holland model are inversely extracted from measurement data included in the H*Wind and best track data using the backward Holland model, i.e. Lambert *W* function,

$$z = f^{-1}\left(ze^z\right) = W\left(ze^z\right) = W\left(-\frac{V_g^2 + V_g \cdot rf}{B \cdot (p_n - p_c)/\rho_a}\right) \tag{2}$$

where $z = -\left(R_m\left(\theta\right)/r\right)^B$. It follows that $R_m\left(\theta\right) = \exp\left(-\ln z / B\right) \cdot r$. To better capture the asymmetric wind field for various velocity ranges, we can solve for $R_m(\theta^i, V_g^j)$ for specified angles θ^i and velocity contours V_g^j. Then, these data-driven model parameters are interpolated in the time domain and passed back to the forward Holland model to simulate wind fields for a user desired fine temporal resolution. For simulation of synthetic hurricane events, the data-driven model parameters extracted from a real hurricane are used to simulate wind fields that resemble a realistic hurricane, but can also have a synthetic track which is simulated to pass close or through the community of interest. The wind field for inner and outer core regions are modeled separately by two sets of asymmetric Holland models, whose parameters are estimated using two different branches of the Lambert *W* function. In addition, the sudden change of the surface wind speed due to the roughness change from water to land is explicitly modeled using a speed conversion process. In this way, the proposed technique successfully overcomes the two shortcomings of the existing Holland-type models and can achieve a higher simulation accuracy.

3. EXAMPLES ON HURRICANE EVENT SIMULATION

The efficacy of the data-driven model was initially evaluated by comparing the simulated wind field to H*Wind data for historical events. The wind field of Hurricane Andrew was used as an example. A comparison result shows that the simulated velocities in the inner core region (marked by squares) are much more accurate when the wind fields in this region are explicitly modeled (Fig. 1b), compared to the case where the inner core region was not explicitly modeled (Fig. 1a). In addition, when comparing the velocity contours between the simulated results and the H*Wind (Fig. 1c), it is seen that the staggered feature of velocity contours due to the sudden change of surface roughness was successfully reproduced by the proposed data-driven model. In addition, a synthetic Category 5 hurricane event was simulated for the city of Orlando, FL. The data-driven model parameters were extracted from Hurricane Andrew. A synthetic track was simulated according to the user-specified landfall location as well as the initial direction for the hurricane heading. One snapshot of the simulated wind field, as well as the track for the synthetic event are shown in Fig. 2. The staggered pattern of the velocity contours was successfully simulated, which reflected the effect of velocity reduction on land.

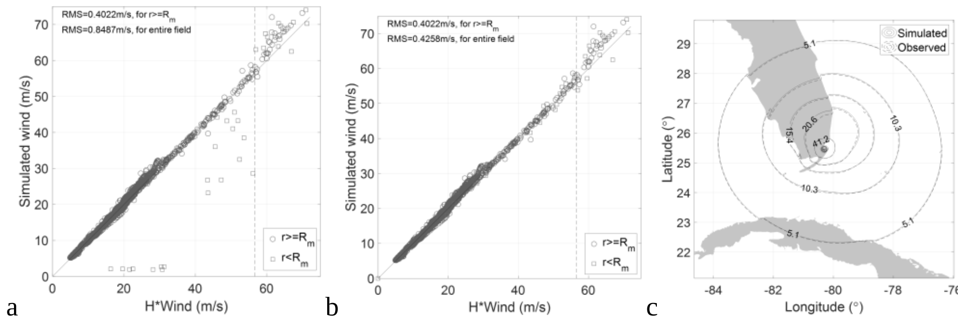

Figure 1. Comparison of simulated and observed velocities: (a) absolute value (without explicitly modeling the wind field in the inner core region), (b) absolute value (with explicitly modeling the wind field in the inner core region), (c) contours.

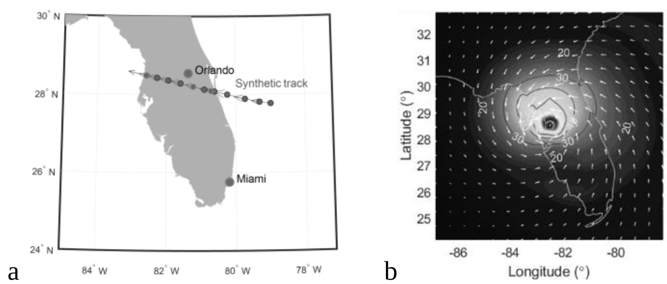

Figure 2. Simulated track and wind field for synthetic hurricane event: (a) track, (b) wind field.

4. CONCLUSIONS

To facilitate community resilience analysis which begins with the simulated hazard event, i.e. hurricane, a novel data-driven hurricane wind field model based on integrated asymmetric Holland models is proposed in this paper to simulate the temporally and spatially varying hurricane wind fields for hindcast and synthetic scenario analysis. The results presented in this paper demonstrated the efficacy of the proposed technique. Specifically, the simulation of the inner core region of hurricanes was significantly improved by separately and explicitly modeling the wind field in this region using the model parameters estimated by the lower branch of the Lambert W function. Then, by introducing a water-land based wind speed conversion process, the staggered pattern of the realistic hurricane wind field due to a sudden roughness change was successfully simulated.

ACKNOWLEDGEMENTS

Funding for this study was provided as part of the cooperative agreement 70NANB15H044 between the National Institute of Standards and Technology (NIST) and Colorado State University. The content expressed in this presentation are the views of the authors and do not necessarily represent the opinions or views of NIST or the U.S Department of Commerce.

REFERENCES

Georgiou, P.N., 1985. Design windspeeds in tropical cyclone-prone regions. 1985, Ph.D. Dissertation, University of Western Ontario: London, Ontario, Canada.

Holland, G.J., 1980. An analytic model of the wind and pressure profiles in hurricanes. Monthly Weather Review, 108, 1212-1218.

Hu, K., Chen, Q. and Kimball, S.K., 2012. Consistency in hurricane surface wind forecasting: an improved parametric model. Natural Hazards, 61, 1029-1050.

An analytical study into the performance of cross-laminated timber structures subject to tornado events

Michael Stoner[a,*], Weichiang Pang [b]

[a]*Clemson University, Clemson, SC, USA, mwstone@clemson.edu*
[b]*Clemson University, Clemson, SC, USA, wpang@clemson.edu*

ABSTRACT:
Tornadoes have long presented a challenge in designing for safety and structural performance as they are difficult to observe, violent in nature, and have a relatively low impact area. The geographically varying hazard also makes it difficult to understand where it may be necessary to design for a more severe tornado event. This study provides insight into the application of Cross-Laminated Timber as materials to resist the hazards of tornadoes in residential structures. The design procedures outlined in ASCE 7-16 were applied to a residential mass timber structure. In addition, the expected performance of mass timber residential archetypes was examined through Monte-Carlo Simulation, considering vertical and the horizontal load paths. Furthermore, the study detailed the benefits of a mass timber residential structure, give examples of achieving these goals through available design provisions, and examine the geographic variation in the hazard associated with tornadoes.

Keywords: Tornado Hazard, Cross-Laminated Timber, Residential Design

1. INTRODUCTION

As monetary loss and fatalities due to tornadoes continue to be present in the United States, efforts have been made to design structures to resist the loads associated with these events. Tornadoes have seen an increase in the insured and total losses due to their violent nature and lack of warning time. Much of this loss comes from damage to residential structures built primarily using wood framing techniques (Ellingwood and Rosowsky, 2004). Provisions in the commentary of Chapter 26 of ASCE 7-16 provide methods for calculating the forces due to tornadoes based on research and observations from tornado events. These provisions require consideration of the response to the increased wind induced pressures associated with tornadoes.

Innovations in the use of wood as a structural material have included the invention of engineered wood products including Cross-Laminated Timber (CLT) for which markets are expanding. CLT is an engineered wood panel typically consisting of three, five, or seven layers of dimension lumber oriented at right angles to one another and glued to form structural panels with high strength, dimensional stability, and rigidity (Karacabeyli and Douglas, 2013). These properties make is suitable to resist loads associated with the hazards of tornadoes and hurricanes.

To better understand the performance of CLT as a structural material that has the potential to resist the hazard associated with tornado events, analyses were performed on CLT residential archetypes. In addition, the geographic variation in the hazard associated with tornado events was considered to determine the locations in the United States where building with CLT may be most advantageous.

* Lead presenter

2. DEVELOPMENT OF PERFORMANCE MODEL

As a method for quantifying the potential of CLT to resist tornado hazards, a series of archetypes was designed using 3-layer CLT. These archetypes were developed based on the geometry of residential archetypes developed for a similar study on light-frame wood residential performance (Amini and van de Lindt, 2013). Each panel in the five archetypes was analysed based on the provisions for tornado design in ASCE 7-16, namely *the Extended Method* (ASCE, 2016). The panel's capacity and demand, given a tornado event was simulated using Monte Carlo Simulation. The failure modes of debris impact failure, panel failure, connection failure, and system level failures of sliding and overturning were considered. The probability of failure for each of the five archetypes given a tornado event was analytically determined from the simulation and expressed using fragility curves in **Figure 1**. The fragility performance, relating tornado wind speed to probability of failure

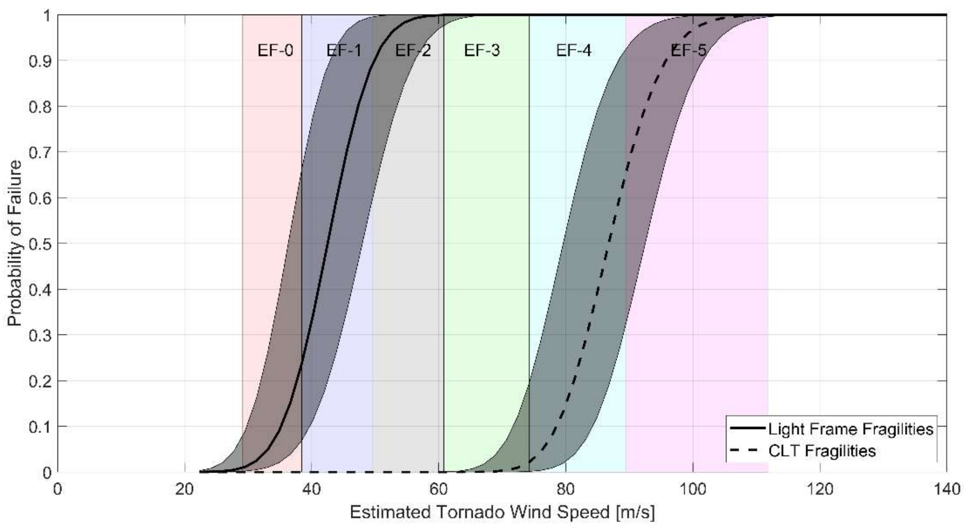

Figure 1. Fragility performance of light-frame and CLT residential structures

3. HAZARD ANALYSIS CLT STRUCTURES SUBJECT TO TORNADO EVENTS

Tornadoes are unique in that their effects are relatively localized, and their hazard is highly geographically dependent. A study that simulated 1 million years of tornado events based on historical data was utilized to determine the geographic variation in hazard associated with tornado events (Fan and Pang, 2019). The tornado hazard was coupled with the simulated performance to calculate the expected failure and loss associated with tornado events for the contiguous United States. Statistics such as the reliability index and annual probability of failure were calculated for locations and an estimated cost comparison was performed between CLT and light-frame residential construction. Reliability index is a measure of the probability of failure where a larger number indicates a lower probability of failure. **Figure 2** shows the probability density function of reliability index for all locations fit to a generalized extreme value distribution. While only 9.4% of the United States has a reliability of less than 2.5, more than 40% of the United States by area has a reliability index less than 3.0, and more than 71% having an index less than 4.0 for residential structures constructed using light-frame construction. Conversely, only 4.6% of residential structures in the United States would have a reliability index less than 4.0 if constructed using CLT. Targets for reliability vary based on the hazard being considered, the consequence of failure, and the likelihood that failure leads to additional damage. Typically, reliability index targets are between 2.0 and 4.0.

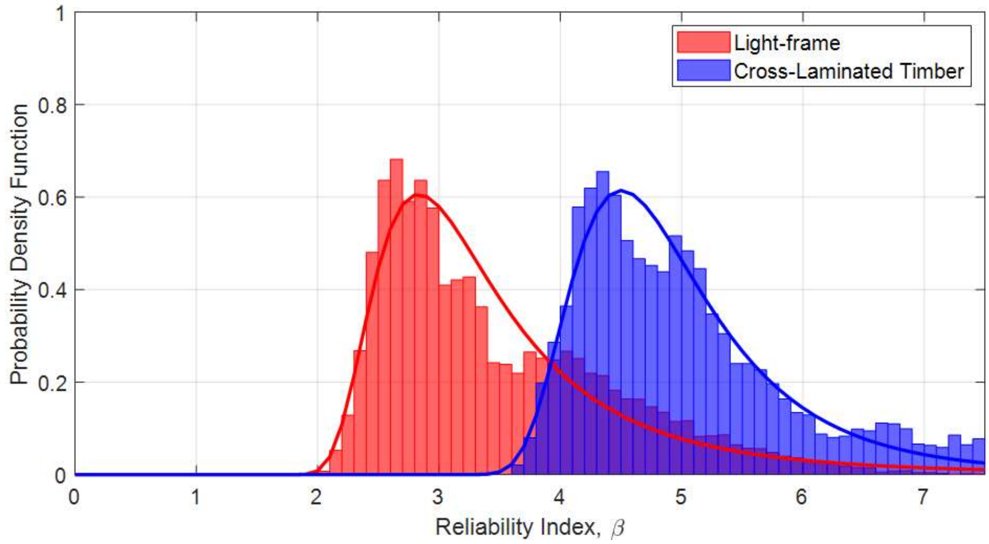

Figure 2. Reliability indices for light-frame and CLT residential structures in the contiguous U.S.

3. CONCLUSIONS

Tornadoes continue to present a challenge to designers as they can produce significant damage to the built environment. Studying alternative building materials, such as CLT, and quantifying its performance when subjected to such events, presents a potential solution to those areas most vulnerable to tornadoes. While CLT may not be a cost-effective solution through the lifetime of typical residential structures, its potential to serve as a resilient structural material could be further developed. In addition, this study presented a framework for analysing the response of structures by simulating its performance in a tornado event and studying the hazard associated with tornadoes.

ACKNOWLEDGEMENTS

The authors would like to acknowledge the assistance of United States Forest Service Grant No. 16-DG-11083150-054 and the National Science Foundation Graduate Research Fellowship Program (Grant No. 2015209393) for their sponsorship of this research. Any opinions, findings, and conclusions or recommendations expressed in this material are those of the author(s) and do not necessarily reflect the views of the National Science Foundation or United States Forest Service.

REFERENCES

Ellingwood, B. R., & Rosowsky, D. V. (2004). Fragility Assessment of Structural Systems in Light-Frame Residential Construction Subjected to Natural Hazards. Structures 2004. doi: 10.1061/40700(2004)119

Karacabeyli, E., Douglas, B., 2013. CLT Handbook: Cross-Laminated Timber. FPInnovations, Pointe-Claire, QC.

Amini, M., and van de Lindt, J. (2013). "Quantitative insight into rational tornado design wind speeds for residential wood-frame structures using fragility approach." J. Struct. Eng., 10.1061/(ASCE)ST.1943-541X.0000914, 04014033

ASCE (2016). Minimum Design Loads for Buildings and Other Structures. Reston, VA: Structural Engineering Institute.

Fan, F., & Pang, W. (2019). Stochastic Track Model for Tornado Risk Assessment in the U.S. Frontiers in Built Environment, 5. doi: 10.3389/fbuil.2019.00037

The 3 March 2020 Cookeville, Tennessee Tornado Damage Report

Jason M. Lopez [a,*], Franklin T. Lombardo [b]

[a]*University of Illinois at Urbana-Champaign, Urbana, Illinois, USA, jasonml2@illinois.edu*
[b]*University of Illinois at Urbana-Champaign, Urbana, Illinois, USA, lombaf@illinois.edu*

ABSTRACT
This damage report focuses on the Cookeville Tornado that struck western and central Putnam County, TN in the early morning of 3 March 2020. The tornado tracked 13.2 km (8.21 miles) long and was about 457.2 m (500 yards) wide. Initially, the tornado caused minor damage, but rapidly intensified causing EF-4 damage within the city limits of Cookeville, TN. This tornado was one of ten tornadoes confirmed during the 2-3 March 2020 outbreak that were spawned by numerous supercell thunderstorms across the southeast region of the United States. This tornado is of particular interest to WERL because it was a fast-moving tornado that tracked through both forested areas and relatively populated areas. Heavily forested areas allow WERL to estimate the tornado wind speeds using tree fall patterns. Densely populated areas are of interest to us and the wider engineering community to examine the performance of structures.

Keywords: Tornado, Damage Survey, Structural Engineering, Wind Damage

1. INTRODUCTION
Cookeville, located in 127 km (79 miles) east of Nashville in the Upper Cumberland Region of Middle Tennessee, was struck by a tornado slightly before 2:00 AM CST on Tuesday, 3 March 2020. The tornado was the "7th" tornado of a series of tornadoes spawned from a single parent storm. Of all the tornadoes that occurred that morning, the Cookeville Tornado caused the most fatalities and the highest wind speeds and was rated an EF-4 by the National Weather Service (NWS). The tornado outbreak of 2-3 March 2020 produced a total of ten confirmed tornadoes which approximately occurred between 10:30 PM and 2:30 AM CST.

2. STORM FORECASTS
The NWS predicted severe weather across the Mid-South portions of the United States, which could include strong winds, large hail, tornadoes, and flash flooding. At 3 PM, a Day 1 outlook was issued that showed 5% and 2% probability of tornadoes for portions of Illinois, Kentucky, Tennessee, Alabama, Mississippi, Arkansas, and Missouri.

3. SUMMARY OF DAMAGE
Based on a NWS Nashville survey the tornado was rated EF-4 on the Enhanced Fujita Scale (McDonald et al. 2006) that tracked across Putnam County, TN starting in Baxter and into Cookeville. Maximum 3-s wind gusts were estimated at up to 78.2 m/s (175 mph). The tornado lasted approximately 8 minutes and had a path length of 13.2 km (8.21 miles) and a path width of 457.2 m (500 yards). The estimated storm motion was East at 28.2 m/s (63 mph) (estimated by NWS). The tornado initially produced EF-0 damage, then intensified rapidly and produced EF-1 and EF-2 damage in Prosperity Pointe Subdivision. The tornado further intensified where it finally reached EF-4 intensity, destroying multiple houses on Charlton Square and McBroom Chapel Rd

* Lead presenter

and causing multiple fatalities. The tornado continued at EF-4 intensity on Hensley drive and eastward to Echo Valley Drive, destroying more structures. The tornado caused EF-2 and EF-3 damage along Broad Street and Herald Ct. The tornado came to an end just west of Cookeville Regional Medical Center.

4 STRUCTURAL LOAD PATH

A tornado has a unique loading on structures compared to other storm types. Tornadoes typically tend to be relatively small and have steep wind gradients from the core. Therefore, it is not uncommon to see structures that are close in proximity for one to be destroyed and the other seemingly undamaged. Structures further from the core of the tornado can experience straight-line winds, whereas structures closer to the radius of maximum winds will be loaded with radial winds. Structures in or near the core of the tornado will have a large vertical load from the updraft of the tornado. The loading is therefore highly dependent on the distance and orientation from the tornado center. Regardless of specific loading type on the structure, a properly engineered structure will provide a continuous load path to ground and resist the wind loading.

4.1. Roof to Wall Connection and Roof Sheathing

The damage progression of a house usually begins with the loss of roof cover then is followed by roof sheathing loss. Roof sheathing acts as diaphragm that provides lateral resistance for the house and transfers the load to the walls (Figure 1a). Thus, it is important to properly secure roof sheathing against vertical uplift forces to retain the lateral resistances provided by the panels. If the roof sheathing is properly secured to the roof structure, the sheathing will remain attached, and the loads will transfer through the truss and to the walls. This is where the roof to wall connections is critical, if roof to wall connections fail, the roof structure can be lifted off the walls and thrown, which could lead to wall collapse (Figure 1b). Figure 1c is another example of weak roof to wall and sill plate to foundation connections. Figure 1d shows another example of roof failure due to poor connections between the column and the porch beams.

4.2 Stud to Sill/Bottom Plate Connection

It is very common to see sill plates securely connected to the foundation with anchor bolts. Many times, after a tornado, when houses are destroyed and removed from the foundation, the sill plates anchored to the foundation are the only remaining component of the house (Figure 1e). Typically, when a wood-framed wall is constructed, the bottom plate of the wall is attached to the stud using face nail connection through the bottom plate and is embedded into the end grain of the stud. For constructability, this connection securely holds the wall together standing and bracing of the walls. The wood sheathing on walls serves to provide lateral in-plane shear resistance to the wall, (i.e., shear wall). Figure 1e illustrates that the inadequacy of only using face nails to studs through sill plate and exterior wood sheathing to resist uplift from a tornado.

4.3 Sill Plate to Floor Joist Connection

It was very common for houses built in Cookeville to have a stem wall CMU foundation. A sill plate was anchored either using a flat metal strap or an j-anchor bolt to the top of the CMU. Built on top of the sill plate is the floor joist system. Figure 1f shows a typical floor joist to sill plate connection found in Cookeville. Experimental research has found that toe-nails alone are inadequate in providing a continuous secure load path under extreme loading (Morrison and Kopp

2011). For the structure in Figure 1f, the wall section above this portion of the floor joists was completely failed, thus the load path was broken before the loads reached the toe-nail connections.

4.4 Foundation/Stem wall

Inadequate installation of foundation straps was found in various houses (Figure 1g). The foundation strap shown in Figure 1g was inserted into a partially filled cell of a concrete masonry unit (CMU). Foundation straps can provide a method of a continuous load path from a rim joist to the concrete footer, but they are not meant to hold CMU together.

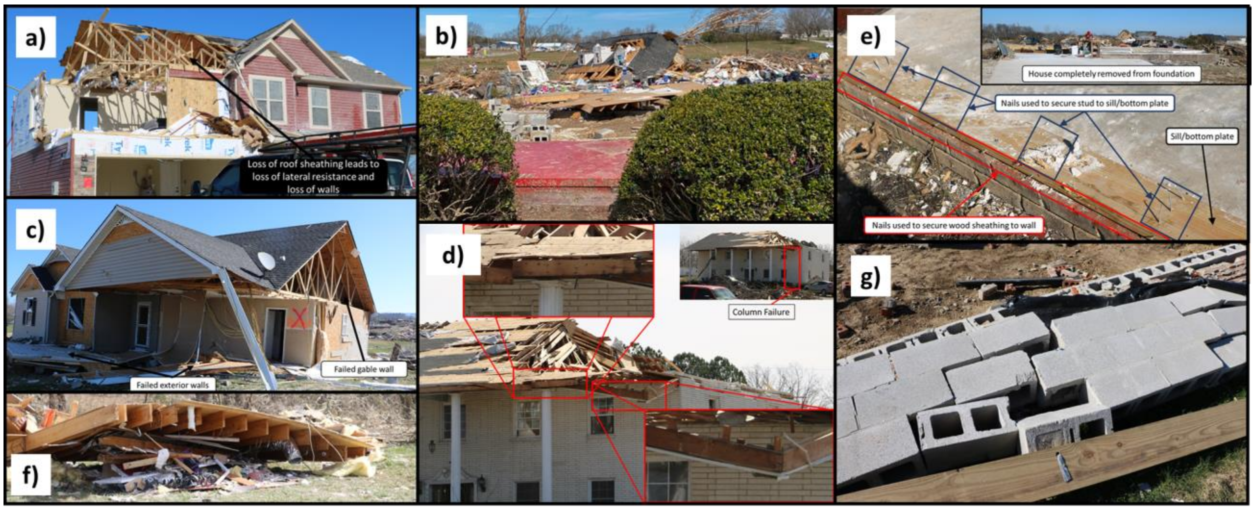

Figure 1. Observed damaged from Cookeville Tornado. a) roof sheathing loss, b) wall collapse, c) wall failure, d) porch beam failure, e) wall detachment from bottom plate, f) floor system detachment, g) stem wall collapse.

5. DISCUSSION/CONCLUSION

Load paths are well understood by engineers, but every year we continue to observe similar damage done by tornadoes. Most of the structures observed were built before the implementation of modern building codes, but some were not. The common theme with all these structures is the break down of the load path in the structures and not component failure. Most of the damage observed in the Cookeville could have been mitigated with the addition of metal straps to tie together the different structural systems. This area of Tennessee would greatly benefit from new building code adoption and stricter building code enforcement.

ACKNOWLEDGEMENTS

This material is based upon work supported by the National Science Foundation Graduate Research Fellowship Program under Grant No. DGE – 1746047. Support to perform the damage surveys was provided by NOAA VORTEX-SE project and ZJU-UIUC Institute (Zhejiang University-University of Illinois at Urbana-Champaign) and they are greatly acknowledged.

REFERENCES

McDonald, J., Mehta, K. C., and Mani, S. (2006). "A recommendation for an enhanced Fujita scale (EF-scale), revision 2." *Texas Tech University Wind Science and Engineering Research Center Rep*.

Morrison, M. J., and Kopp, G. A. (2011). "Performance of toe-nail connections under realistic wind loading." *Engineering Structures*, 33(1), 69-76.

Applicability of DAD methodology for low-rise buildings to European and Italian wind load standards

Daniele Crisman[a,*], Luca Caracoglia[b], Salvatore Noè[a]

[a]*Dept. of Engineering & Architecture, University of Trieste, Italy, daniele.crisman@yahoo.it, noe@units.it*
[b]*Dept. of Civil & Envir. Engr., Northeastern University, Boston, MA, USA, lucac@coe.neu.edu*

ABSTRACT:
In the last decade the DAD (Database-Assisted Design) method has been developed as a reliable calculation procedure to estimate structural wind loads and the design of low-rise, industrial buildings. This approach has been introduced as an alternative to prescriptive design standards. As ASCE7-16 already contemplates the use of DAD (Sec. C31.4.2), application of this method could also be extended to European and Italian standards, resulting in an effective tool for structural design against high wind loads. In this work, maximum bending moments are compared at selected cross sections of steel portal frames of five industrial buildings, calculated using both DAD, European (Eurocode 1, "EC1"), Italian (NTC18 & CNR-DT 207/2008 or "CNR") and American (ASCE 7-16) provisions. The comparisons indicate that the moment magnitudes, estimated through the standards, are similar and conservative compared to DAD results when the building is located into an "open country" exposure scenario. However, the DAD method better reproduces turbulence effects on the variation of the pressure coefficients when a suburban terrain is considered.

Keywords: Database-Assisted Design, aerodynamics, industrial buildings, structural wind forces, bending moments.

1. INTRODUCTION

This work examines the wind-resistant design of low-rise buildings. These structures are either residential or industrial with a roof height less than 20 m and a fundamental natural frequency larger than 1 Hz. Dynamic amplification effects induced by wind loads are usually negligible, and the fluctuating wind forces can be applied quasi-statically. Consequently, an equivalent, static structural analysis under slowly varying fluctuating loads can be used. Wind loads are usually determined as a combination of time-dependent distributed pressures acting on the envelope of the building. The pressure loads are usually expressed in terms of dimensionless aerodynamic pressure coefficients (C_p); the C_p values are employed to estimate the structural loads together with their tributary areas.

In order to improve the structural design against wind loads, the NIST (National Institute of Standard and Technology, USA) has developed the DAD method (e.g., Simiu et al., 2003). Using a large collection of wind tunnel tests, this method employs pressure time histories measured on a reduced-scale model to design the full-scale structure and its main wind force resisting system. The main advantage of this method relies on the possibility of directly applying a representative pressure load field, which simulates the partial temporal pressure load correlation (non-simultaneity of the load peaks or "gust" pressures) without introducing any simplifications or assumptions during the design process.

This work aims at comparing the pressure loads and their effects, i.e. bending moments (Seo and Caracoglia, 2010) extracted through the DAD computer software, against the instructions of the European, Italian and American wind load standards. In particular, the comparison is carried out by examining the maximum internal forces (e.g. peak bending moments) acting in selected cross

* Lead presenter

sections of different steel portal frames. Furthermore, the probabilistic method by Sadek and Simiu (2002) has been considered to evaluate the peak effect accounting for the inherent load randomness. Because estimates obtained using Sadek and Simiu (2002) are based on the whole information contained in the experimental time series, they are more stable than estimates directly based on observed peaks from wind tunnel data. Five prototype industrial buildings have been analyzed with variable geometry (e.g. horizontal-plane dimensions, eave height, roof inclination, structural frame external constraints) and wind exposure: open country with roughness length z_0 = 0.03 m = 0.01 ft, or suburban with z_0 = 0.3 m = 0.1 ft. The aerodynamic databases, from which the C_p time histories have been extracted, are the Western University database (UWO/NIST) and the Tokyo Polytechnic University database (TPU).

2. MODELS AND METHODS

Using the DAD software (*Wind*DESIGN) it is possible to combine the building geometric parameters with the aerodynamic information to obtain the time series of the internal forces at the cross section of interest, produced by turbulent wind pressures referenced to a unit mean-wind speed (1 ft/s) at the eave height. Based on the wind tunnel model buildings, finite-element models of the five structures have been created and, according to the various standard recommendations, wind pressure loads have been applied as equivalent, concentrated loads on the principal structural frames [Fig. 1(a)]. For a "rigid" structure with no dynamic resonance effects, the wind-induced internal forces are proportional to the square value of the mean wind speed. Therefore, the structural analysis results are normalized by the square of the wind speeds to enable the comparisons with the DAD software data.

3. RESULTS AND DISCUSSION

The analysis of the results in Fig. 1(b) suggests that the design standard results are usually consistent, predicting peak internal bending moments very close to each other; estimated moments are usually conservative in comparison with DAD predictions. The DAD method allows to reduce wind loads and their effects, i.e. lead to smaller-size structural elements when the building is located in open country scenario. Furthermore, the DAD method better analyses turbulence effects when a suburban terrain exposure is considered, because the DAD relies on a realistic wind speed profile without any simplifications or initial assumptions.

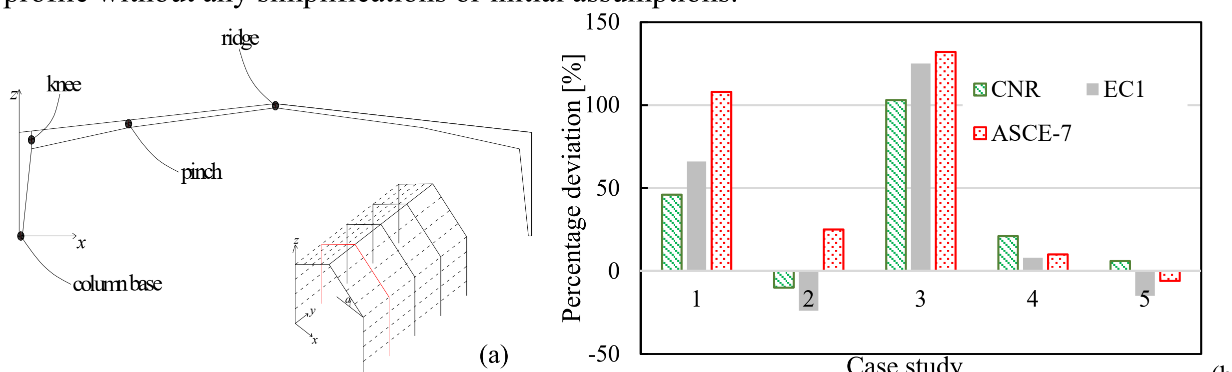

Figure 1. (a) Typical steel portal frame showing cross sections, selected for structural analysis;
(b) Comparison among Italian (CNR), EC1 and ASCE-7 standards – bending moment in the knee cross section.

In Fig. 1(b) a positive percentage deviation means that the bending moment predicted using the standards are larger (i.e. conservative) relative to DAD predictions; on the contrary, a negative deviation underlines that the DAD forecasts a larger-magnitude effect, i.e. more realistically represents the wind pressure field acting on the structure. In all the cases, the peak bending moments estimated by the probabilistic method (Sadek and Simiu, 2002) are more stable and conservative than observed extreme values, extracted from the wind tunnel data records.

4. CONCLUSIONS

The DAD method is a reliable alternative for the structural design against high wind loads and should possibly be considered for implementation into the European and Italian wind load standards. Future research might consider non-linear structural analysis and inelastic response.

ACKNOWLEDGMENTS

Drs. Emil Simiu and DongHun Yeo from the National Institute Standard and Technology are acknowledged for the material and the technical discussions on the DAD.

REFERENCES

Sadek F, Simiu E (2002) Peak non-Gaussian wind effects for database-assisted low-rise building design. Journal of Engineering Mechanics 128(5): 530-539.

Seo D-W, Caracoglia L (2010) Derivation of Equivalent Gust Effect Factors for Wind Loading on Low-Rise Buildings through Database-Assisted-Design Approach. Engineering Structures 32: 328-336.

Simiu E, Sadek F, Whalen TM, Jang S, Lu L-W, Diniz S, Grazini A, Riley MA (2003) Achieving Safer and More Economical Buildings through Database-Assisted, Reliability-Based Design for Wind. Journal of Wind Engineering and Industrial Aerodynamics, 91 (12-15): 1587-1611.

Fatigue performance of wood frame roof-to-wall connections with elastomeric adhesives under uplift cyclic loading

Bilal Alhawamdeh [a,*] , Xiaoyun Shao[b]

[a]Ph.D., Research Assoc at Bronco Construction Research Center, Kalamazoo, MI, Email: byz6845@wmich.edu
[b]Assoc. Professor at Western Michigan Univ, Kalamazoo, MI, Email: xiaoyun.shao@wmich.edu

ABSTRACT:
Roof-to-wall-connection (RTWC) is critical in the loading path of wood-frame residential buildings, whose fatigue performance under varying wind loading is investigated in this study. To get an insight on the wind induced fatigue behavior at low to moderate hourly mean wind speeds and to demonstrate the effects of adhesives on the fatigue performance of RTWC, two types of fatigue experiments, namely the constant and the varying amplitude loading tests, were conducted on three RTWC configurations with and without elastomeric construction adhesives. Based on the constant amplitude loading test results, fatigue life prediction models were developed, and the reduction in the static load capacity due to cyclic loadings were estimated. Adhesives are shown to increase the endurance limit of the RTWCs, which is desirable to enhance the life-cycle performance of wood buildings. The varying amplitude loading test results indicate that buildings in non-hurricane regions are vulnerable to fatigue damage at a low-level mean wind speed. It may induce loadings above the endurance limit of the RTWCs. On the other hand, the linear Miner's cumulative fatigue damage model can be reasonably used to predict fatigue damage of the RTWCs when subject to multi-amplitude wind loadings. The testing results presented herein provide essential data on the hysteresis behavior and failure modes of RTWCs to facilitate future implementation of adhesives in wood constructions.

Keywords: Wind loads; Fatigue analysis; Roof-to-wall connection; Elastomeric adhesives

1 INSTRODUCTION

Roof-to-wall connections (RTWCs) and roof sheathing in residential wood-frame buildings having significant influences on the roof performance under wind loads. The critical role of these connections was also revealed from many post-hurricane/storm damage surveys (e.g., [1]–[3]). Not only will roof failure endanger occupants of the houses, but it also led to water intrusion, resulting in significant subsequent damage to household items inside, such as furniture and appliances.

An experiment conducted by the Insurance for Business & Home Safety (IBHS) on a full-scale house under the impact of open wind turbines shows that the roof failure initiated at the rafter- to-top plate connections due to inadequacy in resisting and transferring loads [4]. Toenails are the most common fasteners used in RTWC in North America, and significant roof structure failures were due to the failure of these conventional connections, among which many were observed at wind speeds below the design level [5]–[7]. The underperformance of the roof connection can mainly attribute to the improper selection and application of construction materials (i.e., fasteners, wood framing, and sheathing) or strength degradation due to aging and long-term service within the intended life span [8].

* Bilal Alhawamdeh

The capacity of toenail connections to uplift loads has been the subject of many studies. For example, [9]–[17] examined various connection strengthening approaches, such as commercial metal straps and construction adhesives. Research on the effect of adhesive materials to wood construction has gained attention. Generally, better performance of structural members (i.e., roof connection, sheathing) under natural hazardous loading conditions was observed when adhesive materials were adopted in the construction [18]. Monotonic loading tests of RTWC specimens demonstrated that increased uplift resistances were achieved with the application of the elastomeric adhesives, which may provide an affordable, efficient, and nonintrusive solution for roof connections in high wind areas.

One way to evaluate the connection's capacity under long-duration wind load might be through low cyclic fatigue experiments, which were adopted in several studies to investigate the fatigue damage of metal roof claddings. Fatigue testing program of mechanical fixation elements of roofed low-rise structures was developed based on the design wind pressure [19], during which wind cycles of certain wind speed was estimated considering the cumulative probability distribution of the 50-year return period. Fatigue performance of light gauge roofing was evaluated based on the cycles to fatigue failure versus loading levels, which were determined using the wind loading spectrum of a design wind event [20]. Another procedure for estimating the wind-induced fatigue damage of roof claddings was developed in [21], [22], during which a rainflow count method was employed to determine the fatigue loading from a measured cyclone wind load history based on a wind tunnel testing of a model house. The S-N curve, where S represents the stress amplitude, and N is the number of cycles until failure, was used to estimate the fatigue damage in conjunction with Miner's rule.

It shall be pointed out that damage accumulation mechanism in low cycle fatigue for metal roof claddings is different from those of nailed connections in wood-framed buildings [23]. Understanding whether the fluctuating wind loading of longer duration and relatively lower amplitude will induce fatigue failure is critical for wind resistance performance evaluation of RTWCs, especially, in non-hurricane regions where toenails still dominate the wood frame constructions. These regions are exposed to winds with low to moderate speeds all year-long, where the damage is not expected due to overloading [24]. Therefore, the objectives of this study are twofold: (i) to estimate the wind-induced fatigue damage of standard toenailed RTWCs (ii) to evaluate wind-induced fatigue mitigation performance of the proposed strengthening method using elastomeric adhesives.

2 METHODOLOGY

The flowchart shown in Figure 1 illustrates the fatigue preformation evaluation of the roof connections employing both the constant and the varying amplitude loading tests. On the left, steps to develop the *S-N* curve are demonstrated, including the determination of the endurance limit based on the constant amplitude loading tests. The mathematical relationship between the applied load and fatigue life, known as the fatigue load-life model, is then established based on the regression analysis. On the right, the rainflow count method is used to determine the wind-induced cyclic load (i.e., the varying amplitude loading protocol) from the wind-force time history. Fatigue damage of the test specimen of each configuration under the varying amplitude loadings is quantified using the *DI* defined in Eq. 1, where N_{fj} is estimated using the fatigue load-life model for the F_{ar} values resulted from the rainflow cyclic counting analysis, while the number of cycles applied (N_j) are directly obtained from the varying amplitude loading tests. The hysteresis curves and displacement behavior are analyzed to provide reasonable explanations for the connections' fatigue performance and failure modes observed from both tests.

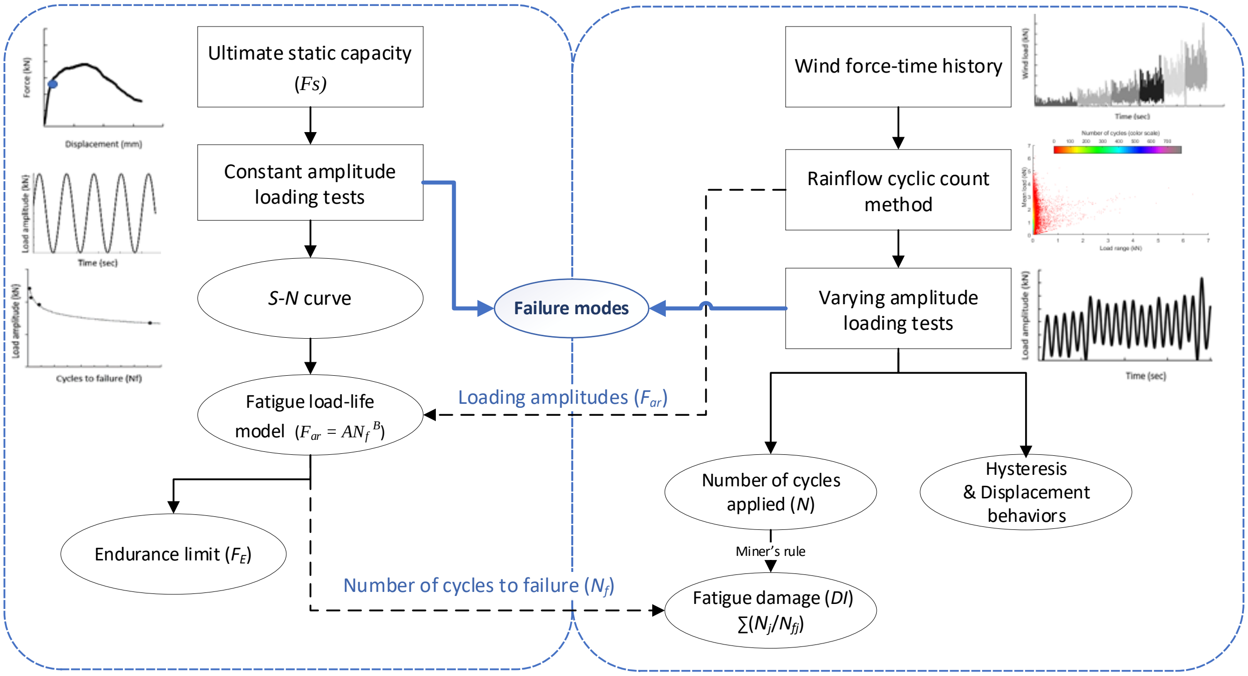

Figure 1. Fatigue performance evaluation using constant and varying amplitude loading tests

In this study, the cumulative fatigue damage index (*DI*) is defined based on Miner's model to quantify the specimen's fatigue damage under multiple load amplitudes:

$$DI = \sum_{j=1}^{m} D_j = \sum_{j=1}^{m} \frac{N_j}{N_{fj}} \qquad \text{Eq. (1)}$$

where D_j is the proportional fatigue damage of the j^{th} loading amplitude ($1 \leq j \leq m$), and m is the total number of loading amplitudes. N_j is the number of cycles applied at the j^{th} loading amplitude, and N_{fj} is the number of cycles to failure under the constant loading of the j^{th} amplitude. According to Miner's rule in Eq. 1, fatigue failure is expected when *DI* reaches unity, that is when 100% of life is exhausted [25].

REFERENCES

[1] J. W. van de Lindt, A. Graettinger, R. Gupta, T. Skaggs, S. Pryor, and K. J. Fridley, "Performance of Wood-Frame Structures during Hurricane Katrina," *J. Perform. Constr. Facil.*, vol. 21, no. 2, pp. 108–116, Apr. 2007, doi: 10.1061/(ASCE)0887-3828(2007)21:2(108).

[2] M. O. Amini and J. W. van de Lindt, "Quantitative Insight into Rational Tornado Design Wind Speeds for Residential Wood-Frame Structures Using Fragility Approach," *J. Struct. Eng.*, vol. 140, no. 7, p. 04014033, 2014, doi: 10.1061/(ASCE)ST.1943-541X.0000914.

[3] M. J. Morrison, G. A. Kopp, E. Gavanski, C. Miller, and A. Ashton, "Assessment of damage to residential construction from the tornadoes in Vaughan, Ontario, on 20 August 2009," *Can. J. Civ. Eng.*, vol. 41, no. 6, pp. 550–558, Jun. 2014, doi: 10.1139/cjce-2013-0570.

[4] "Insurance Institute for Business and Home Safety." https://disastersafety.org/ (accessed Nov. 02, 2017).

[5] FEMA 548, "Summary Report on Building Performance Hurricane Katrina 2005," 2006.

[Online]. Available: https://www.fema.gov/media-library/assets/documents/1054.
[6] FEMA, “Report Hurricane Charley in Florida Observations, Recommendations, and Technical Guidance,” 2005.
[7] FEMA, “Wind retrofit guide for residential buildings,” Department of Homeland Security, Washington, D.C. : U.S., 2010.
[8] D. Henderson, C. Williams, E. Gavanski, and G. A. Kopp, “Failure mechanisms of roof sheathing under fluctuating wind loads,” *J. Wind Eng. Ind. Aerodyn.*, vol. 114, pp. 27–37, 2013, doi: 10.1016/j.jweia.2013.01.002.
[9] T. D. Reed, D. V. Rosowsky, and S. D. Schiff, “Uplift Capacity of Light-Frame Rafter to Top Plate Connections,” *J. Archit. Eng.*, vol. 3, no. 4, pp. 156–163, Dec. 1997, doi: 10.1061/(ASCE)1076-0431(1997)3:4(156).
[10] W. C. Edmonson, S. D. Schiff, and B. G. Nielson, “Behavior of Light-Framed Wood Roof-to-Wall Connectors Using Aged Lumber and Multiple Connection Mechanisms,” *J. Perform. Constr. Facil.*, vol. 26, no. 1, pp. 26–37, Feb. 2012, doi: 10.1061/(ASCE)CF.1943-5509.0000201.
[11] L. Canfield, S. Niu, and H. Liu, “UPLIFT RESISTANCE OF VARIOUS RAFTER-WALL CONNECTIONS,” *For. Prod. J.*, vol. 41, no. 7–8, pp. 27–34, 1991.
[12] J. Cheng, “Testing and analysis of the toe-nailed connection in the residential roof-to-wall system,” *For. Prod. J.*, vol. 54, no. 4, pp. 58–65, 2004.
[13] H. W. Conner, D. S. Gromala, and D. W. Burgess, “Roof Connections in Houses: Key to Wind Resistance,” *J. Struct. Eng.*, vol. 113, no. 12, pp. 2459–2474, Dec. 1987, doi: 10.1061/(ASCE)0733-9445(1987)113:12(2459).
[14] R. Michael and F. Sadek, “Experimental testing of roof to wall connections in wood frame houses,” Gaithersburg, Md. : U.S. Department of Commerce, Technology Administration, National Institute of Standards and Technology, 2003.
[15] M. a. Turner, R. H. Plaut, D. a. Dillard, J. R. Loferski, and R. Caudill, “Tests of Adhesives to Augment Nails in Wind Uplift Resistance of Roofs,” *J. Struct. Eng.*, vol. 135, no. 1, pp. 88–93, Jan. 2009, doi: 10.1061/(ASCE)0733-9445(2009)135:1(88).
[16] D. J. Alldredge, J. A. Gilbert, H. A. Toutanji, T. Lavin, and M. S. Balasubramanyam, “Uplift Capacity of Polyurea-Coated Light-Frame Rafter to Top Plate Connections,” *J. Mater. Civ. Eng.*, vol. 24, no. 9, pp. 1201–1210, Sep. 2012, doi: 10.1061/(ASCE)MT.1943-5533.0000492.
[17] C. Canbek, A. Mirmiran, A. G. Chowdhury, and N. Suksawang, “Development of Fiber-Reinforced Polymer Roof-to-Wall Connection,” *J. Compos. Constr.*, vol. 15, no. 4, pp. 644–652, 2011, doi: 10.1061/(asce)cc.1943-5614.0000194.
[18] B. Alhawamdeh and X. Shao, “Uplift Capacity of Light-Frame Rafter to Top Plates Connections Applied with Elastomeric Construction Adhesives,” *J. Mater. Civ. Eng.*, vol. 32, no. 5, p. 04020078, May 2020, doi: 10.1061/(ASCE)MT.1943-5533.0003152.
[19] H. J. Gerhardt and C. Kramer, “Wind induced loading cycle and fatigue testing of lightweight roofing fixations,” *J. Wind Eng. Ind. Aerodyn.*, vol. 23, pp. 237–247, Jan. 1986, doi: 10.1016/0167-6105(86)90045-0.
[20] M. Mahendran, “Fatigue behaviour of corrugated roofing under cyclic wind loading,” *Trans. Inst. Eng. Aust. Civ. Eng.*, vol. CE32, no. 4, pp. 219–226, 1990.
[21] E. D. Jancauskas, M. Mahendran, and G. R. Walker, “Computer simulation of the fatigue behaviour of roof cladding during the passage of a tropical cyclone,” *J. Wind Eng. Ind. Aerodyn.*, vol. 51, no. 2, pp. 215–227, 1994, doi: 10.1016/0167-6105(94)90005-1.
[22] Y. L. Xu, “Fatigue damage estimation of metal roof cladding subject to wind loading,” *J. Wind Eng. Ind. Aerodyn.*, vol. 72, no. 1–3, pp. 379–388, 1997, doi: 10.1016/S0167-6105(97)00254-7.
[23] T. K. Guha and G. A. Kopp, “Storm duration effects on roof-to-wall-connection failures of a residential, wood-frame, gable roof,” *J. Wind Eng. Ind. Aerodyn.*, vol. 133, 2014, doi: 10.1016/j.jweia.2014.08.005.
[24] A. Tom Smith, “Wind Safety of the Building Envelope | WBDG - Whole Building Design Guide,” 2017. https://www.wbdg.org/resources/wind-safety-building-envelope (accessed

May 09, 2020).
[25] M. A. . Miner, “Cumulative damage in fatigue,” *J. Appled Mech.*, vol. 12, no. 3, pp. 159–164, 1945.

Observations of incoming turbulent flow by dual wind lidar mounted on a bridge deck

Mohammad Nafisifard [a], Jasna Bogunović Jakobsen [b], Etienne Cheynet [c]
Jónas Thor Snæbjörnsson [d], Mikael Sjöholm [e], and Torben Mikkelsen [f]

[a] *University of Stavanger, Stavanger, Norway, mohammad.nafisifard@uis.no*
[b] *University of Stavanger, Stavanger, Norway, jasna.b.jakobsen@uis.no*
[c] *University of Bergen, Bergen, Norway, etienne.cheynet@uib.no*
[d] *Reykjavik University, Reykjavík, Iceland, jonasthor@ru.is*
[e] *Technical University of Denmark, Roskilde, Denmark, misj@dtu.dk*
[f] *Technical University of Denmark, Roskilde, Denmark, tomi@dtu.dk*

ABSTRACT
The paper examines wind conditions along a 168 m long horizontal line perpendicular to a suspension bridge main span. The wind velocity data were recorded by a pair of continuous-wave Doppler lidars (short-range WindScanners) installed on the bridge deck. The measurement data are explored in terms of the mean wind speed and mean wind direction along the approach line upstream of the bridge, in a complex fjord environment. The spectral characteristics of turbulence along the line are investigated and discussed in relation to the limitations in the performance of a continuous-wave lidar at increasing distances from the monitored area. Wind characteristics observed by the lidars are compared to those derived from sonic anemometer data recorded above the bridge deck at the midspan.

Keywords: Suspension bridge, Short-range lidars, WindScanner, Wind turbulence spectra, Sonic anemometer

1. INTRODUCTION

In the past decade, optical remote wind sensing for the assessment of wind conditions in relation to bridge design has been introduced. Several measurement campaigns (Cheynet et al, 2017a; Cheynet et al, 2017b; Ágústsson et al, 2018) have demonstrated the functionality of long-range pulsed lidars to remotely (from shore) monitor the wind flow above the water surface. Such observations are vital to link the wind conditions at the actual bridge site to those observed by anemometers on land.

Continuous-wave Doppler wind lidars have smaller sampling volumes at shorter measurement distances than pulsed Doppler lidars. Smaller sampling volumes introduce a complementary capability to observe wind flow around an existing structure in greater details (Mikkelsen et al, 2017). Further information on the local wind conditions as well as data on wind-structure interaction can thus be gathered. The present paper explores a data set acquired during a measurement campaign in 2014, where synchronized short-range WindScanner lidars were installed at the Lysefjord suspension bridge, which has a main span of 446 m. The overall measurement setup has been previously described in (Cheynet et al, 2016; Cheynet et al, 2017c). The publications focused on the coherence of the incoming flow for separations along the bridge span and the mean characteristics of the bridge deck wake. The present paper examines additional data acquired during the same measurement campaign, that has not been published so far. The data concerns the inflow conditions at distances up to 13B upstream from the deck, where B=12.3 m is the deck width.

Fig. 1 (left) depicts the measurement setup with two continuous-wave Doppler wind lidars, jointly overlooking a 168 m long horizontal line perpendicular to the bridge axis, at the bridge mid-span. The two so-called WindScanners integrate modified ZephIR 150 lidars in a system controlling the lidars' beam direction and the focus distance, in a synchronized fashion. The lidars record the velocity along the line-of-sight in a "thin" bell-shaped volume centered at the focus distance. The thick blue markups in Fig. 1 (left), indicate the size of the sampling volumes, at selected distances, in terms of the so-called full width at half maximum (FWHM), which increases quadratically with the distance from the lidar. The measurements are performed in a horizontal plane 1.4 m above the bridge deck located 55 m above the sea surface.

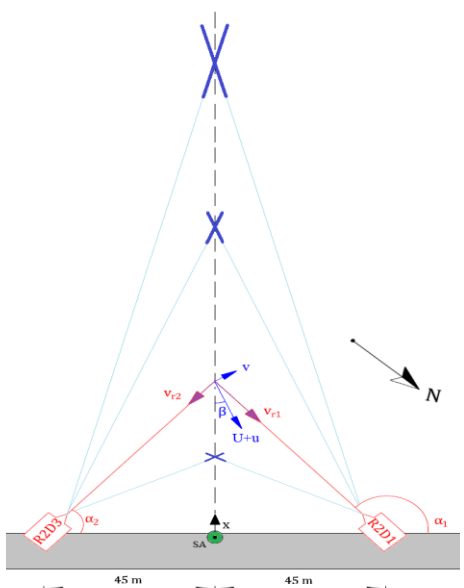

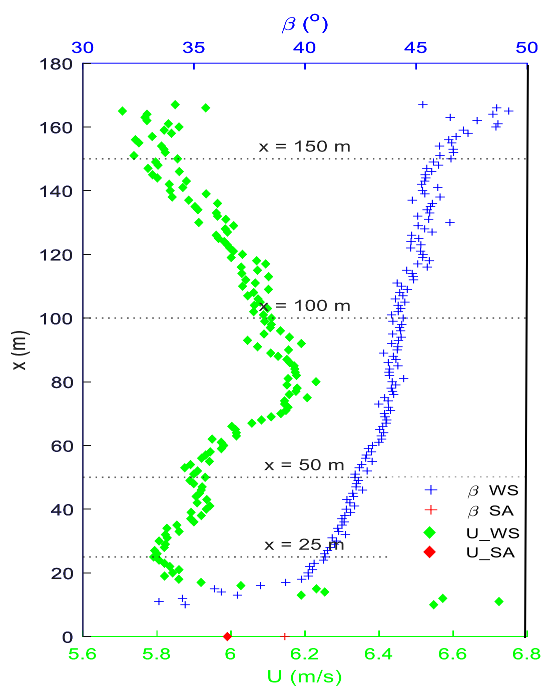

Figure 1. Left: Plan view of the measurement setup with two short-range WindScanners on the bridge deck. Thick blue lines indicate the size of the measurement volumes. Right: Mean wind speed and mean yaw angle recorded by WindScanners and the sonic anemometer at midspan on 22.5.2014 from 12:50 to 13:00.

2. RESULTS

The data analysis starts out by a numerical synchronization of the recorded velocity time-series in the entire measurement domain. With a sampling frequency of 390 Hz, a sweeping cycle counted e.g. from the shortest (x=0.5 m) to the maximum distance (x=168 m), and back is performed once every second.

Fig. 1 (right) displays an example of the mean flow characteristics based on the 10 minutes data recorded on 2014-05-22 from 12:50. An increase in the mean wind speed, from about 5.8 m/s at x=150 m to 6.2 m/s at x=80 m can be identified, associated with a minor decrease in the yaw angle of β=45°, corresponding to 185° from the north. The mean wind speed increase is understood to be due to a narrowing of the fjord inlet at the studied location.

For distances smaller than x=80 m, a reduction in mean wind speed to about 5.8 m/s at x=25 m is observed, as well as an additional reorientation of the flow to a yaw angle of 40°. Closer to the bridge, within two bridge deck widths upstream of the bridge, a significant increase in the mean wind speed is evident. The flow speed-up recorded 1.4 m above the deck, which likely reflects the flow interaction with the deck, is associated with an increased measurement uncertainty, related to a high angle at which the sampling volumes intersect (around 120°). A smaller distance between the lidars in a dedicated measurement setup (see Fig 1, left) would facilitate observations of the wind-deck interaction in greater details, with a lower uncertainty.

Fig. 2 presents the power spectral density of the turbulence components along and across the mean wind direction. The turbulence frequency distribution captured by the WindScanners is shown for three distances from the deck as a function of the wave number $k_1 = 2\pi f/U$. The plot also includes the spectra based on data recorded by a sonic anemometer at the bridge midspan, 6 m above the deck (Snæbjörnsson et al, 2017). While the spectral content derived from the lidar measurements and the sonic data are in an overall agreement, an attenuation of turbulence components for wave numbers above $k_1 = 0.1$ by the WindScanners can be noted for the case at hand, except for some noise around the Nyquist frequency. The attenuation is due to the low-pass filtering effect of the sampling volume (Angelou et al. 2012), which will be studied further based on an extended measurement data set of a couple of hours duration. The data will be further examined in terms of the mean flow characteristics, addressed in Fig. 1.

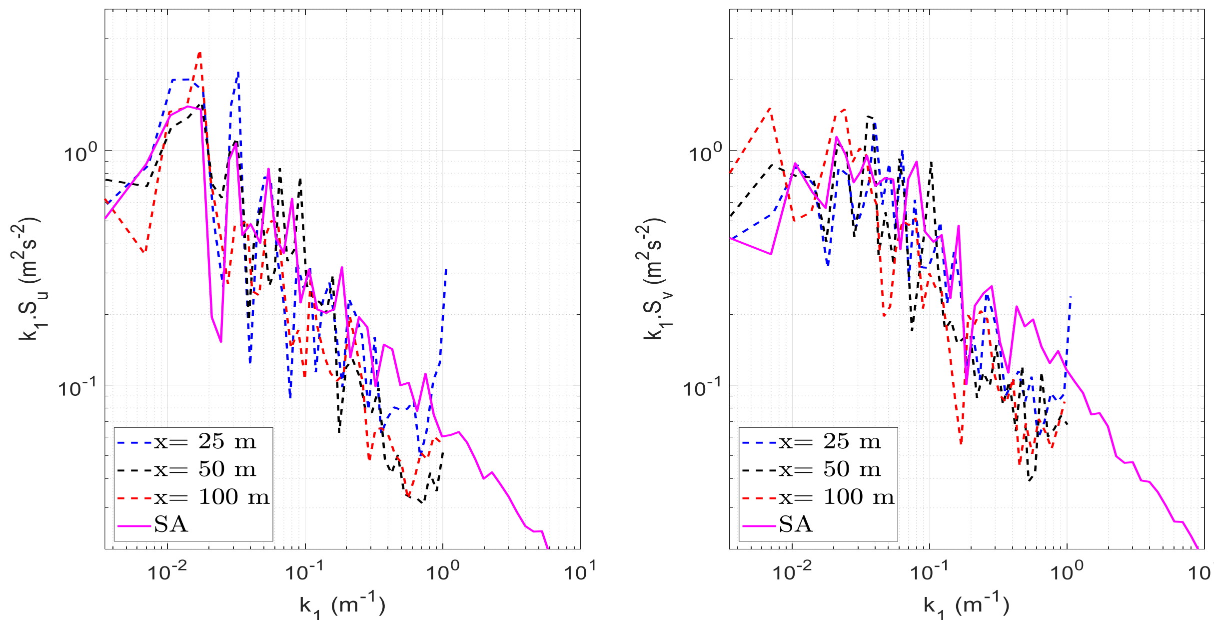

Figure 2. Power spectral density of the along-wind turbulence (left) and the cross-wind turbulence (right) estimated from WindScanners and a sonic anemometer data on 2014-05-22 from 12:50 to 13:00.

References

Ágústsson, H., Grønsleth, M.S., Eriksen, O.K., Undheim, O., Nyhammer, F.K. & Byrkjedal, Ø., 2018. Wind conditions in a Norwegian fjord derived from tall meteorological masts and synchronized doppler LIDARs, EERA DeepWind'2018, 15th Deep Sea Offshore Wind R & D Conference, Trondheim, Jan 17-19, https://www.sintef.no/globalassets/project/eera-deepwind-2018/presentations/c2_agustsson.pdf/

Angelou, N., Mann, J., Sjöholm, M., Courtney, M., 2012. Direct measurement of the spectral transfer function of a laser based anemometer. Review of Scientific Instruments 83(3).

Cheynet, E., Jakobsen, J. B., Snæbjörnsson, J., Reuder, J., Kumer, V., Svardal, B., 2017a. Assessing the potential of a commercial pulsed lidar for wind characterisation at a bridge site. Journal of Wind Engineering and Industrial Aerodynamics, 161, 17-26.

Cheynet, E., Jakobsen, J. B., Snæbjörnsson, J., Mann, J., Courtney, M., Lea, G., Svardal, B., 2017b. Measurements of Surface-Layer Turbulence in a Wide Norwegian Fjord Using Synchronized Long-Range Doppler Wind Lidars. Remote Sensing 9(10), 977.

Cheynet, E., Jakobsen, J. B., Snæbjörnsson, J., Mikkelsen, T., Sjöholm, M., Mann, J., Hansen, P., Angelou, N., Svardal, B., 2016. Application of short-range dual-Doppler lidars to evaluate the coherence of turbulence. Experiments in Fluids, 57:184.

Cheynet, E., Jakobsen, J. B., Snæbjörnsson, J., Angelou, N., Mikkelsen, T., Sjöholm, M., Svardal, B., 2017c. Full-scale observation of the flow downstream of a suspension bridge deck. Journal of Wind Engineering and Industrial Aerodynamics, 171, 261-272.

Mikkelsen, T., Sjöholm, M., Angelou, N., Mann, J., 2017. 3D WindScanner lidar measurements of wind and turbulence around wind turbines, buildings, and bridges. IOP Conf. Series: Mat. Science and Engineering 276.

Snæbjörnsson, J., Jakobsen, J. B., Cheynet, E., Wang, J., 2017. Full-scale monitoring of wind and suspension bridge response. IOP Conf. Series: Materials Science and Engineering 276.

Experimental Investigation of the Aerodynamics and Wind Loading of Buildings with Balconies

Lisette Ludena [a], Maryam Asghari Mooneghi [b*], Arindam Gan Chowdhury [c], Peter Irwin [d]

[a] *Florida International University, Miami, Florida, US, llude001@fiu.edu*
[b] *AECOM, Sacramento, CA, US, masgh002@fiu.edu*
[c] *Florida International University, Miami, Florida, US, chowdhur@fiu.edu*
[d] *Florida International University, Miami, Florida, US, peairwi@fiu.edu*

ABSTRACT
Failure of balcony glass handrail panels has been a frequent occurrence during past windstorms. This paper presents an experimental investigation of the effect of balconies on the aerodynamics of high-rise buildings. Large-scale experiments were performed on models of high-rise buildings with balconies. For small components such as balconies, large-scale testing is preferred as it provides more realistic wind effects compared to typical small-scale studies. However, as the model scale increases, the limited dimensions of wind tunnels do not allow complete simulation of the low frequency end of the turbulence spectrum. Partial Turbulence Simulation (PTS) is a method that compensates for the lack of low-frequency turbulence in post-test analysis. This method is advanced to be used for analysis of data from large-scale experiments on components of high-rise buildings. Results demonstrate the importance of large-scale testing for balconies to better understand the flow pattern and pressure distribution on the buildings with balconies.

Keywords: Wind, Components and Cladding, Balconies, High-rise Buildings, Partial Turbulence Simulation.

1. INTRODUCTION

Balconies constitute an important element of a building. They represent a characteristic component of the local architecture and provide the occupants with an easy access to the environment. Balconies can change the flow pattern around a building and hence influence the wind loading of buildings. Failure of balconies poses safety concerns for the building residents and generates wind-borne debris impacting other structures downwind. To have safe balcony designs, it is important to investigate and understand the wind loading effects on balconies. Wind tunnel testing has generally been accepted as a useful tool for evaluating wind loads on structures. For high-rise buildings usually model scales range from 1:300 to 1:600 (Moravej, 2018). However, for small components such as balconies, large model scales are needed to maintain the model accuracy and allow simulation of high Reynolds number to avoid adverse scale effects. When the model scale is large, the limited dimensions of wind tunnels do not allow proper simulation of the low frequency end of the turbulence spectrum. As a result, many of the large-scale experiments have been performed with less than ideal simulation of turbulence spectrum. This can affect the local flows over the building and balconies' surfaces where the turbulence interacts with shear layers coming off the building walls and balcony corners. Asghari et. al, (2014, 2015) presented the Partial Turbulence Simulation (PTS) method which is a theoretical method for including the effects of lack of low frequency turbulence in post-test analysis. This paper describes the advancement of the PTS methodology to be used for components of high-rise buildings, and the effects of balconies on the wind loading of buildings. Three models at scales 1:180, 1:67 and 1:25 were tested. Pressure distribution on the balcony hand rails as well as building walls are investigated and discussed.

2. METHODOLOGY AND DATA ANALYSIS

A 15-story mid-rise building is selected for this study. The full-scale dimensions of the building are height = 55.2 m and width = 24.5 m. Two series of tests are conducted per scale: one on a model building with no balconies and then on a model building with continuous balconies on two adjacent sides and discontinuous balconies on the other two sides (Figure 1). Experiments are performed in the Wall of Wind (WOW) Experimental Facility at Florida International University. The wind directions considered for testing are 0° to 360° at 3° intervals (Figure 1).

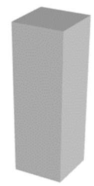
(a)

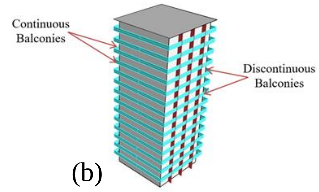

(b)

Building models: (a) without balconies, (b) with balconies.

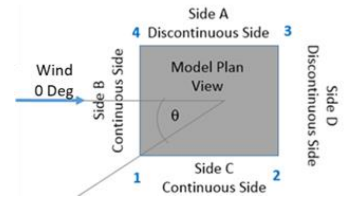

Wind direction convention.

Figure 1. Experimental setup.

Results are presented as peak pressure coefficients based on a 3-second gust dynamic pressure as shown in Equation (1). The net pressure coefficient for the balcony handrail panels is obtained using Equation (2).

$$\mathrm{C_{p\ peak}} = \frac{\mathrm{P_{peak}}}{\frac{1}{2}\rho \mathrm{U}^2_{3\ \mathrm{sec}}} \tag{1}$$

$$\mathrm{Cp_{net}} = \mathrm{Cp_{external}} - \mathrm{Cp_{internal}} \tag{2}$$

Tests are performed in a flow with partial turbulence simulation, hence the turbulence intensity is lower than that of the atmospheric boundary layer which contains the full spectrum of turbulence. In order to estimate peak pressures, PTS method (Asghari et. al, 2015) is used and advanced for components of high-rise buildings. The original PTS method is developed for low-rise buildings and small building appurtenances. In this method, the turbulence is divided into two distinct statistical processes, one at high frequencies which can be simulated correctly in the wind tunnel, and one at low frequencies which can be treated in a quasi-steady manner. The joint probability of loads from the two processes is derived, with one part coming from the wind tunnel data and the remainder from the Gaussian behaviour of the missing low frequency component from which full-scale equivalent data can be obtained. The PTS method is based on quasi-steady assumption. The quasi-steady assumption is valid provided that the eddies that are simulated in the wind tunnel cover wavelengths up to about an order of magnitude greater than the building dimension H (Asghari et. al, 2015). This is acceptable for small structures because with H being so small, this range of wave lengths can be covered in the wind tunnel. For small components of high-rise buildings quasi-steady assumption should still be valid since the larger scale eddies should remain reasonably well correlated over their much smaller dimensions. Another assumption in the PTS method is that, for small structures which are near the ground the flow has a high gradient du/dz. In such conditions the high frequency turbulence responds quickly to low frequency gusts. So, the intensity of the high frequency turbulence stays approximately constant even though the fluctuating velocity of the low frequency gusts varies. For components of high-rise buildings, du/dz reduces with height and the rapid equilibrium of the high frequency turbulence can no longer be assumed. This means that the intensity of the high frequency varies with time. To address this issue, the PTS advancement for components of high-rise buildings considers: (1) At higher levels above ground, the overall turbulence intensity is less than that at near ground level. Therefore, the fluctuations in the high frequency turbulence intensity will be small and this brings up the possibility of using a single representative value of the high frequency turbulence intensity for the level in the building where the component is located. (2) After measuring the pressure coefficients at this representative value of high frequency turbulence intensity, the missing low-frequency fluctuations are compensated using the quasi steady assumption.

3. RESULTS AND DISCUSSION

Figures 2 shows the net pressure coefficients on the balconies versus the external pressure coefficients on the building walls for a 0-degree wind direction. The highest magnitude of the Net $\mathrm{Cp_{min}}$ occurs on the side perpendicular to the wind load (Side B) which is not a predictable behavior compared to the building exterior walls behavior where the highest magnitude of external $\mathrm{Cp_{min}}$ occurs on Sides A and C. For cases where the wind loads are normal to the wall, the behaviour of balconies is driven by the wind flowing towards the inner face face of the top floor balcony where it creates a positive pressure on the inner face and induces negative net pressures at the top floor balcony in the middle zone. It can also be seen that the net pressure coefficients at the lower elevation floors are relatively smaller in value compared to the top floor balcony handrail panels (except in corners).

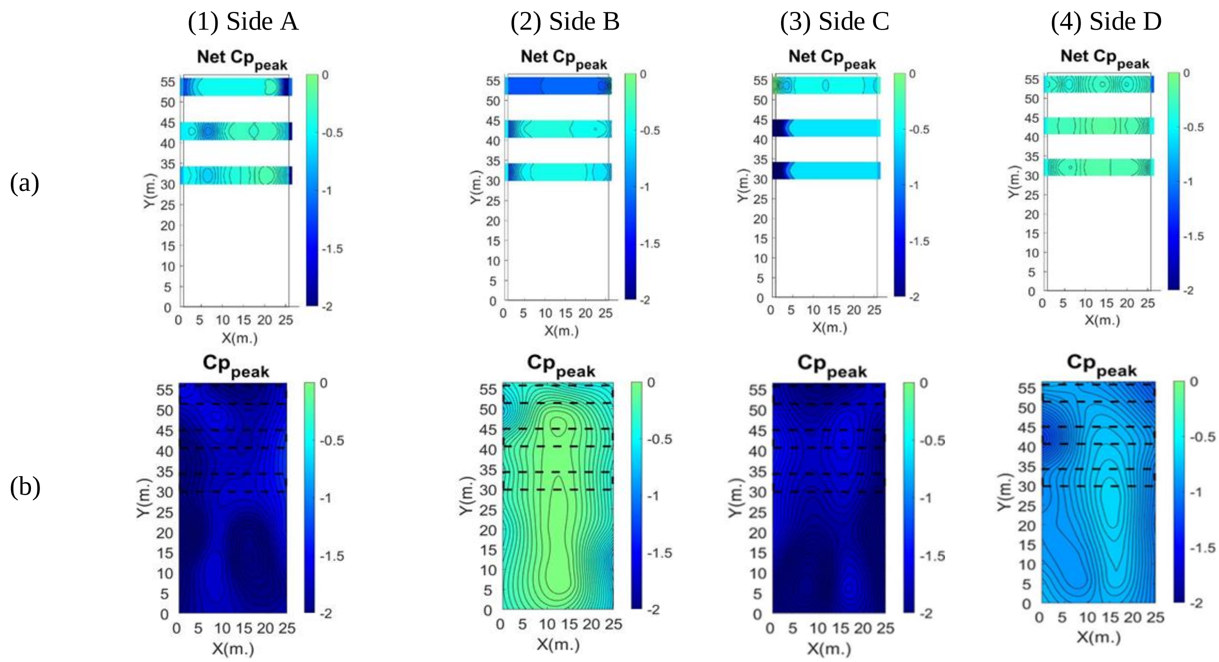

Figure 2. (a) Net Cp_{min}, (b) External Cp_{min} for 0 degrees – Scale 1:67

To study the effect of the tap arrangement and required resolution for pressure taps on the balcony panel handrail corners, four different tap layouts were evaluated at scale 1:25. The results (Figure 3) show that having the pressure taps near the edges is necessary for capturing an accurate measurement of high suctions.

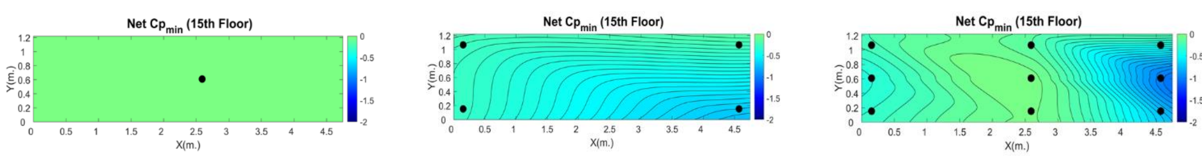

Figure 3 – Effect of pressure tap layout on Net Cp_{min} on 15th floor balcony.

ACKNOWLEDGEMENT

We gratefully acknowledge the financial support of The State of Florida Division of Emergency Management and the National Science Foundation for supporting the NHERI Wall of Wind Experimental Facility with Award# 1520853 for this project. Additionally, we acknowledge the support of the NHERI with Award #2037899.

REFERENCES

Moravej, M. (2018). Investigating Scale Effects on Analytical Methods of Predicting Peak Wind Loads on Buildings. Florida International University.

Asghari Mooneghi, M. (2014). Experimental and Analytical Methodologies for Predicting Peak Loads on Building Envelopes and Roofing Systems Dissertation. FIU Electronic Theses and Dissertations. Florida International University, December 2014.

Asghari Mooneghi, M., Chowdhury, A.G., Irwin, P. (2015). Partial Turbulence Simulation Method for Small Structures. Conference Paper, June 2015.

Index of abstracts by program reference number